Yun Lai Zhou · Magd Abdel Wahab · Nuno M. M. Maia · Linya Liu · Elói Figueiredo *Editors*

Data Mining in Structural Dynamic Analysis

A Signal Processing Perspective

Springer

Data Mining in Structural Dynamic Analysis

Yun Lai Zhou · Magd Abdel Wahab ·
Nuno M. M. Maia · Linya Liu ·
Elói Figueiredo
Editors

Data Mining in Structural Dynamic Analysis

A Signal Processing Perspective

Springer

Editors
Yun Lai Zhou
Department of Civil
and Environmental Engineering
National University of Singapore
Singapore, Singapore

Nuno M. M. Maia
Department of Mechanical Engineering
Technical University of Lisbon
Lisbon, Portugal

Elói Figueiredo
Faculty of Engineering
Lusófona University
Lisbon, Portugal

Magd Abdel Wahab
Faculty of Engineering and Architecture
Ghent University, Laboratory Soete
Ghent, Belgium

Linya Liu
Engineering Research Center of Railway
Environment Vibration and Noise, Ministry
of Education
East China Jiaotong University
Nanchang, China

ISBN 978-981-15-0500-3 ISBN 978-981-15-0501-0 (eBook)
https://doi.org/10.1007/978-981-15-0501-0

© Springer Nature Singapore Pte Ltd. 2019
This work is subject to copyright. All rights are reserved by the Publisher, whether the whole or part of the material is concerned, specifically the rights of translation, reprinting, reuse of illustrations, recitation, broadcasting, reproduction on microfilms or in any other physical way, and transmission or information storage and retrieval, electronic adaptation, computer software, or by similar or dissimilar methodology now known or hereafter developed.
The use of general descriptive names, registered names, trademarks, service marks, etc. in this publication does not imply, even in the absence of a specific statement, that such names are exempt from the relevant protective laws and regulations and therefore free for general use.
The publisher, the authors and the editors are safe to assume that the advice and information in this book are believed to be true and accurate at the date of publication. Neither the publisher nor the authors or the editors give a warranty, expressed or implied, with respect to the material contained herein or for any errors or omissions that may have been made. The publisher remains neutral with regard to jurisdictional claims in published maps and institutional affiliations.

This Springer imprint is published by the registered company Springer Nature Singapore Pte Ltd.
The registered company address is: 152 Beach Road, #21-01/04 Gateway East, Singapore 189721, Singapore

Preface

The structural health monitoring (SHM) field is concerned with increasing demand for improved and more continuous condition assessment of infrastructures to better face the challenges presented by modern societies. Thus, the applicability of computer science techniques for SHM applications has attracted the attention of researchers and practitioners in the last two decades.

This book aims to define and summarize the application of data mining for SHM of infrastructures, including bridges, railway transport systems, wind turbines, buildings, and so on. Data mining comprises selecting the appropriate models and applying those for searching patterns in the features extracted from monitoring data. Herein, the machine learning algorithms play an important role to unveil hidden patterns. The output of the trained algorithms is used to infer knowledge and to support the decision-making process.

Data mining has been a research hotspot in computer science, in the past decades, and it demonstrates a bright future in other fields like civil and mechanical engineering, as it focuses on finding useful information in the data, explaining the theories hidden behind engineering phenomena, which can be used to generate knowledge about the structural state condition.

Various engineers from different fields, who are specialized in the data mining, were invited to write all the chapters. Therefore, this book is expected to provide a common ground for beginners in the fields of structural health monitoring and structural dynamic analysis.

Singapore, Singapore — Yun Lai Zhou
Ghent, Belgium — Magd Abdel Wahab
Lisbon, Portugal — Nuno M. M. Maia
Nanchang, China — Linya Liu
Lisbon, Portugal — Elói Figueiredo

Contents

About the Editors

Yun Lai Zhou Universidade Lusofona, Portugal.

Yun Lai Zhou is Adjunct Professor in Universidade Lusofona, Portugal, and also serves as Research Fellow in the Department of Civil and Environmental Engineering at Hong Kong Polytechnic University, Hong Kong SAR, China. He obtained his Ph.D. in 2015, in civil engineering from Technical University of Madrid, Spain. He has authored and co-authored more than 50 scientific publications in international journals and conference proceedings on the subject of structural health monitoring and structural dynamic analysis, fracture mechanics, he also co-edited three books in structural health monitoring and data mining in structural dynamic analysis, and his research interests include structural dynamic analysis and vibration mitigation, structural health monitoring, system identification, and fracture mechanics. e-mail: yunlai.zhou@alumnos.upm.es

Magd Abdel Wahab Department of Electrical Energy, Metals, Mechanical Constructions and Systems, Ghent University, Belgium.

Magd Abdel Wahab is Professor of applied mechanics in the Soete Laboratory at Ghent University, Belgium. He received his B.Sc., 1988, in civil engineering and his M.Sc., 1991, in structural mechanics, both from Cairo University, Egypt. He completed his Ph.D. in fracture mechanics in 1995 from KU Leuven, Belgium. He was awarded the degree of Doctor of Science from the University of Surrey in 2008. He has published more than 210 scientific papers and technical reports in solid mechanics and dynamics of structures. His research interests include fracture mechanics, damage mechanics, fatigue of materials, durability, and dynamics and vibration of structures. e-mail: magd.abdelwahab@ugent.be

Nuno M. M. Maia Instituto Superior Tecnico, University of Lisbon, Portugal.

Nuno M. M. Maia had his habilitation in mechanical engineering in 2001 from Instituto Superior Tecnico, University of Lisbon, Portugal. He obtained his first degree in 1978 and master's degree in 1985, both in mechanical engineering from Instituto Superior Tecnico, University of Lisbon. He received his Ph.D. in mechanical vibrations (1989) from Imperial College London, UK. He has authored

and co-authored two textbooks and about 200 scientific publications in international journals and conference proceedings on the subject of modal analysis and structural dynamics. He is Associate Editor of the Shock and Vibration Journal, belongs to the Editorial Advisory Board of the Journal of Vibration and Control, is Member of the Editorial Board of the Mechanical Systems and Signal Processing, Member of the Society for Experimental Mechanics (SEM), Member of the International Institute of Acoustics and Vibration (IIAV), and Member of the Portuguese Society of Acoustics (SPA), where he is responsible for the area of vibrations. He has participated in and coordinated various national and international research projects in the area of modal analysis and structural vibrations, and has been responsible for the organization of the International Conference on Structural Engineering Dynamics (ICEDyn), since 2002. His current research interests are modal analysis and modal testing, updating of finite element models, coupling and structural modification, damage detection in structures, modeling of damping, transmissibility in multiple degree-of-freedom systems, and force identification. e-mail: nuno.manuel.maia@tecnico.ulisboa.pt

Linya Liu Engineering Research Center of Railway Environment Vibration and Noise, Ministry of Education, East China Jiaotong University, China.

Linya Liu is Professor of rail system noise and vibration control in East China Jiaotong University, China. He received his B.Sc., 1996, in Southwest Jiaotong University, China; he completed his Ph.D. in 2006 from Tongji University, China, both in highway and railway engineering. He dedicates his research in the field of static and dynamic structural analysis, vibration mitigation, and noise control, especially for the rail system components including floating track slab. He has authored and co-authored several books and more than 60 scientific publications in international journals and conference proceedings. e-mail: lly@ecjtu.edu.cn

Elói Figueiredo Faculty of Engineering, Lusófona University, Portugal.

Elói Figueiredo received his Ph.D. in civil engineering in 2010, M.Sc. in structures of civil engineering in 2007, and licentiate in civil engineering in 2004. He started teaching in 2010 at the Catholic University of Portugal, Portugal, and is currently Associate Professor in the Faculty of Engineering of Lusófona University in Lisbon, Portugal. He is also Technical Consultant in the field of monitoring and maintenance of bridges. He has dedicated his academic career teaching courses in the field of static and dynamic structural analysis, soil mechanics, foundation engineering design, seismic engineering, as well as design of reinforced and prestressed concrete structures. In terms of scientific research, he has mainly worked on structural health monitoring and maintenance of bridges, especially on vibration-based structural identification and evaluation. He has published over 70 scientific publications in international journals and conference proceedings. e-mail: eloi.figueiredo@ulusofona.pt

Damage Detection for Structural Health Monitoring of Bridges as a Knowledge Discovery in Databases Process

Moisés Silva, Adam Santos and Elói Figueiredo

Abstract The structural health monitoring (SHM) field is concerned with the increasing demand for improved and more continuous condition assessment of engineering infrastructures to better face the challenges presented by modern societies. Thus, the applicability of computer science techniques for SHM applications has attracted the attention of researchers and practitioners in the last few years, especially to detect damage in structures under operational and environmental conditions. In the SHM for bridges, the damage detection can be seen as the end of a process to extract knowledge regarding the structural state condition from vibration response measurements. In that sense, the damage detection has some similarities with the Knowledge Discovery in Databases (KDD) process. Therefore, this chapter intends to pose damage detection in bridges in the context of the KDD process, where data transformation and data mining play major roles. The applicability of the KDD for damage detection is evaluated on the well-known monitoring data sets from the Z-24 Bridge, where several damage scenarios were carried out under severe operational and environmental effects.

Keywords Knowledge discovery in databases process · Data mining · Damage identification · Bridge monitoring · Vibration measurements · Structural health monitoring

M. Silva
Applied Electromagnetism Laboratory, Universidade Federal do Pará, R. Augusto Corrêa, Guamá 01, Belém, Pará 66075-110, Brazil

A. Santos
Faculty of Computing and Electrical Engineering, Universidade Federal do Sul e Sudeste do Pará, F. 17, Q. 4, L. E., Marabá, Pará 68505-080, Brazil

E. Figueiredo (✉)
Faculty of Engineering, Universidade Lusófona de Humanidades e Tecnologias, Campo Grande 376, 1749-024 Lisbon, Portugal
e-mail: eloi.figueiredo@ulusofona.pt

CONSTRUCT—Institute of R&D in Structures and Construction, R. Dr. Roberto Frias s/n, 4200-465 Porto, Portugal

© Springer Nature Singapore Pte Ltd. 2019

Y. L. Zhou et al. (eds.), *Data Mining in Structural Dynamic Analysis*,
https://doi.org/10.1007/978-981-15-0501-0_1

1 Introduction

The bridges play a crucial role in modern societies, regardless of culture, geographical location, or economic development. The safest, economical, and most durable bridges are those that are well managed and maintained. Health monitoring represents an important tool in management activities as it permits one to identify early and progressive structural damage [15]. Overall, the massive data obtained from monitoring systems must be transformed to meaningful information to support planning and designing of maintenance activities, increase the safety, verify hypotheses, reduce uncertainty, and widen the knowledge and insight concerning the monitored structure.

Therefore, the process of implementing an autonomous damage identification strategy for civil, mechanical, and aerospace engineering infrastructure is traditionally referred to as structural health monitoring (SHM) [17]. The SHM process involves the observation of a structure over time using periodically sampled response measurements from an array of sensors, the extraction of damage-sensitive features from these measurements, and the statistical analysis of these features to infer the actual structural condition. The structural condition evaluation concept generally follows the damage identification hierarchy composed of five levels (Sect. 2.1). Acknowledging the existence of other levels and their importance for a more comprehensive information on the presence of damage, this chapter poses the SHM process mostly in the context of the first level—damage detection. It is important to note that, nowadays, the SHM is certainly one of the most powerful tools for infrastructure asset management, as it can provide information from the structural condition in real time, which improves the decision making regarding maintenance activities.

The damage detection can also be seen as the end of a process to extract knowledge regarding the structural state condition from vibration response measurements (e.g., displacements and accelerations). Therefore, the entire process for damage detection has some similarities with the Knowledge Discovery in Databases (KDD) process (Sect. 2.2). Basically, KDD is the overall process of extracting and revealing useful information from massive raw data measurements and transforms it into knowledge for decision making. This process is broadly applied in many fields, such as healthcare industry, financial market, advertising, bioinformatics, astronomy, and others [2, 3, 12, 27–29, 35]. The KDD process can be broken down into five steps [18]: data selection, data preprocessing, data transformation, data mining, and data interpretation and evaluation for knowledge discovery. Even though all those steps are important for knowledge generation, this chapter gives more attention to the data transformation (Sect. 3) and data mining (Sect. 4) steps, as those are more directly related to the damage detection.

In most recent years, some concepts of KDD have already been posed in the context of statistical pattern recognition (SPR) paradigm for SHM [17]. The SPR paradigm is composed of four stages: operational evaluation, data acquisition, feature extraction, and statistical modeling for feature classification [21]. As a comparison, the data transformation step is related to the feature extraction stage, where several

techniques are used to unveil signatures from the raw data in a lower dimensional space; data mining and data interpretation and evaluation steps are related to the statistical modeling for feature classification stage, where machine learning algorithms and statistical models are used to uncover hidden patterns (e.g., clusters) and to transform information into knowledge.

Therefore, this chapter intends to pose damage detection for SHM in the context of the KDD process, by presenting, discussing, and applying several feature extraction techniques for data transformation as well as machine learning algorithms for data mining and data interpretation. The applicability of the KDD process for damage detection is evaluated on the well-known monitoring data sets from the Z-24 Bridge, where several damage scenarios were carried out under severe environmental effects (Sect. 5).

2 Knowledge Discovery in Databases for Damage Detection

This section defines the meaning of knowledge in the context of SHM and presents the general concept of the KDD process for damage detection in bridges.

2.1 Knowledge in SHM and the Hierarchical Structure of Damage Identification

In SHM, knowledge is all the relevant information about the structural condition, which can be used to support the decision-making process regarding maintenance and repair of bridges. The structural condition evaluation can be in the form of a damage identification hierarchy, i.e., it can be regarded as a sequence of different levels of knowledge about damage and how it affects the structure.

The damage identification should be as detailed as possible to describe the damage impact on the structural system. Therefore, in a broad sense, developments on damage identification can be divided into three areas: damage detection, damage diagnosis, and damage prognosis. Nonetheless, damage diagnosis can be subdivided to better characterize the damage in terms of location, type, and severity. Thus, as depicted in Fig. 1, the hierarchical structure of damage identification can be decomposed in five levels which answer the following questions [19]:

1. Is the damage present in the system (detection)?
2. Where is the damage (localization)?
3. What kind of damage is present (type)?
4. What is the extent of damage (severity)?
5. How much useful lifetime remains (prognosis)?

The answers to the questions above can only be made in a sequential manner. For example, the answer to the severity of damage can only be made with a priori

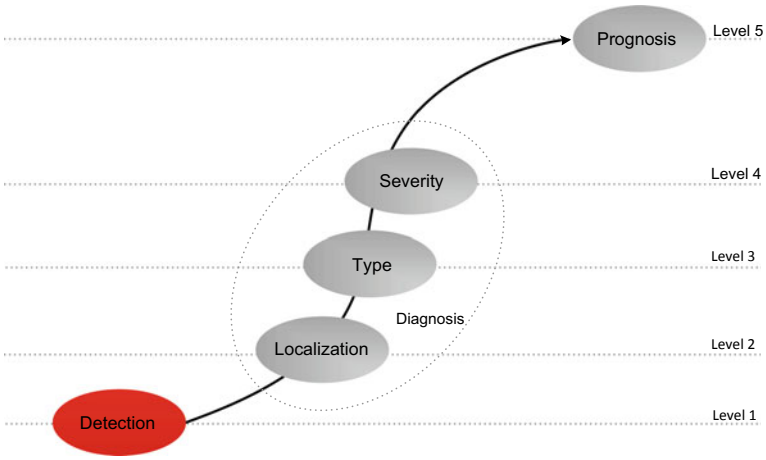

Fig. 1 Hierarchical structure of damage identification

knowledge of the type of damage. When applied in an unsupervised mode, machine learning algorithms are typically used to answer questions regarding the detection and localization of damage [24]. When applied in a supervised mode and coupled with physics-based models, the statistical algorithms can be used to better determine the type of damage, severity, and the remaining useful lifetime [26]. At level five, the damage prognosis cannot be accomplished without an understanding of the damage accumulation process. For further discussion on the concept of damage prognosis, one should read the reference [14]. Herein, only the first level is addressed.

2.2 Knowledge Discovery in Databases

As highlighted in Fig. 2, the KDD process can be described as a five-step approach: data selection, data preprocessing, data transformation, data mining, and data interpretation and evaluation.

Data selection comprises the creation of a target data set from raw data by considering important variables, which can influence the application domain in distinct aspects. For this step, it is crucial significant prior knowledge related to the purpose of the application.

Data preprocessing involves data preparation or cleaning procedures, such as removing noise and outliers when necessary, handling missing and unknown data values, and accounting for time sequence information and known seasonality.

Data transformation includes extracting or estimating informative and useful features to represent the data and applying dimensionality reduction and/or transformation methods to reduce the effective number of variables under consideration or to achieve better representations for the data in new projected dimensions.

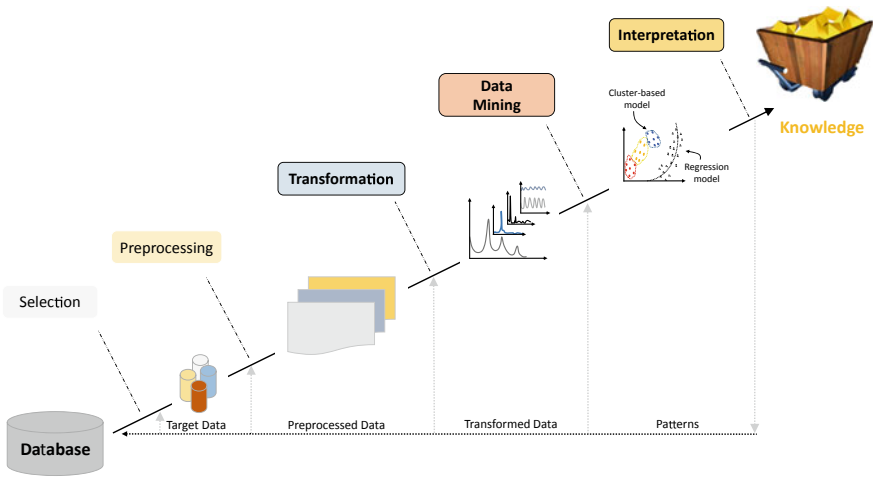

Fig. 2 Traditional five-step KDD process

Data mining comprises selecting the appropriate models (e.g., classification, regression, sequence analysis, or clustering) and applying those for searching patterns in the features extracted from the data. Herein, the machine learning algorithms play an important role to unveil hidden patterns [21]. The output of the fitted models plays an important role in the inferred knowledge, which should be judged by human as useful or not.

Data interpretation and evaluation encompass interpreting and visualizing the extracted patterns, removing irrelevant ones, and converting comprehensive information into knowledge. This step also includes incorporating the knowledge into the decision-making process.

In the context of SHM and damage detection, as highlighted in Fig. 3, after the data be selected and preprocessed, the data transformation step fits a model to the data in order to extract features, forming a new data set. Afterward, statistical models (e.g., machine learning algorithms) perform the mining of patterns related to the undamaged and damaged structural conditions, by means of a training phase in which only the features related to the normal structural condition are learned. The test phase is where the algorithms classify a new condition as undamaged or damaged, whether it deviates from the learned pattern or not, according to a threshold and following an outlier detection perspective. The decision making is then based on the interpretation and evaluation of the classification results in the form of damage indicators (DIs), derived from the mining step. The DIs can then be translated into knowledge, i.e., structural condition evaluation and the need for visual inspections, maintenance, or demolition activities.

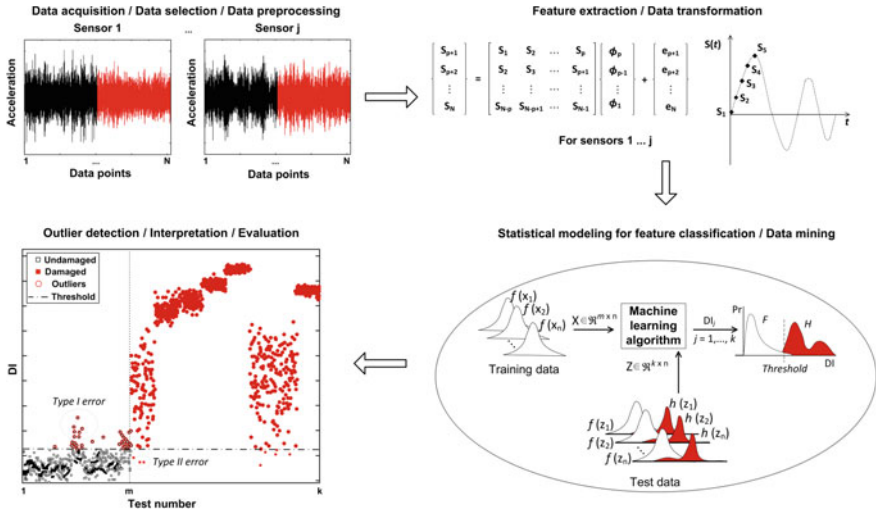

Fig. 3 Relation between the KDD process and SPR paradigm for damage detection (adapted from [46])

3 Data Transformation for Feature Extraction

3.1 Definition of Damage-Sensitive Feature

The data transformation is often described as a key step to ensure the reliability of SHM systems, as it directly affects the effectiveness and accuracy of the damage detection. Basically, with a set of features obtained from the data transformation, carrying information from the structural condition, the data mining step can be performed with less uncertainty and with minimal computational efforts.

During the condition monitoring of a structure, there is often multiple sensors mounted at different locations, acquiring varied types of physical parameters. From the collected raw data, features sensible to damage are extracted to support the structural condition evaluation. Therefore, a damage-sensitive feature is some quantity extracted from the structural response data that is correlated with the presence of damage in a structure (e.g., modal parameters, maximum displacements, regression model parameters, and residual errors). An adequate damage-sensitive feature varies consistently in accordance with the level of damage in the structure. However, in most real-world applications, the features directly extracted from the raw data are often correlated with multiple sources of operational and environmental variability (e.g., traffic, temperature, moisture, and wind speed), which increase uncertainty in the damage detection as it can mask damage-related changes in the features as well as alter the correlation between their magnitude and the damage level [24]. Besides, there is no universal kind of feature or physical variable appropriate for all damage

scenarios. Thus, the type of feature varies with the kind of structure to be monitored and the type of damage to be found. These facts suggest the usage of several techniques to extract alternative features in order to reduce uncertainty and increase the likelihood of damage detection.

3.2 Domains for Data Transformation and Feature Extraction

Many different techniques from alternative domains have been used for data transformation and feature extraction for SHM applications [22]. There is a wide range of features used in current SHM applications from very diverse fields of study (e.g., from econometrics to physical parameters). The most common ones fall into the following domains [58]:

1. Time-domain features: mostly regarded to time-series processing. Common techniques use the coefficients of auto-regressive (AR) models and auto-regressive moving average (ARMA) models as input features [23]. Although providing stable results, they work for slightly damped systems and require a significant number of time-domain samples;
2. Frequency-domain features: conventionally related to the Fourier transform. Frequency components are estimated from raw data in order to decompose and analyze their spectral content [60]. In this domain, the modal properties [1, 8, 10, 13, 20, 36] are vibration parameters (e.g., natural frequencies, mode shapes, modal curvature, and flexibility matrix) as features for damage detection, as they provide global on-site automated continuous monitoring due to their inherent physical properties (stiffness and mass);
3. Time–frequency-domain features: often represented by approaches based on the short-time Fourier transform (STFT), providing an effective characterization of time–frequency patterns of non-stationary signals;
4. Wavelet-based features: used to achieve a reasonable trade-off between frequency and time resolution with multiple choices of basis functions available. Conventionally performed using discrete wavelet transform (DWT) and wavelet packet transform (WPT). They can be very effective features when modeled to match specific characteristics of the structure being monitored;
5. Empirical mode decomposition (EMD) features: performed by advanced signal processing algorithms, they are built to adaptively model time–frequency characteristics of non-stationary and/or nonlinear structural systems. Their end result is usually the decomposition of the input raw data into intrinsic mode functions (IMF).

3.3 Statistical-Based Techniques: Information Theory

The field of information theory also provides numerous approaches to examine and create more general features through analyzing fundamental relationships among data. More recently, these statistical-based techniques have been exploited for system identification applications [39]. These features commonly express uncertainties in random variables in terms of how much significance or representativeness the input data offers to the system. The most important information measures of this category are as follows:

1. Information entropy: also known as Shannon entropy, it is a measure of the uncertainty associated with random variables. In SHM, its most common use is for model updating or model order selection. However, its use as input features has started to attract global attention;
2. Kullback–Leibler divergence: used to measure the difference between probability density functions of random processes. It has also been used to evaluate the relationships of collected raw data;
3. Mutual information: quantifies common dependencies between processes, and similarly to the Leibler Divergence can be extended to evaluate shared information between random variables;
4. Transfer entropy: explores the concept of generalized synchronization and information transfer. Traditionally, it has been used for synchronized mechanical systems. When mechanical components desynchronize, this information can be measured in terms of the amount of transferred information.

3.4 Levels of Feature Extraction

Feature extraction techniques can also be categorized in terms of depth of the extracted features [6, 49, 53]. As feature extraction can be described as a process of feature fusion, it is possible to follow the conventional fusion operation level to divide the techniques into three levels:

1. Data-level fusion: performed on the collected raw data by integrating multisensor signals, comprising a first-level set of extracted features. Most features fall into this category;
2. Feature-level fusion: the process is performed on the first-level features by compressing them into a reduced set of derived variables; these second-level features retain the essential information of the original subset of features with less data;
3. Decision-level fusion: intrinsically related to the feature classification stage, the results of multiple classifiers are combined through majority voting approaches and used to perform further analysis. The output is not a new set of features, but some useful pattern.

The majority of the SHM studies for damage detection have been focused on the first-level feature extraction by identifying the dynamic properties of a monitored structure to relate the changes in the vibration characteristics to the damage occurrence [7, 9, 16, 45, 61]. Although each level can be applied for specific scenarios and different goals, the feature-level fusion is often more effective than the alternative ones, because the first-level features contain richer information about the structural condition and present physical interpretation.

Even though the first-level features work well for intelligent fault diagnosis, they still have deficiencies: (i) the extracted features are handcrafted built from time-domain signals and heavily depend on much prior knowledge and diagnostic expertise; (ii) those features compose very complex information under high influence of normal variability effects, which becomes difficult for the proper discrimination of damaged and undamaged conditions by machine learning algorithms; (iii) as the amount of data increases, more complex information must be learned, which enlarges the number of learned parameters to correctly perform feature classification and to identify the damage occurrence [8].

For these reasons, the second-level feature extraction techniques have been applied for monitoring scenarios where data from damaged conditions is available [31, 55]. However, technical and organizational issues have limited their application by structure managers in practice. Some reasons can be pointed out to the lack of a framework or guideline to perform damage identification, which results in no universally accepted feature extraction approach.

In the case of second-level features, it is possible to infer that their main representative techniques are the ones based on machine intelligence. More specifically using generative models, which model how the data was generated to perform categorization. Therefore, the ones based on principal component analysis (PCA) have been the most widely employed for SHM applications [52].

The traditional linear PCA has been adapted to act as a feature extraction and data normalization technique used to model, mainly, the effects of linear variations [57]. Very often, PCA-based approaches are used to model linear environmental and operational influences from undamaged first-level features. However, a major difficulty with this technique is the limited applicability in real-world SHM systems; if nonlinearities are present in the monitoring data, the linear PCA-based approach might fail to model the normal condition of a structure.

The auto-associative neural network (AANN) is a nonlinear version of the PCA intended to perform feature extraction, dimensionality reduction, and damage identification of multivariate data [56]. As demonstrated by Kramer [34], the AANN is capable of intrinsically performing a nonlinear mapping of the input variables, as it characterizes the underlying dependency of the identified features in terms of unobserved factors, i.e., a nonlinear PCA (NLPCA). The main issue of this approach is to determine the number of normal factors changing the actual behavior of the structure, as the number of factors retained by the model must be handcrafted discovered.

An alternative manner to perform NLPCA is to employ kernel functions along with the traditional linear PCA. The kernel trick allows the mapping of features to high-dimensional spaces, which can provide nonlinear strengths to the traditional PCA,

leading to a kernel PCA (KPCA) [38, 43, 59]. Although this technique achieved satisfactory results for data normalization and can be easily adapted for damage detection, it also revealed some loss of information as the principal components are retained based on 99% of the data variability.

Considered the current breakthrough in artificial intelligence, deep learning-based techniques have the potential to overcome the aforementioned problems of current feature extraction methods [5, 52]. In particular, auto-encoders (AEs) are equipped with extremely powerful mapping operators, yielding an adaptive representation of the input data into its bottleneck layer [30, 47]. These networks can be stacked to form a deep architecture and to perform reliable mapping operations.

Finally, Fig. 4 briefly shows a taxonomy of feature extraction techniques conventionally used for SHM applications. In some cases, techniques used to derive first-level features can be used in a second-level feature extraction fashion. However, most applications fit in one of the stated categories. Additionally, the second-level feature extraction framework for SHM can be summarized as shown in Fig. 5. Although this framework is specifically designed with deep auto-encoders, in fact, it summarizes the steps for any other application using different techniques to extract second-level features. Here, the auto-encoder is specified to illustrate the workflow used by the experimental tests carried out in Sect. 5.

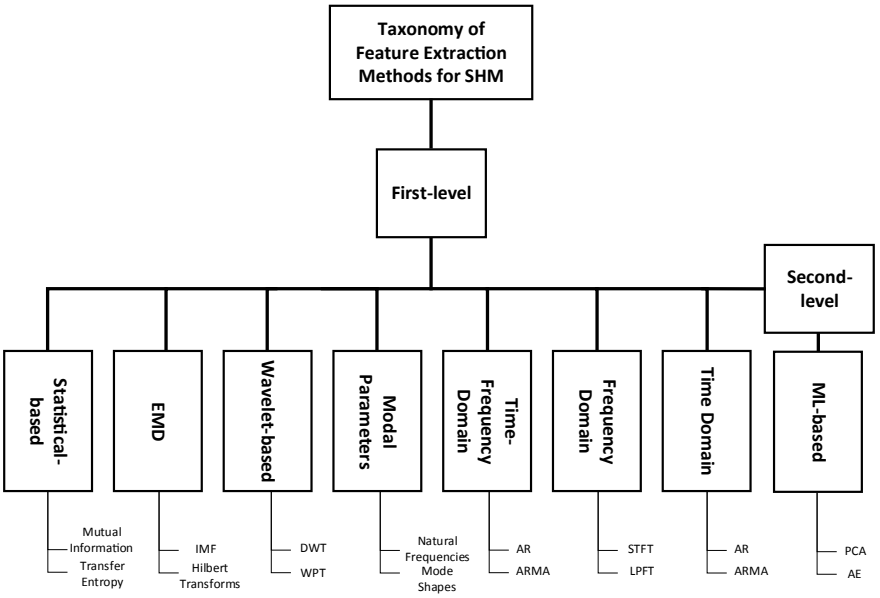

Fig. 4 Taxonomy of feature extraction methods for SHM

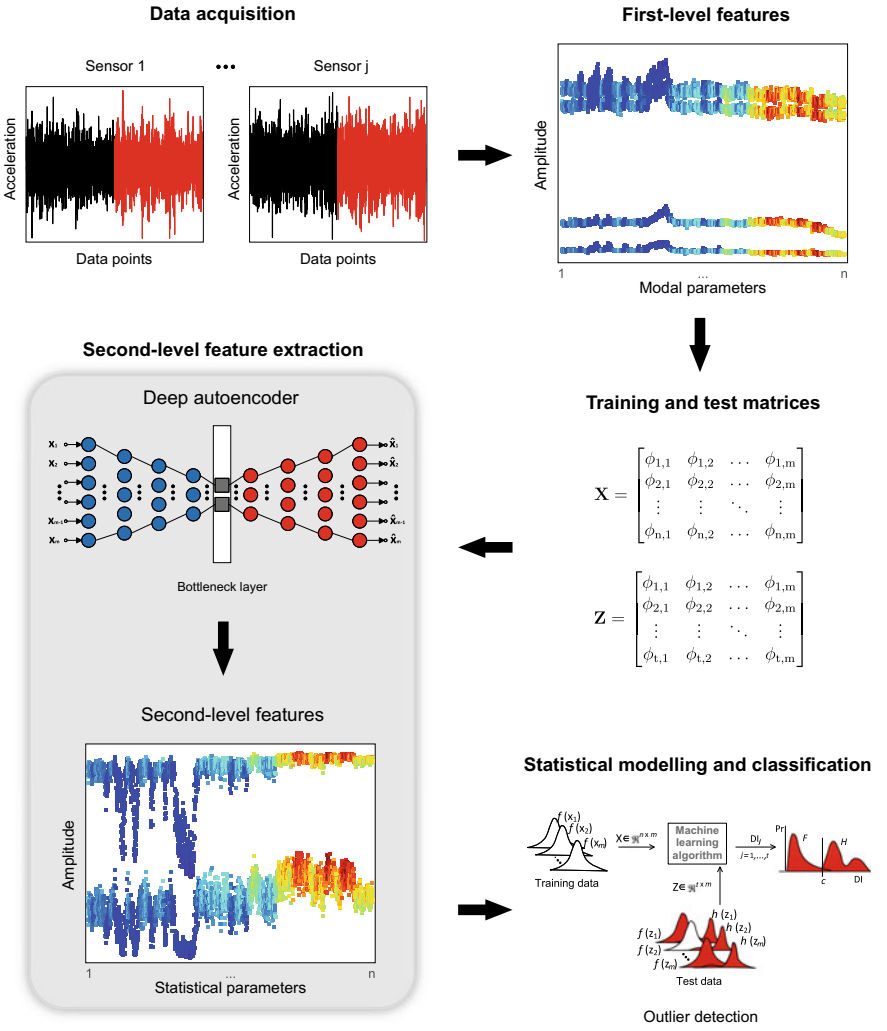

Fig. 5 Second-level feature extraction approach for statistical modeling and classification presented by [51]

4 Data Mining for Feature Classification

Data mining is especially related to the discovery of patterns in the features which comprise normal structural conditions, for posterior feature classification based on an outlier detection perspective. In this section, for illustration purposes, the working principles of two state-of-the-art machine learning algorithms are presented [21], where patterns are highlighted as the formation of clusters associated with structural

state conditions. In the end, this section tries to link data mining and data interpretation and evaluation, for the generation of knowledge about the structural condition.

4.1 An Outlier Detection Perspective: Goals and Challenges

In an outlier detection perspective for feature classification, one possible approach for data mining is a clustering procedure combined with a (dis)similarity metric and a threshold. Thus, the goals of data mining for damage detection are (1) learning clusters that correspond to the normal structural conditions in the training phase; (2) estimating a threshold from training data to classify new feature vectors; (3) computing a DI for each new observation considering the (dis)similarity between this observation and the centers of the clusters; (4) classifying each DI according to a defined threshold.

As shown in [50], the discovered clusters play a crucial role for mining patterns and extracting knowledge from the training data, as they can be correlated with the physical states of the structure under operational and environmental influences. Often, the better the clusters can represent the normal structural conditions, the better is the classification performance.

Some of the challenges in the data mining for feature classification are discussed as follows:

- Updating statistical models as new data becomes available;
- The choice of the machine learning algorithm, for a specific data mining task, must be done as a function of the damage-sensitive features used as well as the distribution of them in the feature space;
- The feature classification is currently posed in the context of a binary classification, with a trade-off between false-positive and false-negative indications of outliers. It recognizes that false-positive classifications may have different consequences than false-negative ones. Therefore, analytical approaches to defining threshold levels must balance trade-offs between false-positive and false-negative indications, minimize false-positives when economic concerns drive the SHM applications, and minimize false-negatives when life safety issues drive the SHM systems.

4.2 Machine Learning Algorithms

In SHM, machine learning is the science of getting computers and algorithms to model the reality without knowing the physical laws of structures [21]. Two machine learning algorithms for data mining are described in the context of SHM. These algorithms are especially relevant in cases where damage-sensitive features are affected by changes caused by operational and environmental variability and changes caused by damage.

For generalization purposes, one should assume a training data matrix, $\mathbf{X} \in \mathbb{R}^{n \times d}$, with d-dimensional feature vectors from n different operational and environmental conditions when the structure is undamaged and a test data matrix, $\mathbf{Z} \in \mathbb{R}^{l \times d}$, where l is the number of feature vectors from the undamaged and/or damaged conditions.

4.2.1 Mahalanobis Squared Distance

The Mahalanobis squared distance (MSD) is a metric for multivariate statistics outlier detection [57]. Considering the training matrix, $\mathbf{X}$, with multivariate mean vector, $\boldsymbol{\mu}$, and covariance matrix, $\boldsymbol{\Sigma}$, the MSD (in the context of SHM, also called as DI) between feature vectors from $\mathbf{X}$ and any new feature vector (or observation) from the test matrix, $\mathbf{Z}$, is computed as

$$\mathrm{DI}\left(\mathbf{z}\right) = \left(\mathbf{z} - \boldsymbol{\mu}\right) \boldsymbol{\Sigma}^{-1} \left(\mathbf{z} - \boldsymbol{\mu}\right)^{\top}. \tag{1}$$

The assumption is that if a new observation is obtained from the data collected on the damaged condition, which might include sources of operational and environmental variability, the observation is further from the mean of the normal condition and might be considered an outlier. On the other hand, if an observation is obtained from a system within its undamaged condition, even with operational and environmental variability, this feature vector is closer to the mean of the normal condition.

4.2.2 Gaussian Mixture Model

The Gaussian mixture model (GMM) carries out a cluster-based model, using multivariate finite mixture models that aim to capture the main clusters/components of features, which correspond to the normal and stable state conditions of a bridge, even when it is affected by extreme operational and environmental conditions. Afterward, an outlier detection strategy is implemented in relation to the chosen main components of states [20]. Basically, the damage detection is carried out based on multiples MSD-based algorithms, where the covariance matrices and mean vectors are functions of the main components.

Suppose that a training matrix $\mathbf{X}$ is available, arising from a mixture of Q distributions [37],

$$f_{\mathrm{mix}}\left(\mathbf{x}\right) = \sum_{q=1}^{Q} \eta_q \, f_q\left(\mathbf{x}|\boldsymbol{\theta}_q\right), \tag{2}$$

with $f_q\left(\mathbf{x}|\boldsymbol{\theta}_q\right)$ being the density of a distribution from a known parametric distribution family $\tau\left(\boldsymbol{\theta}\right)$. In this setting, one is concerned with the estimation of the component parameters $\boldsymbol{\theta} = \left(\boldsymbol{\theta}_1, \ldots, \boldsymbol{\theta}_Q\right)$ and the mixture weights $\eta = \left(\eta_1, \ldots, \eta_Q\right)$ of

the underlying mixture distributions, based on the data $\mathbf{X}$. In this case, one assumes underlying multivariate Gaussian mixture distributions, and therefore, each component density is a d-variate Gaussian function in form of [37]

$$f\left(\mathbf{x}|\boldsymbol{\mu}_q, \boldsymbol{\Sigma}_q\right) = \frac{\exp\left\{-\frac{1}{2}\left(\mathbf{x}-\boldsymbol{\mu}_q\right)^{\top}\boldsymbol{\Sigma}_q^{-1}\left(\mathbf{x}-\boldsymbol{\mu}_q\right)\right\}}{(2\pi)^{d/2}\sqrt{\det\left(\boldsymbol{\Sigma}_q\right)}}, \tag{3}$$

with unknown parameters $\boldsymbol{\theta}_q = \{\boldsymbol{\mu}_q, \boldsymbol{\Sigma}_q\}$, namely mean vectors $\boldsymbol{\mu}_q$ and covariance matrices $\boldsymbol{\Sigma}_q$. The mixture weights are constrained to be $\sum_{q=1}^{Q}\eta_q = 1$. The complete GMM is parameterized by the mean vectors, the covariance matrices, and the mixture weights from all component densities, $\{\boldsymbol{\mu}_q, \boldsymbol{\Sigma}_q, \eta_q\}_{q=1,\ldots,Q}$.

The parameters are estimated from the training data using the classical maximum likelihood (ML) estimation based on the expectation–maximization (EM) algorithm [11]. Other methods can be used to estimate the parameters of a GMM, as proposed in [25]. The Bayesian information criterion (BIC) [4] is used to determine the appropriate number of components, which introduces a penalty term for the number of parameters in the model.

For the outlier detection strategy, and for each observation $\mathbf{z}$, one needs to estimate Q DIs. Basically, for each main component q of the data,

$$\mathrm{DI}_q\left(\mathbf{z}\right) = \left(\mathbf{z}-\boldsymbol{\mu}_q\right)\boldsymbol{\Sigma}_q^{-1}\left(\mathbf{z}-\boldsymbol{\mu}_q\right)^{\top}, \tag{4}$$

where $\boldsymbol{\mu}_q$ and $\boldsymbol{\Sigma}_q$ represent all the observations from the q component of the data, when the structure is undamaged even though under varying operational and environmental conditions. Finally, for each observation, the DI is given by the smallest DI estimated on each component,

$$\mathrm{DI}\left(\mathbf{z}\right) = \min\left[\mathrm{DI}_q\left(\mathbf{z}\right)\right]. \tag{5}$$

4.2.3 Final Considerations: Data Interpretation and Evaluation

The performance of damage detection is a fundamental aspect to generate knowledge, in the context of the KDD process for bridges. Therefore, interpreting and evaluating the DIs, by inferring whether the structure is undamaged or damaged, is fundamental to support the bridge owners to make decisions.

Thus, for the two-class problem in SHM (binary classification), in which the two sets of cases are labeled as damaged (or positive, P) or undamaged (or negative, N), assuming a given threshold, there are four possible outcomes as summarized in Fig. 6. For a positive outcome, the case can be either true-positive (TP) if the observed is positive or false-positive (FP) if the observed is negative. On the other hand, for a negative outcome, the case can be either false-negative (FN) if the observed is

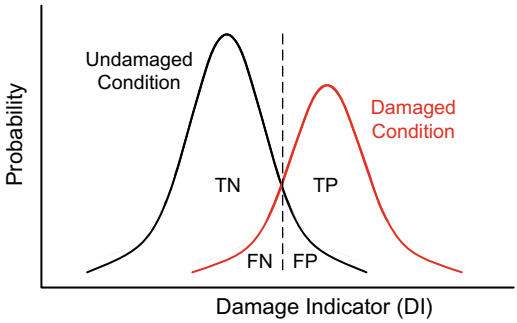

Fig. 6 Distributions from the undamaged and damaged conditions

positive or true negative (TN) if the observed is negative. The misclassifications of FP and FN are also known as Type I error and Type II error, respectively.

Therefore, false indications of damage fall into two categories: (i) false-positive damage indication (indication of damage when none is present, Type I error) and (ii) false-negative damage indication (no indication of damage when damage is present, Type II error). Errors of the first type are undesirable, as they will cause unnecessary downtime and consequent loss of revenue as well as loss of confidence in the monitoring system. More importantly, there are clearly safety issues if misclassifications of the second type occur [15].

5 Applicability and Discussion

This section intends to show the applicability of the KDD process, namely data transformation, data mining, and data interpretation and evaluation on data sets from the Z-24 Bridge. The goal is to compare the performance of a traditional GMM-based machine learning algorithm for data mining and feature classification when fed with first- and second-level features. The second-level feature extraction is performed using a stacked auto-encoder (SAE) recently proposed by [52]. This procedure intends to evaluate the impact of data transformation and data mining for damage detection and knowledge generation.

5.1 The Z-24 Bridge and Monitoring Scenario Description

The Z-24 Bridge was a post-tensioned concrete box girder bridge composed of a main span of 30 m and two side-spans of 14 m, as depicted in Fig. 7. The bridge, before complete demolition, was extensively instrumented and tested with the purpose of providing a reliable benchmark for vibration-based SHM in civil engineering [44]. A

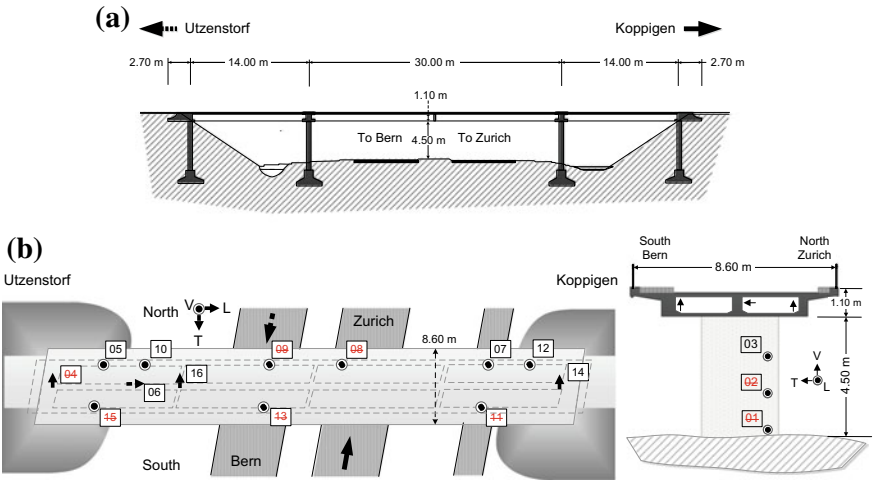

Fig. 7 Longitudinal section (**a**), and the location and orientation of accelerometers (**b**) on the Z-24 Bridge. Marked sensors failed during the monitoring campaign [41]

long-term monitoring test was carried out, from November 11, 1997, until September 10, 1998, to quantify the operational and environmental variability present on the bridge and to detect damage artificially introduced, in a controlled manner, in the last month of operation. Every hour, eight accelerometers captured the vibrations of the bridge as sequences of 65,536 samples (sampling frequency of 100 Hz) and other sensors measured environmental parameters, such as temperature at several locations [32, 33, 41].

Progressive damage tests were carried out in one-month time period (from August 4 to September 10, 1998) before the demolition of the bridge to prove that realistic damage has a measurable influence on the bridge dynamics [42], as summarized in Table 1 (the dates refer to the day that additional vibration tests were performed to fully characterize the structural condition of the bridge). Three examples of damage test scenarios are illustrated in Fig. 8. Note that the monitoring system was still running during the progressive damage tests, which permits one to validate the SHM system to detect cumulative damage on long-term monitoring.

5.2 *First-Level Features: Natural Frequencies*

The natural frequencies of the Z-24 Bridge are used as first-level features. They were estimated using a reference-based stochastic subspace identification method on vibration measurements from the accelerometers [40]. The first four natural frequencies estimated hourly from November 11, 1997, to September 11, 1998, with a total of 3932 observations, are highlighted in Fig. 9. The first 3470 observations

Table 1 Progressive damage test scenarios (the dates refer to the additional vibration measurements)

Date	Scenario description
04-08-98	Reference measur. I (undamaged condition)
09-08-98	After installation of the settlement system
10-08-98	Pier settlement = 2 cm
12-08-98	Pier settlement = 4 cm
17-08-98	Pier settlement = 8 cm
18-08-98	Pier settlement = 9.5 cm
19-08-98	Foundation tilt
20-08-98	Reference measur. II (removal of the settlement system)
25-08-98	Spalling of concrete (12 m^2)
26-08-98	Spalling of concrete (24 m^2)
27-08-98	Landslide at abutment
31-08-98	Concrete hinge failure
02-09-98	Failure of 2 anchor heads
03-09-98	Failure of 4 anchor heads
07-09-98	Rupture of 2 out of 16 tendons
08-09-98	Rupture of 4 out of 16 tendons
09-09-98	Rupture of 6 out of 16 tendons

Fig. 8 Damage scenarios carried out in the Z-24 Bridge: pier settlement (**a**), failure of anchor heads (**b**), and tendon rupture (**c**)

correspond to the undamaged structural condition under effects caused by the operational and environmental variability. The last 462 observations correspond to the damage progressive testing period, which is highlighted, especially in the second frequency, by a clear decay in the magnitude of this frequency.

The damage scenarios were performed in a sequential manner, which caused a cumulative degradation of the bridge. Therefore, this study assumes that the bridge operates within its undamaged condition (baseline or normal condition), under oper-

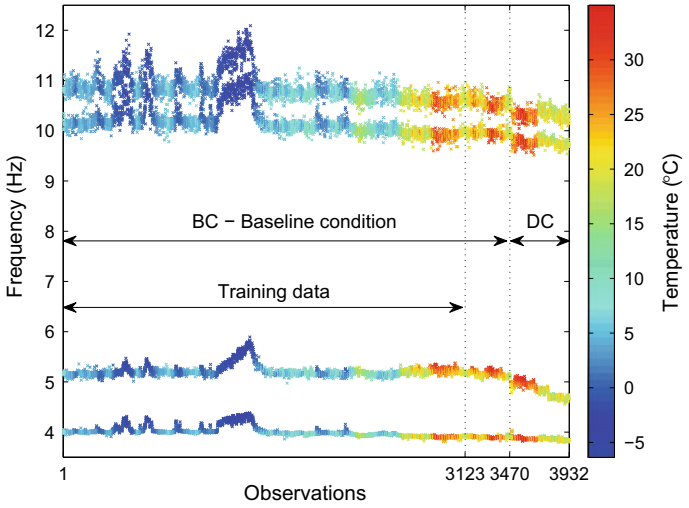

Fig. 9 First four natural frequencies of the Z-24 Bridge: 1–3470 baseline/undamaged condition (BC), 3471–3932 damaged condition (DC)

ational and environmental variability, from November 11, 1997, to August 4, 1998 (1–3470 observations). On the other hand, the bridge is considered damaged from August 5 to September 10, 1998 (3471–3932 observations). For the baseline condition period, the observed jumps in the natural frequencies are associated with the asphalt layer, in cold periods, which contributes, significantly, to the stiffness of the bridge, as evidenced in Fig. 9, indicating the need for a data normalization procedure to attenuate this variability. Besides, the significant influence of the temperature on the natural frequencies, and consequently on the structure dynamics, may be considered as nonlinear with distinguished behaviors below and above 0 °C [41, 42].

5.3 Second-Level Features: Hidden Normal Factors

The proposed SAE model is composed of eight mapping/demapping layers along with the input layer. As the number of nodes in the bottleneck layer implicitly represents the number of main normal factors, the bilinear structural behavior caused by the ambient temperature is represented by two nodes in this layer. The number of nodes in the remaining layers is selected through the procedure described in [54]. Therefore, the network has ten, seven, and three nodes in each one of the remaining mapping and demapping layers, along with four nodes in the input/output layers. The parameters of the network were adjusted based on the four natural frequencies (1–3123) shown in Fig. 9. Figure 10 shows the second-level features extracted at the bottleneck layer of the network as well as their dependency on the temperature.

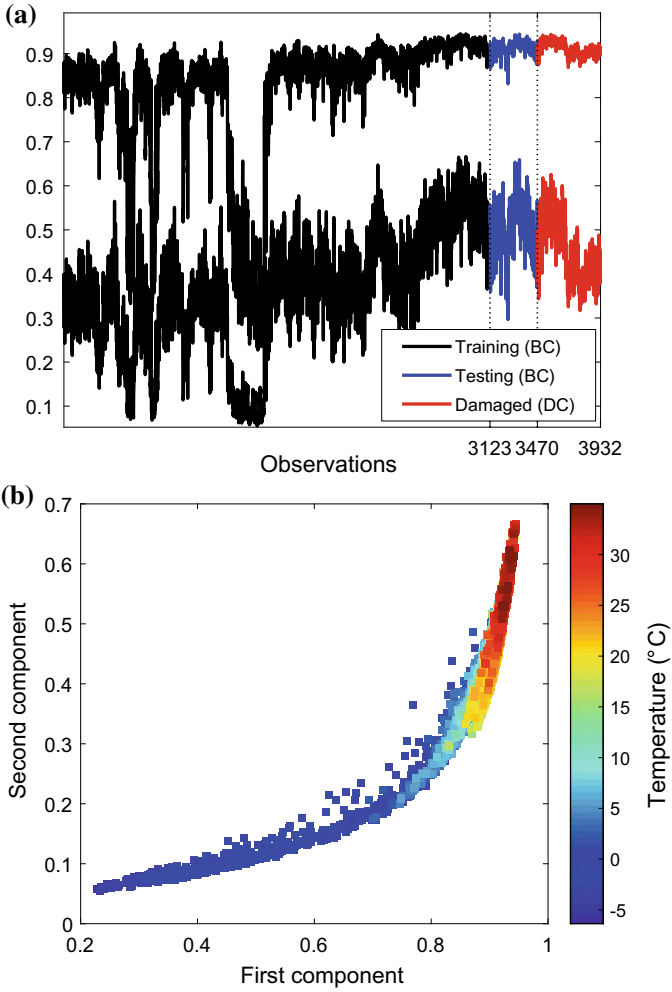

Fig. 10 Extracted second-level features of the SAE-based approach (**a**). Two-dimensional view (**b**)

For comparison purposes, the reliability of the information derived from the extracted features is attested in terms of information entropy. The Shannon's information entropy is the most common metric to verify the average uncertainty provided by a set of random variables [48]. The principle of maximum entropy is based on which probability distribution leaves the largest enduring uncertainty, revealing the maximum amount of information about the data (the maximum entropy). Therefore, Table 2 summarizes the values of entropy for the second-level feature extraction approach along with the first-level set of features composed of natural frequencies. Basically, the SAE-based approach attains the most informative set of features. The

Table 2 Shannon's information entropy for each set of extracted features [48] along with the corresponding number of extracted features

Features	Shannon's entropy	Number of features
First level: natural frequencies	2.3502	4
Second-level: normal factors	7.3084	2

robustness of this approach can be pointed out to the somewhat tedious mapping operations, which result in the ability to compose stronger features. These techniques are capable of learning slight nonlinear variations. Furthermore, the non-orthogonal projections performed by the SAE sustain the mapping of most part of the variance comprised in the natural frequencies, which is the main reason to the superior performance reached by the SAE.

5.4 Data Mining and Damage Detection

The data mining step is performed based on the EM-GMM algorithm implemented in accordance with [50]. For generalization purposes, the damage-sensitive features are split into training and test matrices. As shown in Figs. 10 and 11, the training matrix, $\mathbf{X}^{3123\times4}$, is composed of 90% of the undamaged observations. The remaining 10% is used during the test phase to make sure that the DIs do not fire off before the damage starts. The test matrix, $\mathbf{Z}^{3932\times4}$, is composed of all the data sets, even the ones used during the training phase. The number of normal components (or clusters) discovered for each set of features is summarized in Table 3.

In order to transform information into knowledge, i.e., to detect damage in the bridge and to evaluate the impact of the second-level feature extraction on the damage detection performance, the number of Type I and Type II errors and the DIs for the

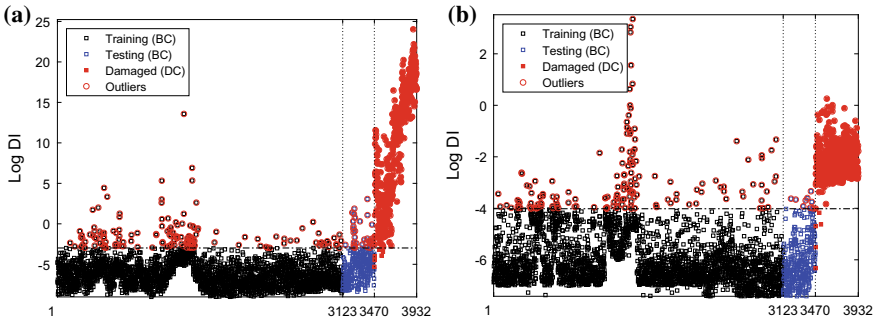

Fig. 11 Outlier detection based on the EM-GMM algorithm using the four natural frequencies (**a**) and two-dimensional extracted features of the second-level approach SAE (**b**)

Table 3 Number and percentage of Type I/II errors for each set of extracted features along with the number of components (Q) learned by the EM-GMM algorithm

Feature	Type I	Type II	Total	Q
First level: natural frequencies	190 (5.48%)	7 (1.52%)	197 (5.01%)	8
Second-level: normal factors	165 (4.76%)	5 (1.08%)	170 (4.32%)	7

test matrix are presented in Table 3 and Fig. 10, respectively. In particular, the GMM-based approach has the best performance in terms of undamaged data classification (4.76% of Type I errors) and total number of errors (4.32%), when the normal factors are used as features. Compared to the natural frequencies, the normal factors have demonstrated to slightly increase the sensitivity of the EM-GMM for the damage occurrence, as indicated by the reduced number of Type II errors, and confirming the information provided by Table 2. In conclusion, it turns out that when one attempts to model the normal condition of the structures, an error trade-off between minimizing Type I and Type II errors is required, which makes the second-level features (normal factors) more robust for damage assessment. Moreover, one can verify a significant decrease in the number of total errors, which means that in this case the second-level features increase the reliability of the entire monitoring system.

References

1. Bernal, D., Gunes, B.: Flexibility based approach for damage characterization: benchmark application. J. Eng. Mech. **130**(1), 61–70 (2004)
2. Bilenko, M., Richardson, M.: Predictive client-side profiles for personalized advertising. In: Proceedings of the 17th ACM SIGKDD International Conference on Knowledge Discovery and Data Mining, KDD '11, pp 413–421. ACM, New York (2011)
3. Borne, K.D.: Astroinformatics: data-oriented astronomy research and education. Earth Sci. Inf. **3**(1), 5–17 (2010)
4. Box, G.E.P., Jenkins, G.M., Reinsel, G.C.: Time Series Analysis: Forecasting and Control, 4th edn. Wiley, Hoboken (2008)
5. Brahma, P.P., Wu, D., She, Y.: Why deep learning works: a manifold disentanglement perspective. IEEE Trans. Neural Netw. Learn. Syst. **27**(10), 1997–2008 (2016)
6. Castanedo, F.: A review of data fusion techniques. Sci. World J. **2013** (2013)
7. Catbas, F.N., Aktan, A.E.: Condition and damage assessment: issues and some promising indices. J. Struct. Eng. **128**(8), 1026–1036 (2002)
8. Catbas, F.N., Gul, M., Burkett, J.L.: Conceptual damage-sensitive features for structural health monitoring: laboratory and field demonstrations. Mech. Syst. Signal Process. **22**(7), 1650–1669 (2008)
9. Cross, E.J., Manson, G., Worden, K., Pierce, S.G.: Features for damage detection with insensitivity to environmental and operational variations. Proc. R. Soc. Lond. A: Math. Phys. Eng. Sci. **468**(2148), 4098–4122 (2012). https://doi.org/10.1098/rspa.2012.0031
10. Cross, E., Koo, K., Brownjohn, J., Worden, K.: Long-term monitoring and data analysis of the tamar bridge. Mech. Syst. Signal Process. **35**(1–2), 16–34 (2013)
11. Dempster, A.P., Laird, N.M., Rubin, D.B.: Maximum likelihood from incomplete data via the EM algorithm. J. R. Stat. Soc. Ser. B (Methodological) **39**(1), 1–38 (1977)

12. Deng, J., Li, J., Wang, D.: Knowledge discovery from vibration measurements. Sci. World J. **2014**(1), 1–15 (2014)
13. Farrar, C.R., Jauregui, D.A.: Comparative study of damage identification algorithms applied to a bridge: II. Numerical study. Smart Mater. Struct. **7**(5), 720 (1998)
14. Farrar, C.R., JLieven N.A.: Damage prognosis: the future of structural health monitoring. Philos. Trans. R. Soc. Lond. A: Math. Phys. Eng. Sci. **365**(1851), 623–632 (2007)
15. Farrar, C.R., Worden, K.: An introduction to structural health monitoring. Philos. Trans. R. Soc. A **365**(1851), 303–315 (2007)
16. Farrar, C.R., Worden, K.: Damage-Sensitive Features, vol. 7, pp. 161–243. Wiley, New York (2012)
17. Farrar, C.R., Doebling, S.W., Nix, D.A.: Vibration-based structural damage identification. Philos. Trans. R. Soc. Lond. A: Math. Phys. Eng. Sci. **359**(1778), 131–149 (2001)
18. Fayyad, U., Piatetsky-Shapiro, G., Smyth, P.: The kdd process for extracting useful knowledge from volumes of data. Commun. ACM **39**(11), 27–34 (1996). https://doi.org/10.1145/240455.240464
19. Figueiredo, E.: Damage identification in civil engineering infrastructure under operational and environmental conditions. Ph.D. thesis, Doctor of Philosophy Dissertation in Civil Engineering, Faculty of Engineering, University of Porto (2010)
20. Figueiredo, E., Cross, E.: Linear approaches to modeling nonlinearities in long-term monitoring of bridges. J. Civ. Struct. Health Monit. **3**(3), 187–194 (2013)
21. Figueiredo, E., Santos, A.: Machine learning algorithms for damage detection, pp 1–39 (2018). https://doi.org/10.1142/9781786344977_0001
22. Figueiredo, E., Park, G., Figueiras, J., Farrar, C., Worden, K.: Structural health monitoring algorithm comparisons using standard datasets. LANL Technical report LA-14393, Los Alamos National Laboratory, Los Alamos, New Mexico, USA (2009)
23. Figueiredo, E., Todd, M.D., Farrar, C.R., Flynn, E.: Autoregressive modeling with state-space embedding vectors for damage detection under operational and environmental variability. Int. J. Eng. Sci. **48**(10), 822–834 (2010)
24. Figueiredo, E., Park, G., Farrar, C.R., Worden, K., Figueiras, J.: Machine learning algorithms for damage detection under operational and environmental variability. Struct. Health Monit. **10**(6), 559–572 (2011)
25. Figueiredo, E., Radu, L., Worden, K., Farrar, C.R.: A Bayesian approach based on a Markov-chain Monte Carlo method for damage detection under unknown sources of variability. Eng. Struct. **80**, 1–10 (2014)
26. Figueiredo, E., Moldovan, I., Santos, A., Campos, P., Costa, J.C.: Finite element-based machine learning approach to detect damage in bridges under operational and environmental variations. J. Bridge Eng. **24**(7), 04019061 (2019)
27. Gerlein, E.A., McGinnity, M., Belatreche, A., Coleman, S.: Evaluating machine learning classification for financial trading: an empirical approach. Exp. Syst. Appl. **54**, 193–207 (2016)
28. Holzinger, A.: Trends in interactive knowledge discovery for personalized medicine: cognitive science meets machine learning. IEEE Intel. Inf. Bull. **15**(1), 6–14 (2014)
29. Holzinger, A., Dehmer, M., Jurisica, I.: Knowledge discovery and interactive data mining in bioinformatics—state-of-the-art, future challenges and research directions. BMC Bioinform. **15**(6), I1 (2014)
30. Kamyshanska, H., Memisevic, R.: The potential energy of an autoencoder. IEEE Trans. Pattern Anal. Mach. Intel. **37**(6), 1261–1273 (2015)
31. Kang, G., Gao, S., Yu, L., Zhang, D.: Deep architecture for high-speed railway insulator surface defect detection: denoising autoencoder with multitask learning. IEEE Trans. Instrum. Meas, 1–12 (2018)
32. Kinemetrics: Operation instructions for FBA 11 force balance accelerometer, part number 105610. Kinemetrics/Systems Inc., 222 Vista Venue, Pasadena, California, 91107 USA (1991)
33. Kinemetrics: Operation instructions for FBA 23 force balance accelerometer, part number 105610. Kinemetrics/Systems Inc., 222 Vista Venue, Pasadena, California, 91107 USA (1991)

34. Kramer, M.A.: Nonlinear principal component analysis using autoassociative neural networks. AIChE J. **37**(2), 233–243 (1991)
35. Ma, M.L., Wang, G.L., Miao, D.M., Xian, G.J.: Applying KDD to a structure health monitoring system based on a real sited bridge: model reshaping case. In: Mechanical Science and Engineering IV, Trans Tech Publications, Applied Mechanics and Materials, vol. 472, pp. 535–538 (2014)
36. Maeck, J., Roeck, G.D.: Dynamic bending and torsion stiffness derivation from modal curvatures and torsion rates. J. Sound Vib. **225**(1), 153–170 (1999)
37. McLachlan, G.J., Peel, D.: Finite Mixture Models. Wiley Series in Probability and Statistics. Wiley, New York (2000)
38. Oh, C.K., Sohn, H., Bae, I.H.: Statistical novelty detection within the Yeongjong suspension bridge under environmental and operational variations. Smart Mater. Struct. **18**(12), 125022 (2009)
39. Overbey LA (2008) Time series analysis and feature extraction techniques for structural health monitoring applications. Ph.D. thesis, UC San Diego
40. Peeters, B., Roeck, G.D.: Reference-based stochastic subspace identification for output-only modal analysis. Mech. Syst. Signal Process. **13**(6), 855–878 (1999)
41. Peeters, B., Roeck, G.D.: One-year monitoring of the Z24-Bridge: environmental effects versus damage events. Earthq. Eng. Struct. Dyn. **30**(2), 149–171 (2001)
42. Peeters, B., Maeck, J., Roeck, G.D.: Vibration-based damage detection in civil engineering: excitation sources and temperature effects. Smart Mater. Struct. **10**(3), 518–527 (2001)
43. Reynders, E., Wursten, G., Roeck, G.D.: Output-only structural health monitoring in changing environmental conditions by means of nonlinear system identification. Struct. Health Monitor. **13**(1), 82–93 (2014)
44. Roeck, G.D.: The state-of-the-art of damage detection by vibration monitoring: the SIMCES experience. Struct. Control. Health Monit. **10**(2), 127–134 (2003)
45. Sampaio, R., Maia, N., Ribeiro, A., Fontul, M., Montalvao, D.: Using the detection and relative damage quantification indicator (drq) with transmissibility. In: Damage Assessment of Structures VII, Trans Tech Publications, Key Engineering Materials, vol. 347, pp. 455–460 (2007)
46. Santos, A., Figueiredo, E., Silva, M., Sales, C., Costa, J.: Machine learning algorithms for damage detection: Kernel-based approaches. J. Sound and Vib. **363**, 584–599 (2016)
47. Schmidhuber, J.: Deep learning in neural networks: an overview. Neural Netw. **61**, 85–117 (2015)
48. Shannon, C.E.: A mathematical theory of communication. Bell Syst. Tech. J. **27**, 623–656 (1948)
49. Shao, H., Jiang, H., Wang, F., Zhao, H.: An enhancement deep feature fusion method for rotating machinery fault diagnosis. Knowl.-Based Syst. **119**, 200–220 (2017)
50. Silva, M., Santos, A., Figueiredo, E., Santos, R., Sales, C., Costa, J.C.: A novel unsupervised approach based on a genetic algorithm for structural damage detection in bridges. Eng. Appl. Artif. Intel. **52**, 168–180 (2016)
51. Silva, M., Santos, A., Santos, R., Figueiredo, E., Sales, C., Costa, J.C.: Composing robust damage-sensitive features with deep neural networks. In: Proceedings of the 9th European Workshop on Structural Health Monitoring, DEStech Publications (2018)
52. Silva, M., Santos, A., Santos, R., Figueiredo, E., Sales, C., Costa, J.C.: Deep principal component analysis: an enhanced approach for structural damage identification. Struct. Health Monit. (2018). https://doi.org/10.1177/1475921718799070
53. Sun, J., Yan, C., Wen, J.: Intelligent bearing fault diagnosis method combining compressed data acquisition and deep learning. IEEE Trans. Instrum. Meas. **67**(1), 185–195 (2018)
54. Van Der Maaten, L., Postma, E., Van den Herik, J.: Dimensionality: a comparative review. Technical report, Tilburg University, Tilburg, Netherlands (2009)
55. Wen, L., Li, X., Gao, L.: A new two-level hierarchical diagnosis network based on convolutional neural network. IEEE Trans. Instrum. Meas. 1–9 (2019)

56. Worden, K.: Structural fault detection using a novelty measure. J. Sound Vib. **201**(1), 85–101 (1997)
57. Worden, K., Manson, G., Fieller, N.R.J.: Damage detection using outlier analysis. J. Sound Vib. **229**(3), 647–667 (2000)
58. Yan, R., Chen, X., Mukhopadhyay, S.C.: Advanced Signal Processing for Structural Health Monitoring, pp. 1–11. Springer International Publishing, Cham (2017)
59. Yuqing, Z., Bingtao, S., Fengping, L., Wenlei, S.: NC machine tools fault diagnosis based on kernel PCA and-nearest neighbor using vibration signals. J. Shock. Vib. **2015** (2015)
60. Zhou, Y.L., Figueiredo, E., Maia, N.M., Sampaio, R., Pereira, R.: Damage detection and quantification using transmissibility coherence analysis. Struct. Control. Health Monit. **22**(10) (2015)
61. Zhou, Y.L., Maia, N.M., Wahab, M.A.: Damage detection using transmissibility compressed by principal component analysis enhanced with distance measure. J. Vib. Control. (2016). https://doi.org/10.1177/1077546316674544

Structural Health Monitoring of Periodic Infrastructure: A Review and Discussion

Junfang Wang and Jian-Fu Lin

Abstract Periodic structure has obtained wide applications in various infrastructures. The structural health monitoring of periodic infrastructures is motivated by the facts that in-service infrastructures are damage-prone, while traditional inspection and nondestructive evolution hardly meet the requirements in continuous surveillance, timely warning and assessment of anomalies, and cost-effective maintenance. In this chapter, the fundamental principles and applications of the periodic structure are first introduced. Then, the recent research activities on the health monitoring of periodic infrastructures using data mining are summarized. It is followed by a review of instantaneous baseline structural health monitoring that was originally presented for diminishing the vulnerability of anomaly detection performance to environmental and operational conditions. Investigations on structural health monitoring using the inherent property of periodic structure are subsequently reviewed, and none of them incorporates both instantaneous baseline and advanced data mining techniques for the anomaly identification oriented classification, prediction, and optimization. Based on the state-of-the-art review, discussions about current investigations and suggestions for future studies are provided in the final section.

Keywords Structural health monitoring · Damage detection · Periodic structure · Instantaneous baseline · Data mining

1 Fundamentals of Periodic Structure

A periodic or repetitive structure is an assembly of identical elements typically coupled in an identical manner. Each element is connected to another in a regular pattern to build up the so-called spatially periodic structure. This type of structures has

J. Wang
The Hong Kong Polytechnic University, Hung Hom, Kowloon, Hong Kong, China
e-mail: flora.wang@connect.polyu.hk

J.-F. Lin (✉)
Center of Safety Monitoring of Engineering Structures, Shenzhen Academy of Disaster Prevention and Reduction, Shenzhen, China
e-mail: linjianf@hotmail.com

© Springer Nature Singapore Pte Ltd. 2019

Y. L. Zhou et al. (eds.), *Data Mining in Structural Dynamic Analysis*,
https://doi.org/10.1007/978-981-15-0501-0_2

obtained wide applications in infrastructures and these infrastructures can be called periodic infrastructures. Examples in engineering applications are building frameworks, multi-span bridges, rail tracks, aircraft fuselages, long-distance pipelines, wind turbines (bladed discs), and ship structures (see Fig. 1). The transmission and reflection of structure-borne waves in periodic structures, say, from layer to layer in a building framework or from span to span along a rail, and the coupling of these waves form a distinctive dispersion phenomenon characterized by so-called passband and stopband. For slight structural damping, passbands are frequencies at which the coupled waves travel in the periodic structure with little transmission loss, while stopbands are frequency zones where the coupled waves drastically decay when propagating. The passbands and stopbands are known as "propagation zones" or "attenuation zones."

A full three-dimensional analysis of the periodic infrastructures is intricate due to the vibrational interactions between structural components. However, a fundamental understanding of the wave propagation and vibration characteristics of periodic infrastructures may be acquired by studying less complicated models such as a beam-type periodic waveguide with a single transmission path and a series of plate elements periodically assembled with the assumption of plane-wave transmission [5]. Conventionally, the wave propagation and vibration characteristics of the periodic structure are obtained by solving each element of the periodic structure successively. The most commonly used methods are the propagation wave approach [5–7] and

Fig. 1 Spatially periodic structures in engineering applications (building, bridge, rail track, and aircraft fuselage) [1–4]

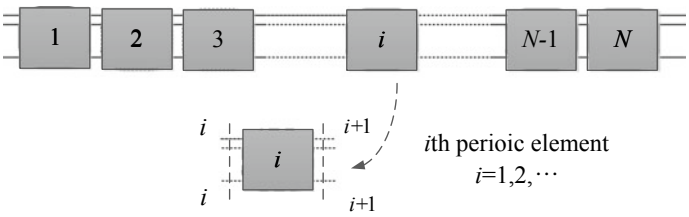

Fig. 2 Block diagram of a multi-coupled periodic structure

the transfer matrix method [8–10]. Other approaches, inclusive of the Z-transform method, energy method, and Fourier transform method, have been also employed [11]. The propagation wave approach is developed based on the Bloch theorem in solid-state physics [12], which is very suitable for analyzing infinite or semi-infinite periodic structures. In addition to infinite or semi-infinite periodic structures, the transfer matrix approach can be conveniently applied to the analysis of finite periodic structures because of the easy incorporation of their boundary conditions into the transfer matrix [11]. Based on Ref. [9], an example using the transfer matrix method to solve the wave propagation characteristics of a one-dimensional or semi-two dimensional waveguide (see Fig. 2) is provided as follows. The derivation of wave propagation characteristics by transfer matrix method, i.e., Eqs. (1)–(6), is performed in the frequency domain.

In the waveguide shown in Fig. 2, the structural-borne wave w at the ith junction/cross section in the ith element is related to the velocity V and force F at this junction in the manner described in Eqs. (1) or (2).

$$\begin{bmatrix} V \\ F \end{bmatrix}_i = [S_w][w]_i \tag{1}$$

$$[w]_i = [S_w]^{-1} \begin{bmatrix} V \\ F \end{bmatrix}_i \tag{2}$$

The transfer matrix of waves at the ith junction $[w]_i$ and the waves at the $(i+1)$th junction between the ith and $(i+1)$th elements $[w]_{i+1}$ is $[P_w]$. It governs the wave propagation between two adjacent junctions.

$$[w]_{i+1} = [P_w][w]_i \tag{3}$$

Combining Eqs. (1)–(3), the vibration transmission between two adjacent junctions of the periodic structure is obtained as

$$\begin{bmatrix} V \\ F \end{bmatrix}_{i+1} = [U_\mu] \times \begin{bmatrix} V \\ F \end{bmatrix}_i \tag{4}$$

where $\left[U_\mu\right]$ is the entire transfer matrix and has the expression as Eq. (5).

$$\left[U_\mu\right] = [S_w][P_w][S_w]^{-1} \tag{5}$$

According to the Bloch theory [13], the wave motions in a linear semi-infinite one-dimensional periodic structure can be described as the superposition of characteristic wave-types of Bloch waves. After the eigendecomposition of $\left[U_\mu\right]$, Eq. (4) takes the form as Eq. (6), where $[v]$ and $[f]$ are a so-called normalized vector for velocity and force. The normalized vector specifies the relative amounts of Bloch wave contribution from different wave-types.

$$\begin{bmatrix} V \\ f \end{bmatrix}_{i+1} = e^{\mu} \begin{bmatrix} v \\ f \end{bmatrix}_{i+1} \tag{6}$$

A periodic structure with n motion coordinates at each junction is known to carry n characteristic-free harmonic independent wave-types. Each wave-type is correspondent to one pair of negative- and positive-going waves and governed by a pair of complex "propagation constants" $\mu_k = \pm(\mu_{Rk} + j\mu_{Ik})$, $k \in [1, n]$; μ_{Rk} and μ_{Ik} are non-negative herein. The real part μ_{Rk} is the attenuation constant representing the exponential decay in wave amplitude per element for the kth characteristic wave-type. The imaginary part μ_{Ik} is the phase constant, of which the cosine value describes the phase change of the kth characteristic wave-type when propagating through each element. The so-called propagation zones or attenuation zones are associated with the values of μ at certain frequency bands. With negligible damping, the frequency bands in which $\mu_k = \pm\mu_{Rk}$ are called "attenuation zones" or "stop bands," whereas the frequency bands where $\mu_k = \pm j\mu_{Ik}$ are "propagation zones" or "passbands."

Analytical models are widely used for obtaining the fundamental understanding of wave propagation and vibration behavior of periodical structures. However, such models can be developed generally when they are ideal simplified representatives of periodic infrastructures. For periodic waveguides with complicated structural pattern and joint connection, their wave behavior can be investigated by finite element and hybrid finite element/wave approaches [14–21]. Finite element methods may be impractical at higher frequencies, while the hybrid approaches show superiority in terms of less computational burden, higher accuracy, and easier acquisition of wave properties for analysis of statistical energy and structural-borne waves. The hybrid approaches post-process the standard finite element model of a small segment in a waveguide by using periodic structure theory. The practical significance of exploring wave and vibration properties lies in structure design [22–24], vibration/noise level assessment and control [25–29], and anomaly identification, etc.

2 Health Monitoring of Periodic Infrastructure Using Data Mining

Subject to degrading, aging, fatigue, and natural disasters and affected by adverse or uncontrolled operational environments, infrastructures are damage-prone, although they are designed for long service life. For examining the integrity of infrastructures and guaranteeing their serviceability and safe operation, various inspection and damage detection techniques were developed. Nondestructive evaluation (NDE) techniques, such as visual inspection, laser interferometry, radioscopy, ultrasonics, eddy-current, electromagnetic, and thermographic inspection [30–32], have made a significant contribution in discovering infrastructure defeats. However, most of the NDE techniques in infrastructure are performed at a regular inspection interval, disregarding the operational condition variations and progressive degradation of infrastructures. Tremendous efforts and budgets have been spent every year on the inspection and maintenance of infrastructures, but damage and failures on infrastructures have been occasionally reported. In an endeavor to enhance the safety and decrease the maintenance costs of infrastructures, the concept of structural health monitoring (SHM) emerges and has gained extensive application over the past three decades. Recognizing the inefficiency of NDE, SHM incorporates condition-based philosophy to offer continuous and automated scrutiny on structural health by taking into account the condition changes and structural degradation [33]. It is indicated that an effective SHM scheme cuts down the total maintenance cost of a transportation system by over 30% [33], along with the considerable enhancement in safety. Through the timely awareness of damage occurrence, location, and severity, SHM is conducive to reducing the costs associated with scheduled inspections and maintenances and enhancing the overall safety of in-service infrastructures.

A great number of infrastructures have been instrumented SHM systems for structural health surveillance [34–36]. Underpinned by advanced data acquisition and transmission technology, a large amount of monitoring data can be collected and accumulated. The monitoring data of infrastructures are characterized by large data size, multiple categories of signals (e.g., acceleration, strain, wind/water speed), and involvement of uncertainties due to environmental and operational conditions. Data mining (DM), explained as "the nontrivial process of identifying valid, novel, potentially useful, and ultimately understandable patterns in data" [37], maybe a promising solution to this problem. Data mining is also known as a knowledge discovery process in the database.

Structural health monitoring using data mining techniques is generally implemented by the following procedures [38, 39]: (1) Sensor placement and data collection; (2) Data preprocessing such as cleansing, construction, and transformation of data; (3) Modeling or pattern discovery for classification, prediction, and optimization by employing one or several data mining techniques; (4) Anomaly detection and structural health assessment with the use of validated model; (5) Visualization for suggesting intervention/maintenance activities (e.g., strengthening, retrofitting, repair, or replacement). Various data mining techniques have been applied to the structural

health assessment of infrastructures or their models and specimens. Artificial neural network (ANN) is utilized for the damage detection of many infrastructures such as bridge, building, and steel frame [40–42]. Fuzzy logic is introduced into the SHM framework of infrastructural systems [43, 44]. Principal component analysis (PCA) is implemented for the damage detection of pipe, aircraft wing, aircraft turbine blade, building, and bridge [45–47]. Support vector machine (SVM)-based infrastructural health monitoring methodology is proposed [48, 49]. Bayesian approaches are developed for meeting the challenges in system identification and damage assessment of infrastructures [50, 51]. Optimization techniques, including genetic algorithm (GA) [52, 53], particle swarm optimization (PSO) [54], and ant colony optimization (ACO) [55], are also employed for damage identification of infrastructures.

Among the aforementioned data mining techniques, ANN has remarkably broad applications in structural health monitoring because of its nonlinear mapping ability and high flexibility. Bayesian neural network [56, 57], fuzzy wavelet neural networks [58, 59], and auto-associative neural network [60] are some of its significant applications in SHM of infrastructures. PCA, well known for its dimension-reduction capability, are commonly seen in structural damage detection of various infrastructures. Featured by its capability of addressing data uncertainty and modeling errors, Bayesian inference is preferred in the probabilistic assessment of structural health. Extensive literature has exhibited the characteristics of data mining tools for practical application [38, 39, 61, 62]. Considering the differences in specific applications and based on the merits and drawbacks of data mining algorithms, one or a combination of some data mining techniques can be utilized to extract effective information from monitoring data.

3 Instantaneous Baseline Anomaly Detection

Although the evolution of information discovery techniques greatly fosters new SHM methodology development, anomaly identification in the context of conventional SHM is based on the comparison of current feature to a pre-stored baseline built when the structure is in a pristine state. This comparison between current data and past pristine baseline data (i.e., baseline subtraction) can bring complications in data management and inability to accommodate effects of varying environmental and operational conditions, followed by false alarm or undetected damage. Therefore, anomaly identification approaches taking into consideration the effects of varying environmental and operational conditions have been developed [60, 63–67]. Hsu and Loh [66] classify these approaches into two categories. Some methods need to measure the varying variables and build the correlation between environmental variables and structural features [60, 63, 64], while others do not [65–67]. They all rely on substantial baseline data recorded over a range of varying conditions.

The recent one or two decades witness the conceiving and development of baseline-free structural health monitoring methods. Instead of using prior baseline

data, these baseline-free methods capitalize on: (1) time-reversal acoustics [68]; (2) polarization of collocating piezoelectric transducers attached on both sides of a thin structure [69] or dual-PZT technique with pairs of specially designed dual-PZT transducers placed only on a single surface when the access to both surfaces is not allowed [70]; (3) instantaneous baseline [71, 72] which is a series of geometrically identical wave-transmission paths designed for crosschecking the path health conditions. The methodology using currently acquired monitoring datasets from the identical paths for cross-validation and anomalous path identification is known as "instantaneous baseline" SHM. The concept of instantaneous baseline has also been applied to fault diagnosis of piezoelectric transducers and validation of the sensor functionality during the monitoring operation [73]. Common features of most paths/sensors differentiate a few damaged ones from the majority. Changes in global or local properties of a structure under surveillance can be associated with defects. In these investigations, local properties rather than global properties (e.g., natural frequency and mode shape) are obtained for baseline-free damage detection, since global properties are less sensitive to defects without noticeable severity. It is largely because most of conventional SHM approaches are vulnerable to environmental and operational variations and burdened by baseline data management that instantaneous baseline SHM is being investigated by many researchers.

Composed of spatially repetitive elements, periodic structures are inherently suitable for the implementation of instantaneous baseline SHM. A prominent application is the damage localization of a periodically stiffened fuselage panel [74, 75], in which all instantaneous baselines are calibrated for removing the discrepancy in the paths due to geometrical imperfection and manufacturing tolerances. A glass-reinforced plastic (GRP) underground water pipeline in Hong Kong's Dongjiang water mains (DJWM) has been instrumented a fiber Bragg grating (FBG) SHM system (see Fig. 3) [76, 77].

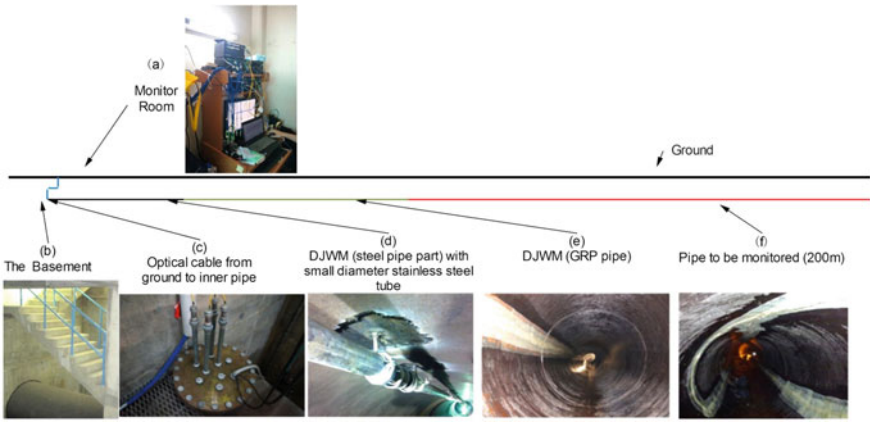

Fig. 3 A 200-m-long GRP underground pipeline with a fiber optic SHM system

The structural integrity of this 200-m-long GRP pipeline comprising 100 repetitive 2-m-long pipes is monitored by FBG sensors in terms of strain, temperature, and flow pressure (see Fig. 4). Three groups of strain, temperature, and pressure sensors are placed at the cross sections of pipes #1 and #50, and three pairs of temperature and pressure sensors are evenly distributed at the cross sections of the other pipes. Although insulated piezoelectric transducers are famous for their capability of wave activation and wave reception, fiber optic sensors are more popular for the monitoring of large structures or large-range monitoring. It is because they have the advantages of small size, lightweight, excellent multi-functionality and multiplexing capabilities, and exempting electric power supply to individual transducers. The instantaneous baseline method is applied for anomaly identification through pattern comparison among different pipe segments of the pipeline. In Figs. 5 and 6, A, B, and C denote the three locations at a cross-section and S and T represent strain and temperature. As shown in Figs. 5 and 6 the patterns for most pipes are consistent, except the one for the 80th pipe. This indicates a defect, sensor malfunction/debonding, or other anomaly have been incurred to the 80th pipe. Advanced data mining techniques will be involved in the authors' ongoing investigations on instantaneous baseline anomaly detection of the GRP pipeline. Without pre-stored baseline data obtained from the pristine structural condition and free from the influence of environmental and operational conditions, instantaneous baseline SHM has great potential to realize in situ damage identification of in-service periodic infrastructures under natural environment.

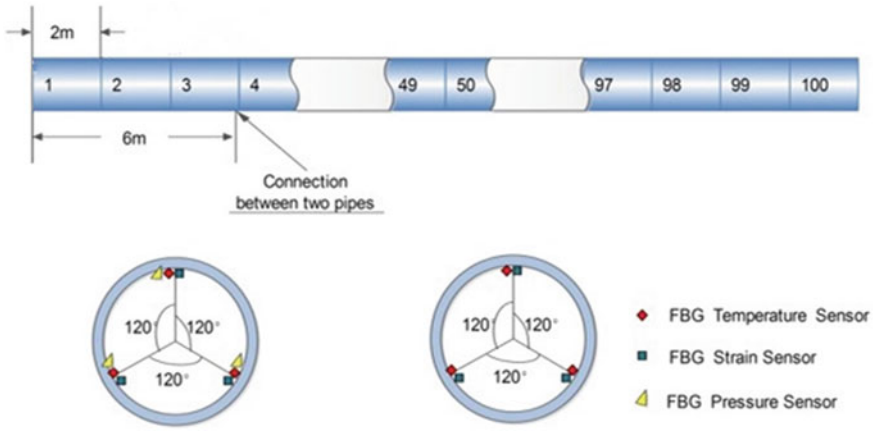

Fig. 4 Sensor placement in the GRP pipe

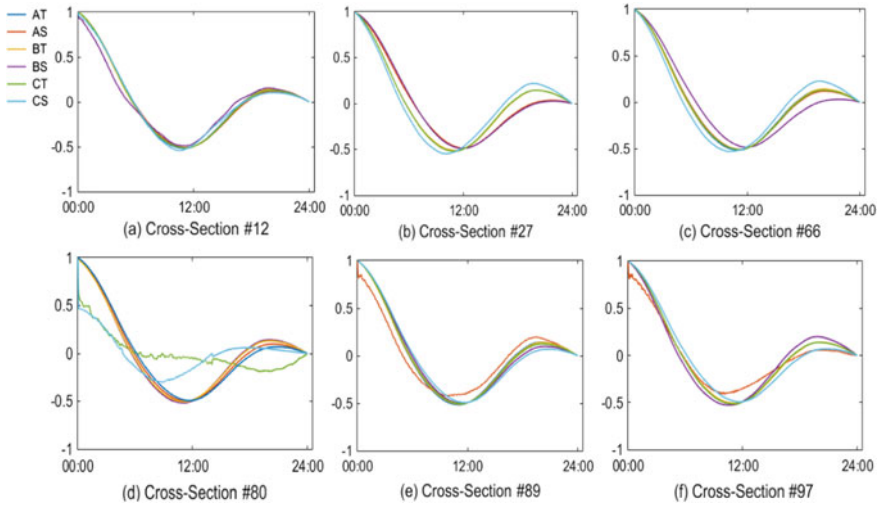

Fig. 5 Patterns at different cross-sections of the GRP pipeline—normalized auto-correlation of the measured temperature and strain

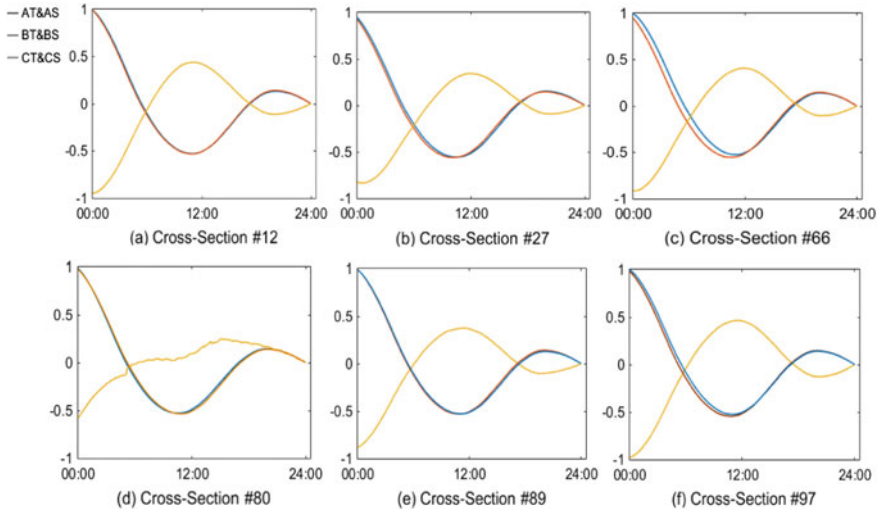

Fig. 6 Patterns at different cross-sections of the GRP pipeline—normalized cross-correlation of the measured temperature and strain

4 Health Monitoring Using Inherent Property of Periodic Structure

In civil and mechanical engineering, most investigations related to periodic structure focus on the unique wave propagation and vibration characteristics of periodic structures [5–24] and the vibration/noise control with periodic structures acting as mechanical bandpass filters [25–29]. Albeit designed and produced with high quality, periodic structures are subject to geometrical uncertainties and manufacturing/assembling tolerances to some extent, and the in-service periodic structures are particularly damage-prone under natural environment. These structural irregularities or disorder can result in the phenomena of vibration localization (e.g., change in mode shape and vibration energy confined to a few elements), threatening the functionality of in-service periodic structures. Therefore, particular attention has been paid to structural health monitoring or damage detection of periodic structures by utilizing the inherent property [74–86], although the literature to date is still limited.

Different from the studies concentrating on instantaneous baseline anomaly detection of periodic structures [74–77], other investigations on structural health monitoring of periodic structures [78–85] involve the development of diverse damage-identification methods, such as nonlinear component detection, anomaly amplification for damage detection of periodic structures via piezoelectric transducer networking, sensitivity index-based damage identification, and probabilistic approach for structural health assessment. Specifically, Peng and Cheng et al. develop a method to identify the position of the nonlinear components in 1D and 2D periodic structures [78, 79]. As the nonlinearity is associated with certain defects of structures (e.g., crack), this study can be included in the framework of structural health monitoring for damage localization. Zhao et al. propose the use of a piezoelectric circuitry network for accentuating the damage effects and intensifying the damage-induced anomaly in the responses of mistuned periodic structures [80, 81]. Its performance is examined by carrying out Monte Carlo simulation on a bladed disc model, and the PCA technique is adopted for de-noising. Zhu et al. investigate the damage identification of mono-coupled periodic structures based on sensitivity analysis of natural frequency [82] and sensitivity analysis of multiple modal parameters [83], and they apply the proposed methodology to the damage detection of a multi-story mono-coupled building model. To accommodate uncertainties associated with measurement noise and modeling error, Yin et al. explore the possibility of utilizing probabilistic approaches for the anomaly detection of periodically supported structures [84, 85]. The sensitivity matrix of the nondimensional frequencies is developed and then solved by the Bayesian method and the Markov chain Monte Carlo (MCMC) simulation [84]. This methodology is validated by numerical simulations for a periodically supported flanged pipeline model and experiments performed for a multi-span aluminum beam specimen with bolted connections in the laboratory. A companion study on a probabilistic methodology for detecting bolt loosening in periodical structure endowed with bolted flange joints is conducted based on measured modal parameters [85]. In this study, Bayesian inference is adopted for determining the most suitable model

class, and particle filter-based approach is introduced for identifying the posterior probability density function of the interested parameters. Besides feature extraction and pattern recognition for damage identification, instrumentation of the interested structures is another significant part of structural health monitoring. In most applications, the sensor locations are determined by experiences and practical constraints. Yin et al. address the optimal sensor placement problem particularly for large-scale periodic structures by utilizing the inherent periodic properties [86]. Recently, Lin and Xu et al. propose a new multi-objective multi-type sensor optimal placement method [87–91] for the damage detection of a large lattice structure. The optimal sensor placement procedure is very time consuming when the number of candidate sensor locations is large. By introducing periodicity conditions for retrofitting the multi-type sensor placement scheme implemented on the large lattice structure, a multi-type sensor placement and damage identification scheme tailor-made for periodic structure may be developed and the calculation complexity may be reduced because of the repetitiveness of periodic elements.

5 Discussion and Future Prospect

This chapter presented a state-of-the-art review on the periodic structure and the structural health monitoring of periodic infrastructures. Based on the literature review, there is no doubt that the combination of data mining techniques and instantaneous baseline potentially has strong applicability to the SHM of periodic structures. Nonetheless, the studies utilizing data mining and pattern identification relied on prestored baseline data for damage detection, and the investigations on instantaneous baseline SHM did not incorporate advanced data mining techniques. The bottleneck limiting development and implementation of an instantaneous baseline SHM system taking advantages of the spatial periodicity and data mining techniques may be the imperfection of periodic structure in reality.

To promote the development of instantaneous baseline SHM methodology incorporating data mining techniques for periodic structures, the following suggestions for future research are provided:

(1) As there exists no ideally periodic structure with perfectly identical periodic elements in engineering applications, the calibration of periodic elements or the normalization of periodic elements in terms of their structural health conditions is the first significant step.
(2) A structural health metric (e.g., index/feature/pattern) characterizing and calibrating/normalizing the health condition of an individual or grouped periodic elements is preferable when it can be conveniently combined with data mining techniques for damage detection.
(3) Methods for building such type of metrics are desired if they are applicable regardless of structural complexity, multiple types of sensory signals, and data

heterogeneity. Relevant data fusion approaches and index establishment procedures in time and frequency domains can be found in Refs. [87, 92–94].

(4) After characterizing and calibrating the health conditions of periodic elements, common feature extraction from these current metrics or abnormal metric identification using appropriate data mining techniques is the subsequent crucial task.

(5) A large structure can be divided into substructures for instantaneous baseline anomaly detection according to the similarities in structural geometry, material, and coupling.

With the assistance of advanced data mining techniques and taking advantages of the inherent property of periodic structures, new SHM methods are potentially able to bring substantial efficacy and rationality improvements in the health assessment and management of periodic infrastructures.

Acknowledgements The authors wish to acknowledge the financial supports from China Earthquake Administration's Science for Earthquake Resilience Project (No. XH204702) and the Guangdong Provincial Science and Technology Plan Project (No. 2018B020207011).

References

1. LMC Steel Buildings Homepage. http://lmcsteel.com/warranty-information/steel_framework2. Accessed 30 Apr 2019
2. HighestBridges.com Homepage. http://highestbridges.com/wiki/index.php?title=China_2012_Bridge_Trip. Accessed 30 Apr 2019
3. JSCE Homepage. http://www.jsce-int.org/a_t/achievement/civil/2011. Accessed 30 Apr 2019
4. DPrint.com Homepage. http://lmcsteel.com/warranty-information/steel_framework2/. Accessed 30 Apr 2019
5. Friis, L., Ohlrich, M.: Coupling of flexural and longitudinal wave motion in a periodic structure with asymmetrically arranged transverse beams. J. Acoust. Soc. Am. **118**, 3010–3020 (2005)
6. Mead, D.J.: Wave propagation and natural modes in periodic systems: I. Mono-coupled systems. J. Sound Vib. **40**, 1–18 (1975)
7. Mead, D.J.: Wave propagation and natural modes in periodic systems: II. Multi-coupled systems, with and without damping. J. Sound Vib. **40**, 19–39 (1975)
8. Yun, Y., Mak, C.M.: A study of coupled flexural-longitudinal wave motion in a periodic dual-beam structure with transverse connection. J. Acoust. Soc. Am. **126**(1), 114–121 (2009)
9. Wang, X., Mak, C.M.: Acoustic performance of a duct loaded with identical resonators. J. Acoust. Soc. Am. **131**(4), 316–322 (2012)
10. Wang, J.F., Mak, C.M., Yun, Y.: A methodology for direct identification of characteristic wave-types in a finite periodic dual-layer structure with transverse connection. J. Vib. Control **18**(9), 1406–1414 (2012)
11. Lin, T.R.: A study of modal characteristics and the control mechanism of finite periodic and irregular ribbed plates. J. Acoust. Soc. Am. **123**, 729–737 (2008)
12. Brillouin, L.: Wave Propagation in Periodic Structures. Dover Publications, New York (1953)
13. Umezawa, H.: Advanced Field Theory: Micro, Macro, and Thermal Physics. American Institute of Physics, New York (1995)
14. Duhamel, D., Mace, B.R., Brennan, M.J.: Finite element analysis of the vibrations of waveguides and periodic structures. J. Sound Vib. **294**, 205–220 (2006)

15. Maess, M., Wagner, N., Gaul, L.: Dispersion curves of fluid filled elastic pipes by standard FE models and eigenpath analysis. J. Sound Vib. **296**, 264–276 (2006)
16. Mencik, J.M., Ichchou, M.: Wave finite elements in guided elastodynamics with internal fluid. Int. J. Solids Struct. **44**, 2148–2167 (2007)
17. Manconi, E., Mace, B.R.: Wave characterization of cylindrical and curved panels using a finite element method. J. Acoust. Soc. Am. **125**, 154–163 (2009)
18. Waki, Y., Mace, B.R., Brennan, M.J.: Numerical issues concerning the wave and finite element method for free and forced vibrations of waveguides. J. Sound Vib. **327**, 92–108 (2009)
19. Søe-Knudsen, A., Sorokin, S.V.: Analysis of linear elastic wave propagation in piping systems by a combination of the boundary integral equations method and the finite element method. Contin. Mech. Thermodyn. **22**, 647–662 (2010)
20. Renno, J.M., Mace, B.R.: Calculation of reflection and transmission coefficients of joints using a hybrid finite element/wave and finite element approach. J. Sound Vib. **332**, 2149–2164 (2013)
21. Renno, J.M., Mace, B.R.: Vibration modelling of structural networks using a hybrid finite element/wave and finite element approach. Wave Motion **51**(4), 566–580 (2014)
22. Mace, B.R., Jones, R.W., Harland, N.R.: Wave transmission through structure inserts. J. Acoust. Soc. Am. **109**, 1417–1421 (2001)
23. Sigmund, O., Jensen, J.S.: Systematic design of phononic band-gap materials and structures by topology optimization. Philos. Trans. R. Soc. A Math. Phys. Eng. Sci. **361**(1806), 1001–1019 (2003)
24. Hussein, M.I., Hulbert, G.M., Scott, R.A.: Dispersive elastodynamics of 1D banded materials and structures: design. J. Sound Vib. **307**(3–5), 865–893 (2007)
25. Szefi, J.T.: Helicopter gearbox isolation using periodically layered fluidic isolators, Ph.D. thesis, The Pennsylvania State University, Pennsylvania, USA (2003)
26. Yilmaz, C., Kikuchi, N.: Analysis and design of passive band-stop filter-type vibration isolators for low-frequency applications. J. Sound Vib. **291**(3–5), 1004–1028 (2006)
27. Asiri, S.: Tunable mechanical filter for longitudinal vibrations. Shock Vib. **14**(5), 377–391 (2007)
28. Jung, W., Gu, Z., Baz, A.: Mechanical filtering characteristics of passive periodic engine mount. Finite Elem. Anal. Des. **46**(9), 685–697 (2010)
29. Wang, J.F., Mak, C.M.: Adaptive-passive vibration isolation between nonrigid machines and nonrigid foundations using a dual-beam periodic structure with shape memory alloy transverse connection. J. Sound Vib. **333**(23), 6005–6023 (2014)
30. Chimenti, D.E.: Guided waves in plates and their use in materials characterization. Appl. Mech. Rev. **50**(5), 247–284 (1997)
31. Achenbach, J.D.: Quantitative nondestructive evaluation. Int. J. Solids Struct. **37**, 13–27 (2000)
32. Rose, J.L.: Guided wave nuances for ultrasonic nondestructive evaluation. IEEE Trans. Ultrason. Ferroelectr. Freq. Control **47**(3), 575–583 (2000)
33. Chang, F.K.: Introduction to health monitoring: context, problems, solutions. In: Proceedings of the 3rd European Pre-workshop on Structural Health Monitoring, Paris, France (2002)
34. Ni, Y.Q., Xia, Y., Liao, W.Y., Ko, J.M.: Technology innovation in developing the structural health monitoring system for Guangzhou New TV tower. Struct. Control Health Monit. **16**(1), 73–98 (2009)
35. Mufti, A.A.: Structural health monitoring of innovative Canadian civil structures. Struct. Health Monit. **1**(1), 89–103 (2002)
36. Ou, J.P.: Research and practice of intelligent heath monitoring systems for civil infrastructures in Main China. In: Proceedings of Third China-Japan-US Symposium on Structural Health Monitoring and Control and Fourth Chinese National Conference on Structural Control, Dalian, China (2004)
37. Fayyad, U.M., et al.: Advance in Knowledge Discovery and Data Mining. MIT Press, Mento Park (1996)
38. Duan, Z., Zhang, K.: Data mining technology for structural health monitoring. Pac. Sci. Rev. **8**, 27–36 (2006)

39. Gordan, M., Razak, H.A., Ismail, Z., Ghaedi, K.: Recent developments in damage identification of structures using data mining. Lat. Am. J. Solids Struct. **14**(13), 2373–2401 (2017)
40. Hung, S., Huang, C.S., Wen, C.M., Hsu, Y.C.: Nonparametric identification of a building structure from experimental data using wavelet neural network. Comput. Aided Civ. Infrastruct. Eng. **18**, 356–368 (2003)
41. Ni, Y.Q., Wang, J.F., Chan, T.H.T.: Structural damage alarming and localization of cable-supported bridges using multi-novelty indices: a feasibility study. Struct. Eng. Mech. Int. J. **54**(2), 337–362 (2015)
42. Padil, K.H., Bakhary, N., Hao, H.: The use of a non-probabilistic artificial neural network to consider uncertainties in vibration-based-damage detection. Mech. Syst. Signal Process. **83**, 194–209 (2017)
43. Abayomi, M.A., David, O.O.: Fuzzy control model for structural health monitoring of civil infrastructure systems. J. Control Sci. Eng. **1**, 9–20 (2015)
44. Jiao, Y., Liu, H., Cheng, Y., Gong, Y.: Damage identification of bridge based on Chebyshev polynomial fitting and fuzzy logic without considering baseline model parameters. Shock Vib. **2015**, 1–10 (2015)
45. Jhonatan, C.N., Magda, R., Rodolfo, V., Luis, M., Jabid, Q.: Features of cross-correlation analysis in a data-driven approach for structural damage assessment. Sensors **18**(5), 1571 (2018)
46. Zucconi, M., Sorrentino, L., Ferlito, R.: Principal component analysis for a seismic usability model of unreinforced masonry buildings. Soil Dyn. Earthq. Eng. **96**, 64–75 (2017)
47. Krishnan, M., Bhowmik, B., Hazra, B., Pakrashi, V.: Real time damage detection using recursive principal components and time varying auto-regressive modeling. Mech. Syst. Signal Process. **101**, 549–574 (2018)
48. Mita, A., Haqiwara, H.: Damage diagnosis of a building structure using support vector machine and modal frequency patterns. Proc. SPIE Int. Soc. Opt. Eng. **5057**, 118–125 (2003)
49. Chong, J.W., Kim, Y., Chon, K.H.: Nonlinear multiclass support vector machine-based health monitoring system for buildings employing magnetorheological dampers. J. Intell. Mater. Syst. Struct. **25**, 1456–1468 (2013)
50. Huang, Y., Shao, C.S, Wu, B., Beck, J.L., Li, H.: State-of-the-art review on Bayesian inference in structural system identification and damage assessment. Adv. Struct. Eng. **2**(6) (2019)
51. Yin, T., Jiang, Q., Yuen, K.: Vibration-based damage detection for structural connections using incomplete modal data by Bayesian approach and model reduction technique. Eng. Struct. **132**, 260–277 (2017)
52. Panigrahi, S.K., Chakraverty, S., Mishra, B.K.: damage identification of multistory shear structure from sparse modal information. J. Comput. Civ. Eng. **27**, 1–9 (2013)
53. Guilherme, F.G., Sebastião, S.C., Antonio, C.A.: Damage detection in aeronautical profile by using frequency changes and optimization algorithms. J. Comput. Sci. **7**(2), 29–43 (2016)
54. Ranginkaman, M.H., Haghighi, A., Vali Samani, H.M.: Inverse frequency response analysis for pipelines leak detection using the particle swarm optimization. Int. J. Optim. Civil Eng. **6**, 1–12 (2016)
55. Majumdar, A., Kumar, D., Maity, D.: Damage assessment of truss structures from changes in natural frequencies using ant colony optimization. Appl. Math. Comput. **218**, 9759–9977 (2012)
56. Arangio, S., Beck, J.L.: Bayesian neural networks for bridge integrity assessment. Struct. Control Health Monit. **19**, 3–21 (2012)
57. Yin, T., Zhu, H.P.: Probabilistic damage detection of a steel truss bridge model by optimally designed bayesian neural network. Sensors **18**(10), 3371 (2018)
58. Adeli, H., Jiang, X.: Dynamic fuzzy wavelet neural network model for structural system identification. J. Struct. Eng. **132**(1), 102–111 (2006)
59. Jiang, X., Mahadevan, S., Adeli, H.: Bayesian wavelet packet denoising for structural system identification. Struct. Control Health Monit. **14**, 333–356 (2007)
60. Zhou, H.F., Ni, Y.Q., Ko, J.M.: Eliminating temperature effect in vibration-based structural damage detection. J. Eng. Mech. **137**, 785–797 (2011)

61. Witten, I.H., Frank, E., Hall, M.A.: Data Mining: Practical Machine Learning Tools and Techniques, 3rd edn. Morgan Kaufmann, Burlington, MA 01803, USA (2011)
62. Alhajj, R., Gao, H., Li, X., Li, J., Zaiane, O.R.: Advanced data mining and applications. In: 3rd International Conference on Advanced Data Mining and Applications (ADMA), Reda, Harbin, China (2007)
63. Ko, J.M., Chak, K.K., Wang, J.Y., Ni, Y.Q., Chan, T.H.T.: Formulation of an uncertainty model relating modal parameters and environmental factors by using long-term monitoring data. In: Proceeding of Smart Structures and Materials 2003: Smart Systems and Nondestructive Evaluation for Civil Infrastructures. International Society for Optical Engineering, San Diego, California, United States (2003)
64. Sohn, H., Worden, K., Farrar, C.R.: Consideration of environmental and operational variability for damage diagnosis. In: Proceedings of SPIE: The International Society for Optical Engineering, Smart Structures and Materials 2002: Smart Systems for Bridges, Structures, and Highways, vol. 4696, pp. 100–111. Society of Photo-Optical Instrumentation Engineers, Bellingham, WA (2002)
65. Oh, C.K., Sohn, H., Bae, I.H.: Statistical novelty detection within the Yeongjong suspension bridge under environmental and operational variations. Smart Mater. Struct. **18**(12), 125022 (2009)
66. Hsu, T.Y., Loh, C.H.: Damage detection accommodating nonlinear environmental effects by nonlinear principal component analysis. Struct. Control Health Monit. **17**(3), 338–354 (2009)
67. Reynders, E., Wursten, G., De Roeck, G.: Output-only structural health monitoring in changing environmental conditions by means of nonlinear system identification. Struct. Health Monit. **13**(1), 82–93 (2014)
68. Park, H.W., Sohn, H., Law, K.H., Farrar, C.R.: Time reversal active sensing for health monitoring of a composite plate. J. Sound Vib. **302**(1–2), 50–66 (2007)
69. Kim, S.B., Sohn, H.: Instantaneous reference-free crack detection based on polarization characteristics of piezoelectric materials. Smart Mater. Struct. **16**(6), 2375–2387 (2007)
70. Sohn, H., Kim, S.B.: Development of dual PZT transducers for reference-free crack detection in thin plate structures. IEEE Trans. Ultrason. Ferroelectr. Freq. Control **57**(1), 229–240 (2010)
71. Anton, S.R., Inman, D.J., Park, G.: Reference-free damage detection using instantaneous baseline measurements. AIAA J. **47**(8), 1952–1964 (2009)
72. Park, S., Anton, S.R., Kim, J.K., et al.: Instantaneous baseline structural damage detection using a miniaturized piezoelectric guided waves system. KSCE J. Civ. Eng. **14**(6), 889–895 (2010)
73. Overly, T.G., Park, G., Farinholt, K.M., Farrar, C.R.: Piezoelectric active-sensor diagnostics and validation using instantaneous baseline data. IEEE Sens. J. **9**(11), 1414–1421 (2009)
74. Salmanpour, M.S., Khodaei, Z.S., Aliabadi, M.H.: Instantaneous baseline damage localization using sensor mapping. IEEE Sens. J. **17**(2), 295–301 (2017)
75. Ferri Aliabadi, M.H., Sharif Khodaei, Z.: Structural Health Monitoring for Advanced Composite Structures. Computational and Experimental Methods in Structures (Book 8), World Scientific Europe Ltd, London (2018)
76. Ni, Y.Q., Wang, J.F., Xie, Q.L., Lam, K.C.: A fiber Bragg grating sensing network for structural integrity monitoring of underground water pipes: analysis of monitoring data. In: The 5th International Forum on Opto-electronic Sensor-based Monitoring in Geo-engineering, Nanjing, China (2014)
77. Xu, C.: Health condition assessment of underground water pipe monitored by fibre Bragg sensory system. The Hong Kong Polytechnic University, Dissertations, Hong Kong (2016). https://theses.lib.polyu.edu.hk/handle/200/9064
78. Peng, Z.K., Lang, Z.Q., Chu, F.L., Meng, G.: Locating nonlinear components in periodic structures using nonlinear effects. Struct. Health Monit. **9**(5), 401–411 (2010)
79. Cheng, C.M., Peng, Z.K., Dong, X.J., Zhang, W.M., Meng, G.: Locating non-linear components in two dimensional periodic structures based on NOFRFs. Int. J. Non-Linear Mech. **67**, 198–208 (2014)

80. Zhao, J., Tang, J., Wang, K.W.: Anomaly amplification for damage detection of periodic structures via piezoelectric transducer networking. Smart Mater. Struct. **20**(10), 105006 (2011)
81. Zhao, J., Tang, J.: Amplifying damage signature in periodic structures using enhanced piezoelectric networking with negative resistance elements. J. Intell. Mater. Syst. Struct. **24**(13), 1613–1625 (2013)
82. Zhu, H., Wu, M.: The characteristic receptance method for damage detection in large mono-coupled periodic structures. J. Sound Vib. **251**(2), 241–259 (2002)
83. Zhu, H.P., Xu, Y.L.: Damage detection of mono-coupled periodic structures based on sensitivity analysis of modal parameters. J. Sound Vib. **285**(1–2), 365–390 (2005)
84. Yin, T., Zhu, H.P., Fu, S.J.: Damage identification of periodically-supported structures following the Bayesian probabilistic approach. Int. J. Struct. Stab. Dyn. **19**(1), 1940011 (2019)
85. Yin, T., Wang, X.Y., Zhu, H.P.: A probabilistic approach for the detection of bolt loosening in periodically supported structures endowed with bolted flange joints. Mech. Syst. Signal Process. **128**, 588–616 (2019)
86. Yin, T., Yuen, K.V., Lam, H.F., Zhu, H.P.: Entropy-based optimal sensor placement for model identification of periodic structures endowed with bolted joints. Comput. Aided Civ. Infrastruct. Eng. **32**(12), 1007–1024 (2017)
87. Lin, J.F., Xu, Y.L.: Two-stage covariance-based multisensing damage detection method. J. Eng. Mech. B4016003 (2017)
88. Lin, J.F., Xu, Y.L.: Response covariance-based sensor placement for structural damage detection. Struct. Infrastruct. Eng. **14**(9), 1207–1220 (2018)
89. Lin, J.F., Xu, Y.L., Law, S.S.: Structural damage detection-oriented multi-type sensor placement with multi-objective optimization. J. Sound Vib. **422**, 1–22 (2018)
90. Lin, J.F., Xu, Y.L., Zhan, S.: Experimental investigation on multi-objective multi-type sensor optimal placement for structural damage detection. Struct. Health Monit. Int. J. **18**(3), 882–901 (2019)
91. Xu, Y.L., Lin, J.F., Zhan, S., F.Y. Wang: Multi-stage damage detection of a transmission tower: Numerical investigation and experimental validation. Struct. Control Health Monit. e2366 (2019)
92. Wang, P.F., Youn, B.D., Hu, C.: A generic probabilistic framework for structural health prognostics and uncertainty management. Mech. Syst. Signal Process. **28**, 622–637 (2012)
93. Hu, C., Youn, B.D., Wang, P., Yoon, J.T.: Ensemble of data-driven prognostic algorithms for robust prediction of remaining useful life. Reliab. Eng. Syst. Saf. **103**, 120–135 (2012)
94. Wang, J.F., Liu, X.Z., Ni, Y.Q.: A Bayesian probabilistic approach for acoustic emission-based rail condition assessment. Comput. Aided Civ. Infrastruct. Eng. **33**(1), 21–34 (2018)

Railway Wheel Out-of-Roundness and Its Effects on Vehicle–Track Dynamics: A Review

Xiao-Zhou Liu

Abstract Wheel out-of-roundness (OOR), as the excitation of railway vehicle-track system, can cause intense vibration and has the potential to impose damage to both track and vehicle components. It may further increase the likelihood of derailment and deteriorate ride comfort. It is therefore necessary to study the effects of wheel OOR on the dynamic performance of these components and structures in operation. This chapter reviews the efforts on numerical simulation to analyse the properties of wheel roughness-induced vibration. The overview of wheel OOR is stated first including the initiation mechanism and consequences of wheel local defects and polygonisation. Several important issues in vehicle–track dynamic simulation for effect analysis of wheel OOR are then reviewed, including wheel defect simulation, wheel–rail contact model, the time-domain and frequency-domain approaches and different vehicle and track models.

Keywords Wheel out-of-roughness (OOR) · Local defect · Polygonal wear · Vehicle–track dynamics · Time- and frequency-domain model

1 Overview of Wheel Out-of-Roundness (OOR)

1.1 Initiation and Development

Main Types of Wheel OOR. Various types of wheel out-of-roundness (OOR)/defects occur on railway wheel tread in service, which influences operational safety and gives rise to high maintenance cost. These defects take on many patterns, such as flats, eccentricities, polygons, corrugations on block-braked wheel treads, missing pieces of tread material owing contact to fatigue cracking and other random irregularities [1, 2]. Generally, they can be categorised into two major types: local defects and periodic OOR all around the wheel, as shown in Fig. 1. The former

X.-Z. Liu (✉)
The Hong Kong Polytechnic University, Hung Hom, Kowloon, Hong Kong, China
e-mail: xiaozhou.liu@connect.polyu.hk

© Springer Nature Singapore Pte Ltd. 2019

Y. L. Zhou et al. (eds.), *Data Mining in Structural Dynamic Analysis*,
https://doi.org/10.1007/978-981-15-0501-0_3

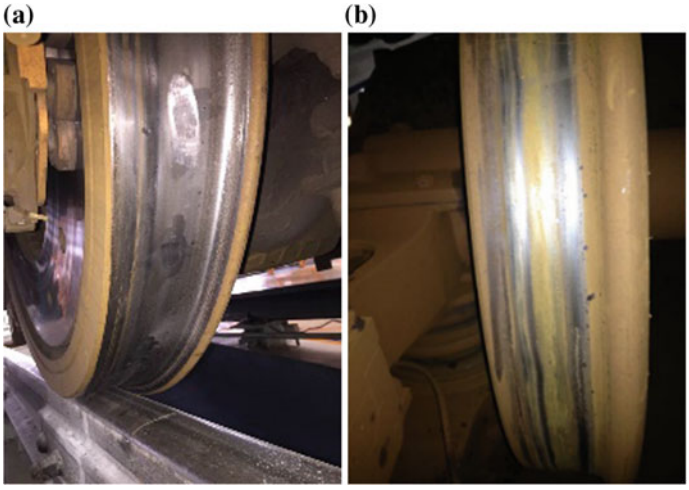

Fig. 1 **a** Wheel local defect and **b** wheel polygonisation

can cause severe repeated wheel–rail impacts, while the latter one leads to abnormal vibrations of vehicle–track system at certain frequencies [3].

Initiation of Wheel Local Defects. Wheel treads are subject to different types of damages such as wear, rolling contact fatigue (RCF), thermal cracks, plastic deformation and flats caused by wheel sliding [4]. These types of damage result in a change in the tread profile, which aggravates wheel–rail contact forces vertically by the wheel OOR and laterally by the impaired vehicle dynamics.

It is generally believed that wheel local defects are caused by poorly adjusted or defective brakes, or incorrect braking procedures. Once the wheels of a vehicle become locked during braking, they slide along the track. The friction initiated during the process adhesively wears a flat spot on the wheel [5]. The high temperatures reached during sliding, followed by a rapid cooling into the adjacent material when the wheel starts rolling again, leading to the formation of brittle martensite within the steel beneath the wheel flat [6]. The thermal impact and the phase transformations will generate large residual stresses which will interact with the rolling contact stresses and will promote crack formation and growth [7]. As a result, damage to the wheel tread can occur, involving cracking and spalling, which is the loss of relatively large pieces of metal [7].

Studies on Mechanism and Prediction of Wheel Wear Development. Three important issues related to development mechanism of wheel wear are thermal cracking, prediction of wheel RCF and wheel tread damage.

Thermal Cracking. A large number of studies have been carried out to understand the correlation between hot spot on wheel tread and the resulting roughness and to identify conditions under which thermal cracks are initiated. Included are numerical simulation to calculate residual stresses distribution along and below the wheel tread and to study the crack propagation on wheel tread [7–15], as well as full-scale tread

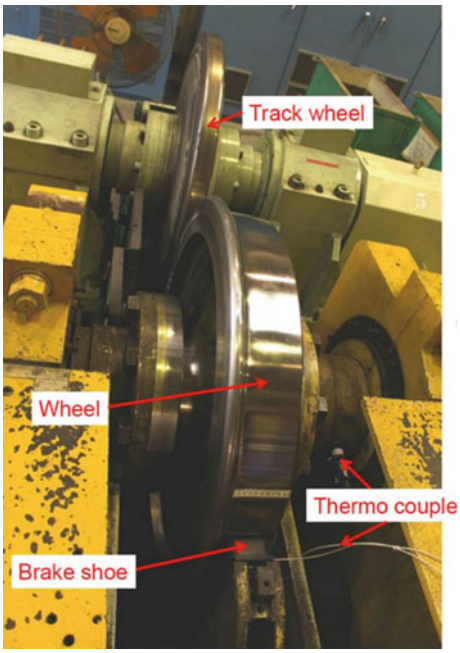

Fig. 2 Set-up of RTRI brake test rig (taken from [8, 15])

braking experiments with thorough metallographic examination to get knowledge about such correlation [6, 8, 9, 15–18]. Figure 2 shows a typical test rig in Railway Technical Research Institute (RTRI), Japan.

Prediction of Wheel RCF and Wheel Tread Damage. The wear of railway wheels is strictly related to RCF damage phenomena, so the prediction of wheel RCF and tread damage can allow operators to effectively define maintenance schedules for wheel re-profiling and can also facilitate the design of vehicles and wheelsets [19]. A fast and reliable wear prediction model was presented by Braghin et al. [19] in which the Derby wear index approach developed by Pearce and Sherratt [20] was used. It was validated by wear tests performed on a full-scale roller rig for mounted wheelsets. The mathematical models to predict wheel RCF mainly include those based on Shakedown theory and frictional energy and use wheel–rail contact forces generated from the vehicle dynamic simulations as input [21, 22]. For modern predictive models, the main focus is computational efficiency, so that they can be integrated with multi-body dynamic simulations of train–track interaction. Examples of integrating railway vehicle and track coupling dynamics with wear prediction models (e.g. Archard wear model) can be found in [23–27]. Some typical predictive models are developed using elasto-plastic finite element method and submodelling technique [28–30]. The stochastic loading in real operation was considered in some of previous research [29, 31].

Effects of Some Factors on Wheel Defect Development. Several factors such as speed, axle load, wheel–rail adhesion, wheel material and braking conditions affect

the wheel defect development [21]. By field experiments in which wheel flats can be formed under controlled conditions, Jergeus et al. [32] studied the relation between the development of wheel flat and the operation conditions, including wheel loads, train speeds, sliding durations and coefficients of friction. For high-speed rail (HSR), wheel wear rate can increase quickly due to the high operation speed, the high-stiffness track, the wide wheel–rail impact frequency, intense vibrations and high-speed airflow [33, 34]. The high wheel velocities can cause the reduction of fatigue life in both mechanical and thermo-mechanical cases [14]. Increasing track stiffness can lead to higher force at certain frequencies due to the track irregularities [3]. It is noteworthy that the ballastless track structure, which offers high stiffness, accounts for up to 70% HSR worldwide. The effect of other related factors, such as curving speed, the curved track super-elevation, the rail cant, short-pitch rail corrugation and stiffness and damping of fasteners on wheel wear, was studied by [35, 36], whereas the role of material imperfections and anisotropy in development of wheel local defects was investigated by [37–39].

Investigations and Studies on Generation of Wheel Polygonal Wear. The polygonal phenomenon of railway vehicle wheels can also be called wheel harmonic wear, wheel periodic OOR, or wheel polygonisation [40]. This problem can be found on metro trains, freight wagons, locomotives and high-speed trains. Polygonal wheels take on the shapes indicated in Fig. 3, mainly including eccentric, elliptic, the *n*th order polygonisation and so forth [2].

The studies of wheel polygonisation started some three decades ago when some of polygonal wheels were detected on metro trains (Netherland and Sweden) and high-speed trains (ICE, Germany) in Europe. Wheel polygonisation with one, three and four harmonics around circumference has been found on disc-braked wheels in ICE, in which the third harmonic dominated for solid steel wheels, while the second harmonic was common for rubber-sprung wheels [3]. An early survey in Netherland Railway (NS) was carried out by Kaper [41], who revealed that polygonal wheel can excite unpleasant noise at frequencies between 60 and 2000 Hz. A thorough investigation into this phenomenon was carried out by Johansson and Andersson [23] who analysed a set of measurement data of peaks and troughs on wheel tread of

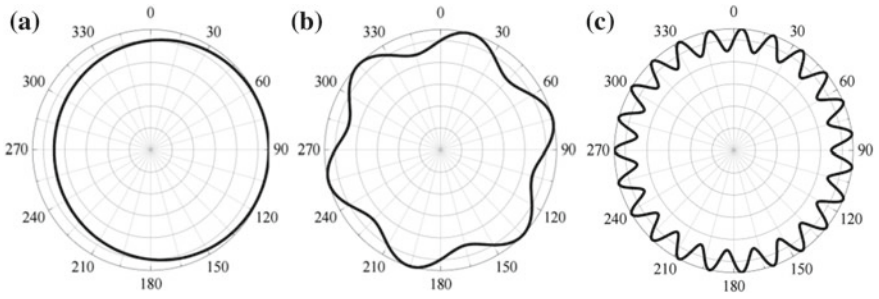

Fig. 3 Definition of wheel polygons described in polar coordinates: **a** the 1st order (eccentricity); **b** the 6th order; **c** the 23rd order [2]

Stockholm subway trains. The investigation found that the maximum peak-to-peak deviation in wheel radius was 1.2 mm, and the dominating wavelength was 0.8 m, which is close to three wavelengths around the circumference of the wheel. Tao et al. [26] investigated the polygonisation phenomenon on electric locomotive in China and revealed that the main centre wavelength in the 1/3 octave bands is 200 mm and/or 160 mm which has the considerable effect on vehicle vibration as suggested by axle box vertical vibration.

Similar to the wheel local defect problem, the reason behind wheel polygonisation has been studied by a number of researchers. They pointed out that the potential factors for polygonisation development are effects of tread braking, stiffness of axle, wheel material, etc. By establishing wheel–rail coupling model [23, 42–45] and conducting extensive investigations and tests [2, 40, 46–48], it is revealed that:

- Nonuniform force on the contact surface, arising from radial vibration from the shaft, led to uneven plastic deformation of the outermost layer, and wave crests and troughs then formed on the wheel tread [47].
- The root cause of low-order polygonisation is dynamic imbalance of the high-speed wheelset [42], while the root cause of high-order polygonal wear is the nonuniform material hardening on the wheel circumference, generated by the wheel–rail impact at high frequencies [46].
- The additional stiffness of the traction bar in braking condition or running on curve track can also cause polygonisation [43].
- The third order polygonisation arises from the fixation procedure during machining of the wheelsets, where the wheelsets were clamped at three equidistant positions on the inside of the wheel rim [23].
- The interaction of wheel out of roundness excitation and moment of inertia wheel increases the development of the wear [48]. The greater was the polygon phase difference of the left and right wheels, the faster was the development of polygonal wear [45]. The first and second bending modes of the wheelset play an important role in the initiation and development of the polygonisation [40, 45].
- The generation of polygonal wheel of metro trains is found to be related to the dominant frequency of wheel–rail dynamics and running speed [44].
- The high-order polygonisation phenomena on high-speed trains are easy to be associated with rail corrugation because both have a dominant wavelength and are assumed to be the counterpart to each other [49]. However, a recent study [2] stated that although the irregularities of the track can increase the growth rate of the wheel high-order polygonal wear, they are not the root causes of polygonal wear initiation.

1.2 Unfavourable Effects of Wheel OOR

Wheel OOR can cause intense vibration and has the potential to impose damage to both track structure (e.g. rails, fasteners, sleepers) and vehicle components (e.g.

wheels, axles, bearings, suspension systems). It can also increase the likelihood of derailment and deteriorate operational safety and ride comfort [1, 50, 51]. Table 1 lists some typical consequences of wheel OOR, as summarised in [52].

Vehicle Vibration. The dynamic force from wheel OOR can be detrimental to wheel/axle/bearing assemblies, and the service lives of these components can be reduced. First of all, wheel defect intuitively shortens the service life of wheel itself as it can result in cracks at surface or brittle martensitic layer at tread. Leaving the defective wheel in service or not adequately re-profiling the defective wheel may lead to further damage to the wheel, as the stresses caused by abnormal wheel–rail interaction may be sufficient to initiate fatigue cracks. In this case, the existing crack may propagate, and new cracks may develop by the action of the rolling contact stresses [5, 32]. For high-speed trains, the high magnitude impact loads generated by a defective wheel can excite various vibration modes for the wheelsets and thereby contribute to abnormal increases in the stress states of wheel axle in high-speed conditions [53]. Moreover, the ride comfort can be compromised by changes of the tread profile [43, 54].

Track and Ground Vibration. Out-of-round wheels generate impact forces at the wheel–rail interface, which can be transferred to track components including rail and rail joints, concrete sleepers, ballast or track slab and finally to subgrade/bridge/tunnel structures. It is also important to include ground vibrations affected by vehicle simulations as part of the problem since the low-frequency vibrations are considered by international standards (e.g. ISO 2631 [55]) as having the most critical effect on buildings and human exposure [33]. A detailed analysis for the influence of wheel OOR on ground vibration was conducted by [56], and results show that differences of up to 20 dB in vibration level are found between good and bad wheels.

Noise Problem. Wheel OOR also results in an increase in the noise generated by the interaction between wheel and rail [57, 58]. It can cause abnormal noise both inside and outside the train which can be annoying for both passengers on the train and residents along the rail line. It is found that the increased roughness level on 50–70 mm wavelength leads to up to 10 dB higher noise level [3]. Dings and Dittrich [59] measured the surface roughness on 150 railway wheels and on the rails of 30 sites in the Netherlands, as an attempt to survey the range of typical roughness appearing on in-service wheels and provide an insight into the absolute roughness levels and their contribution to radiated rolling noise. Furthermore, it is suggested

Table 1 Main consequences of wheel OOR [52]

Category	Description
Rail infrastructure	Rail fatigue, rail joint deterioration, sleeper degradation and failure, ballast and subgrade failure
Vehicle components	Service life reduction of wheel and bearing, degradation of passenger ride comfort
Others	Noise generation both inside and outside the train, fuel consumption

that the most efficient way to decrease the rolling noise levels should be eliminating or minimising the wheel and rail corrugation [17].

Effects of Polygonal Wear. Polygonal wheels can cause intense vibrations of the vehicle–track system in operation [40]. The wheel–rail impact normal force increases with the deepening of the wheel polygonal wear, and the amplitude of the normal force fluctuation depends mainly on the wavelength and depth of the polygonal wear on wheel tread [60]. The local geometry defects with long wavelengths on a wheel tread often lead to the large impact loads and acceleration and friction power of the wheel. It is noteworthy that for HSR, the problems arising from wheel high-order polygonal wear become the main challenges to maintain safety operation [34]. Even small wheel radius deviations within the manufacturing/maintenance tolerance cause considerable variations of the normal forces between wheel and rail [61]. Numerical simulation [53] shows that the stress load cycles induced by wheel polygonisation can considerably increase the propagation of the initial crack in the wheel axle. The noise problems also exist in the presence of wheel polygonisation. Zhang et al. [50, 51] presented a detailed investigation by field tests into the relationships between wheel polygonal wear and wheel/rail noise and the interior noise of high-speed trains. It is found that before and after re-profiling with polygonal wear, the acceleration level differences of the axle box, the bogie frame and the car body reach almost 16–19 dB.

2 Simulation of Vehicle–Track Dynamics Due to Wheel OOR

Numerical simulation evolves as a fast and inexpensive tool for investigating and predicting structural dynamics due to wheel OOR. A variety of methods have been proposed over the past decades to calculate the dynamic response of railway vehicle and rail track structure in the presence of OOR. Based on numerical simulation, a full understanding of the effect of wheel roughness can be gained, and a method to assess wheel condition can be developed. This section reviews the previous studies on characterising the dynamic behaviour of wheel OOR and its effects on vehicle–track system based on numerical simulation.

2.1 Wheel–Rail Interaction Modelling Considering Wheel OOR

The Geometric Models of Wheel Flat and Polygonisation. The widely used model of fresh (newly formed) wheel flat can be expressed by a piecewise function [62]:

$$z_F(\xi) = \begin{cases} R - \sqrt{R^2 - \xi^2}, |\xi| \geq L_0/2 \\ d, |\xi| < L_0/2 \end{cases} \tag{1}$$

where R is the radius of wheel, d is the depth of fresh flat, L_0 is the initial flat length, and ξ is the coordinate according to the direction of the rail that defines the position of the point of the wheel under consideration. The vertex of the fresh flat is a single point at which the contact traction present is so high that it causes the material to yield so that the initial geometry rapidly becomes rounded, and the function of rounded flat is [62]:

$$z_R(\xi) = \begin{cases} R - \sqrt{R^2 - \xi^2}, |\xi| \geq L/2 \\ R - \sqrt{R^2 - \xi^2} + \frac{L^2}{4R\pi^2}\left(1 + \cos\frac{2\pi\xi}{L}\right), |\xi| < L/2 \end{cases} \tag{2}$$

where L is the length of the rounded flat. The geometry of both types of flat with the same depth can be seen in Fig. 4a. On this basis, Pieringer et al. [63] plotted 3D geometry of both wheel flat shapes on a section of the cylindrical wheel surface, as shown in Fig. 4b, c.

For wheel polygonisation, it is a special case of wheel OOR with few dominant wavelengths. Compared to wheel flats, it is always discussed in frequency domain through Fourier analysis of the measured radius deviation data. The polygon order θ is defined by

$$\theta = \frac{2\pi R}{\lambda} \tag{3}$$

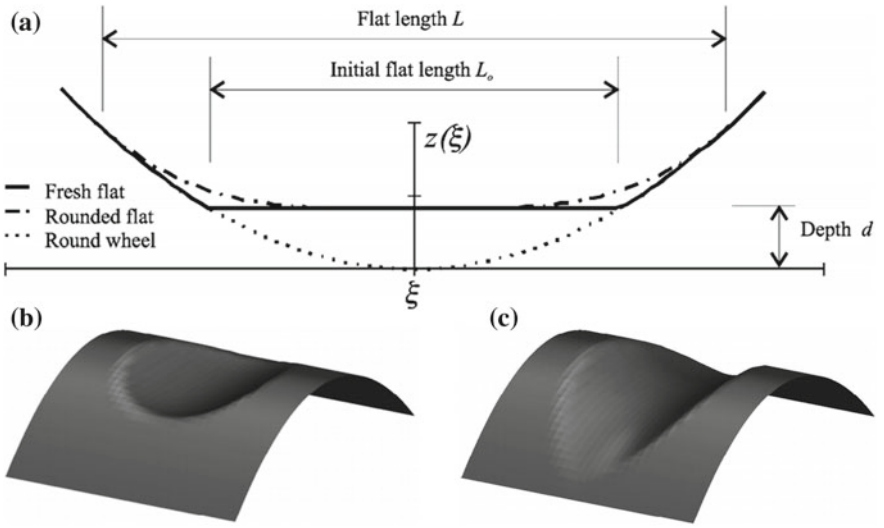

Fig. 4 Geometry of fresh and rounded flats: **a** 2D wheel flat [62]; **b** 3D fresh flat [63]; **c** 3D rounded flat [63]

where λ is the dominant wavelength corresponding to θth-order polygonisation. To investigate the effects of wheel polygonisation with different orders on wheel–rail contact and vehicle–track system dynamics, the expression prescribing wheel radius deviation is required, and it is defined as [3]:

$$z_{\text{irr}} = \sum_i A_i \sin\left(\frac{i}{R}x + \phi_i\right) \tag{4}$$

where i is the ith order of wheel polygonisation, A_i is the amplitude taken from the roughness spectrum, ϕ_i is the phase angle, and x is the coordinate on circumferential direction.

Wheel–Rail Contact Problems: Hertzian Theory. The reliability of the dynamic railway simulations is completely conditional upon the precision with which the wheel–rail contact problem is solved [64]. This chapter focuses on normal contact problems which are more important in discussing dynamic behaviour and detection methods of wheel OOR. Among the existing algorithms for solving the normal problems, the Hertz method is the most widely used in railway dynamic simulations as it combines very low computational costs with an acceptable accuracy in a wide range of conditions [65]. The Hertzian nonlinear elastic contact model provides the solution of the normal contact problem in the case of a cylinder rolling over a flat surface. The model considers only normal elastic force and inertia force by wheel deformation geometry. Hertzian spring is proportional to the elastic contact deflection to the power 3/2, assuming loss of contact does not occur [57]. The nonlinear relationship between the imposed load N and the material deformation d is [33]

$$N = K_H d^{3/2} \tag{5}$$

where the coefficient K_H depends on the radii of arch between the wheel and the rail and the elasticity of material for both bodies. The nonlinear contact stiffness is determined by assuming 3D contact mechanics according to Hertz. For example, if taking the curve radii 0.45 m and ∞ for the wheel and ∞ and 0.30 m for the rail, the Hertzian contact stiffness coefficient will be equal to 9.17×10^{10} N/m$^{3/2}$ [66].

One of the advantages of Hertzian method is that the solution can be expressed by means of elliptical integrals, whereby the computational cost in solving the normal problem is very low [64]. A linearised model is often necessary for frequency-domain analysis, by considering small variations Δd around the nominal value d_0 (Fig. 5).

Limitations of Hertzian Theory and Improvements. The initial fundamental hypotheses of the Hertzian contact model are the geometric requirement: the non-deformed surfaces of the bodies in contact should be elliptic paraboloids. Some assumptions using Hertzian method include [65]: (i) consideration that the bodies in contact have perfectly smooth surfaces; (ii) size of the contact area is significantly small with respect to surface curvature radii; (iii) contact between the surfaces must be frictionless so that only normal forces are transmitted, or the normal and tangential problems must be independent of each other; (iv) The undeformed distance between

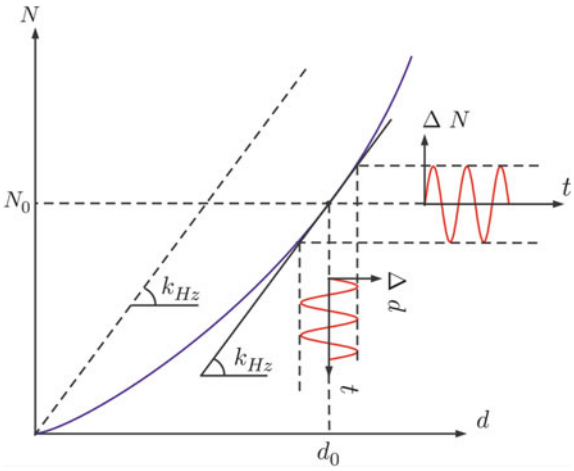

Fig. 5 Wheel/rail contact: Hertz's theory and linearisation [33]

the bodies in the proximity of the contact area can be represented by a quadratic function.

Discussions on whether and how these requirements can be satisfied in wheel OOR simulation have never ceased. It is generally believed that Hertzian theory cannot be used to characterise wheel–rail interaction in presence of wheel flat [3, 67, 68]. Nielsen [3] pointed out that the theory of Hertz is based on a second-order Taylor expansion of the bodies, and the second-order approximation is too primitive to describe a corrugated surface where the size of the characteristic wavelength is small compared to the length of the contact patch. Enblom and Berg [67] stated the geometric conditions of constant curvature and infinite half-space based on Hertz's assumption may be violated at certain locations, including wheel local defects. Baeza et al. [68] revealed that the peak value of the force transmitted as calculated by the non-Hertzian model is significantly lower in most of the cases studied. In the simulations performed, a deviation can be observed from the results of the Hertzian model that can exceed 30% of the real peak value.

To overcome the limitations of the Hertzian contact model, some improvements have been proposed by [65, 69–72], mainly including the semi-Hertzian models and finite element method (FEM). However, a major challenge for adopting non-Hertzian contact in vehicle–track coupling models is that the computational efficiency is likely to be limited by the process to determine the contact area. In contrast to their good precision, non-Hertzian contact models can be much more time consuming and demand high computational resources, whereby it cannot be applied to vehicle–track system dynamic simulations [64, 71].

2.2 Vehicle–Track System Dynamics: Modelling Approaches

Time- and Frequency-Domain Simulation. The dynamic simulation to study the effects of wheel OOR can be conducted either in time domain or frequency domain. Each of the two modelling approaches offers both advantages and drawbacks when compared to the other [3]. The frequency-domain models are linear, generally with higher computational efficiency, whereas the time-domain approach has some inclusion of nonlinear behaviour, particularly the wheel–rail contact [73] and some nonlinear suspension features such as bumpstop impacts and friction damping [74].

Time-Domain Models. Time-domain solution of the equation system allows spring and damping elements to remain nonlinear. This is important in some cases, including most contact conditions with corrugations which are highly nonlinear [75], and the deterioration analysis of the track which depends on the local situation and on a correct treatment of the nonlinear contact mechanics [76]. The drawback is the computation cost, especially in the cases that require the size of the time step must be small enough to capture the frequencies of interest [52].

Frequency-Domain Models. A comprehensive analysis of wheel out-of-roundness should account for the resulting vibration of whole vehicle–track system. However, a coupling model of vehicle, track and bridge, involves a high computational cost if it is simulated and solved in time domain. If the system can be assumed linear, frequency-domain simulations are suitable due to their reduced computational demand [33]. Frequency-domain models offer shorter computing times compared to the time-domain models, especially when the frequencies of excitation are high [57]. In frequency-domain modelling, all the excitations and responses are expressed in frequency domain. The nonlinear characteristics of the actual suspension system are treated as linear springs and viscous dampers. More importantly, the wheel–rail contact is treated as linearised Hertzian contact using the contact stiffness near the static axle load, as described in Sect. 2.1.

Examples of computer programs for vehicle–track system dynamic simulation in frequency domain in combination with the moving roughness model are TWINS and TRACK, whereas DIFF, VIA and VICT are computer programs of time-domain models [3].

Selection of Modelling Approaches. Model selection requires a trade-off between computational accuracy and efficiency. For effect analysis of wheel OOR on vehicle-track system, therefore, the feature of specific defects should be considered carefully. Wheel local defect and polygonal wear have a lot in common, and in many cases, the initiation and development mechanism of them is similar. However, they are so different when serving as excitation source. To achieve both computational accuracy and efficiency, different modelling approaches should be chosen.

For wheel local defects which generate transient high-frequency vibration for both wheel and rail, time-domain model is suitable. In numerical modelling to analyse the effects of wheel local defect, the following aspects should be considered:

(1) the effect of wheel rotation: rotation effect of wheel is discussed later in the same subsection.
(2) simplification in modelling: the time-domain model for high-frequency analysis need to be simplified to achieve a satisfactory computational efficiency, and simplification should meet the requirement of intended use. For most types of wheel local defects, since the primary suspension and fasteners filter the high-frequency vibration originated in the wheel–rail contact, only the gravity loads of car body and bogies should be taken into consideration in dynamic simulation. It is normal to only consider the unsprung masses of the vehicle and rail with discrete supports.

Unlike wheel local defect, wheel polygonal wear mainly leads to an increased low- or mid-frequency dynamic wheel–rail contact force. These may cause further abnormal vibrations on bogie, car body, track slab and bridge (or tunnel, subgrade) as the low-frequency vibration is difficult to be filtered by suspension systems and rail pad. A comprehensive analysis of the effects of polygonal wear therefore should account for the resulting vibration of whole vehicle–track system. However, a coupling model of vehicle, track and bridge, involves a high computational cost if it is simulated and solved in time domain. In view of this, frequency-domain model which has the advantage in computational efficiency can be a good option. Besides, the difference between the nonlinear and linear interactions is found to be small if the roughness level is not extremely high, and a typical static contact preload exists [77]. The radius deviation of the polygonal wheels is normally very small (<0.1 mm for high-speed trains), so it is reasonable to use a linear model to describe the wheel–rail contact.

In summary, if nonlinear behaviour needs to be included in the model, then time-domain simulations are preferable; if the system can be assumed linear, then frequency-domain simulations are suitable due to their reduced computational demand. Therefore, local defect analysis should be conducted in time domain, while the wheel polygonisation can be modelled in frequency domain to achieve both computation accuracy and efficiency.

Simplified Wheel–Rail Coupling Model. Simplified wheel–rail coupling model is always employed in time-domain approach in which the computation cost needs to be reduced. The simplest wheel–rail coupling model is known as mass–spring–beam approach, in which rails are represented by different beam elements, while wheels are approximated as rigid masses [78]. However, when there is a need to describe the dynamics of bogie, car body, sleeper or track slab and subgrade/bridge/tunnel due to wheel OOR, the mass–spring–beam model is no longer appropriate. Yet, it is found that in some cases, the track flexibility influences the frequency content of the wheel–rail forces significantly [79].

In recognition of this, there are some improvements based on mass–spring–beam approach. Whether it is necessary to consider more on vehicle components or more on track structure depends on different research demands. A basic improvement in vehicle modelling is to take the effects of primary suspension into consideration. It is regarded as the ‘a quarter vehicle’ model [80, 81]. The back half of the vehicle is

assumed to be sufficiently distant from the front that it does not need to be included, based on the extent of motion of the vehicle body [52]. For track modelling, multi-layer mass or beam model can be used to characterise the rail and sleeper, or further to the ballast or track slab and elastic foundation.

Track and Vehicle Modelling. It is reasonable to divide the entire system into two subsystems: vehicle and track because the gross motion of a train and a track is dominated by motion in different frequency ranges: low frequencies for the vehicle, 0–100 Hz, while frequencies up to 1500 Hz can be interesting for the track structure dynamics [82]. Track structure should be modelled carefully based on the desired frequency range of the analysis. For vehicle modelling, to analyse the vehicle dynamic responses at mid- and high-frequencies, the vehicle flexibility should be considered. The vehicle modelling approaches mainly depend on the rigid multi-body system dynamics theory, where the components of the vehicle are treated to be rigid bodies, and they are connected with springs and damping elements [34]. Some typical lumped vehicle models contain 5 DOFs, 6 DOFs, 10 DOFs, 27 DOFs, 35 DOFs, etc., determined by the need of dynamic analysis.

Another important issue to be discussed is the rotation effect of wheel. Baeza et al. [62] revealed that under certain conditions, the rotation of the wheel may also play an important role in the high-frequency vehicle–track dynamics. The calculations allow us to compare rigid, non-rotating flexible and rotating flexible wheelset approaches. It is revealed by the wheel flat calculations that the rigid wheelset model overestimates the peak wheel–rail contact force. A more general method, which considers the rotation about the two end points of the wheel flat and calculates the vertical impact force derived from the corresponding momentum in line with gravity centre height change, has been proposed by Steenbergen [83, 84].

Wheel–Rail Interaction and Wheel Defect Modelling by FEM. One of the advantages of FEM in wheel OOR analysis is that it can simulate flexibility of wheel and rail more realistically than multi-body-system (MBS)-programs which neglect the elasticity of the wheel and are valid only for low-frequency analysis [76]. Furthermore, the FEM can represent the actual geometrical and kinematic characteristics of the wheel–rail system when characterising the contact problems [85].

Wu and Thompson [86] studied the wheel–rail impacts using a nonlinear track model in which the rail is represented by an FE model and supported by a nonlinear track foundation and interacts with the wheel through a nonlinear Hertzian contact spring. A relative displacement excitation model is used to calculate wheel–track impact. Relying on current computing technique, it is convenient to use commercial codes to simulate wheelset and rail track where the actual geometrical sizes of the wheel, the rail and the vehicle's unsprung mass. The wheelset modes and corresponding natural frequencies can be obtained through the modal analysis of the finite element (FE) model, and they can be input into the simulation by means of the commercial codes (ADAMS, SIMPACK, NEWEUL, etc.). Besides, the parameters of the track characteristics can also be considered. Liu et al. [28] established a FE model to describe wheel–rail contact in which the wheel and rail were simulated using SOLID45 element, and area contact elements (CONTACT 174 and TARGET

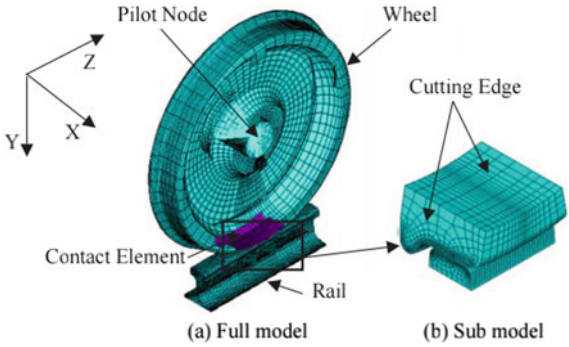

Fig. 6 Wheel–rail contact modelling by FE [28]

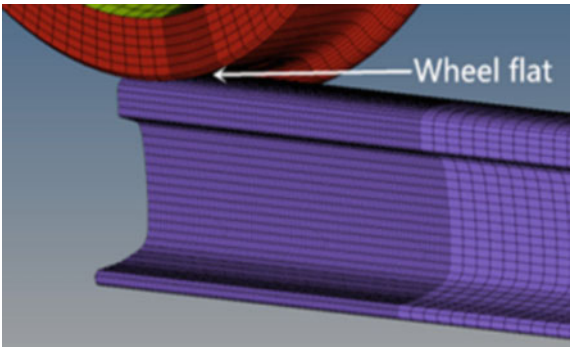

Fig. 7 Wheel flat modelling by surface-to-surface contact [88]

170 in ANSYS) are used corresponding to the geometry mesh of the wheel, as shown in Fig. 6. However, since the aim of that study is to obtain the wheel–rail contact force for the prediction of RCF, the wheel wear was not considered in contact behaviour. Zhao et al. [78] evaluated the wheel–rail interaction at singular rail surface defects using a validated three-dimensional (3D) transient finite element model. The 3D FE model has been validated in the normal and the tangential contact solutions against Hertz theory and Kalker's CONTACT. In this model, the wheelset, rail and sleepers are all meshed using 3D solid elements to include all the important eigen characteristics of the vehicle–track system, as shown in Fig. 8. The transient wheel–rail rolling contact is solved using a surface-to-surface contact algorithm in time domain. The surface-to-surface contact is also used by [87, 88] (Fig. 7).

2.3 Summary

A lot of research efforts have been made to characterise the effects of wheel OOR on different components in vehicle–track system and to facilitate the prediction of wheel wear and RCF. There are various combinations of contact models, vehicle models

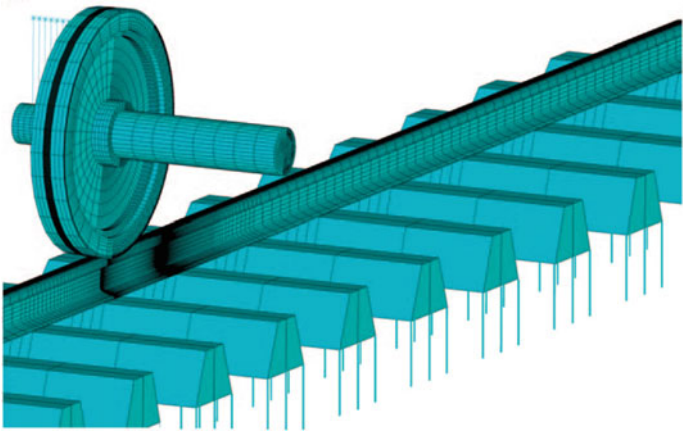

Fig. 8 The representation of the 3D vehicle–track FE model [78]

and track models in these proposed modelling approaches. This chapter would not discuss every study in detail, and here, a summary of these studies is given, including the models of wheel–rail contact, vehicle and track they used, as listed in Table 2.

3 Conclusions and Future Work

3.1 Conclusions

This chapter reviews the previous research relevant to wheel OOR, including causes and consequences of wheel defects and numerical simulations to study the effects of wheel OOR on vehicle–track system dynamics. Based on this review, some conclusions are summarised as follows:

(i) Wheel OOR has considerable dynamic effects on vehicle-track system in operation, especially for HSR. Research on effect assessment of wheel OOR is necessary in terms of enhancing safety and ride comfort and reducing maintenance cost.

(ii) The initiation of wheel local defects can be attributed to defective brakes or incorrect braking procedures, while polygonal wear is caused by the excited resonance of the train–track coupling system in operation. Effects that influence the development of wheel OOR include train speed, track stiffness, wheel maintenance, rail roughness, track normal irregularities and initial defects caused by wheel processing.

(iii) Regarding the selection of contact model, it is concluded that the Hertzian contact model is acceptable in most wheel–rail contact positions. Therefore, the solution based on non-Hertzian contact theory shall not differ too much

Table 2 A summary of research on numerical simulations to study the effects of wheel OOR

References	OOR type[1]	Aim/remarks	Contact model[2]	Vehicle model	Track model
[1]	(a) and (c)	Quantify the vertical wheel–rail contact force and track response for different types of OOR	(a)	Two wheels	Rail (undamped Timoshenko beam) and sleeper (mass)
[23]	(c)	Develop a tool for investigation of 1–20 order wheel polygonalization	(b)	A bogie with two wheels (6 DOFs, FEM)	Rail and sleepers (3D FEM)
[53]	(a) and (c)	Evaluate the stress states of wheelset axle due to wheel defects	(a)	Vehicle with flexible wheelsets (SIMPACK and FE)	Rail and track slab (3D FEM)
[57]	(a)	Predict the consequent noise radiation due to wheel flat	(a)	Wheel	Rail and sleeper
[62]	(a)	Model the kinematics associated with the elastic wheelset for high-frequency analysis	–	Wheelset (FE–3D solid to obtain the mode shape)	Rail and sleeper
[63]	(a)	Study the influence of contact modelling on simulated impact forces due to wheel flats to determine the errors introduced by simplified approaches	(c)	2 DOFs considering the wheelset and the primary suspension stiffness and damping	Rail (Timoshenko beam), sleepers (discrete mass)
[68]	(a)	Compare Hertzian and non-Hertzian contact	(a) and (d)	–	Rail and sleeper
[76]	(a)	Outline the numerical algorithm of the used time-domain model and to demonstrate its capabilities for nonlinear contact mechanics, high-frequency vehicle–track interaction, etc.	(a)	A rigid carbody with two rigid bogies and four elastic wheelsets	Rail, sleeper and ballast

(continued)

Table 2 (continued)

References	OOR type[1]	Aim/remarks	Contact model[2]	Vehicle model	Track model
[85]	(a)	Study the wheel–rail impact response induced by a single wheel flat considering strain rate and thermal stress	(e)	Wheel (FE, LS-Dyna and ANSYS)	Rail (modelling by FE LS-Dyna and ANSYS)
[86]	(a)	Explore the effects on wheel/track impact of the nonlinearity of the railway track supports	(a)	Wheel	Rail (Timoshenko beam), sleepers, rail pad (with nonlinear stiffness) and ballast
[87]	(a)	Thoroughly investigate the effect of wheel flats on impact forces	(e)	Wheel (FE code: ANSYS)	Rail, sleeper and ballast (FE code: ANSYS)
[88]	(a)	Parametric studies (train speed, flat length and axle load)	(e)	Wheelset (Hypermesh, LS-DYNA 3D/explicit code)	Rail (Hypermesh, LS-DYNA 3D/explicit code)
[89]	(a)	Investigate the vertical interactions between railway vehicles and tracks	(a)	A multi-body system with 10 DOFs	Infinite Euler beam supported on a discrete continuous foundation
[90]	(c)	Analyse the high-frequency oscillation and dynamic stress of wheel set axle induced by the polygonal wear	(a)	Vehicle with flexible wheelsets (SIMPACK and FE)	Rail and track slab (3D FEM)
[91]	(a)	Parametric studies (train speed, the wheel flat depth and the type of wheel flat)	(f)	Wheel and primary suspension	Rail and sleeper

(continued)

Table 2 (continued)

References	OOR type[1]	Aim/remarks	Contact model[2]	Vehicle model	Track model
[92]	(b)	Study impact forces at the wheel–rail interface in the presence of wheel flats	(a)	5-DOF pitch plane model: car body, one bogie, two wheelsets	Three-layer track system: rail, sleeper, ballast
[93]	(c)	Investigate vertical dynamic wheel/rail interaction resulting from a polygonal wheel at high speed	(a)	A multi-body system with 10 DOFs	Euler beam flexibly supported by a discrete-elastic foundation of three layers
[94]	(a)	Present 3-D vehicle–track system model considering the effects of wheel flat and track structure nonlinear	(a)	17-degrees of freedom lumped mass vehicle	Rail (Timoshenko beam), sleeper, nonlinear rail pad and ballast considered
[95]	(a)	Propose a hybrid model for the prediction of ground-borne vibration due to discrete wheel and rail irregularities	(a)	3-DOF wheelset	Rail and sleeper

Note [1]Defect types: (a) wheel flat/local defect; (b) multiple flats and distributed flats; (c) wheel polygonisation

[2]Contact models: (a) Hertzian nonlinear elastic contact; (b) modified FASTSIM to allow for general profiles; (c) 3D non-Hertzian contact model based on Kalker's variational method; (d) Kalker's non-conformal normal contact; (e) surface-to-surface contact algorithm; (f) nonlinear contact springs allowing for loss of contact

from the Hertzian solution. But for wheel flat with big size, this model may not be suitable, and novel contact models are needed.

(iv) Models developed for vehicle–track dynamic simulation should be made as simple as possible and should be accurate enough regarding the task they serve for. As for simulations to study the effects of wheel OOR, the prediction of impact forces caused by wheel local defects requires the application of time-domain models, whereas the investigation of wheel roughness at certain frequency ranges (e.g. wheel polygonisation with few dominant wavelengths) can be done by a frequency-domain model.

3.2 Limitations of Current Research and Future Work

Limitations of Studies/Investigations on Wheel OOR and Future Work. To reduce the negative effects of wheel OOR, the investigations on this phenomenon are necessary. As reviewed in this chapter, quite a few experiments and simulations have been conducted. However, the mechanism of occurrence and development of wheel OOR has not yet been explained perfectly, especially for wheel polygonisation. Besides, there is a need to predict the effects of actual wheel defects on both the vehicle components and track infrastructure. However, most of the previous studies only use the standard wear models (e.g. Eqs. 1–4), and simulations conducted to investigate the influence of measured wheel wear on vehicle–track–bridge system have rarely been reported before. In view of these two points, one future work can be investigations on wheel actual roughness of in-service trains based on wheel radius deviation measurement records.

Regarding the polygonisation problem, the phenomena presented by most of previous studies are those with one to five wavelengths around the wheel circumference. However, a new and big challenges in modern HSR are the high-order polygonisation (15–25 orders) with very small radius deviation (<0.05 mm, or <20 dB re 1 μm), as it has caused failures to the bogie components. There is an increasing demand for relative studies on this problem in future.

Limitations of Numerical Simulation for Wheel OOR Effect Analysis and Future Work. Relying on current computing technique, the simulation can be easily conducted based on several commercial codes available for the low-frequency domain, such as GENSYS, NUCARS, ADAMS SIMPACK and VAMPIRE. However, these commercial codes are generally used to analyse railway vehicle dynamics responses at frequencies below 20 Hz, where the influence of rigid motions of the vehicle on wheel–rail contact forces is dominant [81]. They are not suitable for effect analysis of wheel local defects and high-order polygonisation, or any types of OOR in case of high-speed operation. On the other hand, for current models which take full consideration of wheel-rail interaction in the presence of wheel OOR, the calculation speed is very slow and cannot meet the requirements raised by parametric studies of OOR effects. Therefore, a comprehensive modelling strategy needs to be developed, which can combine different modelling techniques to consider the different realistic engineering problems of wheel OOR.

Future Work: Online Detection for Minor Defects. Although numerical simulations evolve as a fast and inexpensive tool for investigating and predicting the development of wheel tread defects and effect analysis of OOR, online wheel condition monitoring and defect detection is still the best way to provide support for maintenance and health management for wheelsets. Through numerical simulation, the defect-sensitive features can be revealed. On this basis, a further research can be carried out to develop wayside or on-board sensing system for different types of wheel OOR. Due to the fact that the existing detectors are mainly designed for detection of large size wheel local defects, future work may focus on proposing a better

design of online wheel condition monitoring system that can detect local defects and polygonisation with small radius deviation.

Following the development of online detector, the next task is to make a rational decision about whether a wheel is healthy or not in light of data collected by online monitoring system. A well-developed data processing procedure is thus required. However, research efforts on development of signal processing method for wheel defect detection are rarely reported. This is partly because the existing codes or rules only stipulate the limits on maximum wheel–rail force, and only a basic amplitude analysis is enough. For modern railway, especially for HSR, as aforementioned, the defect detection should focus on minor defects but the variation of wheel load cannot reveal this kind of minor defects. Therefore, future research on wheel defect detection should consider using data-driven methods and advance signal processing techniques to extract defect-sensitive feature from online monitoring data.

References

1. Johansson, A., Nielsen, J.C.: Out-of-round railway wheels–wheel-rail contact forces and track response derived from field tests and numerical simulations. Proc. Inst. Mech. Eng. Part F J. Rail Rapid Transit **217**(2), 135–146 (2003)
2. Wu, Y., Du, X., Zhang, H.J., Wen, Z.F., Jin, X.S.: Experimental analysis of the mechanism of high-order polygonal wear of wheels of a high-speed train. J. Zhejiang Univ. Sci. A **18**(8), 579–592 (2017)
3. Nielsen, J.: Out-of-round railway wheels. In: Lews, R., Olofsson, U. (eds.) Wheel-Rail Interface Handbook. Woodhead Publishing, UK, pp. 245–279 (2009)
4. Handa, K., Kimura, Y., Mishima, Y.: Surface cracks initiation on carbon steel railway wheels under concurrent load of continuous rolling contact and cyclic frictional heat. Wear **268**(1), 50–58 (2010)
5. Dukkipati, R.V., Dong, R.: Impact loads due to wheel flats and shells. Veh. Syst. Dyn. **31**(1), 1–22 (1999)
6. Ahlström, J., Karlsson, B.: Microstructural evaluation and interpretation of the mechanically and thermally affected zone under railway wheel flats. Wear **232**(1), 1–14 (1999)
7. Jergéus, J.: Martensite formation and residual stresses around railway wheel flats. Proc. Inst. Mech. Eng. Part C J. Mech. Eng. Sci. **212**(1), 69–79 (1998)
8. Esmaeili, A., Walia, M.S., Handa, K., Ikeuchi, K., Ekh, M., Vernersson, T., Ahlström, J.: A methodology to predict thermomechanical cracking of railway wheel treads: From experiments to numerical predictions. Int. J. Fatigue **105**, 71–85 (2017)
9. Kwon, S.J., Seo, J.W., Jun, H.K., Lee, D.H.: Damage evaluation regarding to contact zones of high-speed train wheel subjected to thermal fatigue. Eng. Fail. Anal. **55**, 327–342 (2015)
10. Vernersson, T.: Thermally induced roughness of tread braked railway wheels: part 2: modelling and field measurements. Wear **236**(1), 106–116 (1999)
11. Wallentin, M., Bjarnehed, H.L., Lundén, R.: Cracks around railway wheel flats exposed to rolling contact loads and residual stresses. Wear **258**(7), 1319–1329 (2005)
12. Handa, K., Morimoto, F.: Influence of wheel/rail tangential traction force on thermal cracking of railway wheels. Wear **289**, 112–118 (2012)
13. Zwierczyk, P.T., Váradi, K.: Thermal stress analysis of a railway wheel in sliding-rolling motion. J. Tribol. **136**(3), 031401 (2014)
14. Haidari, A., Hosseini-Tehrani, P.: Fatigue analysis of railway wheels under combined thermal and mechanical loads. J. Therm. Stress **37**(1), 34–50 (2014)

15. Caprioli, S., Vernersson, T., Handa, K., Ikeuchi, K.: Thermal cracking of railway wheels: towards experimental validation. Tribol. Int. **94**, 409–420 (2016)
16. Vernersson, T.: Thermally induced roughness of tread-braked railway wheels: part 1: brake rig experiments. Wear **236**(1), 96–105 (1999)
17. Petersson, M.: Noise-related roughness of railway wheel treads-full-scale testing of brake blocks. Proc. Inst. Mech. Eng. Part F J. Rail Rapid Transit **214**(2), 63–77 (2000)
18. Vakkalagadda, M.R.K., Srivastava, D.K., Mishra, A., Racherla, V.: Performance analyses of brake blocks used by Indian Railways. Wear **328**, 64–76 (2015)
19. Braghin, F., Lewis, R., Dwyer-Joyce, R.S., Bruni, S.: A mathematical model to predict railway wheel profile evolution due to wear. Wear **261**(11), 1253–1264 (2006)
20. Pearce, T.G., Sherratt, N.D.: Prediction of wheel profile wear. Wear **144**(1–2), 343–351 (1991)
21. Bevan, A., Molyneux-Berry, P., Eickhoff, B., Burstow, M.: Development and validation of a wheel wear and rolling contact fatigue damage model. Wear **307**(1), 100–111 (2013)
22. Ekberg, A., Kabo, E., Andersson, H.: An engineering model for prediction of rolling contact fatigue of railway wheels. Fatigue Fract. Eng. Mater. Struct. **25**(10), 899–909 (2002)
23. Johansson, A., Andersson, C.: Out-of-round railway wheels—a study of wheel polygonalization through simulation of three-dimensional wheel–rail interaction and wear. Veh. Syst. Dyn. **43**(8), 539–559 (2005)
24. Johansson, A., Nielsen, J.C.: Rail corrugation growth—influence of powered wheelsets with wheel tread irregularities. Wear **262**(11), 1296–1307 (2007)
25. Li, X., Jin, X., Wen, Z., Cui, D., Zhang, W.: A new integrated model to predict wheel profile evolution due to wear. Wear **271**(1), 227–237 (2011)
26. Tao, G.Q., Du, X., Zhang, H.J., Wen, Z.F., Jin, X.S., Cui, D.B.: Development and validation of a model for predicting wheel wear in high-speed trains. J. Zhejiang Univ. Sci. A **18**(8), 603–616 (2017)
27. Luo, R., Shi, H., Teng, W., Song, C.: Prediction of wheel profile wear and vehicle dynamics evolution considering stochastic parameters for high-speed train. Wear **392**, 126–138 (2017)
28. Liu, Y., Stratman, B., Mahadevan, S.: Fatigue crack initiation life prediction of railroad wheels. Int. J. Fatigue **28**(7), 747–756 (2006)
29. Liu, Y., Liu, L., Stratman, B., Mahadevan, S.: Multiaxial fatigue reliability analysis of railroad wheels. Reliab. Eng. Syst. Saf. **93**(3), 456–467 (2008)
30. Taraf, M., Zahaf, E.H., Oussouaddi, O., Zeghloul, A.: Numerical analysis for predicting the rolling contact fatigue crack initiation in a railway wheel steel. Tribol. Int. **43**(3), 585–593 (2010)
31. Sandström, J.: Subsurface rolling contact fatigue damage of railway wheels-a probabilistic analysis. Int. J. Fatigue **37**, 146–152 (2012)
32. Jergeus, J., Odenmarck, C., Lunden, R., Sotkovszki, P., Karlsson, B., Gullers, P.: Full-scale railway wheel flat experiments. Proc. Inst. Mech. Eng. Part F J. Rail Rapid Transit **213**(1), 1–13 (1999)
33. Kouroussis, G., Connolly, D.P., Verlinden, O.: Railway-induced ground vibrations—a review of vehicle effects. Int. J. Rail Transp. **2**(2), 69–110 (2014)
34. Jin, X.S.: Key problems faced in high-speed train operation. J. Zhejiang Univ. Sci. A **15**(12), 936–945 (2014)
35. Jin, X., Xiao, X., Wen, Z., Guo, J., Zhu, M.: An investigation into the effect of train curving on wear and contact stresses of wheel and rail. Tribol. Int. **42**(3), 475–490 (2009)
36. Ekberg, A., Kabo, E., Nielsen, J.C., Lundén, R.: Subsurface initiated rolling contact fatigue of railway wheels as generated by rail corrugation. Int. J. Solids Struct. **44**(24), 7975–7987 (2007)
37. Ekberg, A.: Rolling contact fatigue of railway wheels. Chalmers University of Technology, Goteborg, Sweden (2000)
38. Ekberg, A., Marais, J.: Effects of imperfections on fatigue initiation in railway wheels. Proc. Inst. Mech. Eng. Part F J. Rail Rapid Transit **214**(1), 45–54 (2000)
39. Ekberg, A., Sotkovszki, P.: Anisotropy and rolling contact fatigue of railway wheels. Int. J. Fatigue **23**(1), 29–43 (2001)

40. Jin, X., Wu, L., Fang, J., Zhong, S., Ling, L.: An investigation into the mechanism of the polygonal wear of metro train wheels and its effect on the dynamic behaviour of a wheel/rail system. Veh. Syst. Dyn. **50**(12), 1817–1834 (2012)
41. Kaper, H.P.: Wheel corrugation on Netherlands railways (NS): origin and effects of "polygonization" in particular. J. Sound Vib. **120**(2), 267–274 (1988)
42. Meinke, P., Meinke, S.: Polygonalization of wheel treads caused by static and dynamic imbalances. J. Sound Vib. **227**(5), 979–986 (1999)
43. Ma, W., Luo, S., Song, R.: Abnormal vertical dynamic performance of subway vehicles. Chin. J. Mech. Eng. (English Edition) **23**(2), 174–179 (2010)
44. Ma, W., Song, R., Luo, S.: Study on the mechanism of the formation of polygon-shaped wheels on subway vehicles. Proc. Inst. Mech. Eng. Part F J. Rail Rapid Transit **230**(1), 129–137 (2016)
45. Meywerk, M.: Polygonalization of railway wheels. Arch. Appl. Mech. **69**(2), 105–120 (1999)
46. Cui, D.B., Lin, L., Song, C.Y.: Out of round high-speed wheel and its influence on wheel/rail behavior. J. Mech. Eng. **49**, 8–16 (2013)
47. Pan, R., Zhao, X., Liu, P., Ren, R.: Micro-mechanism of polygonization wear on railroad wheels. Wear **392**, 213–220 (2017)
48. Brommundt, E.: A simple mechanism for the polygonalization of railway wheels by wear. Mech. Res. Commun. **24**(4), 435–442 (1997)
49. Enblom, R.: Deterioration mechanisms in the wheel–rail interface with focus on wear prediction: a literature review. Veh. Syst. Dyn. **47**(6), 661–700 (2009)
50. Zhang, J., Han, G.X., Xiao, X.B., Wang, R.Q., Zhao, Y., Jin, X.S.: Influence of wheel polygonal wear on interior noise of high-speed trains. J. Zhejiang Univ. Sci. A **15**(12), 1002–1018 (2014)
51. Zhang, J., Xiao, X.B., Han, G., Deng, Y., Jin, X.S.: Study on abnormal interior noise of high-speed trains. In: Noise and Vibration Mitigation for Rail Transportation Systems, pp. 691–698. Springer, Berlin, Heidelberg (2015)
52. Barke, D.W., Chiu, W.K.: A review of the effects of out-of-round wheels on track and vehicle components. Proc. Inst. Mech. Eng. Part F J. Rail Rapid Transit **219**(3), 151–175 (2005)
53. Wu, X., Chi, M.: Study on stress states of a wheelset axle due to a defective wheel. J. Mech. Sci. Technol. **30**(11), 4845–4857 (2016)
54. Ikeuchi, K., Handa, K., Lundén, R., Vernersson, T.: Wheel tread profile evolution for combined block braking and wheel-rail contact: Results from dynamometer experiments. Wear **366**, 310–315 (2016)
55. ISO 2631-2: Mechanical vibration and shock—evaluation of human exposure to whole-body vibration—part 2: vibration in buildings (1 Hz to 80 Hz). International Organization for Standardization; Geneva, Switzerland (2003)
56. Nelain, B., Huber, P., Mirza, A., Oppel, M., Müller, R.: Field test measurement report—the influence from vehicle design on the generation of ground-borne vibration. RIVAS (SCP0-GA-2010-265754), Deliverable 5.6, October 2013
57. Wu, T.X., Thompson, D.J.: A hybrid model for the noise generation due to railway wheel flats. J. Sound Vib. **251**(1), 115–139 (2002)
58. Verheijen, E.: A survey on roughness measurements. J. Sound Vib. **293**(3), 784–794 (2006)
59. Dings, P.C., Dittrich, M.G.: Roughness on Dutch railway wheels and rails. J. Sound Vib. **193**(1), 103–112 (1996)
60. Li, L., Xiao, X.B., Jin, X.S.: Interaction of subway LIM vehicle with ballasted track in polygonal wheel wear development. Acta. Mech. Sin. **27**(2), 297–307 (2011)
61. Morys, B.: Enlargement of out-of-round wheel profiles on high speed trains. J. Sound Vib. **227**(5), 965–978 (1999)
62. Baeza, L., Fayos, J., Roda, A., Insa, R.: High frequency railway vehicle-track dynamics through flexible rotating wheelsets. Veh. Syst. Dyn. **46**(7), 647–659 (2008)
63. Pieringer, A., Kropp, W., Nielsen, J.C.: The influence of contact modelling on simulated wheel/rail interaction due to wheel flats. Wear **314**(1), 273–281 (2014)
64. Alonso, A., Giménez, J.G.: Wheel–rail contact: roughness, heat generation and conforming contact influence. Tribol. Int. **41**(8), 755–768 (2008)

65. Alonso, A., Giménez, J.G.: A new method for the solution of the normal contact problem in the dynamic simulation of railway vehicles. Veh. Syst. Dyn. **43**(2), 149–160 (2005)
66. Nielsen, J.C., Oscarsson, J.: Simulation of dynamic train–track interaction with state-dependent track properties. J. Sound Vib. **275**(3), 515–532 (2004)
67. Enblom, R., Berg, M.: Impact of non-elliptic contact modelling in wheel wear simulation. Wear **265**(9), 1532–1541 (2008)
68. Baeza, L., Roda, A., Carballeira, J., Giner, E.: Railway train-track dynamics for wheelflats with improved contact models. Nonlinear Dyn. **45**(3–4), 385–397 (2006)
69. Alonso, A., Giménez, J.G.: Some new contributions to the resolution of the normal wheel–rail contact problem. Veh. Syst. Dyn. **44**(sup1), 230–239 (2006)
70. Piotrowski, J., Kik, W.: A simplified model of wheel/rail contact mechanics for non-Hertzian problems and its application in rail vehicle dynamic simulations. Veh. Syst. Dyn. **46**(1–2), 27–48 (2008)
71. Quost, X., Sebes, M., Eddhahak, A., Ayasse, J.B., Chollet, H., Gautier, P.E., Thouverez, F.: Assessment of a semi-Hertzian method for determination of wheel–rail contact patch. Veh. Syst. Dyn. **44**(10), 789–814 (2006)
72. Li, S., Li, Z., Núñez, A., Dollevoet, R.: New insights into the short pitch corrugation enigma based on 3D-FE coupled dynamic vehicle-track modeling of frictional rolling contact. Appl. Sci. **7**(8), 807 (2017)
73. Grassie, S.L.: Models of railway track and vehicle/track interaction at high frequencies: results of benchmark test. Veh. Syst. Dyn. **25**(sup1), 243–262 (1996)
74. Evans, J., Berg, M.: Challenges in simulation of rail vehicle dynamics. Veh. Syst. Dyn. **47**(8), 1023–1048 (2009)
75. Baeza, L., Vila, P., Xie, G., Iwnicki, S.D.: Prediction of rail corrugation using a rotating flexible wheelset coupled with a flexible track model and a non-Hertzian/non-steady contact model. J. Sound Vib. **330**(18), 4493–4507 (2011)
76. Ripke, B., Knothe, K.: Simulation of high frequency vehicle-track interactions. Veh. Syst. Dyn. **24**(sup1), 72–85 (1995)
77. Wu, T.X., Thompson, D.J.: Theoretical investigation of wheel/rail non-linear interaction due to roughness excitation. Veh. Syst. Dyn. **34**(4), 261–282 (2000)
78. Zhao, X., Li, Z., Liu, J.: Wheel–rail impact and the dynamic forces at discrete supports of rails in the presence of singular rail surface defects. Proc. Inst. Mech. Eng. Part F J. Rail Rapid Transit **226**(2), 124–139 (2012)
79. Chaar, N., Berg, M.: Simulation of vehicle–track interaction with flexible wheelsets, moving track models and field tests. Veh. Syst. Dyn. **44**(sup1), 921–931 (2006)
80. Zhai, W.M., Wang, Q.C., Lu, Z.W., Wu, X.S.: Dynamic effects of vehicles on tracks in the case of raising train speeds. Proc. Inst. Mech. Eng. Part F J. Rail Rapid Transit **215**(2), 125–135 (2001)
81. Nielsen, J.C., Ekberg, A., Lundén, R.: Influence of short-pitch wheel/rail corrugation on rolling contact fatigue of railway wheels. Proc. Inst. Mech. Eng. Part F J. Rail Rapid Transit **219**(3), 177–187 (2005)
82. Andersson, C., Abrahamsson, T.: Simulation of interaction between a train in general motion and a track. Veh. Syst. Dyn. **38**(6), 433–455 (2002)
83. Steenbergen, M.J.: The role of the contact geometry in wheel–rail impact due to wheel flats. Veh. Syst. Dyn. **45**(12), 1097–1116 (2007)
84. Steenbergen, M.J.: The role of the contact geometry in wheel–rail impact due to wheel flats: part II. Veh. Syst. Dyn. **46**(8), 713–737 (2008)
85. Jing, L., Han, L.: Further study on the wheel–rail impact response induced by a single wheel flat: the coupling effect of strain rate and thermal stress. Veh. Syst. Dyn. **55**(12), 1946–1972 (2017)
86. Wu, T.X., Thompson, D.J.: The effects of track non-linearity on wheel/rail impact. Proc. Inst. Mech. Eng. Part F J. Rail Rapid Transit **218**(1), 1–15 (2004)
87. Bian, J., Gu, Y., Murray, M.H.: A dynamic wheel–rail impact analysis of railway track under wheel flat by finite element analysis. Veh. Syst. Dyn. **51**(6), 784–797 (2013)

88. Han, L., Jing, L., Liu, K.: A dynamic simulation of the wheel–rail impact caused by a wheel flat using a 3-D rolling contact model. J. Mod. Transp. **25**(2), 124–131 (2017)
89. Zhai, W.M., Sun, X.: A detailed model for investigating vertical interaction between railway vehicle and track. Veh. Syst. Dyn. **23**(sup1), 603–615 (1994)
90. Wu, X., Chi, M., Wu, P.: Influence of polygonal wear of railway wheels on the wheel set axle stress. Veh. Syst. Dyn. **53**(11), 1535–1554 (2015)
91. Pieringer, A., Kropp, W.: A fast time-domain model for wheel/rail interaction demonstrated for the case of impact forces caused by wheel flats. In: 7th European Conference on Noise Control 2008, EURONOISE 2008, Paris; France; 29 June 2008 through 4 July 2008
92. Uzzal, R.U.A., Ahmed, A.K.W., Rakheja, S.: Analysis of pitch plane railway vehicle—track interactions due to single and multiple wheel flats. Proc. Inst. Mech. Eng. Part F J. Rail Rapid Transit **223**(4), 375–390 (2009)
93. Liu, X., Zhai, W.: Analysis of vertical dynamic wheel/rail interaction caused by polygonal wheels on high-speed trains. Wear **314**(1), 282–290 (2014)
94. Uzzal, R.U.A., Ahmed, A.K.W., Bhat, R.B.: Modelling, validation and analysis of a three-dimensional railway vehicle–track system model with linear and nonlinear track properties in the presence of wheel flats. Veh. Syst. Dyn. **51**(11), 1695–1721 (2013)
95. Nielsen, J.C., Lombaert, G., François, S.: A hybrid model for prediction of ground-borne vibration due to discrete wheel/rail irregularities. J. Sound Vib. **345**, 103–120 (2015)

Dynamic Response Analysis of Wind Turbines Under Long-Period Ground Motions

Wanrun Li, Jie Huang and Yongfeng Du

Abstract Due to the lack of reliable long-period ground motion records, the influence of long-period ground motion on seismic performance of wind turbines is not studied sufficiently. Therefore, we have selected three sets of ground motion records with significant long-period components from 1999 Taiwan Chi-Chi earthquake and 2010 New Zealand Darfield earthquake in order to discuss the characteristics of their absolute acceleration amplification coefficient spectra and the relative displacement response spectrum. In addition, the paper took a typical 80-meter-high wind turbine structure in Northwest China as an example and investigated the seismic performance of the wind turbine via an integrated finite element model of the blade–cabin–tower. Three sets of ground motion records were taken as inputs to carry out the time-history analysis under the rare earthquake of the seismic fortification intensity zone 8. The results show that the displacement, acceleration, stress, and internal force of the wind turbine structure under long-period ground motions are relatively significant, which indicates that enough attention should be paid to the influence of long-period ground motions on the seismic performance of the flexible structure with large period.

Keywords Wind turbines · Long-period seismic wave · Spectrum analysis · Seismic response analysis

1 Introduction

In recent years, long-period ground motion has attracted extensive interest from scholars because of the rapid increase in the number of highly flexible structures, such as high-rise buildings and wind turbines. In 1983, a magnitude 7.7 earthquake occurred in the central Japan, located in Niigata City, 270 km from the epicenter. The

W. Li (✉) · J. Huang · Y. Du
Institute of Earthquake Protection and Disaster Mitigation, Lanzhou University of Technology, Lanzhou 730050, China
e-mail: ce_wrli@163.con

W. Li · Y. Du
International Research Centre of Seismic Mitigation and Isolation of Gansu Province, Lanzhou University of Technology, Lanzhou 730050, China

© Springer Nature Singapore Pte Ltd. 2019

Y. L. Zhou et al. (eds.), *Data Mining in Structural Dynamic Analysis*,
https://doi.org/10.1007/978-981-15-0501-0_4

storage tank overflowed and was damaged in 10 s. An earthquake of magnitude 8.1 occurred in Mexico in 1985, causing serious damage to high-rise buildings within 400 km of the epicenter. In the 2003 Tokachi-oki earthquake in Japan, the oil storage tank with a natural vibration period of 5–12 s was similar to the seismic characteristic period (7–8 s), and the fire occurred, there are different degrees of damage. With the rapid development of the economy, more and more high-rise buildings have emerged in the Midwest development of China, and some have been established in the high-intensity regions of earthquakes. In addition, some large cities and infrastructure are often built in sedimentary basins, and loose sedimentary layers will further amplify the long-period components of seismic waves, thereby increasing the risk of long-period ground motions.

Long-period ground motions are distinct from ordinary periodic earthquakes, and there are large differences in ground motion parameters. When considering the effects of long-period ground motions, the design seismic response spectrum given by the specification is obviously insufficient from the current specification both morphologically and numerically. Therefore, when determining the design response spectrum and selecting seismic waves, the influence of the long-period part on the structure should be fully considered [1]. Early analog strong earthquake recorders only recorded high-frequency-based short-period components and could not obtain long-period components with accuracy. With the large-scale use of digital strong earthquake recorders in recent years, some long-period seismic waves have been recorded, but the number is not enough to form a reliable long-period seismic response spectrum [2–4]. Therefore, there are relatively few studies on the characteristics of long-period ground motion and its influence on structures. Xie et al. [5] and Wang et al. [6] discussed the effects of site conditions, distances, and magnitudes on long-period ground motion characteristics. Wang et al. [7] investigated the seismic response spectrum of long-period ground motion. Shoji and Shibui [8] studied the seismic response of PC cable-stayed bridges under long-period ground motions. Hu et al. [9] proposed a three-segment curve model (in log–log space) to model the Q-F relationship and then manifested the impact of long-period ground motions on the seismic response of high-rise buildings through a numerical study. Yan et al. [10] and Zhenxuan [11] analyzed the long-period seismic response of the high-rise frame structure and obtained that the displacement response of the frame structure under long-period ground motion is significantly larger than that under ordinary earthquakes, and the seismic response characteristics of high-rise structures under long-period earthquakes are studied. Jialiang [12] studied the response of the base-isolated structure under long-period ground motions and explored its displacement, velocity, and acceleration response spectra. Shuqing et al. [13] applied time-history method to analyze the elastoplastic response of structures under long-period ground motions and obtained the preliminary results of the response under long-period ground motions greater than ordinary ground motions.

In the context of the energy crisis, wind energy has been valued and exploited by countries around the world as a green energy source. The wind turbine is mainly composed of a rotating wind wheel that captures wind energy, a cabin with a relatively heavy weight similar to a steel body, a tall and flexible tower structure, and foundation

Fig. 1 Wind turbine tower

group that support the above part of the generator (see Fig. 1). In order to obtain greater power production capacity, the size and weight of wind turbines continue to increase substantially, requiring higher support towers to lift components such as the nacelle and impellers higher, and this requirement makes the wind turbine structure a highly flexible structure with a large basic natural period of vibration. At present, there are some analysis results of seismic response of wind turbine structures. Due to the limited performance of wind turbines icy under cold conditions, Zanon et al. [14] proposed a numerical method that can simulate the phenomenon of ice accretion and its impact on wind turbine performance. Zhi et al. [15] studied the failure mode of wind turbine structures under ground motion with different frequency spectral characteristics. Ke et al. [16] proposed an effective method for predicting wind-induced fatigue caused by aeroelastic and yaw effects of large horizontal axis wind turbine coupling tower structures. Rahimi et al. [17] used three-dimensional computational fluid dynamics (CFD) data to study different methods for calculating the angle of attack and potential induced velocity of wind turbine blades. It can be seen from the literature that the current seismic response analysis of wind turbine structures is not comprehensive enough, especially the response under long-period ground motion is necessary.

In the light of the above, a detailed finite element model is established and discussed in this study, and three long-period ground motions are selected as input. This study investigated the model analysis of the wind turbine and the response spectrum

of long-period ground motions and then conducted the time history analysis of wind turbines under long-period earthquakes. Based on the numerical results, some preliminary analysis recommendations are finally made.

2 Long-Period Ground Motion Record and Spectral Characteristics Analysis

Three long-period ground motions were selected from Taiwan Chi-Chi earthquake and New Zealand Darfield earthquake, namely TCU141 seismic wave, CHY002 seismic wave, and Christchurch Hospital seismic wave. These three ground motions have characteristics of the low acceleration peak and long vibration time. However, long-period waves have more long-components than these three waves. Table 1 shows the basic information of long-period ground motions. The acceleration time history is shown in Fig. 2.

The Fourier amplitude spectrum reflects the distribution of ground motion energy in the frequency domain, which indicates the energy is carried by sine waves of different frequencies. As the distance from the epicenter increases, the attenuation of the high-frequency part is more significant than that of the low-frequency part, and its excellent frequency gradually shifts toward the low-frequency direction [18].

Figure 3 is the seismic wave Fourier amplitude spectrum. It can be seen from Fig. 3 that the long-period seismic wave has a large energy in the low frequency band, and the excellent frequency is mainly distributed in a lower frequency range. For example, the Christchurch Hospital seismic wave in New Zealand is mainly distributed between 0.1 and 1 Hz.

The seismic response spectrum is the response of a series of single-degree-of-freedom systems to reflect the frequency spectral characteristics of the earthquake. It can characterize the relationship between the structural ground motion response peak and its dynamic characteristics and then understand the influence of seismic wave spectral characteristics on structural seismic response. In order to further understand the spectral characteristics of long-period ground motions, the acceleration response spectrum and displacement response spectrum of three long-period ground motions

Table 1 Selected ground motion records

Seismic wave	Station name	Peak acceleration/g	Duration/s	Magnitude	Time
Chi-Chi, Taiwan-04	TCU141	0.05282	132.485	6.2	1999
Chi-Chi Taiwan-04	CHY002	0.04994	110.988	6.2	1999
Darfield New Zealand	Christchurch hospital	0.20939	110.79	7	2010

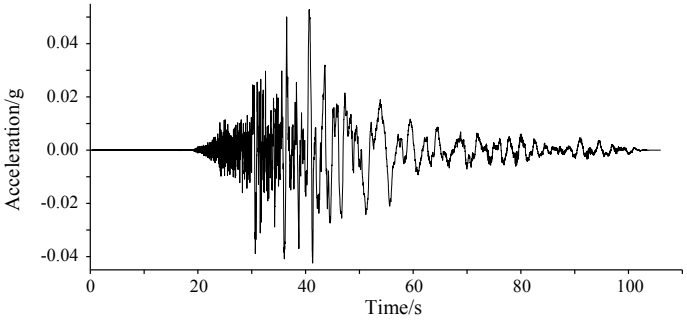

(a) TCU141 wave

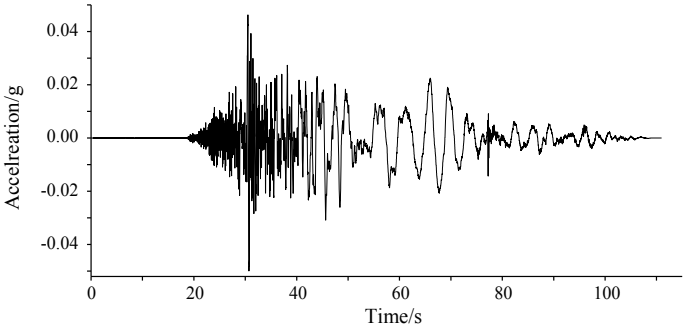

(b) CHY002 wave

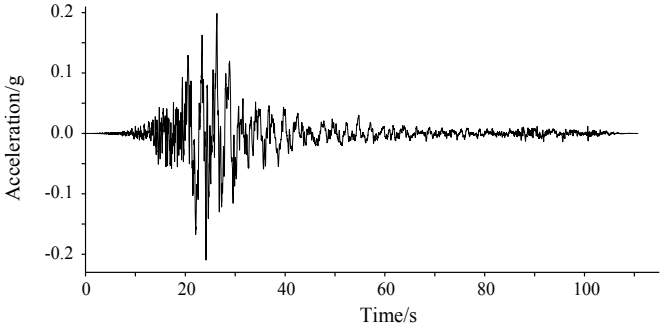

(c) Christchurch hospital wave

Fig. 2 Acceleration time-history curves of seismic waves

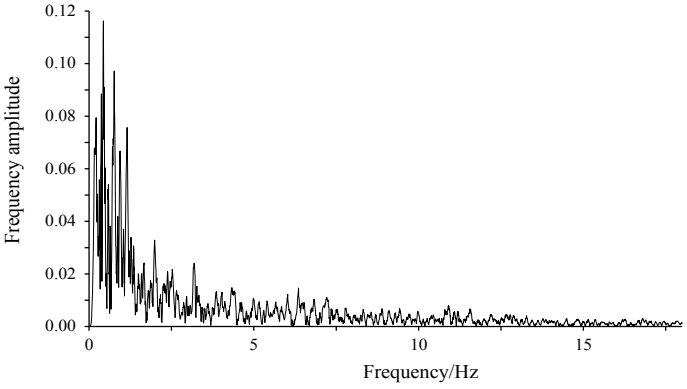

(a) TCU141 wave

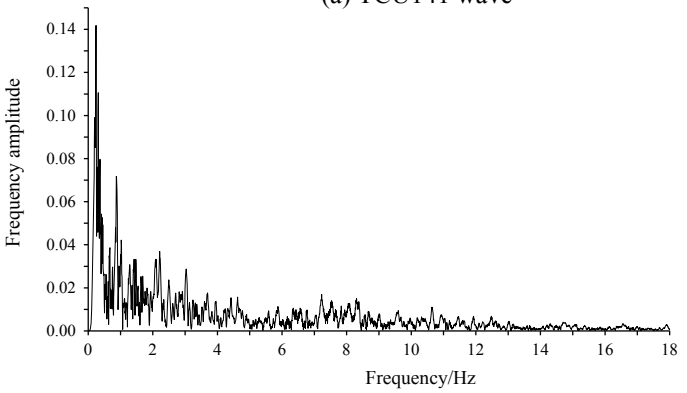

(b) CHY002 wave

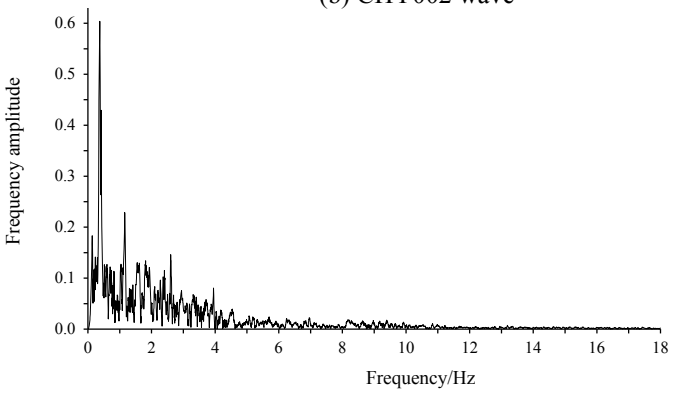

(c) Christchurch hospital wave

Fig. 3 Ground motion Fourier amplitude spectrums

are calculated. Considering the far-field properties of long-period seismic waves and the particularity of the recorded soil layer, the peak acceleration is not adjusted, and the original seismic record values are directly used.

It can be seen from the acceleration response spectrum in Fig. 4a that the predominant period of the TCU wave is 1.32 s, the predominant period of the CHY wave is 1.42 s, and the predominant period of the Christchurch Hospital wave is 0.7 s. The three seismic waves are not significantly attenuated in the long period of the response spectrum (4–8 s) and present obvious long-period vibration characteristics. Figure 4b is the displacement response spectrum, and after the period exceeds 2 s, the displacement response of the long-period ground motion increases sharply and reaches the peak at about 6 s and then begins to slowly decline. It also can be seen that the long-period ground motion has a great influence on the acceleration and displacement response of the flexible structure.

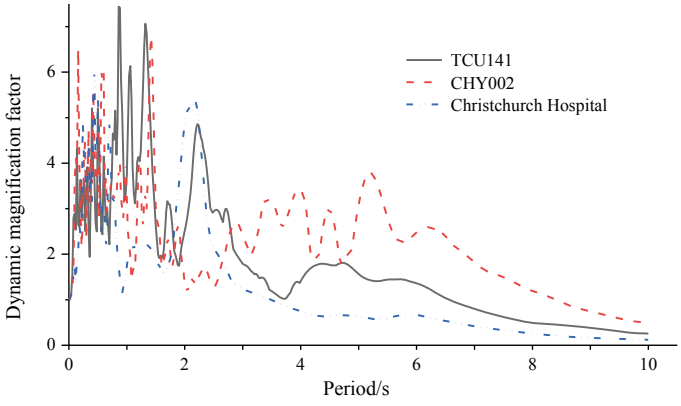

(a) Acceleration response spectrum (ξ=0.5%)

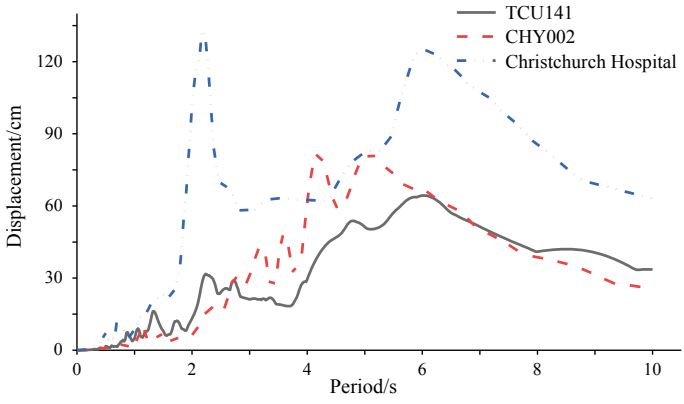

(b) Displacement response spectrum

Fig. 4 Ground motion acceleration and displacement response spectra

3 Finite Element Modeling and Modal Analysis

3.1 Modeling

The most typical 2 MW three-blade horizontal axis wind turbine in a wind farm in Northwest China was selected as the original model. The diameter of the rotor is 49 m, and the angle between the blades is 120°, and the rated speed is 18 r/min. The weight of wheel hub, each blade, and nacelle are 12 t, 14 t, and 60 t, respectively. During the analysis, the internal members of the nacelle were omitted to simplify it into a rectangle with a length of 5.4 m, a width of 3.6 m, and a height of 3.2 m. The height of the steel tower is 85 m, the bottom of the tower is 5.6 m in diameter, and the bottom of the tower is 30 mm thick. The top of the tower has a diameter of 3.87 m and the top wall has a wall thickness of 20 mm. Steel tower wall thickness varies linearly along height. The wind turbine tower is made of Q345 steel with the modulus of elasticity of 2.1×10^{11} Pa and density of 7850 kg/m^3. The properties of the wind turbine are expressed in Table 2.

The finite element model is established by using the commercial software ANSYS (see Fig. 5). The wind turbine tower is simulated by the shell element (shell181), and the nacelle and the hub at the top of the tower are regarded as a whole, the beam 189 element is utilized for simulation, and the three blades are simulated by the finite element strain beam element (beam189). A multi-point constraint equation is applied between the different component units to realize the coupling interaction. The bottom of the tower and the ground are consolidated.

Table 2 2-MW wind turbine properties

Wind turbine property	Value
Rated power	2 MW
Rated wind speed	18 r/min
Tower height	80 m
Lower section diameter	5.6 m
Lower section thickness	30 mm
Top section diameter	3.87 m
Top section thickness	20 mm
Nacelle mass	60 t
Blade mass	14 t
Rotor mass (with hub)	12 t

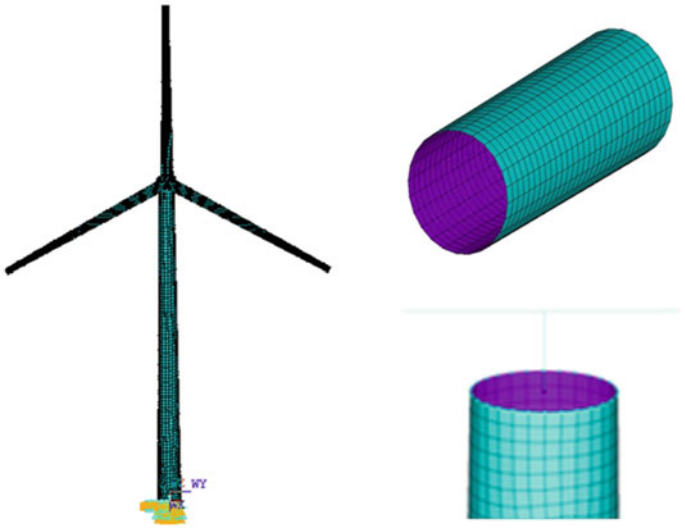

Fig. 5 Finite element model of wind turbine

3.2 Modal Analysis

The structural dynamic characteristics of wind turbines are distinct, and the seismic response will be very different. Especially if the basic natural period of vibration of the wind turbine is consistent with the excellent period of the input seismic wave, the reaction value will increase due to resonance. Therefore, it is very important to master the dynamic characteristics of the wind turbine beforehand in the seismic design of the wind turbine. In order to determine the basic vibration characteristics of the wind turbine structure, Lanczos Block is used for modal analysis. The natural frequencies of the first eight orders of the wind turbine structure are shown in Table 3. Figure 6 shows the eighth-order vibration pattern of the wind turbine tower, the first-order

Table 3 Natural frequency of wind turbine

Mode	Frequency describe	Frequency (Hz)
1	1st support side-to-side	0.2821
2	1st support fore-aft	0.2850
3	1st blade flapwise yaw	0.8467
4	1st blade flapwise pitch	1.0769
5	1st blade edgewise yaw	1.3206
6	1st blade edgewise pitch	1.3251
7	2nd support fore-aft	2.4865
8	2nd support side-to-side	3.3101

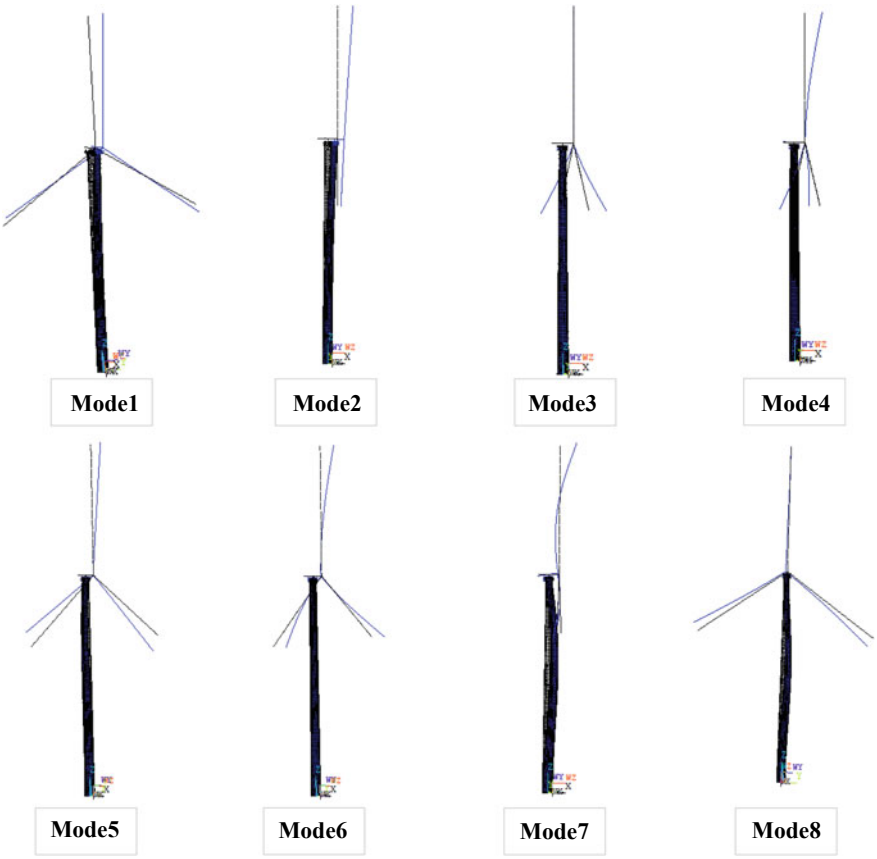

Fig. 6 The first eight flexural modes of the wind turbine tower

mode is mainly dominated by the lateral bending vibration of the tower, the second-order mode is mainly dominant by the front and rear bending deformation of the tower, the third- to sixth-order vibration mode mainly related to the local vibration vane, the seventh- and eighth-order vibration modes are mainly dominant by the second-order bending of the tower. In the reaction characteristics of wind turbines, even if the first-order mode occupies a main role, high-order mode reactions may occur under different types of ground motion.

4 Dynamic Response of Wind Turbine Structure Under Long-Period Ground Motion

In accordance with the provisions of the Code for Seismic Design of Buildings (GB 50011-2010), the acceleration peaks of each long-period ground motion are uniformly adjusted to 400 cm/s^2 in the light of the eight-degree rare earthquake. In order to simulate the dynamic response of the wind turbine structure under earthquake action, the three components of each seismic wave were considered in the elastic time-history analysis and referred to the relevant specified the accelerations along the horizontal principal direction (*X*-direction), the lateral direction (*Y*-direction), and the vertical direction (*Z*-direction) were proportioned with the scaling coefficients of 1.0:0.85:0.65, respectively. The dynamic response analysis of the structure is carried out, and the displacement, acceleration, stress, and base internal force of the wind turbine structure are obtained.

4.1 Displacement Response

The displacement response of the wind turbine structure along the tower height under long-period ground motion is presented in Fig. 7.

Figure 7a–c is the displacement responses of the wind turbine tower in the horizontal *X*-direction, the horizontal *Y*-direction, and the vertical *Z*-direction, respectively, under long-period ground motions. Figure 7d is the time-history curve of the displacement in the horizontal *X*-direction of the top of the wind turbine tower. It can be seen from the figure that the maximum nodal displacement of the wind turbine tower in the horizontal *X*-direction gradually increases along the height of the tower, and the displacement at the top of the tower reaches the maximum. The maximum top displacements of the wind turbine tower under the action of TCU141 wave, CHY002 wave and Christchurch Hospital wave can reach 1.15 m, 2.01 m, and 1.35 m, respectively (see Fig. 7d). The influence of wind turbine generators with low redundancy and high flexibility structure is not negligible and should be highly valued in the seismic design of wind turbine structures. The maximum nodal displacement of the wind turbine tower in the horizontal *Y*-direction has the same trend along the height of the tower, which is the same as the horizontal *X*-direction, that is, increases with the height of the tower (see Fig. 7b). It is worth noting that the maximum nodal displacement at the top of the tower in the horizontal *Y*-direction is still greater than 1 m. The maximum nodal displacement of the wind turbine tower in the vertical *Z*-direction shows a slight increase with the increase of the tower height, and the nodal displacement reaches a maximum at the top of the tower from the top 10 m (see Fig. 7c). The maximum nodal displacement of the wind turbine tower in the vertical *Z*-direction is nearly 60 mm, which will cause the tower to have dynamic pulling force. Because of the high strain rate, the steel becomes brittle. The tower

Fig. 7 Displacement along the wind turbine height

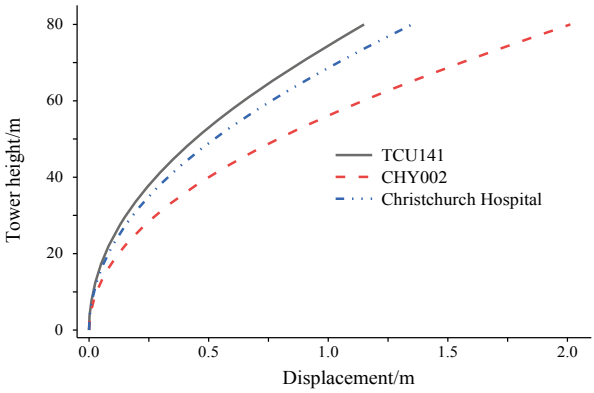

(a) X-direction horizontal displacement

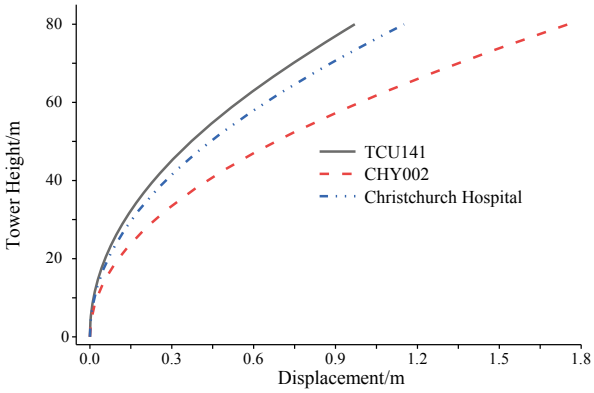

(b) Y-direction horizontal displacement

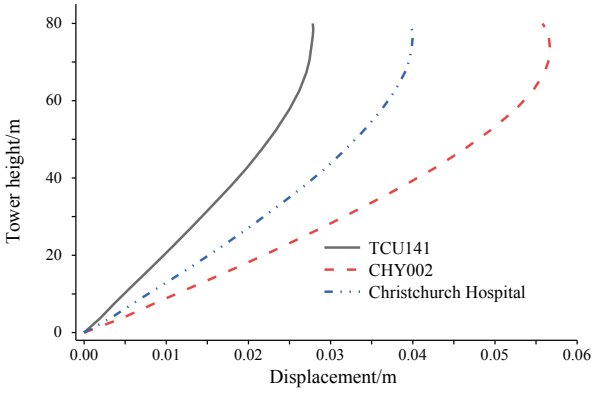

(c) Z-direction displacement

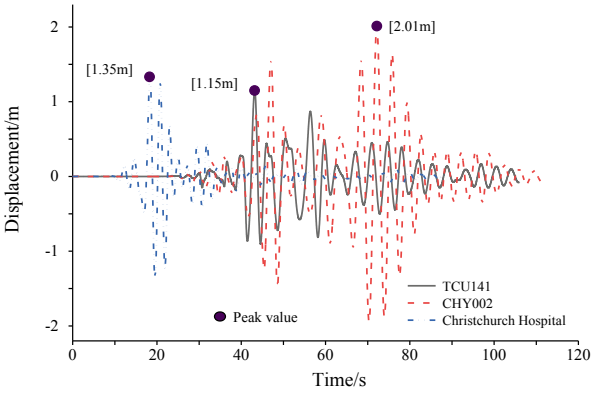

(d) Displacement time-history curve at the top of the tower

Fig. 7 (continued)

is mainly affected by the bending moment and the shearing force, which causes the shearing ability to decrease and the horizontal fracture.

4.2 Acceleration Response

The acceleration response of the wind turbine structure along the tower height under long-period ground motion is externalized in Fig. 8. The acceleration response of a wind turbine is expressed by the acceleration amplification coefficient, which is the ratio of the maximum acceleration response of the wind turbine structure over the peak long-period ground acceleration (PGA).

Figure 8a–c is the acceleration response of the wind turbine structure under long-period ground motions in the horizontal *X*-direction, the horizontal *Y*-direction, and the vertical *Z*-direction, respectively. Figure 8d is the acceleration time-history response curve of the wind turbine tower in the horizontal *X*-direction under long-term ground motion. The acceleration amplification coefficient of the wind turbine tower increases with the height of the tower in the horizontal *X*-direction, and the acceleration amplification factor at the top of the tower reaches the maximum value, which has the same trend as the displacement response of the wind turbine (see Fig. 8a). The displacement and acceleration response of the wind turbine under three long-period ground motions are controlled by its first-order vibration mode. The dynamic amplification coefficient of the wind turbine structure under the action of TCU141 wave and CHY002 wave can reach 13–16 times, and the amplification effect on the structure is obvious. The acceleration amplification coefficient of the wind turbine tower increases with the height of the tower in the horizontal *Y*-direction, and the maximum power amplification coefficient can reach 13 times (see Fig. 8b). The acceleration amplification coefficient of the wind turbine tower in the vertical

Fig. 8 Acceleration along the wind turbine height

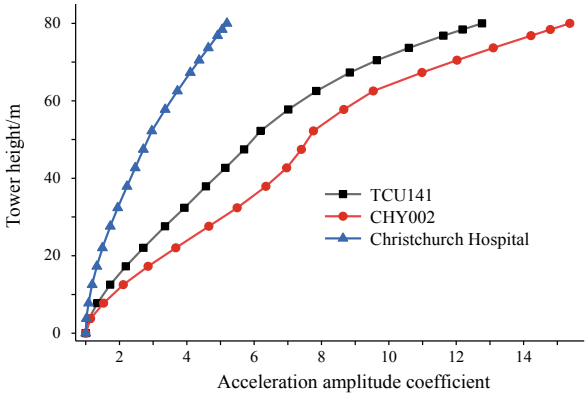

(a) X-direction acceleration amplitude coefficient

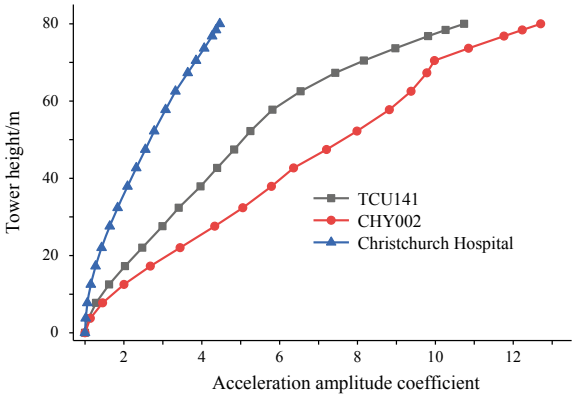

(b) Y-direction acceleration amplitude coefficient

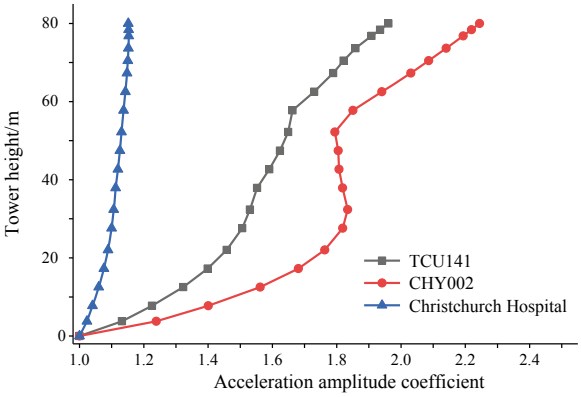

(c) Z-direction acceleration amplitude coefficient

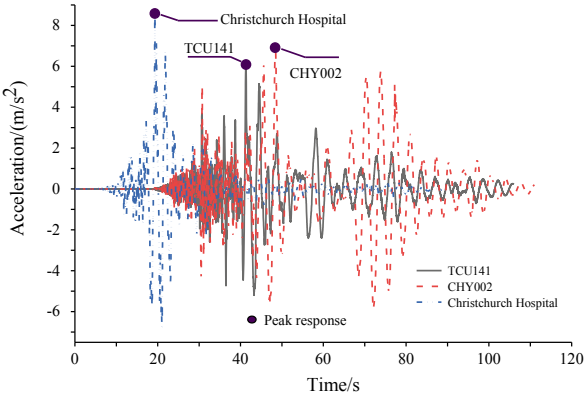

(d) Acceleration time-history curve at the top of the tower

Fig. 8 (continued)

Z-direction generally increases, and its maximum value is about two times, which may have a significant impact on the connection between the tower and the nacelle and the performance of the wind turbine after the earthquake.

4.3 Stress Response

The stress response of the wind turbine structure under long-period ground motion uses Von Mises stress to represent the stress of the shape of the wind power tower in Fig. 9.

Figure 9a shows the Von Mises stress response of the wind turbine structure along the tower height under long-period ground motion. Overall, as the height of the tower increases, the maximum Von Mises stress shows a decreasing trend despite some fluctuations. These fluctuations appear corresponding to the change of the wall thickness of the tower tube and the bending stiffness, indicating the economical and rationality of the tapered design of the wind turbine tower. Figure 9b is the stress time-history curve at the maximum Von Mises stress along the height of the tower. Taking the stress response maximum Christchurch Hospital wave as an example, the maximum Von Mises stress is 237 MPa, and the tower steel is Q345 steel, which is within the range of steel. Figure 10 expresses the stress contour of the wind turbine tower under the action of Christchurch Hospital wave. The maximum value of the Von Mises stress appears at the bottom of the tower or 2/3 along the height of the tower. Sufficient attention should be paid to the seismic design of wind turbine structures.

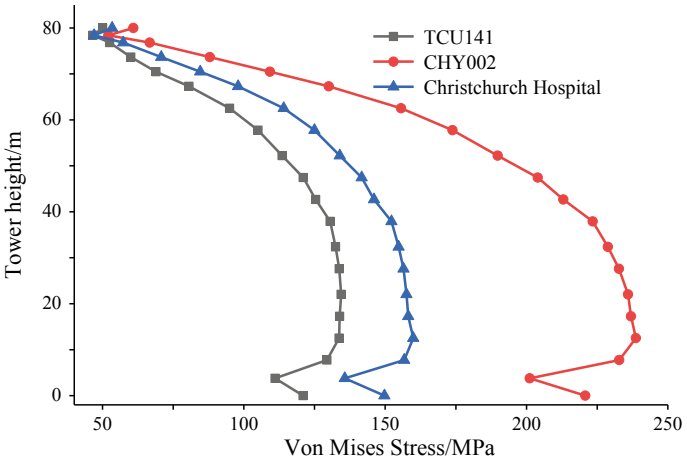

(a) Stress level of tubular tower

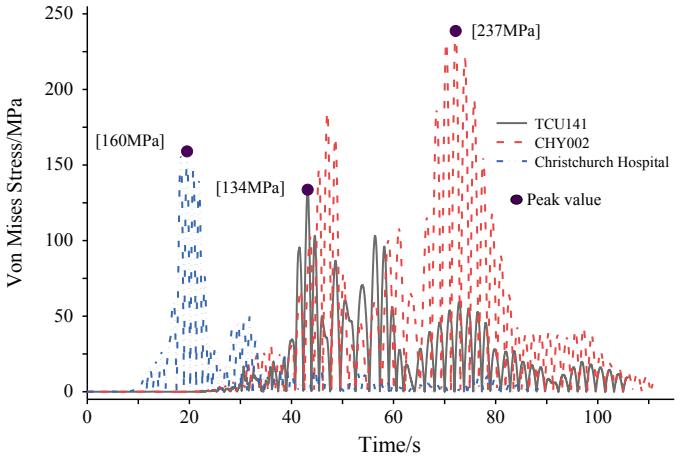

(b) Stress time-history curve at the 12m height of the tower

Fig. 9 Stress along the wind turbine height

4.4 Internal Force Analysis

The internal force of the wind turbine structure under long-term ground motion is presented in Table 4.

The base shear, axial force, bending moment, and torque of the wind turbine structure under long-period ground motions are shown in Table 4. The shear response

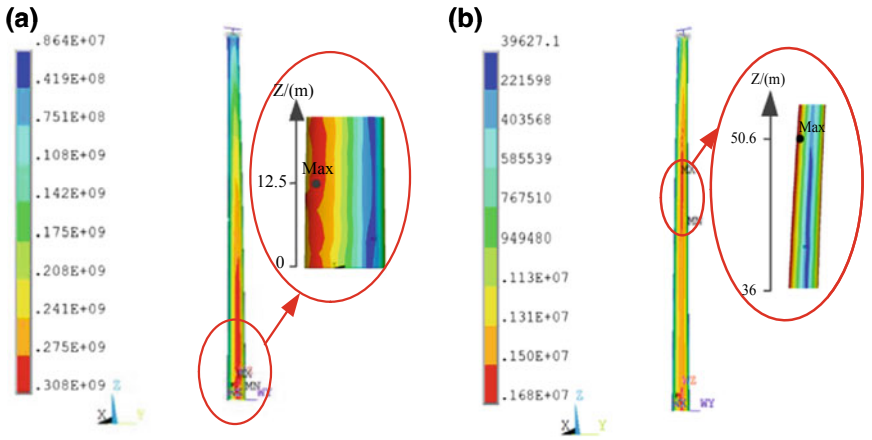

Fig. 10 Stress contour of the wind turbine tower

of the base of the tower base in the horizontal *X*-direction and the horizontal *Y*-direction is obvious, and the bending moment response about the *X*-axis and the *Y*-axis is much larger than the torque along the *Z*-axis, reflecting that the wind turbine belongs to the bending-shear structure. Under the long-period ground motion, the axial force of the wind turbine tower along the *Z*-direction is greater than 600 kN, and the wind turbine is a typical top-heavy structure with a large top mass. In the case of large displacement of the tower, the seismic capacity of the wind turbine structure will be reduced, and the geometric nonlinear influence in the wind turbine structure will be evaluated as the P-△ effect. Figure 11a, b is time-history curves of the base shear force and bending moment of the wind turbine structure along the horizontal *X*-direction under long-period ground motion, respectively.

5 Conclusion

This paper focuses on the seismic dynamic response of the 2 MW wind turbine in Northwest China under long-term ground motions. The analysis results reveal that the response of the displacement, acceleration, stress, and internal force of the wind turbine tower are very significant. The horizontal displacement gradually increases along the height of the tower, and the maximum value appears at the top of the tower. The maximum nodal displacement can reach 2 m, which can cause the geometric nonlinear influence of the wind power tower, thereby reducing the seismic performance of the structure. At the same time, the vertical seismic acceleration at the tower of the wind turbine is twice as large as the ground acceleration, which may have a significant impact on the normal use of the wind turbine after the earthquake.

Table 4 Comparison of maximum internal force responses

Seismic wave	Shear force in *X*-direction/KN	Shear force in *Y*-direction/KN	Axial force in *Z*-direction/KN	Bending moment in *X*-axis/(KN·m)	Bending moment in *Y*-axis/(KN·m)	Torsion in *Z*-axis/(KN·m)	Additional bending/(KN·m)
TCU141	539.00	439.99	– 648.54	– 34808.20	41642.90	419.91	1395.52
CHY002	1033.08	1004.60	700.38	– 75321.70	76221.70	808.21	2475.07
Christchurch hospital	– 791.98	– 651.39	678.63	43735.40	– 52179.60	– 491.83	1646.01

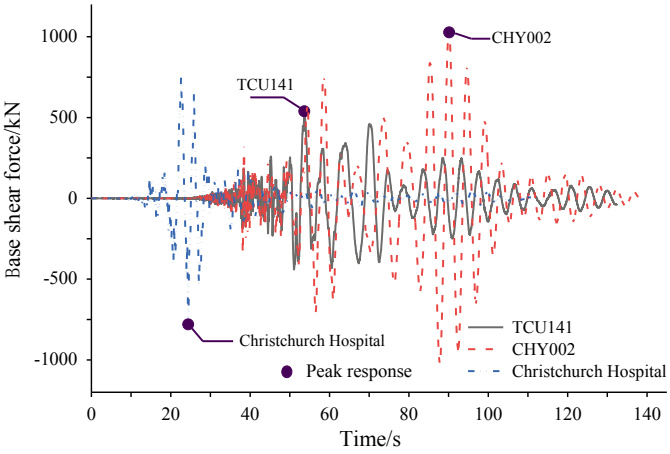

(a) Base shear force time history in X-direction

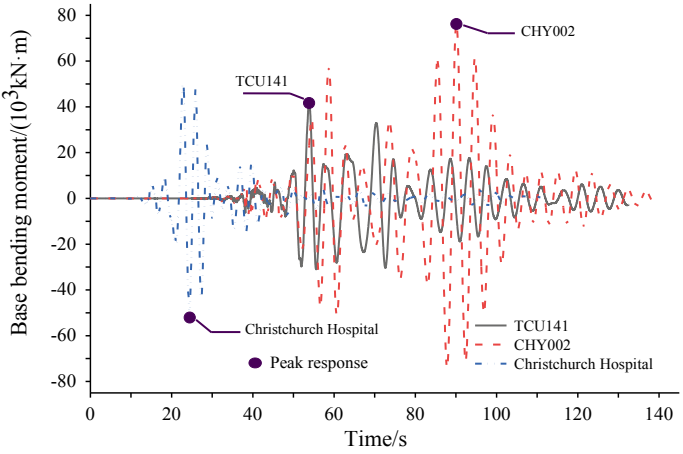

(b) Base bending moment time history (about Y-axis)

Fig. 11 Base internal force time-history curves

Acknowledgements The authors would like to gratefully acknowledge the supports from the National Natural Science Foundation of China (Grant No. 51568041), and the Hongliu Excellent Young Scholar Support Program of Lanzhou University of Technology.

References

1. Weilin, Y., Shengchu, Z., Haichun, H.: Analysis of the characteristics of the far-field vibration of Wenchuan earthquake and its influence on long-period structure. J. Disaster Prev. Mitig. Eng. **29**(4), 473–478 (2009)
2. Koketsu, K., Miyake, H.: A seismological overview of long-period ground motion. J. Seismolog. **12**(2), 133–143 (2008)
3. Yamada, N., Iwata, T.: Long-period ground motion simulation in the Kinki area during the MJ7.1 foreshock of the 2004 off the Kii peninsula earthquakes. Earth Planets Sp. **57**(3), 197–202 (2005)
4. Asako, I., Tomotaka, I.: Simulation of long-period ground motion in the Osaka sedimentary basin: performance estimation and the basin structure effects. Geophys. J. Int. **181**(2), 1062–1076 (2010)
5. Li, X., Zhou, Y., Hu, C., et al.: Characteristics of response spectra of long-period earthquake ground motion. Earthq. Eng. Eng. Vib. **10**(1), 1–2 (1990)
6. Bo, W., Boquan, L., Tao, W.: Low-frequency pulse characteristics and response spectrum analysis of long-period ground motions. Earthq. Eng. Eng. Vib. **38**(3), 142–151 (2018)
7. Wang, S.Y., Yu, Y.X., Hongshan, L.: Study of characteristics of long-period ground motion response spectra by using broad-band records of the Chinese digital Seismograph Network. Acta Seismol. Sin. **11**(5), 557–564 (1998)
8. Shoji, G., Shibui, T.: Evaluation of seismic response of a PC cable-stayed bridge subjected to a long-period ground motion and effectiveness of dampers. In: JSCE Earthquake Engineering Symposium. J. Japan Soc. Civil Eng. **65**(1), 291–305 (2009)
9. Hu, R.P., Xu, Y.L., Zhao, X.: Long-period ground motion simulation and its impact on seismic response of high-rise buildings. J. Earthq. Eng. **22**(7), 1285–1315 (2017)
10. Yan, G., Wenguang, L., Wenfu, H.E., et al.: Dynamic response analysis of super high-rise frame-core tube structure under long-period ground motions. J. Build. Struct. **38**(12), 68–77 (2017)
11. Zhenxuan, Z.: A comparative study on long-period seismic responses for high-rise structures. Struct. Eng. **25**(4), 78–84 (2009)
12. Jialiang, C.: The seismic response prediction of long-period seismic isolated structures based on response spectrum theory. China Civ. Eng. J. **44**(9), 50–58 (2011)
13. Shuqing, L., Xingzhu, P., Xiaosong, Z., et al.: Elastic-plastic analysis of earthquake response of structures under the long-period earthquake motion. Build. Struct. **35**(5), 24–27 (2005)
14. Zanon, A., De Gennaro, M., Kühnelt, H.: Wind energy harnessing of the NREL 5 MW reference wind turbine in icing conditions under different operational strategies. Renew. Energy **115**(1), 760–772 (2017)
15. Zhi, Z., Kaoshan, D., Ximeng, Z., et al.: Failure analyses of a wind turbine tower under ground motions with different frequency characteristics. Eng. Mech. **35**(s), 293–299 (2018)
16. Ke, S., Wang, T., Ge, Y., et al.: Wind-induced fatigue of large HAWT coupled tower-blade structures considering aeroelastic and yaw effects. Struct. Des. Tall Spec. Build. **27**(9), 1–4 (2018)
17. Rahimi, H., Schepers, J.G., Shen, W.Z., et al.: Evaluation of different methods for determining the angle of attack on wind turbine blades with CFD results under axial inflow conditions. Renew. Energy **125**, 866–876 (2018)
18. Hui, X., Zhengliang, L., Zhitao, Y., et al.: The relation between the earthquake response spectrum, power spectrum and Fourier spectrum. Sichuan Buil. Sci. **37**(2), 171–179 (2011)

Intelligent Image Analysis Technology and Application for Rail Track Inspection

Peng Dai, Shengchun Wang and Zichen Gu

Abstract Based on the deep learning technology, the track image intelligent recognition algorithm has been developed, which has made significant progress in the analysis of rail track infrastructure inspection. The main work includes as follows: (1) research on intelligent recognition method of fastener defect based on convolutional neural network—by modeling the deep network from the fasteners image of the nationwide rail line, the detection rate of abnormal fasteners has been significantly improved and the false alarm rate has been greatly reduced. The research achievement has been applied in China's railway inspection. (2) Research on foreign object recognition algorithm in ballastless track based on heuristic deep learning—aiming at the problem of foreign objects falling in the roadbed of the ballastless track, the system has a single type of foreign object recognition capability by labeling and iterative training of the limited samples. Then, by adding the new foreign objects found in the model to the training set for iterative training, a heuristic learning framework is constructed, which makes the system recognize a variety of foreign objects and has been put on probation in China's high-speed rail to verify the outstanding performance of the recognition algorithm. The research work shows that the development of artificial intelligence technology and industry integration will collide with a fierce spark, and the continuous absorption of new technologies and new methods is the way to promote technological innovation in the industry.

Keywords Deep learning · Intelligent recognition · Fastener defect · Foreign object recognition

P. Dai · S. Wang (✉)
Infrastructure Inspection Research Institute, China Academy of Railway Sciences Co., Ltd, Beijing 100081, China
e-mail: wangshengchun@rails.cn

P. Dai
e-mail: daipeng@rails.cn

Z. Gu
Beijing IMAP Technology Co., Ltd, Beijing 100081, China

© Springer Nature Singapore Pte Ltd. 2019

Y. L. Zhou et al. (eds.), *Data Mining in Structural Dynamic Analysis*,
https://doi.org/10.1007/978-981-15-0501-0_5

1 Introduction

High-speed railways have high requirements for safety risk control for the fast driving speeds. Therefore, the status inspection of the track structural components could be implemented by automated ways. The noncontact dynamic detection method is used to patrol the track component condition and find defects rapidly. The detection method based on laser ranging scanning [1] and the detection method based on visible light imaging [2] have become mainstream. The detection method of visible light imaging is widely used to detect the condition of the rail [3, 4] or the contact network components [5], etc., due to the good visibility and traceability of the data obtained and the automation and intelligence of the data analysis. On the basis of this development, the track patrol system and the integrated patrol train or other automatic detection equipment have become more popular in China's railway transportation system after years of development.

As the key module of the inspection system, the intelligent recognition technology of the track image represents the technical level of the inspection equipment. In recent years, many researchers have developed identification algorithms for rail surface scratches, fastener abnormalities, fishplate cracking, and sleeper cracking. Because the image data of the inspection vehicle is captured in the running state, the space span is large and the environmental conditions are varied along the rail line. Therefore, the accuracy of the machine recognition algorithm is far from the cooperative artificial visual inspection. Especially in the traditional pattern recognition framework, based on the "artificial design features" to analyze the changes in the edge and corner features formed by the component structure in the image, the robustness of the recognition is poor, which brings trouble to the system engineering application.

With the development of artificial intelligence technology represented by deep learning, the pattern recognition system that designs a deep network to automatically learn features from data sets shows the advantages against the traditional "artificial design features." The concept of deep learning stems from artificial neural networks, by combining low-level features to form more abstract high-level representation attribute categories or features, to discover distributed feature representations of data and to achieve performance superior to human visual recognition accuracy in multiple tasks in the machine vision field. In this paper, the important progress made in the work of fastener defect recognition based on deep learning and the intelligent identification technology of foreign objects in ballastless trackbed is expounded.

2 Fastener Defect Identification Technology

The ballastless track fastener is the basic component that links the seamless rail and concrete trackbed, and its defects may cause the rail to shift and cause the train to derail. The high-speed rail line is long, and the total number of fasteners is large

in China. It is urgent to use automated and intelligent detection technology to find fastener defects accurately and efficiently.

The machine identification method for fastener defects usually takes the track as an input image, extracts the fastener sub-picture by image segmentation operation, and identifies the defect sub-picture state to detect the defect. The early method identifies the edge and corner feature changes formed by the fastener bolts, clips, and other components in the image [6–8]. This method belongs to the primary machine vision level, and the detection accuracy and noise resistance are poor. After the technique development, by the reference of "face recognition," "pedestrian detection," and other machine vision problem solutions, many "artificial design features" are developed with statistical pattern recognition classifier for identification, such as Haar feature with latent Dirichlet allocation (LDA) classifier [9], AdaBoost classifier [10], HOG feature with K-nearest neighbor classifier [11, 12], support vector machine (SVM) [13, 14] classifiers. This kind of method is based on the "expert design" operator to describe the fastener model and establishes the classifier through statistical learning, which improves the recognition accuracy and robustness to a certain extent, but the generalization is weak when dealing with non-homologous data, and there is a trouble in engineering practice due to the high false positive and false negative of defective fasteners.

The fastener defect recognition technology consists of two steps. The first is the precise positioning algorithm of the fastener subregion. The calculation process of the fastener subregion positioning is shown in Fig. 1. First, a large area containing the fastener is divided from the track image, and then, the fastener subregion is obtained by the image matching algorithm.

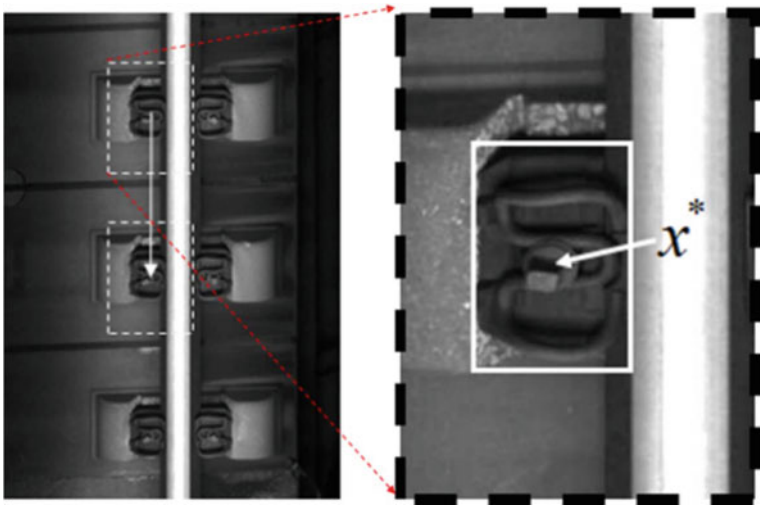

Fig. 1 Schematic diagram of the fastener positioning process

The second part is based on the deep learning-based intelligent recognition modeling, which is divided into three steps.

2.1 Fastener Data Set Construction

The fastener subregion is extracted in batches by using the fastener positioning algorithm from a large number of track images collected from different lines in the previous stage. The image includes as many different types of fasteners as possible. Figure 2 shows an example of the extracted fastener subregions. It can be seen from the figure that the fastener is covered by the ballast and the illumination is abnormally complicated. For the complexity of the fastener image, all fastener subregions are divided into four subcategories. Each category contains about 100,000 samples. The fastener subregions are sorted to form a data set for conducting defect identification studies. Among them, the normal fastener type can include different kinds of fastener subregions.

To further enhance the diversity of training data, data imbalance and equalization sampling are used to adjust the unbalanced basic data set to obtain a data set more suitable for deep learning network modeling. The data enhancement methods mainly include: (1) after mirroring the image of the abnormal fastener sample, gamma correction, etc., adding to the data set to expand the sample size; (2) occluding the normal fastener, the ballast, uneven illumination, etc. Types of fastener sample data sets are screened to maintain a reasonable range of ratios between different types of fasteners.

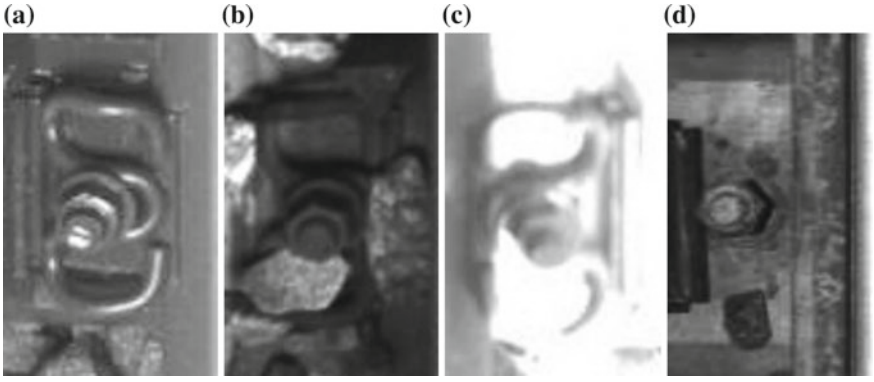

Fig. 2 Typical defect patterns in several fastener subgraphs: **a** normal fasteners, **b** ballast cover, **c** uneven lighting, **d** damaged fasteners

2.2 Deep Learning Modeling

Image convolutional neural network recognition of typical deep learning first extracts the features of the input image through the convolutional neural network and then calculates the training error using the softmax loss function according to the features of the extracted image and the label corresponding to the input image. After learning, a network and classifier are finally available for the image pattern recognition. In the field of computer vision recognition, open public research data sets such as the ImageNet project (a large visual database for visual object recognition research and the total size of the database is over 14 million images) present many available network structures such as the famous AlexNet and ResNet. During the research process, the recognition accuracy and efficiency of these networks on the fastener data set were verified. It was found that the existing network is not suitable for the deep learning modeling of fastener defect recognition, due to the deep network layers, large model parameters, and easy over-fitting on the fastener data set. In addition, the model layer is too deep; the saved model parameter file will take up a lot of storage space and make the detection run at a slower speed, so they cannot be used directly.

We build a 10-layer convolutional neural network based on the convolutional neural network design principle. It contains basic structures such as a convolutional layer, batchnorm layer, and pooling layer. In the design of the convolution layer, considering the small size of the fastener image, a minimum 3×3 convolution kernel is used. The input image of the network is the subregion of the fastener extracted from the track image. The nonlinear feature is extracted from the input image through the convolutional layer. After the main feature is retained by the pooling layer, the spatial dimension is reduced and finally passed. The full connection layer outputs four feature values representing the recognition result of the input image.

2.3 Model Verification and Fine-Tuning

On the basis of completing the deep network design, the network is trained on the constructed data set. The training parameters are set as follows. The initial learning rate is 0.01, and the learning rate decreases with the convergence degree of the network. After training 50 epochs, the network basically converges (see Fig. 3).

Then, the network is further trained by combined with the online track image acquired from the real railway, which is a benefit with the generalization to the new railway line. In addition, the false detection and the missing detection are supplemented and the training is performed again for improving the detection performance ceaselessly (see Fig. 4).

At present, this technology has been promoted and applied in local railway companies including the Guangzhou Railway Group's rail defect detection train, the inspection system carried on the Wuhan Railway Bureau's detection train, the rail

Fig. 3 Training learning curve

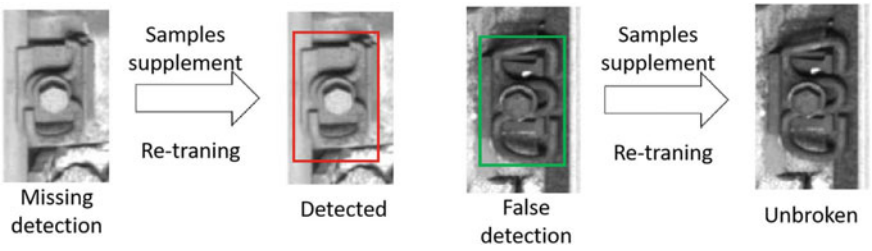

Fig. 4 Iterative training results

track inspection train of the Jinan West high-speed railway section, and the high-speed railway comprehensive inspection train. The effective detection rate of fastener abnormalities has reached more than 95% on average, the accuracy has reached more than 90% in the ballastless line, and the accuracy of detection has reached more than 70%.

3 Intelligent Identification Technology for Foreign Objects in the Trackbed

The foreign matter in the trackbed is a foreign object appearing on the railway trackbed, usually including broken fasteners, broken stones, animal carcasses, and the others (see Fig. 5). In the ballastless track, foreign objects on the trackbed will bring great hidden dangers to the driving safety of the train. Therefore, it is necessary to develop a visual detection algorithm to detect foreign matter on the bed in time. Because of the variety of foreign objects in the ballastless trackbed and the image acquisition equipment has been in high-speed motion, the visual inspection of the foreign object in the trackless track has always been a difficult problem in the track intelligent inspection.

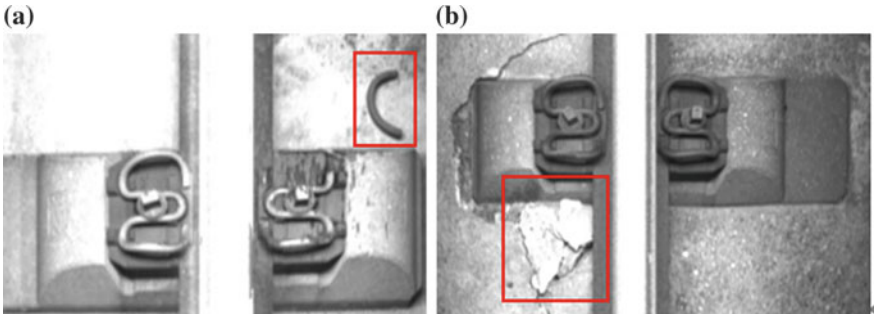

Fig. 5 Typical roadbed foreign body sample: **a** fracture clip and **b** bed gravel

3.1 Background of Foreign Object Identification in the Trackbed

Foreign object intrusion detection is a classic problem in computer vision. This type of problem usually involves foreign object intrusion detection of video captured by a fixed position camera. Since the camera is fixed in position, the problem of foreign matter is often detected by background modeling.

For the railway image, in the two sets of railway inspection vision systems GX-02 and GX-03 that we currently use (see Fig. 6), the camera is mounted on the bottom of the inspection vehicle for high-speed movement, and there is almost no overlap

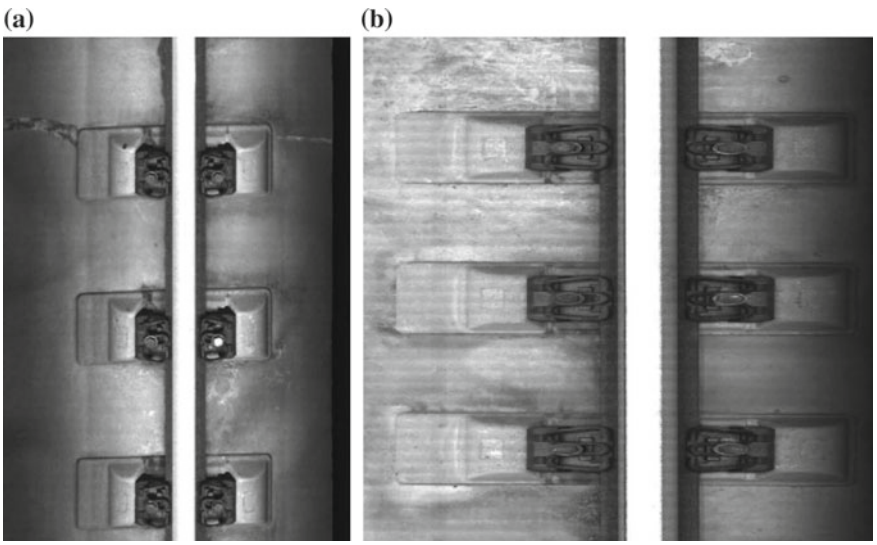

Fig. 6 Track image acquired by the existing system: **a** GX-02 inspection system collects data and **b** GX-03 inspection system collects data

between each image. Background modeling cannot be used to solve foreign object detection problems very well.

In addition to background modeling, foreign objects can be detected by means of target detection for foreign objects of known categories. In the traditional method, the foreign matter detection needs to extract the traditional visual features from the known foreign object images and then find the foreign objects matching the template in the image by sliding the window and the template matching. The adoption of such a conventional method not only has an extremely low accuracy rate, but also has poor generalization, and it is impossible to recognize a foreign object having a slightly larger gap from the template of foreign matter image (Fig. 7).

In recent years, with the deepening of relevant research, deep learning and big data-related algorithms have greatly improved the accuracy and generalization of target detection [15–19]. The deep learning target detection algorithm is mainly based on the deep convolutional neural network (CNN, see Fig. 8). It collects a large number of foreign object samples and organizes them according to different foreign object types as the training data of the deep learning algorithm. By training the deep neural network model, the foreign objects are classified by category. At present, the mainstream deep learning target detection algorithms are divided into

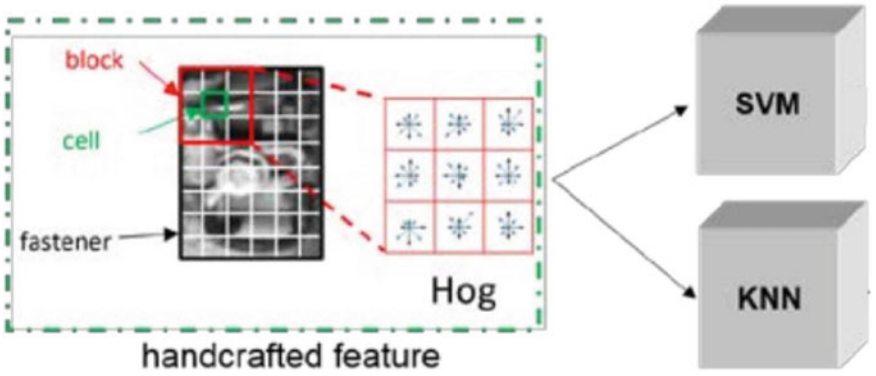

Fig. 7 Target detection algorithm based on the traditional method

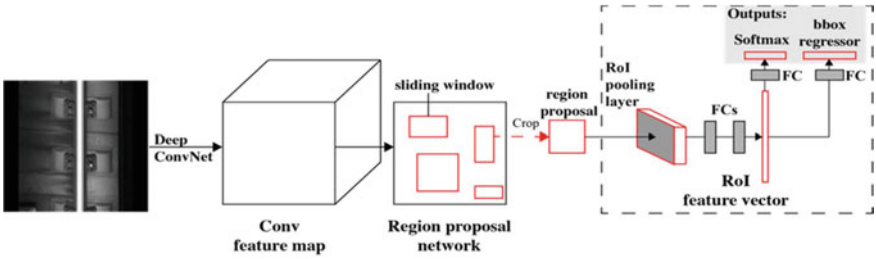

Fig. 8 Target detection based on deep learning

region proposal based algorithms: faster RCNN, R-FCN, etc., and direct regression method: YOLO, SSD, etc.

The above-mentioned deep learning method can classify the foreign matter of a known kind, but for the foreign matter in the trackbed, the type of the foreign matter is "singularly strange," and it is impossible to exhaust all the foreign matter types and find the corresponding sample. For unknown types of foreign objects, a heuristic algorithm is needed to estimate unknown foreign objects based on known foreign object types.

3.2 Trackbed Foreign Object Detection Algorithm Based on Heuristic Learning

Foreign matter samples dropped on the high-speed railroad are very rare. Therefore, it is necessary to establish a heuristic learning framework to gradually realize the identification of many types of foreign objects.

(a) Classical Deep Network Sample Evaluation and Screening:
In the beginning of the study, a model study of approximately 200 foreign beds collected from the bed was conducted. Taking into account the easy accessibility of the sample, we chose 99.5% of the fasteners left in the trackbed as a foreign object target, and another animal carcass image. First, the known foreign objects in the image are labeled, and then, the depth learning target detection algorithm framework is evaluated on this data set (Fig. 9).
In the railway inspection system, each kilometer of the railway will take about 500 images at equal intervals, so the processing speed of the target detection algorithm is also an important consideration. As shown in Table 1, we tested the framework of target detection algorithms such as faster RCNN (ZF, VGG16, ResNet50), R-FCN (ResNet101), SSD (Inception v2), and YOLO v3. By modeling 130 samples, the remaining images were used as test samples. After testing, it was found that the four methods of faster RCNN (ResNet50), R-FCN (ResNet101), SDD, and YOLO v3 can achieve a high detection rate in the test data, but YOLO v3 has an absolute advantage in the processing speed and can

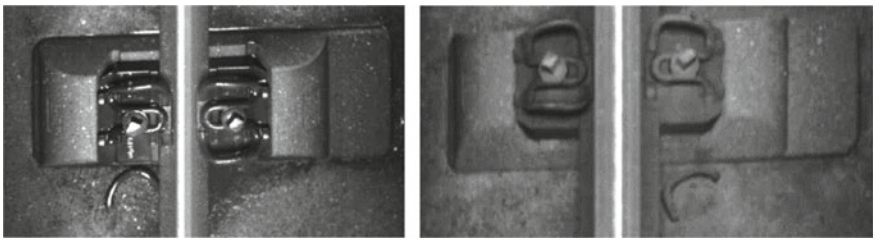

Fig. 9 Example of a training set foreign object

Table 1 Algorithm speed comparison per frame

Method	Time cost (ms)	Detection speed (km/h)
Faster RCNN ResNet50	170	42
Faster RCNN ResNet50 low proposal	100	72
R-FCN ResNet101	150	48
R-FCN ResNet101 low proposal	100	72
SSD Inception v2	50	144
Yolo v3	45	160

support the real-time processing of the inspection train at a speed of 160 km/h. In additional, the YOLO v3 framework also has a good negative sample suppression capability, which can be suppressed by adding images that are easily misdetected in the training set.

(b) A single category foreign object recognition model.
Based on the above research, the YOLO v3 framework was selected as the basic framework for foreign object detection. YOLO v3 is a target detection algorithm based on direct regression (see Fig. 10). After three generations of evolution, it combines the advantages of multiple target detection algorithms and is the master of the current target detection algorithm framework. The framework consists of a 53-layer deep convolutional neural network that uses multi-scale connections to accurately position targets of different sizes.
In the training data collection, among the 200 foreign object image data collected by us in the previous period, 199 images contain the broken fastener clips. The broken fastener clips account for a considerable proportion of the foreign matter

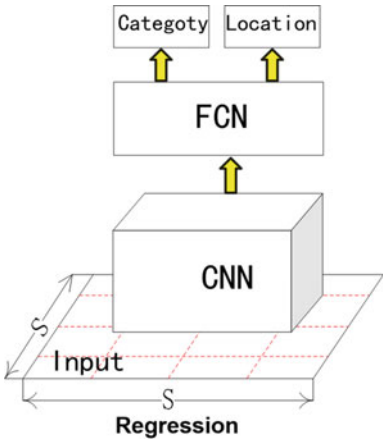

Fig. 10 YOLO v3 network framework

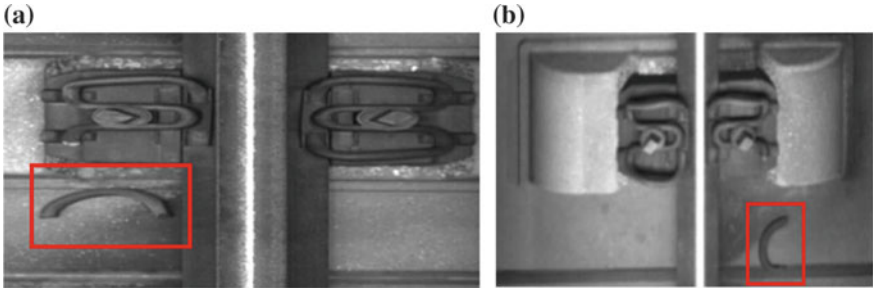

Fig. 11 Sample of broken elastic bars detected: **a** newly detected broken clip by GX 3 and **b** newly detected broken clip by GX 2

in the ballastless bed, and this type of foreign matter will have a greater impact on driving safety. Therefore, first training a foreign object detection model for the broken clips has high practical value. Then, using 199 pieces of real broken clip images and some artificial data made by image editor software as training samples, a foreign objects detection model of broken clips was trained. As shown in Fig. 11, the model can accurately detect the foreign matter of the broken clips on the ballastless line.

Using this model, foreign objects were detected in millions of innocent track test images, and hundreds of broken fastener clips were detected. This part of the newly discovered data is re-added to the training data set for model training and then re-tested in the test image. By repeating this process through iterations, the ability of the model to detect a single foreign object such as a broken clip is continuously improved.

(c) Identification of multiple foreign bodies and unknown foreign objects under the heuristic learning framework.

In the process of actual line detection, in addition to detecting many foreign bodies of broken clips, the model also detects some non-clip foreign objects similar to the clips, including crushed stones, broken rubber, etc. (see Fig. 12). These different patterns of foreign objects can be constructed into a variety of foreign data sets.

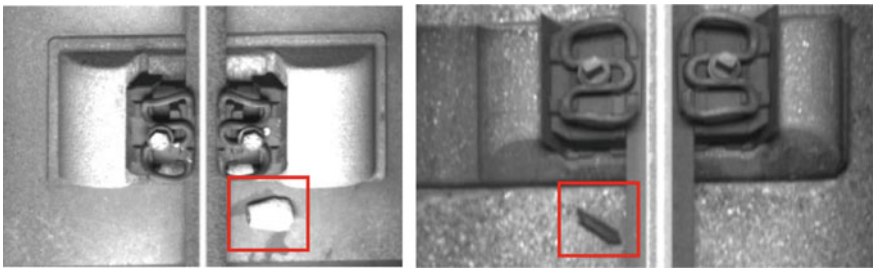

Fig. 12 Broken rubber detected by the detected stone fragments

Using the data of the foreign body accumulated in the previous period, a small amount of non-ballistic foreign body data, and a previously collected animal carcass data (see Fig. 13), we train a new deep neural network foreign body recognition model and wish the network can heuristically obtain the ability to recognize foreign bodies of trackbed from these different kinds of foreign objects.

Through multiple rounds of training detection iterations, a multi-class ballastless foreign object detection model was successfully constructed. In addition to detecting known kinds of foreign bodies such as broken clips and gravel, the model can also detect different types of animal carcasses and some other types of foreign objects (see Fig. 14).

(d) Misdetection of the model and ways to overcome it.

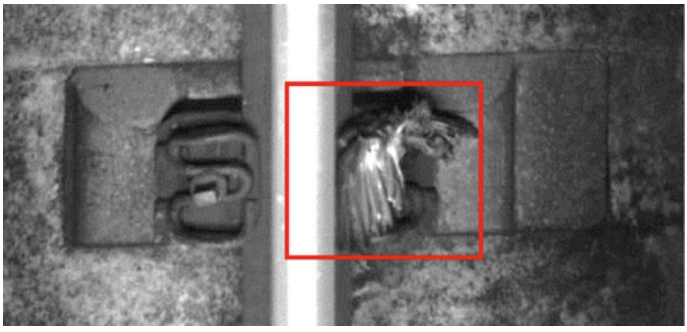

Fig. 13 Collected animal carcasses

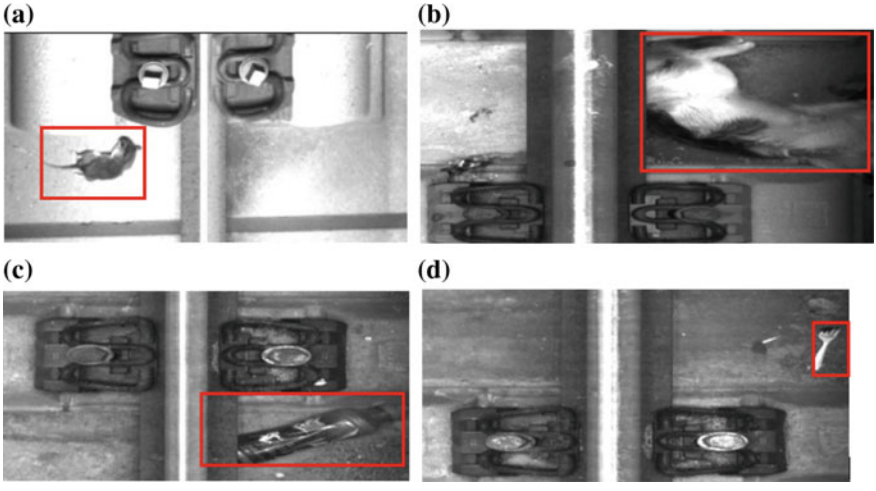

Fig. 14 Other types of foreign objects: **a** small animal, **b** large animal, **c** bottle, **d** fork

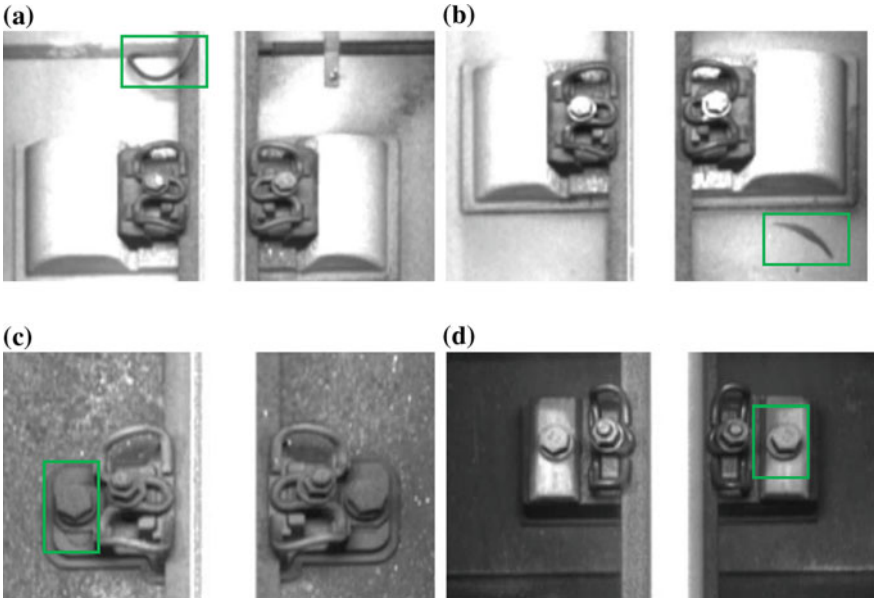

Fig. 15 Misdetection caused by areas similar to the texture and shape of foreign objects in the image: **a** cable, **b** stain, **c,** and **d** bolt

Due to the technical level of the computer vision development, targets with similar features may be identified as targets of interest during the recognition process. In the process of constructing the trackbed foreign body detection model, in addition to the correct detection of foreign objects in the trackbed, there is also a certain amount of false detection. Some misdetected samples are shown in Fig. 15.

The target objects of false detection can be divided into two categories. First, because the pattern features are very similar to foreign objects, the problem is limited by the intelligence of computer vision, so it is difficult to avoid it for guaranteeing the effective detection rate, which would be a direction for continuous improvement of research work. Another type of misdetection belongs to the shortcoming of deep neural networks; it can be suppressed by adjusting the training data, i.e., to update the training by adding some images that are prone to false detection as new training samples to the training set.

4 Conclusion

Based on the deep learning technology, the detection rate of the fastener defect-recognition function module in the track inspection system is significantly improved,

and the recognition function of the foreign object falling in the high-speed rail trackbed is developed. Deep learning technology is a representative technology of AI development, combining it with the specific problems in the field of railway infrastructure detection, significantly improving the intelligence of data analysis and processing algorithms, and achieving good application results. In the further research, the application of unsupervised learning, reinforcement learning, and generative adversarial networks in the field of visual inspection of railway infrastructure will be explored, and it will be used to solve the defect detection of the contact wire and trackside electronic equipment.

References

1. Çaglar, A., Yousef, R., Dogru, S., et al.: Railway fastener inspection by real-time machine vision. IEEE Trans. Syst. Man Cybern. Syst. **45**(7), 1101–1107 (2015)
2. Xu, G., Shi, T., Ren, S., et al.: Development of on-board track inspection system based on computer vision. China Railway Sci. **34**(1), 139–143 (2013)
3. Ren, S., Li, Q., Xu, G., et al.: Research on robust real-time rail surface scratch detection algorithm. China Railway Sci. **32**(1), 25–29 (2011)
4. Li, Q., Zhang, H., Ren, S., et al.: Rail-wave grinding detection method based on frequency domain characteristics of rail images. China Railway Sci. **37**(1), 24–30 (2016)
5. Zhou, W., Sun, Z., Ren, S., et al.: Measurement method of contact net geometry parameters based on multi-view stereo vision. China Railway Sci. **36**(5), 104–109 (2015)
6. Maeeeo, P.L., Stella, E., Ancona, N., et al.: Visual detection of hexagonal headed bolts using method of frames and matching pursuit. In: The second Iberian conference on pattern recognition and image analysis, pp. 277–284. Estoril, Portugal (2005)
7. Marino, F., Distance, A., Mazzeo, P.L., et al.: A Real time visual inspection system for railway maintenance: automatic hexagonal headed bolts detection. IEEE Trans. Syst. Man Cybern. Part C Appl. Rev. **37**(3), 418–428 (2007)
8. Li, Y., Ttinh, H., Haas, N., et al.: Rail component detection, optimization, and assessment for automatic rail track inspection. IEEE Trans. Intell. Transp. Syst. **15**(2), 760–770 (2014)
9. Feng, H., Jiang, Z., Xie, F., et al.: Automatic fastener classification and defect detection in vision-based railway inspection systems. IEEE Trans. Instrum. Meas. **63**(4), 877–888 (2014)
10. Li, Y.: Research on State Detection Algorithm of Railway Line Based on Machine Vision. Southwest Jiaotong University, Chengdu (2013)
11. Li, Y., Li, B., Xiong, Y., et al.: State detection of railway fasteners based on hog characteristics. Sens. Microsyst. **32**(10), 110–113 (2013)
12. Liu, J., Wang, K., Yuan, J., et al.: Optimization of RBF-SVM model in railway fastener image detection. Comput. Eng. Appl. **50**(15), 30–33 (2015)
13. Liu, X., Mu, Y., Zhang, B.: Study on the detection algorithm of rail fastener based on computer vision. J. East China Jiaotong Univ. **34**(2), 72–77 (2017)
14. Dou, Y., Huang, Y., Qingyong, L., et al.: A fast template matching-based algorithm for railway bolts detection. Int. J. Mach. Learn. Cybern. **5**(6), 835–844 (2014)
15. Gibert, X., Patel, V.M., Chellappa, R.: Material classification and semantic segmentation of railway track images with deep convolution neural networks. In: IEEE International Conference on Mobile Adhoc & Sensor Systems, pp. 92–101. Dallas, USA (2015)
16. Gibert, X., Patel, V.M., Chellappa, R.: Deep multi-task learning for railway track inspection. IEEE Trans. Intell. Transp. Syst. **18**(1), 153–164 (2017)
17. Du, X., Dai, P., Li, Y., et al.: Automatic detection algorithm for railway plug based on deep learning. China Railway Sci. **38**(3), 89–96 (2017)

18. Xia, Y., Xie, F., Jiang, Z.: Broken railway fastener detection based on adaboost algorithm. In: International Conference on Optoelectronics and Image Processing, pp. 314–317. Haikou, China (2010)
19. Liu, J., Xiong, Y., Li, B., et al.: Research on automatic detection algorithm of track fastener defects based on computer vision. J. China Railway Soc. **38**(8), 73–80 (2016)

Investigation on the Effect of High-Frequency Torsional Impacts on the Torsional Vibration of an Oilwell Drill String in Slip Phase

Liping Tang, Xiaohua Zhu and Yunlai Zhou

Abstract The drilling system usually encounters detrimental stick-slip vibration to the drilling process. One of the approaches for controlling the stick-slip vibration is using high-frequency torsional impact (HFTI). However, how the HTFI will affect the vibration of the drill string is still unknown. This study proposed a mechanical model of the drill string by using continuous system to investigate the effect of HFTI on the vibration of a drill string in slip phase, wherein the HFTI is considered in the model. The mechanical model is investigated through using mode superposition method and conducting case studies. Results show that the HFTI is more sensitive to the drill string close to the drill bit and that the HFTI has little effect on the vibration of drill string. During the drilling process, the HFTI aggravates the rock damage and rock failure, which actually improves the drilling efficiency and mitigates the stick-slip vibration.

Keywords High-frequency torsional impact · Drill string · Stick-slip vibration · Drill bit · Mode shape

1 Introduction

Oil and gas are two types of fossil energy generated by natural processes taking millions of years to form. Although oil and gas are continually being generated through natural processes, they are usually regarded as non-renewable resources [1, 2]. With the rapid development of economy, consumption of oil and gas in the world increases and the oil and gas are being consumed much faster than new ones are being made [3]. After the exploration and development of oil and gas in the past several decades, the drilling works are toward deep wells (≥3000 m) and ultra-deep

L. Tang · X. Zhu (✉)
School of Mechatronic Engineering, Southwest Petroleum University, Chengdu 610500, People's Republic of China
e-mail: zxhth113@163.com

Y. Zhou
Department of Civil and Environmental Engineering, The Hong Kong Polytechnic University, Hong Kong SAR, China

© Springer Nature Singapore Pte Ltd. 2019

Y. L. Zhou et al. (eds.), *Data Mining in Structural Dynamic Analysis*,
https://doi.org/10.1007/978-981-15-0501-0_6

wells (≥6000 m) [4]. The drilling cost occupies more than half of the fees used in the exploration and development of oil and gas. As a result, drilling companies all over the world try to reduce the drilling cost and improve the drilling efficiency.

In the drilling industry, one of the most popular drilling methods is the rotary steering drilling. Rotary steering equipment used to compose a drill string that is rotated to deepen the wellbore [5]. During the drilling process, the drill string encounters serious dynamic problems which may lead to drilling accident, such as buckling, vibration, and fracture. Due to the hostile environment of the drilling process, the dynamic behavior of the drill string is very complex [6]. Field observations show difference in vibration surveillance in downhole and on surface which indicates BHA undergoes severe vibrations. Drill string vibration is regarded as the primary reason for the premature failure of drilling tools, and the subject of vibration in the drilling system is an ongoing challenge for the engineers [7, 8].

Among the common vibration modes (including single modes and coupled modes), stick-slip vibration is considered as one of the primary reasons of drilling performance deterioration as it wastes drilling energy, leads to tool failure, reduces the penetration rate, and increases the drilling cost [9, 10]. Due to the large length-to-diameter (LTD) of a drill string, for example, the LTD of a 3,000 m drill string is bigger than 23,000, stick-slip vibration is very common [11]. It is reported that stick-slip vibration is more likely to appear in deep drilling systems [12–14]. Two reasons may be used to explain this (1) LTD of the drill string increases with an increase in the well depth and (2) rock hardness and rock strength increase with increasing the well depth. In field application, a large weight on bit is used to maintain the rate of penetration because of high rock strength, but this leads to a high possibility of generating or aggravating the stick-slip vibration.

Belokobyl'skii and Prokopov [15] studied the friction-induced vibration of drill string, which is thought to be the earliest publication related to stick-slip vibration of drill string. Their work was furthered by many other researchers. Richard et al. [16] investigated the root cause of stick-slip phenomenon of stick-slip in oilwell drill string using a simplified model that considered the interaction between the drill bit and rock formation. Patil and Teodoriu [17] studied the effects of system factors on the stick-slip vibration of drill string. Tang et al. [18–20] revealed the mechanism of stick-slip vibration and effects of drilling parameters on this type of phenomenon. Mihajlovic et al. [21] used an experimental drill string apparatus to study the causes of friction-induced stick-slip phenomenon. Lai et al. [22] reported the field measurement of stick-slip vibration using surface-based torque and presented the correlation between downhole and surface data. Puebla and Alvarez-Ramirez [23] developed a control method based on modeling error compensation to mitigate stick-slip motion in drill string. It is found that many literatures have focused on the stick-slip phenomenon, but there are still many challenges.

Many methods have been used to control the stick-slip vibration, including active ones and passive ones [10], and one of them is the high-frequency torsional impact (HFTI) drilling [24]. For this drilling technique, HFTI is supplemented to the drill bit through an impactor installed directly above the drill bit. Results of our previous studies showed that the HFTI can reduce the stick-slip vibration of the drill bit [18].

Since an additional impact is added onto the drill string, it is easy to believe that the HFTI may aggravate or be a source of drill string vibration.

For a drilling system with stick-slip vibration, the drill bit moves alternately between stick phase and slip phase. In the stick phase, the drill bit keeps still (referred to as being constrained). While in the slip phase, the drill bit is not constrained. In this paper, the investigation is conducted to know the effects of HFTI on the vibration of a drill string in slip phase.

2 Drill String Vibration Model

The drill string is regarded as vertical, elastic, homogeneous, and isotropic, and the flow of the drilling fluid and flow-induced vibration is neglected. The vibration model of the drill string is shown in Fig. 1, where x-axis is the longitudinal direction of the drill string, $x = 0$ means the rotary table, and $x = l$ means the drill bit. $\theta(x, t)$ denotes the angular displacement of the cross section of the drill string at x and time t, and the gradient of the angular displacement can be expressed as

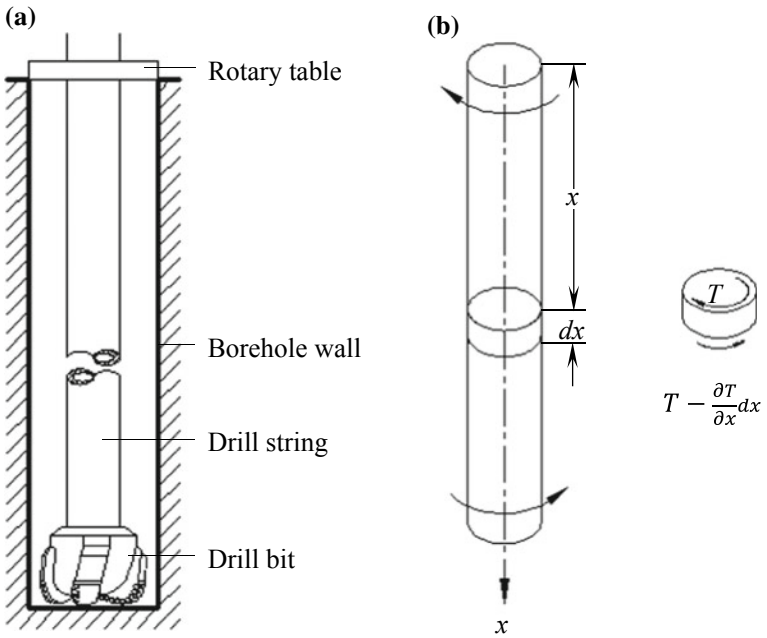

Fig. 1 Vibration model of the drill string: **a** general view of the drill string system; **b** vibration model of the continuous drill string

$$\frac{\partial \theta}{\partial x} = \frac{T}{GI_p(x)} \tag{1}$$

where T indicates the torque acted on the cross section of drill string, G means the shear modulus of the drill string, and $I_p(x)$ represents the polar moment of inertia at x. For a drill string element dx shown in Fig. 1b, the motion differential equation of the torsional vibration can be expressed as

$$GI_p(x)\frac{\partial^2 \theta}{\partial x^2}(x,t) - J(x)\frac{\partial^2 \theta}{\partial t^2}(x,t) - \beta\frac{\partial \theta}{\partial t}(x,t) = M(x,t), x \in (0,l), t > 0 \tag{2}$$

where $J(x)$ denotes the rotational inertia, β represents the viscous damping coefficient of the drilling fluid, and $M(x, t)$ refers to the external torque acted on the drill string.

For a dynamic mode that is feasible in physics, it can be realized by superposition of the basic modes of the system. The mode superposition method (MSM) transforms the geometric displacement coordinate into modal amplitudes and characterizes the system vibration as a linear combination of the mode shapes. Mode shape is an intrinsic parameter of the system like the density. To solve Eq. (2), its homogeneous form is firstly studied.

$$GI_p(x)\frac{\partial^2 \theta}{\partial x^2}(x,t) - J(x)\frac{\partial^2 \theta}{\partial t^2}(x,t) - \beta\frac{\partial \theta}{\partial t}(x,t) = 0, x \in (0,l), t > 0 \tag{3}$$

One method of solving partial differential equations is the variable separation method. The solution is assumed in the form

$$\theta(x,t) = \phi(x)Q(t) \tag{4}$$

where $\phi(x)$ means a function representing the mode shape and is independent with t, and $Q(t)$ indicates the generalized coordinate representing the amplitude and is dependent with t.

By substituting Eq. (4) into Eq. (3)

$$\frac{\rho I_p \ddot{Q}(t) + \beta \dot{Q}(t)}{Q(t)} = \frac{GI_p\phi''(x)}{\phi(x)} \tag{5}$$

where (.) denotes the derivation with respect to time t, $(')$ indicates the derivation with respect to x, and ρ represents the density of the drill string. By introducing a term $C = -\omega^2$, two equations are satisfied.

$$\rho I_p \ddot{Q}(t) + \beta(x)\dot{Q}(t) + \omega^2 Q(t) = 0 \tag{6}$$

$$GI_p\phi''(x) + \omega^2\phi(x) = 0 \tag{7}$$

The solution of Eq. (7) is then given as

$$\phi(x) = C_1 \times \sin\left(\omega\sqrt{\frac{\rho}{G}}x\right) + C_2 \times \cos\left(\omega\sqrt{\frac{\rho}{G}}x\right) \tag{8}$$

where C_1 and C_2 mean integration constant determined by the boundary condition and ω indicates the natural frequency of the drill string system.

3 Drill String Dynamics Under Torsional Impacts

3.1 Natural Frequency and Mode Shape

At the beginning of the slip phase, the driving torque acted on the drill string balances with the frictional torque acted on the drill bit. The drill string is twisty. After the slip phase is initiated, the bottom hole assembly vibrates violently and the rotary table moves steadily. For a drill string in slip phase, the relative movement between the drill bit and the rotary table can be regarded as the movement of a vertical beam with fixed boundary condition at the upper end and free boundary condition at the lower end. For the torsional vibration of a drill string, it can be obtained by superimposing the relative movement with effect of rotation of the rotary table on each mode shape. In the slip phase, kinetic frictional torque is acted on the drill bit. The kinetic frictional torque is regarded as external load. The boundary conditions can be given as

$$T(l,t) = GI_p\frac{\partial\theta}{\partial x} = 0 \tag{9}$$

$$\theta(0,t) = 0 \tag{10}$$

Upon substituting into Eq. (4), two equations can be obtained

$$\phi'(l) = 0 \tag{11}$$

$$\phi(0) = 0 \tag{12}$$

Substituting Eqs. (11) and (12) into Eq. (8) gives

$$C_2 = 0 \tag{13}$$

$$\cos\frac{\omega l}{\sqrt{G/\rho}} = 0 \tag{14}$$

The natural frequencies of the system can be found from Eq. (14) to be

$$\omega_i = \frac{(2i-1)\pi\sqrt{G/\rho}}{2l}, i = 1, 2, 3, \ldots \tag{15}$$

Hence, the expression for mode shape i can be of the form

$$\phi_i(x) = C_1 \times \sin\frac{(2i-1)\pi x}{2l}, i = 1, 2, 3, \ldots \tag{16}$$

3.2 Generalized Moment of Inertia and Generalized Load

The generalized modes of the drill string, by determining $C_1 = 1$, is

$$\phi_i(x) = \sin\frac{(2i-1)\pi x}{2l}, i = 1, 2, 3, \ldots \tag{17}$$

And the generalized moment of inertia (generalized mass) is

$$\overline{J}_i = \int_0^l J\phi_i^2(x)\mathrm{dx} = \int_0^l J\left(\sin\frac{(2i-1)\pi x}{2l}\right)^2 \mathrm{dx} = \frac{1}{2}\mathrm{Jl} \tag{18}$$

where J indicates the moment of inertia of each unit length of drill string. The generalized load is

$$\overline{M}_i(t) = \int_0^l \phi_i(x)M(x,t)\mathrm{dx} \tag{19}$$

The HFTI generator is placed on a certain position of the drill string. The coordinate of this position is regarded as y in the x-axis. For the HFTI torque, it can be regarded as a distributed load which acts on a small segment $(y - \Delta, y + \Delta)$, with its section length is 2Δ. The load intensity of the HFTI is $\left(\frac{A}{2} + \frac{A}{\pi}\sin(\omega_0 t) + \frac{A}{2\pi}\sin(2\omega_0 t)\right)/2\Delta$ (the HFTI load is discussed in Appendix A). Based on Eq. (19), the generalized load of the HFTI can be given as

$$\overline{M}_{i1}(t) = \int_0^l \phi_i(x)M(x,t)\mathrm{dx}$$

$$= \int_{0}^{y-\Delta} \phi_i(x) M(x,t)\mathrm{dx} + \int_{y-\Delta}^{y+\Delta} \phi_i(\mathrm{x})\mathrm{M}(\mathrm{x},\mathrm{t})\mathrm{dx} + \int_{y+\Delta}^{1} \phi_i(\mathrm{x})\mathrm{M}(\mathrm{x},\mathrm{t})\mathrm{dx}$$

$$= \int_{y-\Delta}^{y+\Delta} \sin\frac{(2i-1)\pi y}{2l} \times \left(\frac{A}{2} + \frac{A}{\pi}\sin(\omega_0 t) + \frac{A}{2\pi}\sin(2\omega_0 t)\right) \Big/ 2\Delta\mathrm{dx}$$

$$= \sin\frac{(2i-1)\pi y}{2l} \times \left(\frac{A}{2} + \frac{A}{\pi}\sin(\omega_0 t) + \frac{A}{2\pi}\sin(2\omega_0 t)\right) \tag{20}$$

Apart from the HFTI, kinetic frictional torque acts on the drill bit ($y = l$). The frictional torque is treated as external load, and its generalized form is expressed as

$$\overline{M}_{i2}(t) = \sin\frac{(2i-1)\pi y}{2l} \times \mu_K W_B \overline{R}_B = \sin\frac{(2i-1)\pi l}{2l} \times \mu_K W_B \overline{R}_B = \mu_K W_B \overline{R}_B \tag{21}$$

where μ_K indicates the kinetic frictional coefficient, W_B means the weight on bit, and $\overline{R}_B$ represents the equivalent diameter of the drill bit.

3.3 Generalized Coordinate

In complex systems, coordinates used to describe the system may not be independent; some of the coordinates may be related to each other by constraint equations. Generalized coordinate is a type of independent coordinate used to resolve the constraint equations. The MSM is to be used. Theoretically, there are infinitely many mode shapes should be superposed for a continuous system. Practically, however, only the mode shapes that provide the main contribution are included. For a drill string, using the MSM means the transformation of a continuous system into a discrete system. The solution of the equation of motion of the drill string is expressed as

$$\theta(x,t) = \sum_{i=1}^{\infty} \phi_i(x)\, Q_i(t) \tag{22}$$

where $\phi_i(x)$ represents the regularized modal function and $Q_i(t)$ indicates the generalized coordinate that denotes the amplitude of the ith mode shape at time t.

By combining Eqs. (2) and (22), a differential equation of the generalized coordinate can be obtained (refers to Appendix C)

$$\ddot{Q}_i(t) + 2\xi_i\omega_i \dot{Q}_i(t) + \omega_i^2 Q_i(t) = \frac{\overline{M}_i}{\overline{J}_i} \tag{23}$$

The problem of obtaining the system response is obtaining the generalized coordinates that are composed of a series of single degree of freedom (SDOF). The initial conditions of Eq. (23) are expressed by Eqs. (C.5) and (C.6). Once the generalized coordinates are obtained, the dynamics of the drill string can be obtained in terms of Eq. (22). The solution of Eq. (23) has two parts: a general solution related to the associated homogeneous equation and a particular solution. The associated homogeneous equation of Eq. (23) is

$$\ddot{Q}_i(t) + 2\xi_i\omega_i\dot{Q}_i(t) + \omega_i^2 Q_i(t) = 0, i = 1, 2, 3\ldots \tag{24}$$

Combining with Eqs. (C.5) and (C.6), the initial conditions of a drill string in the slip phase can be obtained

$$Q_1(0) = \frac{1}{\overline{J}_1}\int_0^l J\theta_0(x)\sin\left(\frac{\pi x}{2l}\right)\mathrm{dx} = \frac{1}{\overline{J}_1}\int_0^l J\theta_0(l)\left[\sin\left(\frac{\pi x}{2l}\right)\mathrm{dx}\right]^2 = \theta_0(l) \tag{25}$$

$$Q_2(0) = \frac{1}{\overline{J}_2}\int_0^l J\theta_0(x)\sin\left(\frac{3\pi x}{2l}\right)\mathrm{dx} = \frac{1}{\overline{J}_2}\int_0^l J\theta_0(l)\left[\sin\left(\frac{3\pi x}{2l}\right)\mathrm{dx}\right]^2 = \theta_0(l) \tag{26}$$

$$Q_3(0) = \frac{1}{\overline{J}_3}\int_0^l J\theta_0(x)\sin\left(\frac{5\pi x}{2l}\right)\mathrm{dx} = \frac{1}{\overline{J}_3}\int_0^l J\theta_0(l)\left[\sin\left(\frac{5\pi x}{2l}\right)\mathrm{dx}\right]^2 = \theta_0(l) \tag{27}$$

$$\dot{Q}_1(0) = \dot{Q}_2(0) = \dot{Q}_3(0) = 0 \tag{28}$$

The generalized coordinate response determined by the initial conditions is then equals

$$Q_{i1}(t) = \eta_i e^{-\xi_i\omega_i t}\sin(\omega_{id}t + v) \tag{29}$$

where

$$\eta_i = \sqrt{Q_i^2(0) + \left(\frac{\dot{Q}_i(0) + \xi_i\omega_i Q_i(0)}{\omega_{id}}\right)^2} = \sqrt{(\theta_0(l))^2 + \left(\frac{\xi_i\theta_0(l)}{\sqrt{1-\xi_i^2}}\right)^2} \tag{30}$$

$$v_i = \arctan\frac{\omega_{id}Q_i(0)}{\dot{Q}_i(0) + \xi_i\omega_i\dot{Q}_i(0)} = \arctan\frac{\sqrt{1-\xi_i^2}}{\xi_i} \tag{31}$$

For the drill string dynamics induced by initial conditions, the proportion of each generalized coordinate is inversely proportional to the square of frequency. Considering the first three orders of mode shape, their proportions are 225/259, 25/259, and 9/259, respectively.

For the drill string in slip phase, a kinetic frictional torque acts on the drill bit ($y = l$). The proportion of each generalized coordinate determined by the frictional torque is also inversely proportional to the square of the frequency, which can be described as

$$Q_{i2}(t) = \frac{M_F}{\overline{J}_i \omega_i^2} \sin \frac{(2i-1)\pi y}{2l} \tag{32}$$

where M_F can be determined by Eq. (21).

The constant term of the generalized impact torque is $\frac{A}{2} \sin \frac{(2i-1)\pi y}{2l}$, the corresponding generalized coordinate determined by it can be written as

$$Q_{i3}(t) = \frac{A}{2\overline{J}_i \omega_i^2} \sin \frac{(2i-1)\pi y}{2l} \tag{33}$$

According to Eq. (19), the generalized impact torque of the second term (the term with ω_0) of Eq. (A.10) is $\frac{A}{\pi} \sin(\omega_0 t) \sin \frac{(2i-1)\pi y}{2l}$, and the corresponding generalized coordinate equals

$$Q_{i4}(t) = \frac{\overline{M}_{i1}}{\overline{J}_i \omega_i^2} \times \frac{1}{\sqrt{(1-\gamma_{i1}^2)^2 + (2\xi_i \gamma_{i1})^2}} \times \sin(\omega_0 t - \beta_{i1}) \tag{34}$$

where $\overline{M}_{i1} = \frac{A}{\pi} \sin \frac{(2j-1)\pi y}{2l}$ indicates the coefficient of the jth generalized impact torque whose natural frequency is ω_0, γ_{i1} means the ratio of the excitation frequency ω_0 and the ith natural frequency, β_{i1} is the initial phase of the ith generalized coordinate when the harmonic term of natural frequency equals to ω_0, and γ_{i1} and β_{i1} can be written as

$$\gamma_{i1} = \omega_0 \big/ \omega_i \tag{35}$$

$$\beta_{i1} = \arctan \frac{2\xi_i \gamma_{i1}}{1-\gamma_{i1}^2} \tag{36}$$

According to Eq. (19), the generalized impact torque of the third term (the term with $2\omega_0$) of Eq. (A.10) is $\frac{A}{2\pi} \sin(2\omega_0 t) \sin \frac{(2i-1)\pi y}{2l}$, and the corresponding generalized coordinate equals

$$Q_{i5}(t) = \frac{\overline{M}_{i2}}{\overline{J}_i \omega_i^2} \times \frac{1}{\sqrt{(1-\gamma_{i2}^2)^2 + (2\xi_i \gamma_{i2})^2}} \times \sin(2\omega_0 t - \beta_{i2}) \tag{37}$$

where $\overline{M}_{i2} = \frac{A}{2\pi} \sin \frac{(2j-1)\pi y}{2l}$ indicates the coefficient of the jth generalized impact torque whose natural frequency is $2\omega_0$, γ_{i2} represents the ratio of the excitation frequency $2\omega_0$ and the ith natural frequency, β_{i2} means the initial phase of the ith principal coordinate when the harmonic term of natural frequency equal $2\omega_0$, and γ_{i2} and β_{i2} can be written as

$$\gamma_{i2} = 2\omega_0 \big/ \omega_i \tag{38}$$

$$\beta_{i2} = \arctan \frac{2\xi_i \gamma_{i2}}{1 - \gamma_{i2}^2} \tag{39}$$

For a drill string with initial angular displacement and under the action of frictional torque and impact torque, the generalized coordinate [Eq. (23)] of using MSM can be expressed as

$$Q_i(t) = Q_{i1}(t) + Q_{i2}(t) + Q_{i3}(t) + Q_{i4}(t) + Q_{i5}(t) \tag{40}$$

4 Case Study

To obtain a quantitative understanding of the drill string dynamics, a case study is to be conducted with a specific drill string shown in Table 1 to be analyzed. The rotary table velocity is assumed to be 100 rpm ($\varphi = 10.5$ rad/s); the impact frequency is 600 times per minute (10 Hz); the first order of damping ratio is $\xi_1 = 0.05$; and the position of the impact torque is 1 m above the drill bit ($y = 2999$ m). For the impact generator, the impact torque is 366 N m when the impact frequency is 600 times per minute. The system parameters are $\overline{J}_1 = \overline{J}_2 = \overline{J}_3 = 46.64$ Kg m^2, $\omega_1 = 1.672$ rad/s, $\omega_2 = 5.015$ rad/s, $\omega_3 = 8.358$ rad/s, $\xi_1 = 0.05$, $\xi_2 = 0.0167$, $\xi_3 = 0.01$, $l = 3000$ m, $A = 366$ N m, $y = 2999$ m, $\omega_0 = 62.83$ rad/s. Regarding the static frictional coefficient $\mu_S = 0.8$, $\mu_K = 0.5$, W_B= 160 kN, and $\overline{R}_B = 72$ mm, then $\overline{M}_{i2}(t) = 5760$ N m. Part of the parameters can be obtained from the works by Navarro-López and Cortés [25], Tang et al. [20], and Tang [26].

For the drill string analyzed, the first three mode shapes are shown in Fig. 2

For the 3000-m-drill string, its torsional stiffness is 317 N m/rad. When the drill bit steps into the slip phase, the initial angular displacement of the drill bit is 29.07 rad (the drill bit lags behind the rotary table, and the value is determined by the static frictional torque). When there is no impact torque, the motion of the drill string is a

Table 1 Physical parameters of the drill string

Length l	External diameter D_p	Internal diameter d_p	Shear modulus G	Density ρ
(m)	(mm)	(mm)	(Pa)	(kg/m^3)
3000	127.0	108.6	8.0×10^{10}	7850

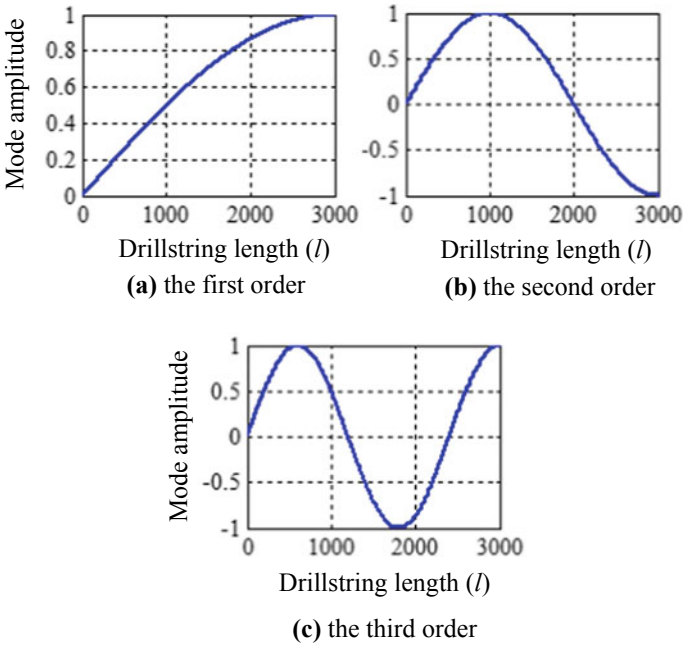

Fig. 2 First three mode shapes of the drill string

type of damped vibration determined by the initial angular displacement and static frictional torque, the first three orders of generalized coordinate can be given as

$$Q_1(t) = 225 \times \begin{pmatrix} -10.925 \times e^{-0.05\times 1.67t} \times \sin(1.66t + 1.521) \\ -(10.5t/\phi_1(x) + 18.17) \end{pmatrix} \Big/ 259 \quad (41)$$

$$Q_2(t) = 25 \times \begin{pmatrix} -10.908 \times e^{-0.0167\times 5.015t} \times \sin(5t + 1.554) \\ -(10.5t/\phi_2(x) + 18.17) \end{pmatrix} \Big/ 259 \quad (42)$$

$$Q_3(t) = 9 \times \begin{pmatrix} -10.905e^{-0.01\times 8.358t} \times \sin(8.32t + 1.561) \\ -(10.5t/\phi_3(x) + 18.17) \end{pmatrix} \Big/ 259 \quad (43)$$

For a drill string in slip phase and with the action of torsional impact, part of the frictional torque acted on the drill bit can be offset by the impact torque. The initial angular displacement of the drill bit is herein less than that of the conventional drilling (without impact torque). Under this condition, dynamics of the drill string are related to the initial condition, frictional torque, viscous damping, and impact torque (including constant term and the harmonic terms), the first three orders of generalized coordinate can be given as

$$\begin{aligned} Q_1(t) = 225 \times \left[-10.925e^{-0.05\times 1.67t} \times \sin(1.66t + 1.521) - (10.5t/\phi_1(x) + 17.59)\right] \Big/ 259 \\ + \ 6.33 \times 10^{-4} \times \sin(62.83t + 0.0027) + 7.91 \times 10^{-5} \times \sin(125.66t + 0.0013) \end{aligned} \quad (44)$$

$$Q_2(t) = 25 \times \left[-10.908e^{-0.0167\times5.015t} \times \sin(5t + 1.554) - (10.5t/\phi_2(x) + 17.59)\right] \Big/ 259 + 6.37 \times 10^{-4} \times \sin(62.83t + 0.0009) + 7.92 \times 10^{-5} \times \sin(125.66t + 0.0004) \quad (45)$$

$$Q_3(t) = 9 \times \left[-10.905e^{-0.01\times8.358t} \times \sin(8.32t + 1.561) - (10.5t/\phi_3(x) + 17.59)\right] \Big/ 259 + 6.44 \times 10^{-4} \times \sin(62.83t + 0.0005) + 7.94 \times 10^{-5} \times \sin(125.66t + 0.0003) \quad (46)$$

Substituting the above equations into Eq. (22), the following equation can be obtained by using MSM

$$\theta(x, t) = \phi_1(x)Q_1(t) + \phi_2(x)Q_2(t) + \phi_3(x)Q_3(t) \quad (47)$$

where $\phi_1(x)$, $\phi_2(x)$, and $\phi_3(x)$ are given by Eq. (16).

Figures 3 and 4 show the torsional dynamics of the drill string with and without the action of impact torque. From the figures, the torsional impact torque will aggravate slightly the drill string vibration. In general, the HFTI seems more significant to the vibration of the bottom hole assembly. The effect of HFTI on the rock breaking is not considered in this section.

Figure 5 shows the time response of the relative angular displacement between the drill bit and the rotary table when the drill string is in slip phase. In this section, the drill bit is regarded to overcome a same frictional torque, though the HTFI can balance part of the frictional torque. From the figure, even in the drill bit, the effect of HFTI on vibration of the drill bit is very small.

In the actual drilling process, the HFTI aggravates the rock damage and rock failure. As a result, the required torque developed to shear the rock reduces, which means the relative angular displacement between the drill bit and the rotary table is less than that of the drilling without HFTI. In our previous work [18], it is shown

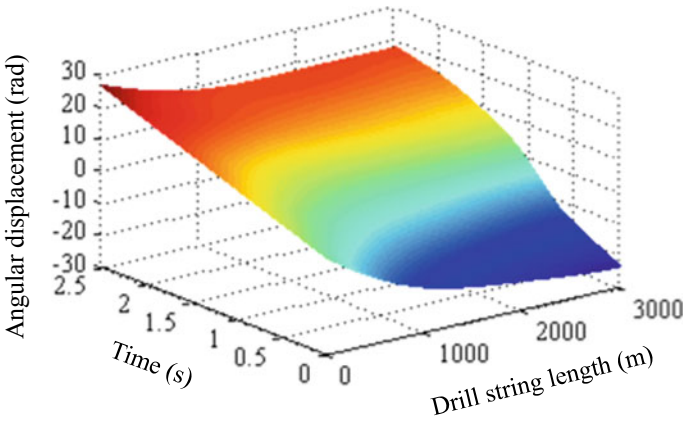

Fig. 3 Angular displacement of the drill string during the slip phase in the case no HFTI acts on the drill string (assuming that the initial relative angular displacement between the drill bit and the rotary table is determined by the static frictional torque)

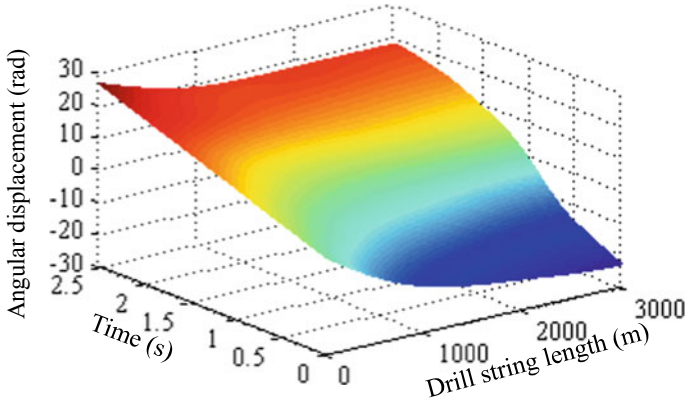

Fig. 4 Angular displacement of the drill string during the slip phase in the case HFTI acts on the drill string (assuming that the initial relative angular displacement between the drill bit and the rotary table is determined by the static frictional torque as well as the HTFI)

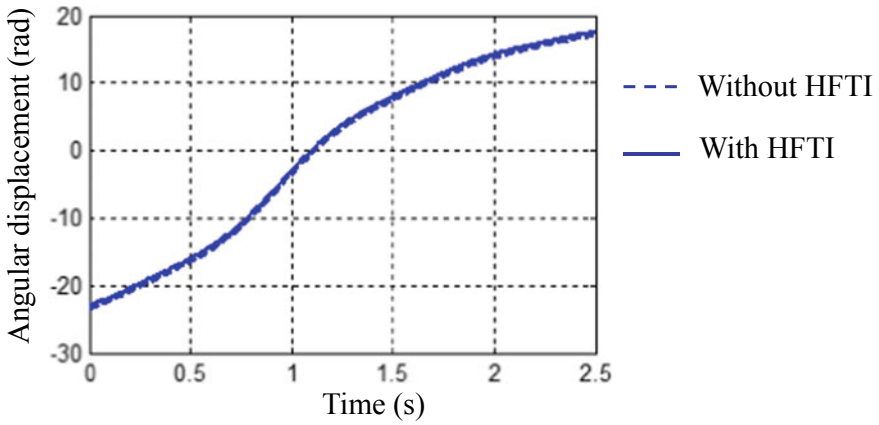

Fig. 5 Relative angular displacement of the drill bit for the cases with and without HFTI

that the frictional torque becomes 8150 N m when the HFTI is 600 times per minute and the corresponding relative angular displacement is 25.71 rad/s (the drill bit lags behind the rotary table). When the effect of HFTI on rock breaking is considered, the first three orders of mode shape shall be given as

$$Q_1(t) = 225 \times \left[-8.145e^{-0.05\times 1.67t} \times \sin(1.66t + 1.521) - (10.5t/\phi_1(x) + 17.59)\right] \Big/ 259 + 6.33 \times 10^{-4} \times \sin(62.83t + 0.0027) + 7.91 \times 10^{-5} \times \sin(125.66t + 0.0013) \quad (48)$$

$$Q_2(t) = 25 \times \left[-8.128e^{-0.0167\times 5.015t} \times \sin(5t + 1.554) - (10.5t/\phi_2(x) + 17.59)\right] \Big/ 259 + 6.37 \times 10^{-4} \times \sin(62.83t + 0.0009) + 7.92 \times 10^{-5} \times \sin(125.66t + 0.0004) \quad (49)$$

$$Q_3(t) = 9 \times \left[-8.125e^{-0.01\times 8.358t} \times \sin(8.32t + 1.561) - (10.5t/\phi_3(x) + 17.59)\right] \Big/ 259 + 6.44 \times 10^{-4} \times \sin(62.83t + 0.0005) + 7.94 \times 10^{-5} \times \sin(125.66t + 0.0003) \quad (50)$$

Figure 6 presents the actual dynamics of the drill string by considering the effect of HFTI on rock breaking. Figure 7 shows the relative angular displacement between the drill bit and the rotary table with considering the effect of HFTI on rock breaking. From the figure, for the actual drilling, the HTFI will mitigate the torsional vibration of the drill string. In addition, the HFTI is more sensitive to the drill string close to

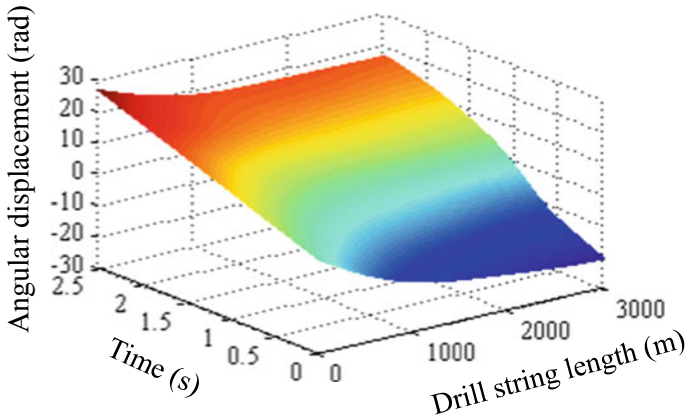

Fig. 6 Drill string dynamics with considering the effect of HFTI (600 times per minute) on the rock breaking

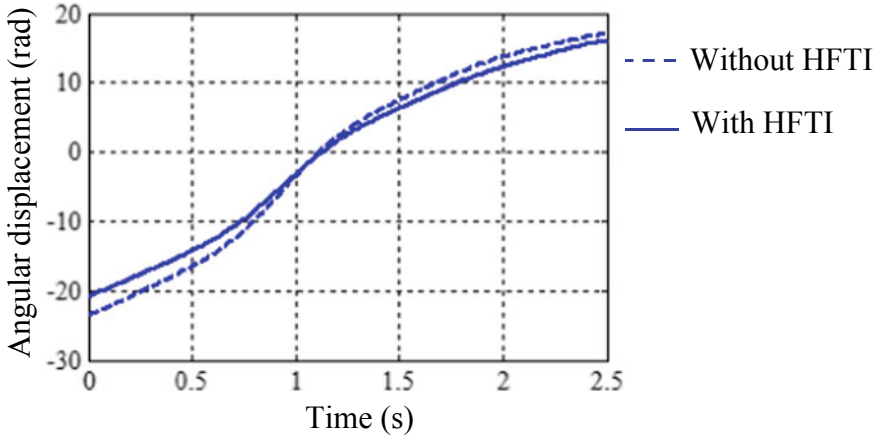

Fig. 7 Relative angular displacement of the drill bit for the cases with and without HFTI (for the case with HFTI, the effect of HFTI on rock breaking is considered)

the drill bit. The HFTI is beneficial to the drilling process as well as the mitigation of stick-slip vibration.

5 Conclusions

This study addresses the problem of stick-slip vibration that usually occurs in the drilling of hard formation. In recent years, the HFTI is used to improve the drilling efficiency. Field applications show that the HFTI is beneficial to the rock breaking and mitigation of stick-slip vibration. Since the high-frequency torsional impact drilling is realized by adding HFTI onto the drill string, the HFTI may aggravate or be a source of drill string vibration. In this study, the effect of HFTI on the torsional vibration of a drill string in slip phase is investigated. Firstly, a mechanical model of the continuous drill string is developed, with the HFTI is treated as external load. Secondly, the motion equation of the drill string is resolved through using MSM, with the HFTI is regarded as Fourier series. Finally, case studies are conducted to reveal the effects of HFTI on drill string vibration, wherein a 3000-m-drill string is analyzed, and the impact parameters are obtained from the laboratory experiments. Results show that the HFTI has little influence on the vibration of a drill string in slip phase, which also means that the HFTI will not give rise to or aggravate the drill string vibration. In fact, the HFTI aggravates the rock damage and rock failure. In this way, the HFTI changes the response of angular displacement and finally leads to the mitigation of stick-slip vibration.

Acknowledgements This research is supported by the Key Research Project of Sichuan Province (No. 2017GZ0365), National Natural Science Foundation of China (No. 51674214), Open Research Subject of MOE Key Laboratory of Fluid and Dynamic Machinery (No. szjj2016-062), Youth Scientific Research Innovation Team Project of Sichuan Province (No. 2017TD0014), and Scientific Research Starting Project of SWPU (No. 2015QHZ011).

Appendix A

In this appendix, the approach of processing the impact torque is presented. For the HFTI, it acts on a certain cross section of the drill string. The impact torque is assumed to be periodical pulses shown in Fig. A.1, wherein τ is the load period and A is the load amplitude.

According to the figure, the expression of the impact torque can be given as

$$p(t) = A \times \left(1 - \frac{t}{\tau}\right), \ 0 \le t \le \tau \tag{A.1}$$

Fig. A.1 Impact torque

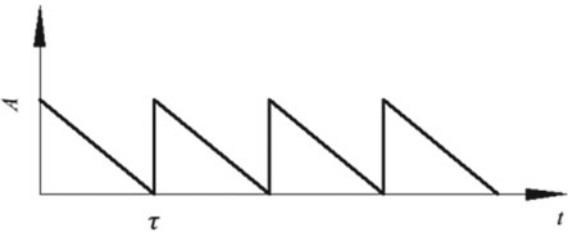

From the figure, the impact torque is piecewise, which leads to difficulties in solving the equations. The Fourier series is used to solve this matter. The $p(t)$ can be given as

$$\begin{aligned} p(t) &= \frac{a_0}{2} + a_1\cos(\omega t) + a_2\cos(2\omega t) + \cdots + b_1\sin(\omega t) + b_2\sin(2\omega t) + \cdots \\ &= \frac{a_0}{2} + \sum_{n=1}^{\infty}\left(a_n\cos(n\omega t) + \cdots + b_n\sin(n\omega t)\right) \end{aligned} \tag{A.2}$$

where $\omega = 2\pi/\tau$ is the fundamental frequency, and $a_1, a_2, \ldots, b_1, b_2, \ldots$ are given as

$$a_0 = \frac{\omega}{\pi}\int_0^{2\pi/\omega} p(t)dt = \frac{2}{\tau}\int_0^{\tau} p(t)dt \tag{A.3}$$

$$a_n = \frac{\omega}{\pi}\int_0^{2\pi/\omega} p(t)\cos(n\omega t)dt = \frac{2}{\tau}\int_0^{\tau} p(t)\cos(n\omega t)dt \tag{A.4}$$

$$b_n = \frac{\omega}{\pi}\int_0^{2\pi/\omega} p(t)\sin(n\omega t)dt = \frac{2}{\tau}\int_0^{\tau} p(t)\sin(n\omega t)dt \tag{A.5}$$

By substituting Eq. (A.1) into Eqs. (A.1)–(A.5), the results become

$$a_0 = \frac{\omega}{\pi}\int_0^{2\pi/\omega} p(t)dt = A \tag{A.6}$$

$$a_n = \frac{\omega}{\pi}\int_0^{2\pi/\omega} p(t)\cos(n\omega t)dt = 0, n = 1, 2, 3\ldots \tag{A.7}$$

$$b_n = \frac{\omega}{\pi}\int_0^{2\pi/\omega} p(t)\sin(n\omega t)dt = -\frac{A}{n\pi}, n = 1, 2, 3\ldots \tag{A.8}$$

The expression of impact torque can be given as

$$p(t) = \frac{A}{2} + \frac{A}{n\pi}\sum_{n=1}^{\infty}\sin(n\omega_0 t) \tag{A.9}$$

where ω_0 is the impact frequency. By using the first three orders, Eq. (A.9) can be rewritten as

$$p(t) = \frac{A}{2} + \frac{A}{\pi}\sin(\omega_0 t) + \frac{A}{2\pi}\sin(2\omega_0 t) \tag{A.10}$$

Appendix B

The orthogonal character is presented. Equation (7) can be rewritten as

$$GI_p\phi_i''(x) = -\omega_i^2\phi_i(x) \tag{B.1}$$

Multiplying the first term of Eq. (B.1) by $\phi_j(x)$ and integrating it can obtain

$$\int_0^l GI_p\phi_j(x)\phi_i''(x)\mathrm{dx} = \mathrm{GI_p}\phi_\mathrm{j}(\mathrm{x})\phi_\mathrm{i}'(\mathrm{x})|_0^1 - \int_0^1 \mathrm{GI_p}\phi_\mathrm{j}'(\mathrm{x})\phi_\mathrm{i}'(\mathrm{x})\mathrm{dx} \tag{B.2}$$

Eq. (B.2) can be rewritten as

$$\int_0^l GI_p\phi_j(x)\phi_i''(x)\mathrm{dx} = \int_0^1 \mathrm{GI_p}\phi_\mathrm{j}''(\mathrm{x})\phi_\mathrm{i}(\mathrm{x})\mathrm{dx} \tag{B.3}$$

If fixed boundary condition or free boundary condition is applied on the drill string end, the second term of Eq. (B.2) equals 0. Equation (B.2) can then be written as

$$\int_0^l GI_p\phi_j(x)\phi_i''(x)\mathrm{dx} = -\int_0^1 \mathrm{GI_p}\phi_\mathrm{j}'(\mathrm{x})\phi_\mathrm{i}'(\mathrm{x})\mathrm{dx} \tag{B.4}$$

Multiplying Eq. (B.1) by $\phi_j(x)$ and integrating it shall have

$$\int_0^l GI_p\phi_j'(x)\phi_i'(x)\mathrm{dx} = \int_0^1 \omega_\mathrm{i}^2\phi_\mathrm{i}(\mathrm{x})\phi_\mathrm{j}(\mathrm{x})\mathrm{dx} \tag{B.5}$$

Exchanging the corner marks i and j, Eq. (B.4) becomes

$$\int_0^l GI_p\phi_i'(x)\phi_j'(x)\mathrm{dx} = \int_0^1 \omega_\mathrm{j}^2\phi_\mathrm{j}(\mathrm{x})\phi_\mathrm{i}(\mathrm{x})\mathrm{dx} \tag{B.6}$$

Eqs. (B.5) and (B.6) lead to

$$\left(\omega_i^2 - \omega_j^2\right)\int_0^l \phi_i(x)\phi_j(x)\mathrm{dx} = 0 \tag{B.7}$$

If $i \neq j$, then $\omega_i \neq \omega_j$; we therefore have

$$\int_0^l \phi_i(x)\phi_j(x)\mathrm{dx} = 0 \tag{B.8}$$

Equation (B.8) indicates that the mode shapes are orthogonal with respect to the mass and stiffness.

Appendix C

The derivation process of Eq. (23) is to be discussed. As the mode shapes are orthogonal with respect to the inertia (or mass) and stiffness, then we obtain

$$\int_0^l J\phi_i(x)\phi_j(x)\mathrm{dx} = 0, \mathrm{i} \neq \mathrm{j} \tag{C.1}$$

$$\int_0^l J\phi_i(x)\phi_j(x)\mathrm{dx} = 1, \mathrm{i} = \mathrm{j} \tag{C.2}$$

$$\int_0^l GI_p\frac{d^2\phi_i(x)}{\mathrm{dx}^2}\phi_j(x)\mathrm{dx} = 1, \mathrm{i} = \mathrm{j} \tag{C.3}$$

Substituting Eq. (22) into Eq. (2), we have

$$\sum_{i=1}^{\infty} GI_p\frac{d^2\phi_i(x)}{\mathrm{dx}^2}Q_i(t) - \sum_{i=1}^{\infty} J\phi_i(x)\ddot{Q}_i(t) - \sum_{i=1}^{\infty}\beta(x)\phi_i(x)\dot{Q}(t) = M(x,t) \tag{C.4}$$

The corresponding initial conditions are

$$\theta(x,0) = \theta_0(x) = \sum_{i=1}^{\infty} \phi_i(x) Q_i(0) \tag{C.5}$$

$$\frac{\partial \theta(x,0)}{\partial t} = \dot{\theta}_0(x) = \sum_{i=1}^{\infty} \phi_i(x) \dot{Q}_i(0) \tag{C.6}$$

Multiplying Eq. (C.4) by $\phi_j(x)$ and integrating it, combining with Eqs. (C.1)–(C.3), and (B.3), we have

$$\int_0^l GI_p \frac{d^2\phi_j(x)}{\mathrm{dx}^2}\phi_j(x)\mathrm{dxQ_j(t)} - \int_0^1 \mathrm{J}\phi_j^2(\mathrm{x})\mathrm{dx}\ddot{\mathrm{Q}}_\mathrm{j}(\mathrm{t})$$
$$-\sum_{i=1}^{\infty}\int_0^l \beta(x)\phi_i(x)\phi_j(x)\mathrm{dx}\,\dot{Q}_i(t) = \int_0^l \phi_j(x)M(x,t)\mathrm{dx} \tag{C.7}$$

By conducting similar operations to Eqs. (C.5) and (C.6), we have

$$Q_j(0) = \frac{1}{\overline{J}_j}\int_0^l J\theta_0(x)\phi_j(x)\mathrm{dx} \tag{C.8}$$

$$\dot{Q}_j(0) = \frac{1}{\overline{J}_j}\int_0^l J\dot{\theta}_0(x)\phi_j(x)\mathrm{dx} \tag{C.9}$$

Combining with Eqs. (18), (19), and (B.1), the first term of Eq. (C.7) can be written as

$$\int_0^l GI_p \frac{d^2\phi_j(x)}{\mathrm{dx}^2}\phi_j(x)\mathrm{dxQ_j(t)} = -\omega_j^2\overline{J}_j Q_j(t) \tag{C.10}$$

and Eq. (C.7) becomes

$$\overline{J}_j\ddot{Q}_j(t) + \omega_j^2\overline{J}_j Q_j(t) + \sum_{i=1}^{\infty}\int_0^l \beta(x)\phi_i(x)\phi_j(x)\mathrm{dx}\,\dot{Q}_j(t) = \overline{M}_j \tag{C.11}$$

For the third term of Eq. (C.11), the non-diagonal matrix will lead to difficulties in equation decoupling. In order to decouple the third term of Eq. (C.11), the viscous damping is assumed to be

$$\beta(x) = aJ \tag{C.12}$$

Defining the jth damping ratio ξ_j is

$$\xi_j = \frac{a}{2\omega_j} \tag{C.13}$$

where a is constant. By combining Eqs. (C.11)–(C.13), Eq. (23), which is a decoupled differential equation of the generalized coordinate, can be obtained.

References

1. Bauer, N., Hilaire, J., Brecha, R.J., Edmonds, J., Jiang, K., Kriegler, E., Rogner, H.H., Sferra, F.: Assessing global fossil fuel availability in a scenario framework. Energy **111**, 580–592 (2016)
2. Faramawy, S., Zaki, T., Sakr, A.A.E.: Natural gas origin, composition, and processing: a review. J. Nat. Gas Sci. Eng. **34**, 34–54 (2016)
3. Tsvetkova, A., Partridge, M.D.: Economics of modern energy boomtowns: do oil and gas shocks differ from shocks in the rest of the economy? Energy Econ. **59**, 81–95 (2016)
4. Guzek, A., Shufrin, I., Pasternak, E., Dyskin, A.V.: Influence of drilling mud rheology on the reduction of vertical vibration in deep rotary drilling. J. Petrol. Sci. Eng. **135**, 375–383 (2015)
5. Biscaro, E., D'Alessandro, J.D., Moreno, A., Hahn, M., Lamborn, R., Al-Naabi, M.H., Bowser, A.C.: New rotary steerable drilling system delivers extensive formation evaluation for high build rate wells. In: SPE Western Regional Meeting. Society of Petroleum Engineers (2015)
6. Bakhtiari-Nejad, F., Hosseinzadeh, A.: Nonlinear dynamic stability analysis of the coupled axial-torsional motion of the rotary drilling considering the effect of axial rigid-body dynamics. Int. J. Nonlinear Mech. **88**, 85–96 (2017)
7. Ghasemloonia, A., Rideout, D.G., Butt, S.: A review of drillstring vibration modeling and suppression methods. J. Petrol. Sci. Eng. **131**, 150–164 (2015)
8. Lian, Z., Zhang, Q., Lin, T., Wang, F.: Experimental and numerical study of drill string dynamics in gas drilling of horizontal wells. J. Nat. Gas Sci. Eng. **27**, 1412–1420 (2015)
9. Patil, P.A., Teodoriu, C.A.: A comparative review of modelling and controlling torsional vibrations and experimentation using laboratory setups. J. Petrol. Sci. Eng. **112**, 227–238 (2013)
10. Zhu, X., Tang, L., Yang, Q.: A literature review of approaches for stick-slip vibration suppression in oilwell drillstring. Adv. Mech. Eng. **6**, 1–16 (2014)
11. Baumgart, A.: Stick-slip and bit-bounce of deep-hole drillstrings. ASME J. Energy Resour. Technol. **32**, 78–82 (2006)
12. Gulyaev, V.I., Khudolii, S.N., Glushakova, O.V.: Self-excited of deep-well drill string torsional vibrations. Strength Mater. **41**, 613–622 (2009)
13. Gulyaev, V.I., Lugovoi, P.Z., Glushakova, O.V., Glazunov, S.N.: Self-excitation of torsional vibrations of long drillstring in a viscous fluid. Int. Appl. Mech. **52**, 155–164 (2016)
14. Pelfrene, G., Sellami, H., Gerbaud, L.: Mitigation stick-slip in deep drilling based on optimization of PDC bit design. In: Proceedings of Drilling Conference and Exhibition, pp. 1–12. Amsterdam, The Netherlands (2011)
15. Belokobyl'skii, S.V., Prokopov, V.K.: Friction induced self-excited vibration of drill rig with exponential drag law. Int. Appl. Mech. **18**, 1134–1138 (1982)
16. Richard, T., Germay, C., Detournay, E.: A simplified model to explore the root cause of stick-slip vibrations in drilling systems with drag bits. J. Sound Vib. **305**, 432–456 (2007)
17. Patil, P.A., Teodoriu, C.A.: Model development of torsional drillstring and investigating parametrically the stick-slip influencing factors. ASME J. Energy Resour. Technol. **135**, 1–7 (2013)

18. Tang, L., Zhu, X., Shi, C.: Effects of high-frequency torsional impacts on mitigation of stick-slip vibration in drilling system. J. Vib. Eng. Technol. **5**, 111–122 (2016)
19. Tang, L., Zhu, X., Shi, C., Sun, J.: Investigation of the damping effect on stick-slip vibration of oil and gas drilling system. J. Vib. Eng. Technol. **4**, 79–86 (2016)
20. Tang, L., Zhu, X., Qian, X., Shi, C.: Effects of weight on bit on torsional stick-slip vibration of oilwell drill string. J. Mech. Sci. Technol. **31**, 4589–4597 (2017)
21. Mihajlovic, N., van Veggel, A.A., van de Wouw, N., Nijmeijer, H.: Analysis of friction-induced limit cycling in an experimental drill string system. ASME J. Dyn. Syst. Meas. Control **126**, 709–720 (2004)
22. Lai, S.W., Wood, M.J., Eddy, A.J., Holt, T.L., Bloom, M.R.: Stick-slip detection and friction factor testing using surface-based torque and tension measurements. In: Proceedings of the SPE Annual Technical Conference and Exhibition, pp. 1–18. Amsterdam, The Netherlands (2014)
23. Puebla, H., Alvarez-Ramirez, J.: Suppressing of stick-slip in drillstring: a control approach based on modeling error compensation. J. Sound Vib. **310**, 881–901 (2018)
24. Deen, A., Wedel, R., Nayan, A., Mathison, S., Hightower, G.: Application of a torsional impact hammer to improve drilling efficiency. In: Proceedings of the SPE Annual Technical Conference and Exhibition, pp. 1–11. Denver, USA (2011)
25. Navarro-López, E.M., Cortés, D.: Avoiding harmful oscillations in a drill string through dynamical analysis. J. Sound Vib. **307**, 152–171 (2007)
26. Tang, Y.: Advanced structural dynamics. Tianjin University Press, Tianjin (2007)

Carriage–Rail–Viaduct Coupling Analysis Using Dynamic Flexibility Method

Linya Liu, Zhiyuan Zuo, Yun Lai Zhou and Jialiang Qin

Abstract This study compares the two-layer model and three-layer model in the coupling analysis of the vehicle–rail–viaduct systems, especially for the vertical vibration investigation. This study applies dynamic flexibility in establishing the dynamic model of vehicle–rail–viaduct in frequency domain through the wheel–rail interaction and interaction model between rails and viaducts. By simplifying the subsystems of vehicles, rails, and viaducts in order to obtain two-layer model and three-layer model, the dynamic responses are hereinafter analyzed for the influences of subsystems to the final vibration responses. The results shall suggest the prediction of dynamic responses for the vehicles, rails, and viaducts.

Keywords Dynamic flexibility method · Coupling analysis · Viaduct · Multiple-layer model

1 Introduction

Structural coupling problem has been a critical affair in both engineering fields and theoretical fields. Previous investigations have undergone various developments for the coupling analysis in various structures like bridges, large-scale structures like high-rise buildings. In terms of vehicle–rail–viaduct coupling system, a lot of researchers have done in unveiling the hidden interrelation between subsystems, and the interrelation between them as well [1–4].

Researchers developed various layer models for different occasions in engineering, such as two-layer model, three-layer model, and four-layer model. These models have been applied in specific problems, and they have seldom been compared between each other.

L. Liu · Z. Zuo · J. Qin
Engineering Research Center of Railway Environment Vibration and Noise Ministry of Education, East China Jiaotong University, Nanchang 330013, China

Y. L. Zhou (✉)
Department of Civil Engineering, Lusófona University, Campo Grande, 376, 1749-024 Lisbon, Portugal
e-mail: zhou.yunlai@163.com

© Springer Nature Singapore Pte Ltd. 2019

Y. L. Zhou et al. (eds.), *Data Mining in Structural Dynamic Analysis*,
https://doi.org/10.1007/978-981-15-0501-0_7

For the dynamic analysis of the coupling system, the dynamic flexibility method has been widely applied [5–10]. For instance, in [5], a new slab track plate design is analyzed with dynamic flexibility method for studying the vibration mitigation effect; in [6], the damping pad under CRTS-III ballastless track in high-speed rail viaduct is analyzed for the noise and vibration mitigation performance using dynamic flexibility method; similarly, in [7], the noise mitigation performance for box girder viaduct is analyzed. In addition, the vehicle-line-bridge coupled vibration is analyzed using dynamic flexibility method in [8, 9], and the characteristics of temperature and frequency change dynamics of elastic pad in high-speed rail-free track fastener is studied in [10].

This study aims to illustrate the coupling analysis of simplified multiple composite beam models in viaducts which has several forms: two layers (rail is mounted to the viaduct), three layers (rail is mounted to the slabs, and CA mortar is filled between the slab and viaduct) and so on, and remaining sections shall give detailed discussion.

2 Theory Deviation

2.1 Multiple-Layer Model for Vehicle–Rail–Viaduct Dynamic Analysis

This study takes CRH380A high-speed train and high-speed railway box girder viaduct as an example; a dynamic flexibility method is applied to study the dynamic responses of the vehicle–rail–viaduct coupling system. The two-layer and three-layer vehicle–rail–viaduct coupling systems are shown in Figs. 1 and 2, respectively.

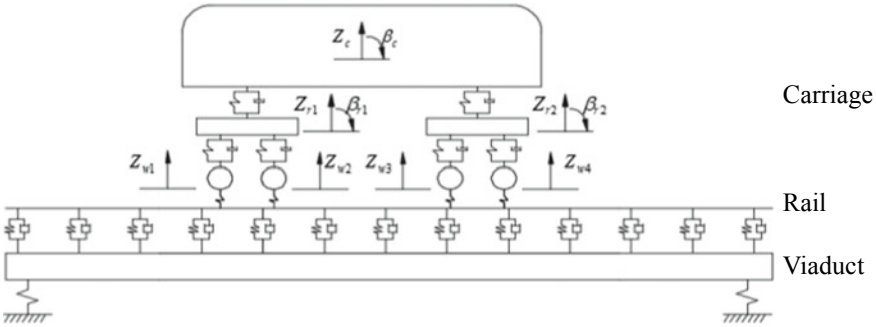

Fig. 1 Two-layer model

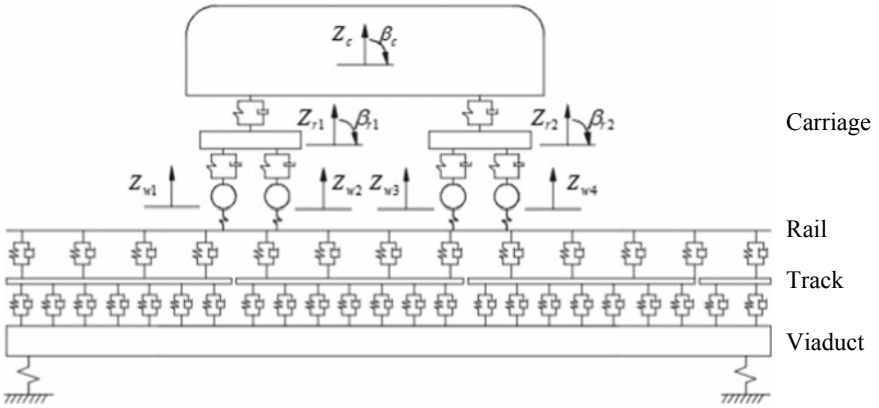

Fig. 2 Three-layer model

2.2 Dynamic Flexibility Method

By considering the single rail, the vehicle subsystem will be taken only in half, the carriage body and bogie are considered with vertical displacements only, and then single carriage model has 10 degrees of freedom, the vibration equation as follows:

$$[M_V]\{\ddot{Z}_V(t)\} + [C_V]\{\dot{Z}_V(t)\} + [K_V]\{Z_V(t)\} = \{p(t)\} \tag{1}$$

where $[M_V]$ means the mass matrix of vehicle system, $[C_V]$ indicates the damping matrix for the vehicle system, $[K_V]$ means the stiffness matrix of the vehicle system; $\{Z_V(t)\}$, $\{\dot{Z}_V(t)\}$, and $\{\ddot{Z}_V(t)\}$ mean the displacement, velocity, and acceleration of the carriage system; $\{p(t)\}$ means the wheel–rail interaction force resulted from the track irregularity.

As to dynamic compliance, the dynamic flexibility $\beta^v_{i,j}$ indicates displacement of ith wheel–rail contacting point when harmonic unit load acting at jth wheel–rail contacting point. Such wheel dynamic flexibility can be expressed as

$$\beta^V = [\beta^V_{ij}] \quad i, j = 1, 2, 3, 4 \tag{2}$$

Details for this theory can refer to [6–10].

Table 1 Parameters of the CRH380A vehicle

Parameter/Symbol/Unit	Value
Rated carriage weight/M_c/kg	42934
Weight of bogie/M_b/kg	3300
Weight of wheel pair/M_w/kg	1780
Rotating inertia of body nodding/J_c/(kg m^2)	1.712×10^6
Bogie nodding moment of inertia/J_b/(kg m^2)	1807
Vertical stiffness of primary suspension/k_1/(N m^{-1})	1.176×10^6
Vertical damping of primary suspension/c_1 (N s/m)	1.0×10^4
Vertical stiffness of second suspension/k_2/(N m^{-1})	2.4×10^5
Vertical damping of second suspension/c_2/(N s/m)	2.0×10^4
Length of carriage/l_c/m	25
Length between truck centers/l_b/m	17.5
Length between axles/l_w/m	2.5

3 Model Parameters

3.1 Parameters for the Train

The high-speed train uses CRH380A as an example, and related parameters are listed in Table 1.

The viaduct uses high-speed single-line box girder viaduct, and the parameters for the viaduct are listed in Table 2.

3.2 Irregularity Spectrum of the Rail

In terms of the carriage, the velocity for the carriage is taken as 300 km/h, and the irregularity spectrum is taken with the rail roughness amplitude limit from ISO 3095:2005 [11]

$$20\lg\left(\frac{R}{r_0}\right)=\begin{cases}18.435\lg\lambda+27.194, 0.01\le\lambda\\ -9.7, 0.00315\le\lambda<0.01\end{cases} \tag{3}$$

$$\lambda=\frac{2\pi V}{\omega} \tag{4}$$

Table 2 Parameters of track bridge

Components	Description/Symbol/Unit	Value
Rail	Young's modulus/E_r/(N/m^2)	2.059e11
	Moment of Inertia/I_r/(m^4)	3.217e−5
	Density/ρ_r/(kg/m^3)	7850
	Section area/A_r/(m^2)	7.745e−3
	Shear modulus/G_r/(N/m^2)	7.7e10
	Section coefficient/κ	0.45
	Loss factor/η_r	0.01
Fasteners	Distance between fasteners/(m)	0.625
Slab track	Young's modulus/(N/m^2)	3.6e10
	Moment of Inertia/(m^4)	1.7e–3
	Density/(kg/m^3)	2750
	Section area/(m^2)	0.51
	Loss factor	0.1
Viaduct	Length/(m)	32
	Young's modulus/(N/m^2)	3.45e10
	Moment of Inertia/(m^4)	5.757
	Density/(kg/m^3)	2650
	Section area/(m^2)	4.416
	Loss factor	0.1
Bearing	Stiffness/(MN/m)	6e9
	Distance between bearings/(m)	32
	Loss factor	0.25

where r_0 is reference roughness value. $r_0 = 10^{-6}$ m; λ is wavelength in m; V is the velocity of the carriage; and ω is the circular frequency of the excitation.

3.3 Scenarios in Computation

In order to analyze the influence of the multiple-layer beam model in a vibration of the carriage–rail–viaduct vertical coupling vibration, two scenarios are considered with two-layer and three-layer beam model, respectively, as illustrated in Table 3.

4 Results Analysis

Figure 3 shows the results of accelerations of carriage body calculated by aforementioned two models, and these they agree well with each other. The main frequency

Table 3 Operating scenarios in computation

Scenarios	Parameters considered
Scenario 1: two-layer beam model	Carriage, rail, fasteners, viaduct, bearing
Scenario 2: three-layer beam model	Carriage, rail, fasteners, slab track, CA mortar, viaduct, bearing

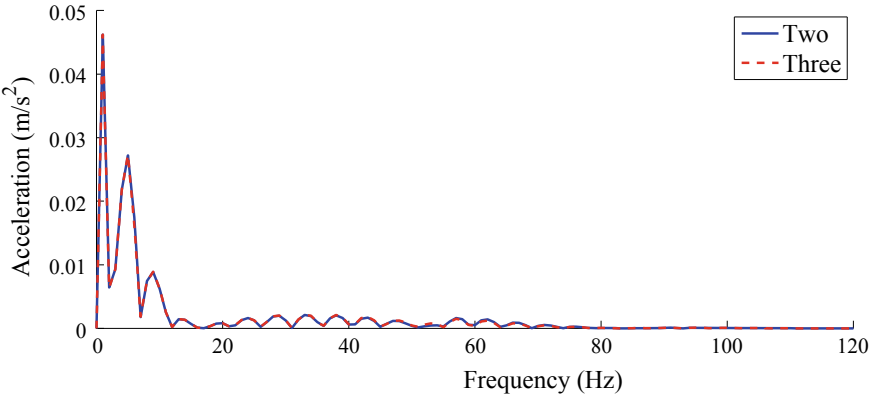

Fig. 3 Acceleration of the carriage body

peak occurs around 1 Hz. This implies that these two models do not have a noticeable difference in analyzing the accelerations for the carriage body during investigating the rail–viaduct coupling.

As demonstrated in Fig. 4, the acceleration of the bogie mainly occurs below 80 Hz. In the frequency range below 30 Hz, these two models, two-layer and three-layer beam models, obtain the almost same results; in the frequency range [30, 54] Hz, the two-layer beam model leads to more conservative acceleration estimation for the bogie compared with the three-layer beam model; in the frequency range [54, 120] Hz, the three-layer model obtains the more conservative acceleration estimation for the bogie. At the frequency 58 Hz, the two-layer model obtains 0.3694 m/s^2 and the three-layer model gives 0.3216 m/s^2. Such difference comes from the effect of slab track and CA mortar, which can mitigate the vibration effectively in the frequency range [54, 120] Hz.

Figures 5, 6, and 7 display the spectrums for wheel pair acceleration, wheel–rail force, and rail acceleration, respectively. As can be seen in Figs. 5, 6, 7, these aforementioned two modes generally agree with each other in assessing the vibration responses for the wheel pair, wheel–rail force, and the rail as well. In the frequency range below 30 Hz, the responses agree with each other; in the frequency range [30, 52] Hz, the predicted responses from the two-layer model are less than those assessed by the three-layer model; in the frequency range [52, 120] Hz, the predicted responses from the two-layer model are higher than those assessed by the three-layer model for wheel pair, wheel–rail force, and rail as well.

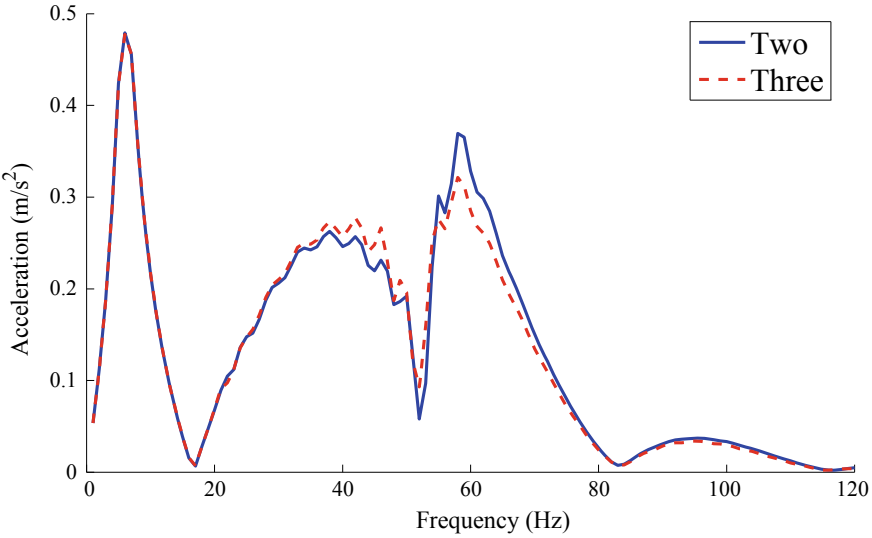

Fig. 4 Acceleration of the bogie

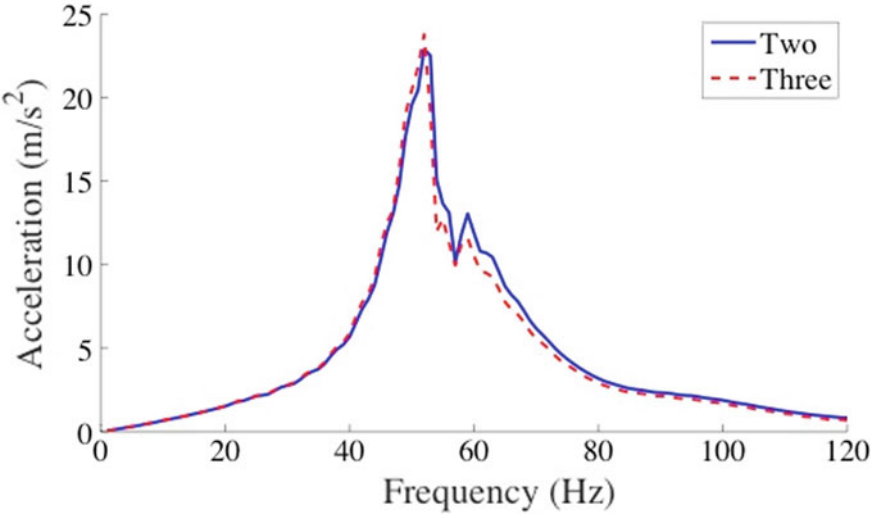

Fig. 5 Acceleration of the wheel pair

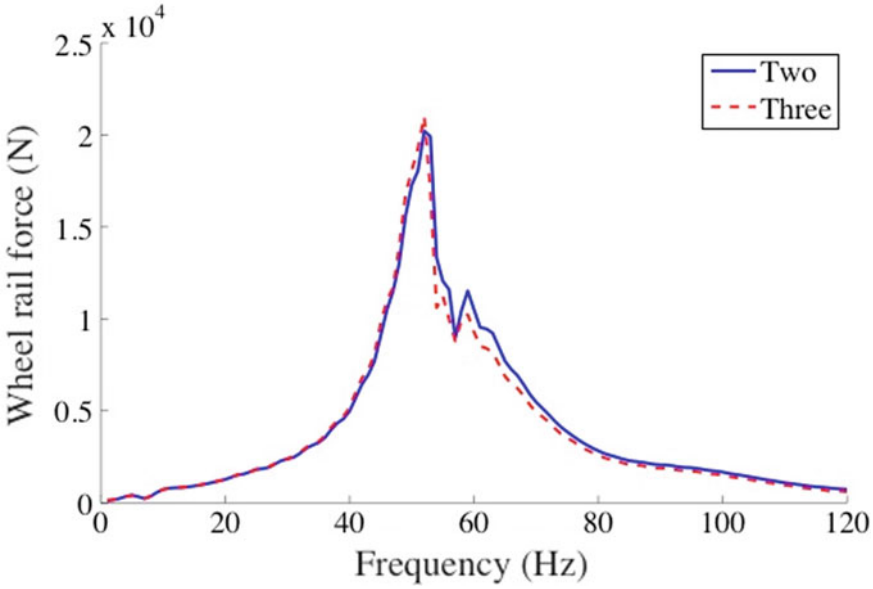

Fig. 6 Wheel rail force

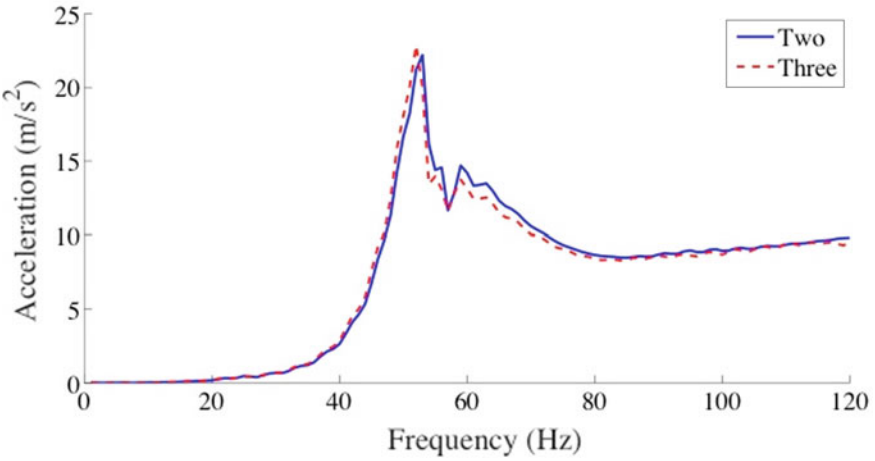

Fig. 7 Acceleration of the rail

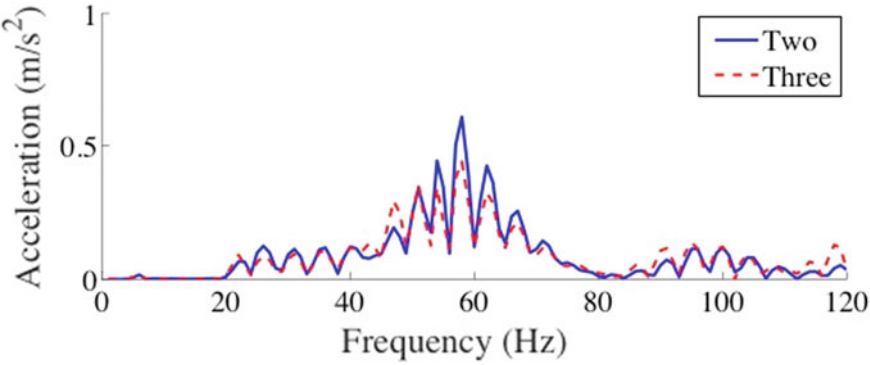

Fig. 8 Acceleration of the viaduct

In summary, as increasing the layers, the slab, CA mortar, and so on shall mitigate the high-frequency vibration effectively.

Figure 8 illustrates the acceleration responses of the viaduct assessed by the two models. In Fig. 8, the frequency range is lower than 20 Hz, and the results from the two models agree well with each other; the peaks of the accelerations for two-layer model and three-layer model are 0.6095 (m/s^2) and 0.4403 (m/s^2), respectively, both at 58 Hz. It is also obvious that as increasing the layer in the model, the acceleration peak of the acceleration has been clearly decreased. This suggests that the slab track, CA mortar, and so on can mitigate the vibration of the system effectively.

5 Conclusions

This study applies the dynamic flexibility method in constructing the frequency domain dynamic model for the vehicle–slab–viaduct coupling system and studies the vibration responses considering the influences of the subsystem. Conclusions can be summarized as follows:

Two-layer and three-layer vehicle–rail–viaduct dynamic models agree well in the vertical accelerations evaluation, and in the high-frequency range, they have influences in the accelerations of the bogie and wheel pair.

When using more layers in the dynamic model, the slab track, CA mortar, and so on shall mitigate the high-frequency vibration.

When using more layers, for instance, using three layers for the dynamic model, the damping shall be increased and further affect the corresponding vibration responses.

References

1. Carlone, L., Thompson, D.J.: Vibration of a rail coupled to a foundation beam through a series of discrete elastic supports. ISVR. University of Southampton (2001)
2. Wu, T.X., Thompson, D.J.: On the parametric excitation of the wheel/track system. J. Sound Vib. **278**(4–5), 725–747 (2004)
3. Lei, X.: High Speed Railway Track Dynamics: Model, Algorithm and Application. Science Press, Beijing (2015)
4. Zhai, W.: Vhhicle-Track Coupled Dynamics (Fourth Edition). Science Press, Beijing (2007)
5. Liu, L., Wang, X., Zhou, Y.-L., Qin, J.: Vibration mitigation effect investigation of a new slab track plate design. Sensors **19**(1), 168 (2019)
6. Liu, L., Song, R., Zhou, Y.-L., Qin, J.: Noise and vibration mitigation performance of damping pad under CRTS-III ballastless track in high speed rail viaduct. KSCE J. Civ. Eng. **23**(8), 3525–3534 (2019)
7. Liu, L., Qin, J., Zhou, Y.-L., Xi, R., Peng. S.: Structural noise mitigation for box girder viaduct using acoustic modal contribution analysis. Struct. Eng. Mech. Int. J. (2019) (In press)
8. Shi, G., Yang, J., Yang, X., Zhang, X.: Vertical coupled vibration analysis of vehicle-line-bridge based on dynamic flexibility method. J. Central South Univ. (Natural Science Edition) **48**(04), 1119–1126 (2017)
9. Yang J.: Study on prediction of high speed vehicle-bridge coupling vibration and viaduct bridge structure noise radiation. Lanzhou Jiaotong University, Master thesis (2015)
10. Zhang, P.: Study on the characteristics of temperature and frequency change dynamics of elastic pad in high-speed rail free track fastener system. Southwest Jiaotong University, Master thesis (2016)
11. International Organization for Standardization, ISO 3095: 2005: Railway applications-acoustics-measurement of noise emitted by rail bound vehicles (2005)

Dynamic Response Reconstruction to Supplement the Data Insufficiency

Chaodong Zhang, Jia He and Xiaohua Zhang

Abstract Due to sensor cost and installment accessibility, it is not practical to instrument sensors on every point of a structure and the measured set of dynamic responses is thus usually incomplete, thus the need to perform dynamic response reconstruction always arises, especially for a large civil structure. This study presents the novel Kalman filter (KF) based response reconstruction methods under known and unknown excitations. The underlying state estimation theories under known and unknown excitation are first introduced. Then dynamic response reconstruction methods are developed based on the state estimation in the framework of KF. For easy explanation and demonstration, a simple 4-story shear-type frame is employed in numerical study. The performances of the proposed KF based response reconstruction are examined. The effect of process and measurement noises covariance and spatial location of the measurement sensors to the reconstruction accuracy is investigated and discussed.

Keywords Dynamic response reconstruction · Kalman filter · Joint response · Excitation reconstruction

1 Introduction

Acquiring the dynamic response is vital for the vibration-based structural control and condition monitoring. The measurement insufficiency always arises due to the fact that the deployed sensors are always limited considering the fact that it is not rational

C. Zhang
Institute of Urban Smart Transportation & Safety Maintenance, College of Civil Engineering, Shenzhen University, Nanhai Ave 3688, Shenzhen 518060, Guangdong, China

J. He (✉)
Key Laboratory of Wind and Bridge Engineering of Hunan Province, College of Civil Engineering, Hunan University, Changsha 410082, China
e-mail: jiahe@hnu.edu.cn

X. Zhang
College of Civil Engineering, Fuzhou University, No. 2 Xueyuan Road, University Town, Fuzhou 350108, Fujian, China

© Springer Nature Singapore Pte Ltd. 2019

Y. L. Zhou et al. (eds.), *Data Mining in Structural Dynamic Analysis*,
https://doi.org/10.1007/978-981-15-0501-0_8

to install sensors on all components of a large-size civil structure. And the point-wise nature of current conventional sensors does not enable sensing the entire structural safety, especially the locations that are not accessible under in-service condition. This demand may be fulfilled through implementation of response reconstruction, which is to reconstruct the desired response of locations where no sensors are installed using the limited sensor measurement.

The dynamic response reconstruction methods can be generally classified into three types: the transmissibility concept based method, the empirical mode decomposition (EMD) based method, and the state estimation based method. For the transmissibility concept based methods, the responses of a structure at the inaccessible locations during its operation are reconstructed by transforming the response at other locations. Kammer [1] presented a transmissibility based response reconstruction method, in which the transmission matrix is formatted using the Markov parameter matrix. Basing on the generalized transmissibility concept in the frequency domain proposed by Ribeiro and Maia [2], Law and Ding [3] adopted this concept for dynamic response reconstruction in a substructure and also extended it to the wavelet domain function [4, 5]. However, for all applications using transmissibility concept, it requires to know the locations where forces or moments are applied. Since the pseudo-inverse operation is used, it is generally required that the number of reconstructed sensor channels should be no larger than the number of measurement sensor. Zhang et al. [6] utilized the truncated mode shape matrix in the forming of transmissibility matrix for response reconstruction.

In the EMD based method, the measurement data available at limited locations are decoupled into several intrinsic mode functions (IMFs) using the EMD method. Those IMFs are applied to extrapolate the dynamic response for the critical locations where the direct response measurements are unavailable. He et al. [7] presented a new method for structural response reconstruction at critical locations using measurements from remote sensors basing on the empirical mode decomposition with intermittency criteria and transformation equations derived from finite element modeling. Wan and Li [8] developed this method by combining transmissibility concept and made it applicable to the situation where closely spaced modes were presented and periodic excitation were applied. Ma et al. [9] reconstructed the transient response using Karhuen–Loeve mode decomposition. In general, this type of methods tremendously depends on the EMD techniques, and thus, the reconstruction accuracy is hard to be guaranteed.

In the state estimation based method, various estimators can be employed in kind of method. The Kalman filter is the most renowned estimator with a broad range of applicability. Zhang et al. [10] and Xu et al. [11] presented a Kalman filter (KF) based dynamic response reconstruction method, in which the state vector of generalized coordinates was obtained using the real-time responses measured by limited sensors; then the response at the locations of interest can then be reconstructed by multiplying their mode shapes with the estimated state vector. Kalman filter under unknown input was also used by Lourens et al. [12] for response reconstruction under unknown excitation using acceleration measurement. Liu et al. [13] derived an extended Kalman filter under unknown (EKF-UI) similar to the procedures of

KF-UI and applied the filter to estimate structural displacement and unknown inputs by fusing of displacement and acceleration. The optimal multi-type sensors placement for response reconstruction under unknown excitation has been investigated by Zhang and Xu [14], and in this following-up study, the reconstructed response and excitations are used for damage identification [15, 16].

This paper presents the Kalman filter based response reconstruction method. The feasibility and the performance of these methods are also investigated. The remaining section of this paper is outlined as follows. Some theoretical foundations for the Kalman filter based response reconstruction under known and unknown excitation will be introduced in Sect. 2. In Sect. 3, a 4-floor shear frame is employed to demonstrate the procedure as well as to examine the effectiveness of the proposed Kalman filter based response reconstruction. The effect of process and measurement noises covariance and spatial location of the multi-type sensors to the reconstruction accuracy is also investigated. Finally, some concluding remarks are given in Sect. 4.

2 Kalman Filter Based Response Reconstruction

2.1 State Space Equations of a Structure in Modal Coordinate

The vibration of a structure discretized into n degrees of freedom (DOFs) can be expressed as the superposition of the first several mode responses, i.e. $d(t) = \Phi^s q^s(t)$, where $\Phi^s \in \Re^{n\times s}$ is the collection of the selected s mass-normalized mode shapes and $q(t) \in \Re^s$ is the modal displacement vector. The dynamics can be represented in state space representation as

$$\dot{x}(t) = A_c x(t) + B_c u(t) \tag{1}$$

with

$$A_c = \begin{bmatrix} 0 & I \\ -\Omega^{s2} & -2\Xi^s\Omega^s \end{bmatrix}, B_c = \begin{bmatrix} 0 \\ \Phi^{sT} L \end{bmatrix} \tag{2}$$

where $x(t) = \{q^s(t)\ \dot{q}^s(t)\}^T \in \Re^{2s}$ denotes the state vector; $A_c \in \Re^{2s\times 2s}$ and $B_c \in \Re^{2s\times r}$ represent the continuous state matrix and input matrix; $\Omega^s \in \Re^s$ and $\Xi \in \Re^s$ are the diagonal matrices containing the eigenfrequencies ω_i, and the modal damping ratio ξ_i, respectively. The vector $u(t) \in \Re^r$ contains r inputs and the matrix $L \in \Re^{n\times r}$ is the mapping matrix relating the external excitation with the corresponding DOFs of the structure. If the observation vector includes displacement $d(t)$ and acceleration $\ddot{d}(t)$, the associated observation equation writes

$$y^m(t) = C_c^m x(t) + D_c^m u(t) \tag{3}$$

with

$$y^m(t) = \begin{Bmatrix} d(t) \\ \ddot{d}(t) \end{Bmatrix}, C_c^m = \begin{bmatrix} S_d \Phi^s & 0 \\ -S_{\ddot{d}} \Phi \Omega^{s2} & -2S_{\ddot{d}} \Phi^s \Xi^s \Omega^s \end{bmatrix}, D_c^m = \begin{bmatrix} 0 \\ S_{\ddot{d}} \Phi^{sT} \Phi^s L \end{bmatrix} \quad (4)$$

in which $y^m(t)$ is the observation vector. S_d and $S_{\ddot{d}}$ are the displacement and acceleration output distribution matrices, of which the jth row has one in the column corresponding to the number of the degree of freedom being measured in the jth row of the output vector $y^m(t)$ and zeros everywhere else.

Integrating over the sampling interval Δt and including the modeling error and measurement noise corruption, the continuous-time state space formulation in Eqs. (1) and (3) can be transferred into a discrete-time state space formulation as

$$x_{k+1} = A_d x_k + B_d u_k + w_k \quad (5)$$

$$y_k^m = C_d^m x_k + D_d^m u_k + v_k \quad (6)$$

where $x_k = x(k\Delta t)$ is the discrete-time state vector with $k = 0, 1, 2, \ldots$; Δt is the sampling interval; $w_k \in \Re^{2s} \sim N(0, Q)$ and $v_k \in \Re^m \sim N(0, R)$ represent the independent, white, and normally distributed processing and measurement noise vectors with covariance matrices Q and R, respectively. The relationship between continuous system and discrete system depends on the assumption made for the inter-sample behavior of the excitation u_k.

2.2 Dynamic Response Reconstruction Under Known Excitation

By combing the system Eq. (5) with the measurement Eq. (6), an unbiased and minimal variance estimator of state vector $\hat{\mathbf{x}}_k^+$ can be derived by virtue of Kalman filter as

$$\hat{x}_k = \left(I - K_k C_d^m\right)\left(A_d \hat{x}_k + B_d u_{k-1}\right) + K_k\left(y_k^m - D_d^m u_k\right) \quad (7)$$

in which the Kalman gain is

$$K_k = P_k C_d^{mT}\left(C_d^m P_k^x C_d^{mT} + R\right)^{-1} \quad (8)$$

Then the reconstructed responses are expressed

$$y_k^e = C_d^e \hat{x}_k + D_d^e u_k \quad (9)$$

in which C_d^e and D_d^e represent the output matrix and transmission matrix, respectively, corresponding to the DOFs of the key location, whose responses are to be reconstructed.

2.3 Dynamic Response Reconstruction Under Unknown Excitation

Assuming the filter with the initial unbiased estimate x_0^- and the error variance P_0^{x-}, the excitation and state estimates can be estimated recursively by the three steps in the following form:

$$\hat{x}_{k+1}^- = A_d \hat{x}_k^+ + B_d \hat{u}_k \tag{10}$$

$$\hat{u}_k = M_k\left(y_k^m - C_d^m \hat{x}_k^-\right) \tag{11}$$

$$\hat{x}_k^+ = \hat{x}_k^- + K_k\left(y_k - C_d^m \hat{x}_k^- - D_d^m \hat{u}_k\right) \tag{12}$$

where $\hat{x}_k^-$ and $\hat{x}_k^+$ denote the priori and posteriori state estimates at time instant k, respectively. The minimum-variance unbiased estimate of excitation $\hat{u}_k$ is obtained by Eq. (11) with the gain matrix M_k given by

$$M_k = \left(D_d^{mT} \tilde{R}_k^{-1} D_d^m\right)^{-1} D_d^{mT} \tilde{R}_k^{-1} \tag{13}$$

$$\tilde{R}_k = C_d^m P_k^{x-} C_d^{mT} + R^m \tag{14}$$

The minimum-variance unbiased estimate of the state vector $\hat{x}_k^+$ is obtained by Eq. (12) with the filter gain expressed as

$$K_k = P_k^{x-} C_k^{mT} \tilde{R}_k \tag{15}$$

The corresponding state estimation error covariance is now updated to the posterior state estimation error covariance as

$$P_k^{x+} = P_k^{x-} - K_k\left(\tilde{R}_k - D_d^m P_k^u D_d^{mT}\right) K_k^T \tag{16}$$

in which $P_k^u = \left(D_d^{mT} \tilde{R}_k^{-1} D_d^m\right)^{-1}$ denotes the excitation estimate error covariance. Then the optimal state estimate $\hat{x}_k^+$ at time instant k is propagated to the next time instant priori estimate $\hat{x}_{k+1}^-$ using Eq. (12) and its error covariance matrix is

$$P_{k+1}^{x-} = \begin{bmatrix} A_d & B_d \end{bmatrix} \begin{bmatrix} P_k^{x+} & P_k^{xu} \\ P_k^{ux} & P_k^{u} \end{bmatrix} \begin{bmatrix} A_d^T \\ B_d^T \end{bmatrix} + Q \tag{17}$$

in which $P_k^{xu} = \left(P_k^{ux}\right)^T = E\left[\left(x_k - \hat{x}_k^+\right)\left(u_k - \hat{u}_k\right)^T\right] = -K_k D_d^m P_k^u$ is the cross covariance of the estimate errors of both state and excitation. Consequently, unbiased minimum-variance estimates of state and excitation are simultaneously derived using the above three-step recursive filter. After the minimum-variance unbiased estimates $\hat{x}_k^+$ and $\hat{u}_k$ are obtained, the reconstructed responses y_k^e are expressed as

$$y_k^e = C_d^e \hat{x}_k^+ + D_d^e \hat{u}_k \tag{18}$$

We can see that the excitation sequences can be recursively estimated, provided that three-step filter is well structured by choosing the proper measurement locations and the number. It is worth highlighting that the sensor configuration should be optimally designed since improper sensor placement could cause divergence in state and input estimation, and thus, degrade the response reconstruction accuracy.

3 Numerical Study

3.1 The Shear Frame

A 4-story shear-type frame structure fabricated in steel as shown in Fig. 1 is employed as a numerical study. The column section and floor section are 10 mm × 30 mm and 60 mm × 30 mm, respectively. The corresponding story mass is 8.424 kg and lateral floor stiffness is 10.08 kN/m. The natural frequencies of the frame can be obtained through modal analysis as 6.05, 17.41, 26.67, and 32.72 Hz. Rayleigh damping model is adopted to include to damping effect, and the mass and stiffness damping coefficients are 0.53 and 1.44 × 10.4, respectively, corresponding to the first two modal damping ratios as 0.01.

The shear-type frame is horizontally excited by a base excitation. The force sequence is stochastic with the standard deviation of 10.0 N. The displacement and acceleration on each floor are calculated using Eqs. (6) and (7), in which the sampling interval is $\Delta t = 0.002$ s, and the sample duration is 20 s. Measurement noises are modeled as the Gaussian white noise with the standard deviation (STD) as 0.05 times the STD of noise-free responses, i.e., $R_0 = \text{diag}\{2.74 \times 10^{-8}, 9.30 \times 10^{-8}, 1.66 \times 10^{-7}, 2.16 \times 10^{-7}, 0.560, 0.646, 0.649, 0.925\}$. The process noise is set as $Q_0 = 1 \times 10^{-11}$ I, where I is the unit matrix with the dimension of the system model order 4. The standard deviation ratio between noise and noise-free response as shown in Eq. (19) lies between 5.01 and 6.66% as Tabulated in Table 1.

$$\text{RDP} = \frac{\text{std}(y_n - y_r)}{\text{std}(y_r)} \times 100 \tag{19}$$

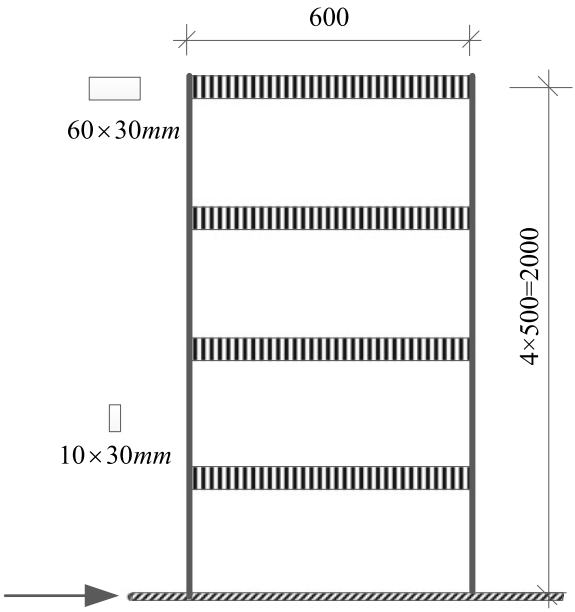

Fig. 1 Geometric configuration of a shear-type frame

3.2 Dynamic Response Reconstruction

The noise-corrupted displacement and acceleration on the fourth floor are utilized as the measurements to reconstruct the displacement and acceleration on other floors as well as the fourth floor. The performance of KF based response reconstruction is examined under the circumstances of known and unknown excitation, respectively. The four modes are all used in formatting Eqs. (1)–(2). Table 1 lists the RDP between the reconstructed responses and the real ones under known and unknown excitation. For comparison, the RDPs of the noise-corrupted responses are also tabulated in Table 1, in which y_r, y_n, y_e^k, and y_e^u denotes the real, noise-corrupted, estimated under known and unknown excitation, respectively. It is noted that when the excitations time histories are available, the displacement and acceleration RDP on the fourth floor is remarkably reduced from 5.06 and 5.44 to 0.07 and 0.18, respectively. It evidences that the KF based response reconstruction could partly remove the noises on the measurement sensors. The overall RDP average of the displacement and acceleration of these four floors is reduced from 5.03 and 6.20 to 0.04, and 0.23, respectively, indicating the KF based response reconstruction works well under known excitation. The time histories and the spectrum of the reconstructed displacement on the first floor (D1) and acceleration on the fourth floor (A4) are depicted in Figs. 2 and 3, respectively. It can be seen that the reconstructed responses match pretty well with the real ones in both time domain and frequency domain.

When the excitation time histories are unknown (excitation location are pre-defined), the performance of the proposed KF based response reconstruction degrades

Table 1 KF-based response reconstruction results

	D1	D2	D3	D4	A1	A2	A3	A4	$\overline{D}$	$\overline{A}$
y_n	5.06	5.02	5.02	5.01	6.46	6.45	6.45	5.44	5.03	6.20
y_e^k	0.07	0.04	0.02	0.03	0.30	0.20	0.23	0.18	0.04	0.23
y_e^u	3.01	2.80	2.12	1.80	10.97	15.55	12.66	5.47	2.43	11.16

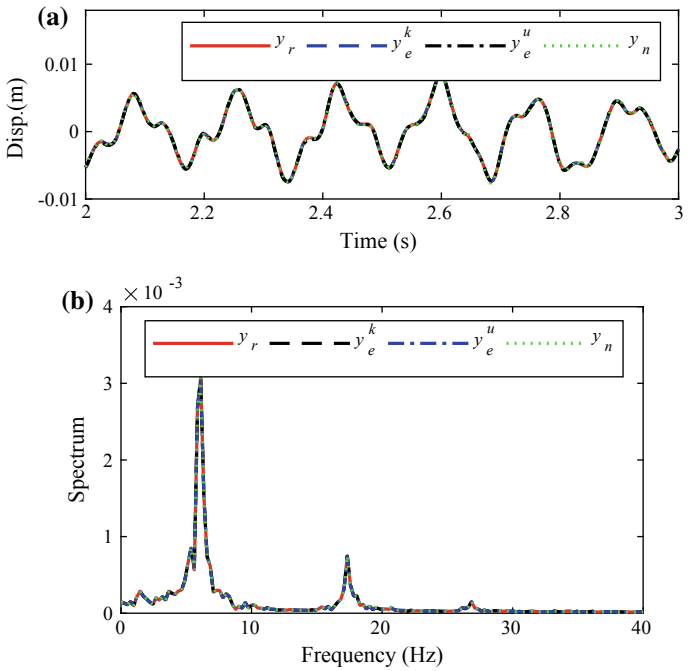

Fig. 2 Reconstructed displacement on the first floor: **a** time history and **b** the spectrum

slightly. The displacement RDP average decreases from 5.03 to 2.43, while the displacement RDP average increases from 6.20 to 11.16. The possible reason is that acceleration contains more vibrations of high modes. Figure 4 depicts the comparison between the reconstructed and the real excitation. The reconstructed excitation coincides with the real one. Figures 2 and 3 also show the time history and spectrum of the reconstructed responses (D1 and A4). The reconstructed responses match quite well with the real ones even under unknown excitation.

We can see that the proposed KF based response reconstruction works well for the circumstance of both known and unknown excitations. It should be pointed out that in this simulation study, the process noise and measurement noise (presented by the covariance matrices) are assumed known accurately, which probably contribute to the excellent response reconstruction results.

3.3 Discussion

The effect of Q and R. It is evident that the reconstruction accuracy is related to the process and measurement noise covariance. Although several methods have been proposed to estimate the values [17], the estimated values may be not accurate

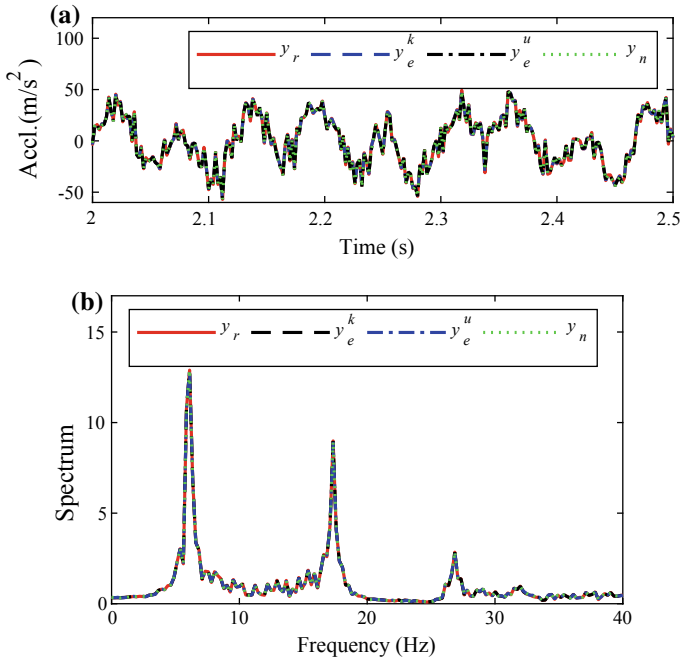

Fig. 3 Reconstructed acceleration on the fourth floor: **a** time history and **b** the spectrum

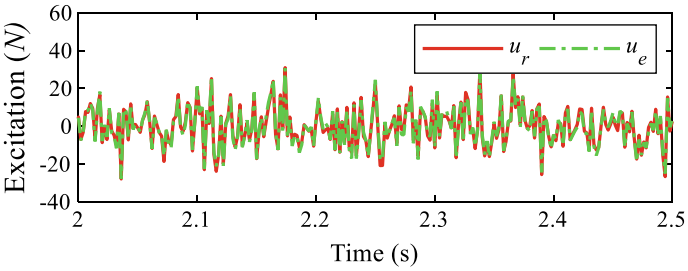

Fig. 4 Reconstructed excitation under unknown excitation

enough. To investigate the effect of Q and R to the response reconstruction results, the performances of proposed method are examined when Q and R are 100 times the accurate ones, i.e., $Q = 100\,Q_0$ and $R = 100\,R_0$. The results are tabulated in Table 2. The displacement and acceleration average RDPs are a bit larger than that in Table 1, but still keep a small value. These results demonstrate the robustness of the proposed method, especially the response reconstruction under unknown excitation.

The effect of sensor placement. The measurement sensors may be deployed in different locations. To investigate the effect of sensor placement, the accelerations on the first and fourth floor (A1 and A4) are assumed to be the measurement channels

Table 2 Response reconstruction with inaccurate Q and R

	D1	D2	D3	D4	A1	A2	A3	A4	$\overline{D}$	$\overline{A}$
y_e^k	0.92	0.60	0.52	0.53	4.08	4.02	4.82	2.70	0.64	3.91
y_e^u	3.01	2.80	2.12	1.81	10.97	15.54	12.64	5.47	2.43	11.16

in this case study. The reconstructed displacement on the first floor is shown in Fig. 5 when the excitation is known and in Fig. 6 when the excitation is unknown. We can see that the proposed method still produces quite excellent results when the excitations are known. However, when the excitations are unknown, the reconstructed response diverges. The reconstructed excitation as shown in Fig. 7 also testifies this point. Thus, for response reconstruction, the sensor types, location, and number should be properly selected, especially for the response reconstruction under unknown excitation.

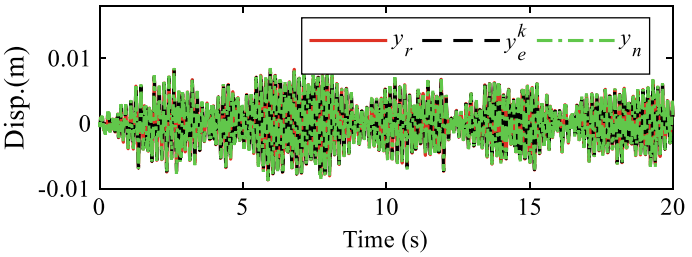

Fig. 5 Reconstructed D1 under known excitation when A1 and A4 are used as the measurement channels

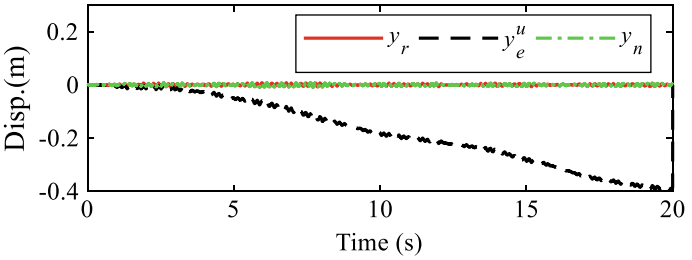

Fig. 6 Reconstructed D1 under unknown excitation when A1 and A4 are used as the measurement channels

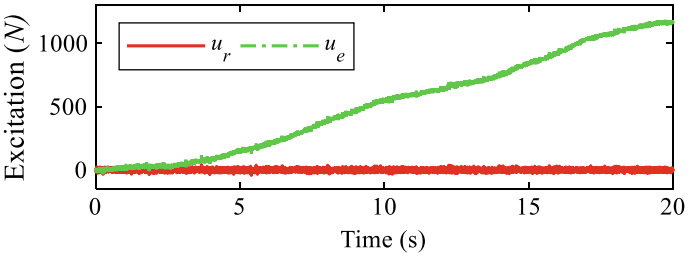

Fig. 7 Reconstructed excitation on under unknown excitation

4 Concluding Remarks

The Kalman filter based dynamic response reconstruction under known and unknown excitation has been introduced in this study. The feasibility and the effectiveness of the proposed methods have been examined through a simple 4-floor shear frame. Some concluding remarks can be given as:

(1) The proposed KF based method shows excellent capacity in reconstructing dynamic responses under known and unknown excitation. For the case of unknown excitation, the reconstruction accuracy is a bit degraded compared with that of known excitation.
(2) Multi-type responses (for instance, displacement and acceleration in the simulation study) could be fused to improve the reconstruction accuracy. Dynamic response of different types to the measurement could be reconstructed (for instance, measured acceleration could be used to reconstruct displacement).
(3) The performance of the proposed method is robust to the assignment of process and measurement noise covariance.
(4) The measurement sensors should be deployed selectively to ensure the proposed method function properly, especially for the response reconstruction under unknown excitation.

References

1. Kammer, D.C.: Estimation of structural response using remote sensor locations. J. Guid. Control Dyn. **20**(3), 501–508 (1997)
2. Ribeiro, J.S., Maia, N.: On the generalization of the transmissibility concept. Mech. Syst. Signal Process. **14**, 29–36 (2000)
3. Law, S.S., Li, J., Ding, Y.: Structural response reconstruction with transmissibility concept in frequency domain. Mech. Syst. Signal Process. **25**, 952–968 (2010)
4. Li, J., Law, S.S.: Substructural response reconstruction in wavelet domain. J. Appl. Mech. **78**, 041010 (2011)
5. Li, J., Law, S.S.: Damage identification of a target substructure with moving load excitation. Mech. Syst. Signal Process. **30**, 78–90 (2012)
6. Zhang, X.H., Zhu, S., Xu, Y.L., Hong, X.J.: Integrated optimal placement of displacement transducers and strain gauges for better estimation of structural response. Int. J. Struct. Stab. Dyn. **11**(3), 581–602 (2011)
7. He, J., Guan, X., Liu, Y.: Structural response reconstruction based on empirical mode decomposition in time domain. Mech. Syst. Signal Process. **28**, 348–366 (2012)
8. Wan, Z., Li, S.: Structural response reconstruction based on the modal superposition method in the presence of closely spaced modes. Mech. Syst. Signal Process. **42**, 14–30 (2014)
9. Ma, X., Vakakis, A.F., Bergman, L.A.: Karhunen-Loeve modes of a truss: transient response reconstruction and experimental verification. AIAA J. **39**(4), 687–696 (2001)
10. Zhang, X.H., Zhu, S., Xu, Y.L.: Multi-type sensor placement for structural health monitoring. In: 12th East Asia-Pacific Conference on Structural Engineering and Construction, Hong Kong, China (2011)

11. Xu, Y.L., Zhang, X.H., Zhu, S., Zhan, S.: Multi-type sensor placement and response reconstruction for structural health monitoring of long-span suspension bridges. Sci. Bull. **61**(4), 313–329 (2016)
12. Lourens, E., Papadimitrioua, C., Gillijnsc, S., Reyndersa, E., De Roeck, G., Lombaer, G.: Joint input-response estimation for structural systems based on reduced-order models and vibration data from a limited number of sensors. Mech. Syst. Signal Process. **29**, 310–327 (2012)
13. Liu, L., Su, Y., Zhu, J., Lei, Y.: Data fusion based EKF-UI for real-time simultaneous identification of structural systems and unknown external inputs. Measurement **88**, 456–467 (2016)
14. Zhang, C.D., Xu, Y.L.: Optimal multi-type sensor placement for response and excitation reconstruction. J. Sound Vib. **360**, 112–128 (2016)
15. Zhang, C.D., Xu, Y.L.: Structural damage identification via multi-type sensors and response reconstruction. Struct. Health Monit. **15**(6), 715–729 (2016)
16. Zhang, C.D., Xu, Y.L.: Structural damage identification via response reconstruction under unknown excitation. Struct. Control Health Monit. **24**(8) (2016). https://doi.org/10.1002/stc.1953
17. Odelson, Brian J., Rajamani, Murali R., Rawlings, James B.: A new auto-covariance least-squares method for estimating noise covariances. Automatica **42**(2), 303–308 (2006)

A Proposed Method for the Use of the IBIS-FS in Experimental Modal Analysis of Buildings

Massoud Sofi, Elisa Lumantarna, Priyan Mendis and Lihai Zhang

Abstract This chapter attempts to simplify experimental modal analysis for use in structural health monitoring through remote sensing of vibrations using the microwave interferometry technology. The commercially available Image By Interferometric Survey-Frequency for Structures (IBIS-FS) radar has been used in bridge and historical building monitoring with comparable results to accelerometers. In this chapter, a repeatable method for experimental modal analysis of a high-rise building with an irregular plan using the IBIS-FS is presented.

Keywords IBIS-FS · High-rise building · Experimental modal analysis

1 Introduction

The structural health of a building is typically monitored through changes in its dynamic properties. Significant deviations in natural frequencies or mode shapes can indicate a potential loss of stiffness in the structure. Experimental Modal Analysis (EMA) is a commonly used method to determine the dynamic properties of buildings. Vibration data for the EMA is conventionally captured by accelerometers placed strategically in a building to capture an envelope of the building's response to dynamic excitations. This method is often time-consuming, costly, impractical, intrusive to the building's operations and risky in buildings close to collapse [1, 2]. This research aims to develop a method that utilises the Image By Interferometric Survey-Frequency of Structures (IBIS-FS) radar to collect vibration data on medium- and high-rise buildings remotely for experimental modal analysis.

The following chapter documents the relevant literature that was reviewed in this research project. The literature is divided into Structural Health Monitoring (SHM), Experimental Modal Analysis (EMA) and the Image by Interferometric Survey-Frequency of Structures (IBIS-FS) radar. The first section explains the relevance of EMA to SHM, whilst the second covers the various methods of EMA detailing their advantages and disadvantages with respect to the objectives of the research.

M. Sofi · E. Lumantarna · P. Mendis · L. Zhang (✉)
Department of Infrastructure Engineering, University of Melbourne, Melbourne, Australia
e-mail: lihzhang@unimelb.edu.au

© Springer Nature Singapore Pte Ltd. 2019

Y. L. Zhou et al. (eds.), *Data Mining in Structural Dynamic Analysis*,
https://doi.org/10.1007/978-981-15-0501-0_9

The final section presents the available information on the IBIS-FS radar, including the method and reliability in which it captures data, the advantages over other data capturing options and the various applications that the IBIS-FS has successfully been applied for EMA.

2 Review

2.1 Structural Health Monitoring

Structural health monitoring is the regular observation of a structure's performance through various sensing techniques to identify any damage to prevent failure [3]. Damage, in a more general term, is any variation of the system that has an adverse effect on the structural performance. The identification of dynamic characteristics of structures in high seismic risk area is extremely important, as well as structures that have been exposed to severe events such as fires, explosions and tornadoes. Since damage can only be identified by a comparison of current and initial states, continuous monitoring of the structure is required.

There is increasing research in vibration-based damage identification methods in order to detect and prevent the likelihood of severe infrastructure failures that cause loss of life and tremendous economic loss. Vibration-based damage detection utilises the fact that the modal properties of a building are functions of its physical properties, where the physical properties such as the mass, damping and stiffness are proportional to the natural frequency, mode shapes and critical damping of a building.

Therefore, any changes in stiffness of a structure and hence any damage can be detected through analysis of a building's modal parameters [4]. When a structural model is used in conjunction with vibration-based damage identification methods, the achievable damage identification levels can be increased from levels 1 and 2 to level 3 [5]. Level 4 requires greater analysis of the fatigue life analysis of the structural members to provide a prediction on the remaining service life of the structure.

The shift in natural frequencies is commonly used in damage detection of structures. Farrer and Doebling's study on damage detection of Alamosa Canyon Bridge found that either very precise measurements or large levels of damages are required due to the low sensitivity of frequency shifts [5]. They also reported that using the shift in natural frequency as a measure of damage had less statistical variation from random error sources than other modal parameters, such as mode shapes or critical damping. When natural frequencies are found to be noticeably lower than expected, it can be concluded that there is an abnormal loss of stiffness [6]. Begg et al. [7] identified limitations of the method in that higher modes are more sensitive to damage identification, but higher modes are typically harder to identify due to their lower energy content in comparison with the dominant primary natural frequencies.

The other large limitation in the method is that because natural frequencies are a global characteristic of the structure, it cannot provide spatial localised information of damage.

2.2 Experimental Modal Analysis

Experimental Modal Analysis (EMA) is a method that seeks to determine the dynamic properties of a system, sometimes referred to as the modal properties. In the context of a structural system, the dynamic properties include the critical damping ratio, natural frequencies and vibration mode shapes [8], where the natural frequencies are the inverse of the natural periods, which is the time taken for a mode shape to complete a cycle. This research was focused on capturing the natural frequencies of buildings through EMA.

Data Collection Methods
EMA involves the collection of data from a structural system's excitation and its conversion into a power spectral density (PSD) for analysis to determine the dynamic properties. A structural system's response data can be in the form of displacements, velocities or accelerations due to a dynamic force. These quantities can be recorded in several ways and can be captured as a result of ambient, free or forced vibrations of a structure. Ambient vibrations in a structure are typically caused by traffic, wind or earthquake loadings, forced vibration is instigated by artificial means such as mechanical shakers, and free vibrations are caused by dropping large weights upon the structure [9].

Ambient loading is often preferred over artificial excitation in EMA as it is freely available, accurately represents the expected dynamic loading of the building, does not require building access and does not affect neighbouring structures and the people using the building [10]. However, earthquake response of a building is better captured due to the unpredictability of earthquakes [11].

Data Analysis
The PSD can be obtained by applying a discrete Fourier transform to the dynamic displacement data of a building, negating the need for knowing the forcing function [12]. When applying a Fourier transform to a typical displacement quantity, a PSD is produced as in Fig. 1 [9]. The natural frequencies of a structure are the frequencies at which an applied oscillating force causes an amplified response in the system [13]. Several methods of identifying natural frequencies of a system from the FRF have been developed, each has advantages and a typical approach for researchers is to use a combination of methods to compare the results from each method [14, 15].

Methods of Modal Identification
Two main methods of output modal identification are used, nonparametric and parametric, where the former is developed in the frequency domain and the latter in the time domain [16].

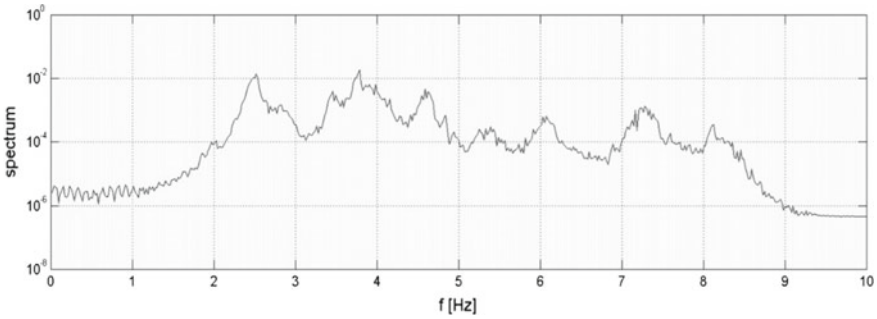

Fig. 1 Power spectral density of an SDOF system [9]

The simplest form of nonparametric modal identification is the basic frequency domain or Peak Picking (PP) technique [17]. Through visual inspection of the PSD of a system, the natural frequencies can be detected as the corresponding frequencies of abnormally sharp peaks in the amplitude. Figure 1 shows a PSD produced from experimental data.

This technique is desirable as it is simple and quick to adopt, making it ideal for repeatability by other engineers with a grasp of basic structural dynamics. However, because the frequency selection is subjective it is not always an accurate assessment of the natural frequencies. This is a problem if the natural frequencies are closely spaced on the frequency spectrum or if no peaks are prominent in a PSD.

The Frequency Domain Decomposition (FDD) method is an attempt to remove the uncertainty of the PP method by decomposing every frequency line in the PSD into a set of Auto-Spectral Density Functions (ASDFs) that correspond to a specific Single Degree of Freedom (SDOF) using the Singular Value Decomposition (SVD) technique. Figure 2 shows graphically how two frequencies can be separated into two SDOF systems using the SVD technique. The natural frequency is identified where a strong correlation between the dominant singular vector (eigenvector) and the singular values (eigenvalue) of the SVD for a particular SDOF is found [18].

The FFD and EFDD methods overcome the limited applicability of the PP method to structures with closely spaced modes indistinguishable by eye [18]. The disadvantage of using the FFD and EFDD methods is their additional effort in computational time.

Parametric Modal Identification

Parametric modal identification seeks to attain a system model instead of a physical model for a dynamic system, where a physical model is produced based on the fundamental laws of physics and a system model uses calibration of experimental data to model input and output behaviour through system identification [20].

Parametric models are created by the assumption that a mathematical model formulated from a set of parameters estimated during the system identification can represent what occurs and is usually in the form of a differential equation [21]. Parametric modal identification of output-only systems focuses on system identification with

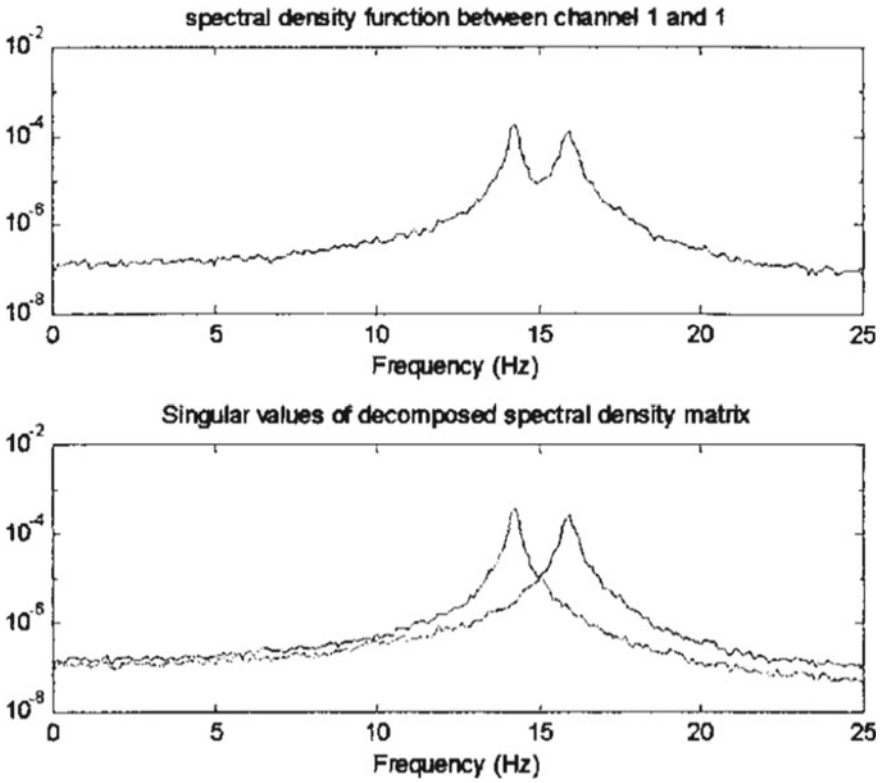

Fig. 2 Graphical representation of the decomposition of an FRF into singular values [19]

an assumption that the unknown input to the system is replaced by white Gaussian noise [10, 22]. There are many system identification methods that exist for output-only systems; however, their complexity often makes them impractical for quick assessment of modal parameters and methods such as the Autoregressive Moving Average Vector (ARMAV) have never achieved an acceptable level of robustness and efficiency for civil engineering applications due to issues with convergence, sensitivity to initial values and large computational burdens for multivariate systems such as buildings [10]. The Stochastic Subspace Identification in its covariance-driven (SSI-Cov) and data-driven forms (SSI Data) are both commonly applied parametric techniques for EMA. The SSI Data method functions solely on the measured output response, whereas the SSI-Cov method requires estimated covariance functions from the output time histories to estimate the modal parameters [23].

3 Microwave Interferometric Radars

Microwave interferometry has emerged as a new technology to remotely measure the vibration response of a range of structures. The Image by Interferometric Survey-Frequency for Structures (IBIS-FS) is a commercial radar instrument with interferometric capacity that was designed and constructed by the Italian company Ingegneria Dei Sistemi (IDS, Pisa, Italy). It has been commonly used as a remote sensing tool to measure the dynamic response of bridges, historical and modern buildings, stay cables and guyed masts. The IBIS-FS radar utilises the Stepped-Frequency Continuous Wave (SF-CW) [24] and differential interferometry techniques [25] to accurately measure both static and dynamic displacements of several points of a structure simultaneously on a radial plane (Fig. 3). Each discontinuity of a surface represents a potential source of reflection of electromagnetic waves sent out by the radar, acting as a series of virtual sensors [26]. These points are defined in the IBIS-FS software as range bins (Rbins), and any number of them can be used in combination as a source of displacement data. The red line in Fig. 3 shows the span from which an Rbin could be selected based on the set-up of the IBIS-FS.

The IBIS-FS has a dual purpose, to identify the position of a target and to detect the differential displacements over time through changes in phase information of reflected microwave signals [1]. Figure 4 shows how the displacement of an object alters the phase information received from a reflected microwave. It then follows that the change in phase is proportional to the displacement of the target from the original measurement. The software provided with the IBIS-FS allows the user to obtain the Signal-to-Noise Ratio (SNR) of a particular Rbin as well as a polar plot of the phasor data for an Rbin's time history, where the phasor is the complex number that describes the amplitude and phase values of the received signal for each Rbin.

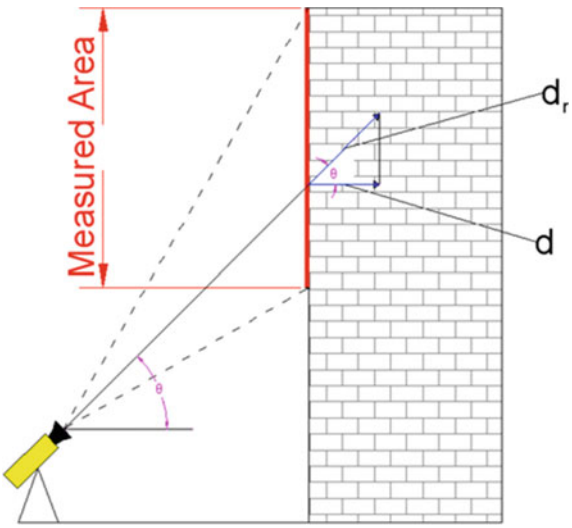

Fig. 3 Illustration of radial and projected displacement

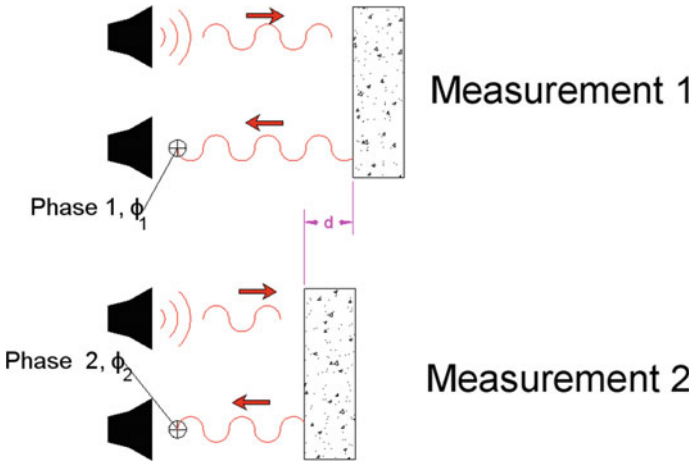

Fig. 4 Relationship between differential displacement and reflected phase information

IBIS-FS User Considerations

The instrument's highest sampling rate of 200 Hz occurs up to a distance of approximately 200 m (Fig. 5), with respect to range resolution, where the range resolution is the minimum distance between two targets in the same line of sight of the IBIS-FS radar [27]. As this research is only concerned with capturing one target along a line of sight on a building, the green line of Fig. 5 will be most relevant, and hence only buildings that are taller than 250 m will cause a drop-in sampling rate. Obstructions such as trees and light poles will cause microwaves to be reflected and giving the observer a false sense of the deflections of the intended target, and this can be avoided by tilting the angle of the IBIS-FS to ensure that any objects obstructing the view of

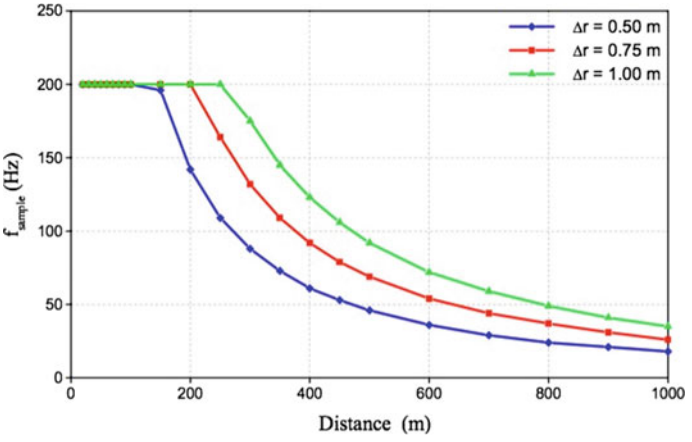

Fig. 5 Relationship of sampling rate to distance from the target, for three range resolutions

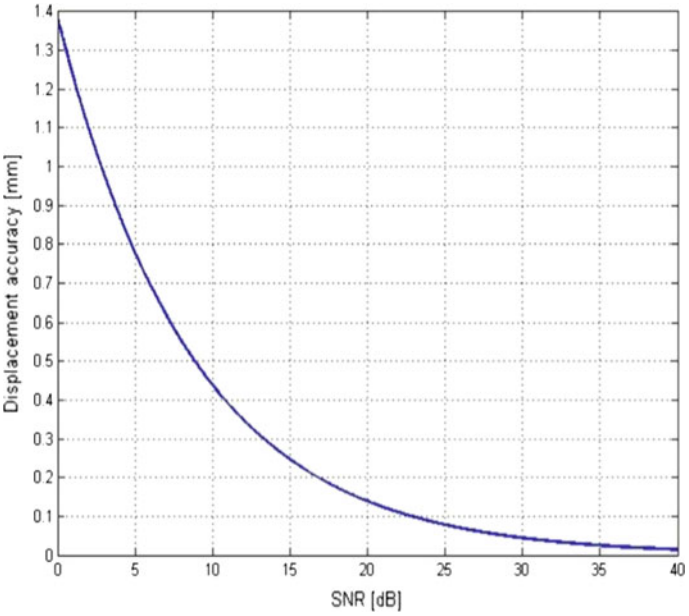

Fig. 6 Relationship between displacement accuracy and SNR of the IBIS radar

the target are not within range or by planning in advance a suitable location for the set-up of the equipment.

Accuracy of the displacement data captured by the IBIS-FS reduces proportionally with the SNR, which is an indication of the reflectivity of the target n. Figure 6 shows the relationship between the SNR in dB and displacement accuracy. The SNR can be improved by installing artificial reflectors at the specific points where the displacement is being monitored [28].

However, this process would remove the appeal of the IBIS-FS being a remote sensing system that does not require installation of devices to the target building. Even with considerably low SNR, the IBIS is still able to produce accuracy within 1.4 mm.

3.1 Applications of IBIS-FS

As IBIS-FS is able to simultaneously detect the displacements of different targets located at different distances from the sensor, it can be utilised to identify dynamic responses and modal parameters of a cable-stayed bridge from a single measurement. By considering the cables as a taut string, the tension force can be obtained from natural frequencies measured. Benedettini and Gentile [29] and Luzi, Crosetto and Cuevas-González [2] conducted dynamic tests using IBIS-FS on stay cables and a

guy, respectively; tension forces of the members were successfully computed from the natural frequencies measured.

IBIS-FS interferometric radar only provides a displacement plot in a radial line of sight. Therefore, it is most suitable for structures with a dominant dimension, for instance, bridges that span longer in horizontal direction and towers as they span in vertical direction. IBIS-FS can be used for ambient vibration tests for structural health monitoring of bridges, as well as measurement of vertical deflections of bridge under live load as part of reception tests of new bridges [26]. Conservation of ancient towers and minarets, which are part of World Heritage, is extremely important, and hence continuous surveillance on structural health is needed. The IBIS-FS radar has been used for structural health monitoring of numerous famous ancient towers in Italy, such as the bell tower of the Cathedral of Florence [30] and the Leaning Tower of Pisa [31].

The IBIS-FS radar cannot provide a bidirectional displacement measurement [32]. Therefore, IBIS-FS is not as widely used on buildings. There is less literature on applications of IBIS-FS on high-, medium- and low-rise buildings. One of them is measurements of ambient vibrations of a reinforced concrete wall building which includes a double basement, a ground floor and 10 storeys and is also irregular in geometry and rigidity [33].

3.2 Alternative Vibration Sensing Devices

Accelerometers

Accelerometers are commonly used in vibration testing of large structures, but have many drawbacks. The limitation of accelerometers is that they need to be installed at the point where the vibration is occurring and connected to a computer for data transmission. When needing to analyse a structure quickly from several points, the set-up time involved with accelerometers can be tedious and intrusive to building occupants. Complex wiring is required to connect all the accelerometers in their desired locations to a central computer. Additional time is needed to process the acceleration data through double integration into the displacement quantities for modal analysis [34].

Alternative Remote Sensing Devices

Remote sensing devices that use lasers are less suited for global structural monitoring as they only capture a single point of data, where several points along a building's plane of motion are required to construct the mode shapes and determine the natural frequencies [1]. Terrestrial Laser Scanning (TLS) has been reported as insufficient for SHM as displacement errors up to 10 mm were recorded [35]. However, whilst scanning laser vibrometry using lamb waves has been found to be enough in identifying local damage in metallic structures [35], they are not useful for identifying global natural frequencies and mode shapes of a building.

Global Positioning System (GPS) technology has been used in SHM but has failed to be successful due to a low sampling rate of approximately 10 Hz [34]. GPSs require remote sensors to be installed atop the target building for data collection, and this means that this data collection method is not entirely remote from the building, unlike the IBIS-FS which is entirely remote [36]. One study found that an error of 7 mm ± (baseline length in km) occurred with the use of GPS technology and described its main limitations are its inability to capture oscillatory movements and the 20 min time delay between observation and availability of measurement [36].

Advantages of Using IBIS-FS

Using IBIS-FS for capturing dynamic displacement data is advantageous as:

1. It takes approximately 20 min to set up and begin recording from arriving at the site. Compared with the lengthy process of setting up an array of accelerometers throughout a building, the IBIS-FS is relatively simple to set-up.
2. Its high sensitivity results allow acquisition of signals and identification of the characteristics of key vibration modes from up to 1 km away [28, 31].
3. Dynamic testing can be accomplished without accessing the structure, and there is no effect on daily operation of the structure.
4. It is not affected by adverse weather conditions and can operate at day and night times.
5. The simplicity of the radar technology is particularly useful when applied to the measurement of dynamic characteristics of structural elements such as tall buildings, damaged structures, ancient towers and stay cables that are costly or very difficult to access by conventional techniques such as contact sensors.
6. It captures displacements in the time domain making it compatible with both parametric and nonparametric EMA method categories.
7. The provided software (IBISDV) processes the raw data in real time, where each measurement set undergoes removal of linear and mean trends and has a 0.5 Hz high-pass filter and a cosine tapering with a damping of 20% applied before a Fourier transform is performed to reduce the data processing time for the user and to allow for immediate feedback of the data quality [4].

Few papers detail a method for passively excited EMA of building structures using the IBIS-FS despite its potential for improving the process of EMA of buildings by superseding traditional accelerometers for data capture. The IBIS-FS is limited in the fact that it can only take measurements of one building face at a time, where a set of 4 or more accelerometers could be used to construct an envelope of a building's dynamic response. For torsional responses of a building, at least three IBIS-FS machines will be required to capture a 3D envelope of the building's displacement.

The aim of this research was to determine the situations in which the IBIS-FS provides reliable results and when should the user exercise caution in interpretation of the results from the radar.

3.3 Case Study

The field measurement methodology is one aspect that is important when using remote sensing system towards data collection. It was chosen because the system of methods within field measurement allows the researchers to conduct testing in real-world conditions, unlike in theoretical or laboratory testing. Similarly, a survey or literature review methodology would be inefficient in achieving the objectives of this research as there are few engineers that could be questioned on the topic and there are few papers describing the use of IBIS-FS in EMA of buildings. By conducting field measurements, the researchers are able to identify through first-hand experience, the optimal conditions and limitations associated with the application of the IBIS-FS radar in EMA of buildings. The results obtained using this methodology will have higher prestige but will require extremely detailed accounts of testing methods in order to validate results and withstand scrutiny.

3.4 Methodology

The aim of the pilot study was to produce an easily repeatable and reliable method for the identification of the first few modes of a building's structure using the IBIS-FS equipment in conjunction with EMA. As shown above in the literature review, the IBIS-FS captures comparable results to accelerometers, which are currently a popular instrument in EMA but are limited to capturing data of a single point [1, 4]. The method undertaken in this research to develop a repeatable method for the use of IBIS-FS in EMA on buildings was to conduct field experiments and parametric studies on the collected data. Two noticeably different buildings with varying ambient conditions were the subjects of the field experiments.

Parameters of Interest
Parametric studies were performed on two different buildings located in Melbourne, Australia. The buildings had significantly different physical and dynamic characteristics.

1. The Redmond Barry Building (RBB) at the University of Melbourne's Parkville Campus and
2. A residential High-rise Building in Docklands (HBD), Melbourne CBD. This building's anonymity will be preserved for legal reasons.

The parameters were demarcated into three sections: the IBIS-FS set-up, building layout and ambient conditions. The parameters collected for each test are summarised in Table 1.

Data Collection and Analysis
The displacement data of both buildings was captured under ambient conditions with strong winds being the chosen method of building excitation. In both cases, the

Table 1 Parameters of IBIS-FS field test on buildings

	RBB	HBD
1. *IBIS-FS set-up*		
Tilt of IBIS-FS (°)	45	60
Height of IBIS-FS (m)	1.2	1.2
Distance from building (m)	24	50
Eccentricity to building's centre of rigidity	Unknown	0 m
2. *Building layout*		
Height (m)	39	100
Primary structural stability system	Shear walls	Core and podium[a]
Weak axis direction	North	North
Primary façade material	Brick	Glass[b]
3. *Ambient conditions*		
Wind speed (km/h)	35	37.8
Wind direction	North	North
Presence of vibrations from machinery or construction	No	Alimak on side of building, not in operation

[a]Podium from ground floor to fourth floor
[b]At the time of testing, the HBD was in the final stages of façade construction, and as such, some of the façades were not complete. The researchers used this to their advantage as the exposed slabs and columns were potentially strong virtual reflective surfaces

wind speeds were equal to or greater than 35 km/h at the time of displacement data collection and acted in the direction parallel with the buildings' weaker axis. The two days for testing were selected in advance based on wind speed forecasting provided from WillyWeather who supplies information based on data from the Bureau of Meteorology for the Olympic Park gauging station [37]. The wind speed was also checked during the time of testing to get an estimate of the actual wind speed at the time of data collection.

Floor layouts indicating the centre of rigidity of the HBD were obtained prior to testing of that building. This was used to plan the location of the IBIS-FS radar in relation to the building so as to align the radar with minimal eccentricities from the building's theoretical line of motion. The height of the HBD building was taken from the construction drawings, but the buildings' actual height was not measured to confirm this. The theoretical natural modes of the structure were obtained from a finite element model constructed in ETABS by the building's designers.

Information on the RBB was less readily available, and researchers deemed the creation of a finite element model of the building out of the scope of the research. The height of the RBB was estimated by counting the floors, and assuming an average floor height, this value was not confirmed on site.

Similarly, the distances from the IBIS-FS set-up to the buildings' faces were not measured accurately. The distance was paced out for the RBB test and estimated from trigonometry in the HBD test.

For the HBD and RBB, at least 4 Rbins with relatively high SNRs were selected up to the height of the building for analysis of their displacement–time histories. The displacement–time histories obtained from the IBIS-FS had a moving average of four points applied to it before being converted into the frequency domain using the fast Fourier transform capabilities of an Excel spreadsheet. The resulting PSDs were then put into a logarithmic scale, and 10 and 0.1 Hz low- and high-pass filters were applied to allow for clearer viewing of the peaks in amplitude. The peak picking method was employed to estimate the first three natural frequencies of the building where it was applicable.

Alternate frequency domain PSD plots of the same Rbins were also obtained from the IBISDV software to compare the quality of the PSD plots created by the researchers using a basic data formatting method and the method employed by the IBISDV software.

The resulting natural frequencies obtained from the PSD plots for the HBD were then compared with the theoretical natural frequency output of the ETABS finite element modelling as done in the research of [38, 39]. In the absence of a finite element model of the RBB, the PSD plots were compared with two empirical equations for determining the natural frequency of buildings [40, 41]:

$$f = b \cdot 0.09 \cdot H \tag{1}$$

$$f = 46/H \tag{2}$$

where

H Height of building.
b Dimension of building parallel to loading.

4 Results and Discussion

4.1 Method for Use of IBIS-FS in Building EMA

The natural frequencies recorded of the HBD test were obtained by using the following method:

1. *Prior to testing*:
    a. Obtain or create a finite element model of the building with a sufficiently high level of detail of the structural system to determine its centre of rigidity and the first few modes of vibration.

b. Obtain a building floor plan to plot the centre of rigidity and potential points of IBIS-FS set-up points with consideration for surrounding obstructions.
c. Visit the site to confirm possible locations where the line of sight of the IBIS-FS would have an uninterrupted view in line with the building's weakest axis and centre of rigidity.
d. Monitor the wind forecast speed and direction from appropriate local weather gauging station.
e. Select a day for testing from the forecast where wind speed is equal to or greater than 35 km/h.

2. *Collect data (as per IBIS-FS manual)*
3. Data processing

a. Elect appropriate Rbins along the length of the building based on largest SNR.
b. View polar chart of a Rbin's data reliability to determine if a suitable Rbin has been selected.
c. Repeat (a) and (b) until 4 or more Rbins are selected.
d. Obtain PSD from the IBISDV software for PP analysis.
e. For a closer examination of data, download displacement data from IBIS-FS to perform an FFT so that the user can apply high- and low-pass filters, moving averages and data exclusion techniques to clean up data making natural frequencies more apparent.

The method followed for the test at RBB was essentially the same as shown above with the only points of difference being the building itself, the lack of a finite element model, the unknown eccentricity of the measurement and the accessibility of the land surrounding the building. The HBD had a greater choice of positions to set up the IBIS-FS, whilst RBB was limited to a single place governed by surrounding trees and other buildings.

4.2 Range bin Selection

Figures 7 and 8 show the variance of the SNRs of the Rbins spread up the height of the target building. The X-axis shows the Rbin number in ascending order relative to the height of the building, and the Y-axis shows the SNR of that particular Rbin.

4.3 Frequency Plots

Raw data collected from the measurements taken for the HBD and RBB was processed, and the PSD obtained from displacement–time histories is presented in Figs. 9

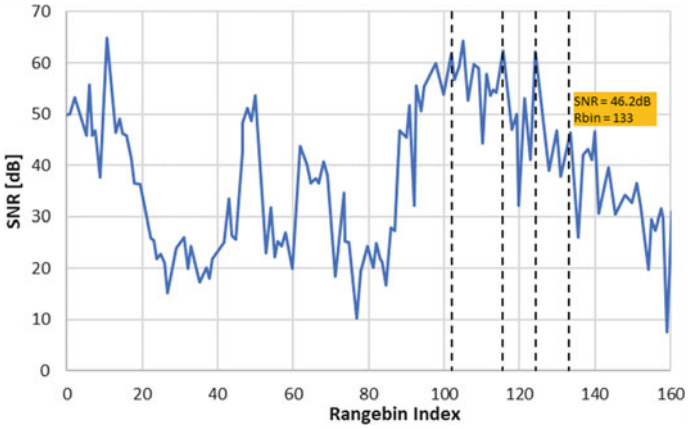

Fig. 7 Graph showing SNR of each Rbin up to a height of HBD

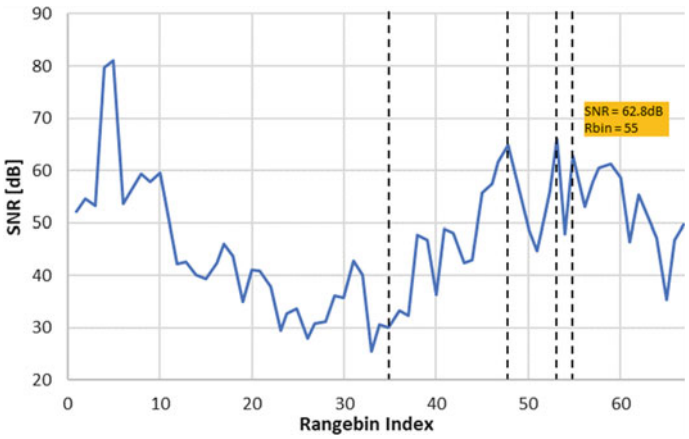

Fig. 8 Graph showing SNR of each Rbin up to a height of RBB

and 11, respectively. PSD plots obtained from the IBISDV software for the HBD and RBB are shown in Figs. 10 and 12. Rbin analysed is shown in Fig. 7.

High-Rise Building in Docklands

The first three obvious peaks of the PSD graphs from both methods were identical, and they gave the first three natural frequencies of the building's structure to be 0.324 Hz, 0.416 Hz and 0.72 Hz, respectively.

There were no identifiable peaks in the PSD obtained from the FFT in the Excel spreadsheet for the RBB, and as such, no frequencies could be identified. However, the PSD obtained from the IBISDV software did have one significant peak, indicating that the first natural frequency was at 0.88 Hz.

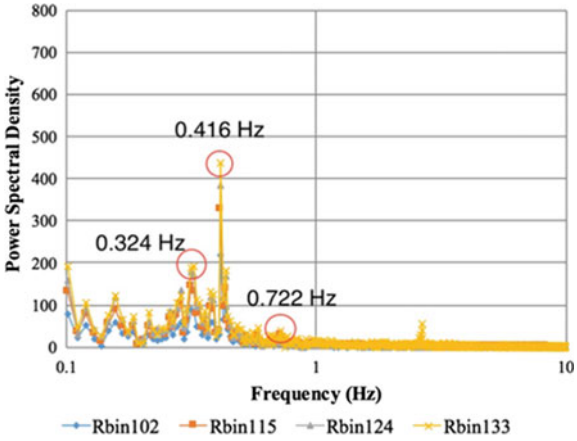

Fig. 9 PSD of HBD selected Rbins obtained from FFT analysis performed in Excel

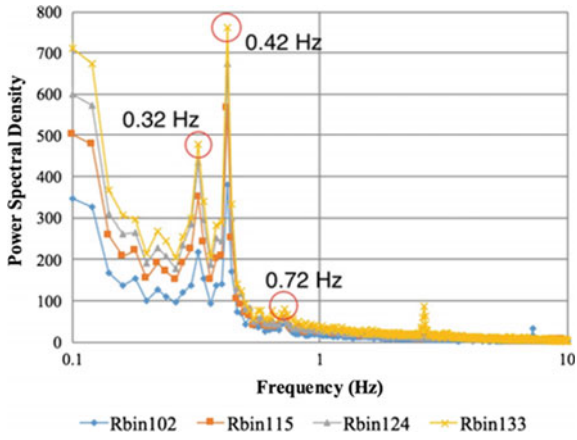

Fig. 10 PSD of HBD selected Rbins obtained from IBISDV software

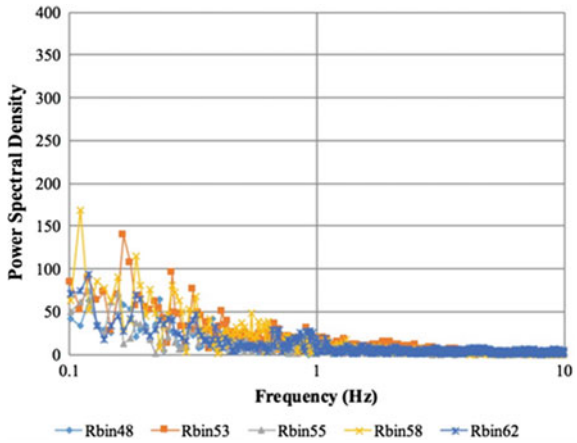

Fig. 11 PSD for RBB selected Rbins obtained from FFT analysis (Excel)

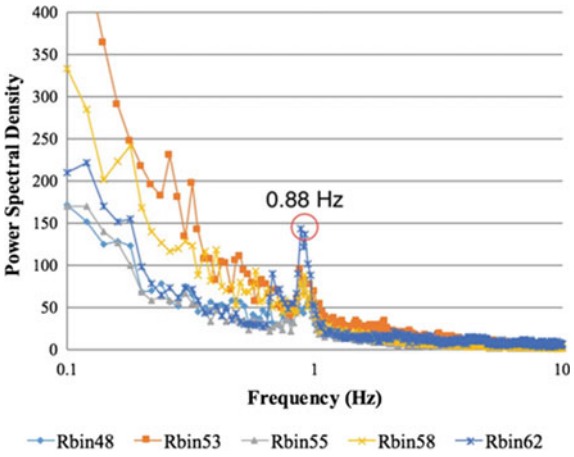

Fig. 12 PSD of RBB selected Rbins obtained from (IBISDV software)

Table 2 Comparison of theoretical and experimental natural frequencies

Building	Mode	Frequency (Hz)				
		Theoretical		Experimental	Error (%)	
HBD	First	0.362		0.324	10.4	
	Second	0.543		0.416	23.3	
	Third	0.841		0.722	14.1	
RBB	First	0.99	1.18	0.88	11.1	25.4

Redmond Barry Building

Comparison of theoretical and experimental natural frequencies.

Table 2 shows a comparison of the theoretical and experimental natural frequencies. The theoretical frequencies of the HBD were obtained from a detailed ETABS finite element model. The theoretical first natural frequencies of the RBB were obtained from the two empirical Eqs. (1) and (2), respectively.

4.4 Phasor Polar Charts

The following phasor charts were obtained from random Rbins in the HBD and RBB tests as shown in Figs. 13 and 14, respectively. The radial coordinate represents the amplitude, and the angular coordinate represents the phase angle of the received signal, where the phase represents a position on the wave signal that relates to an oscillatory movement.

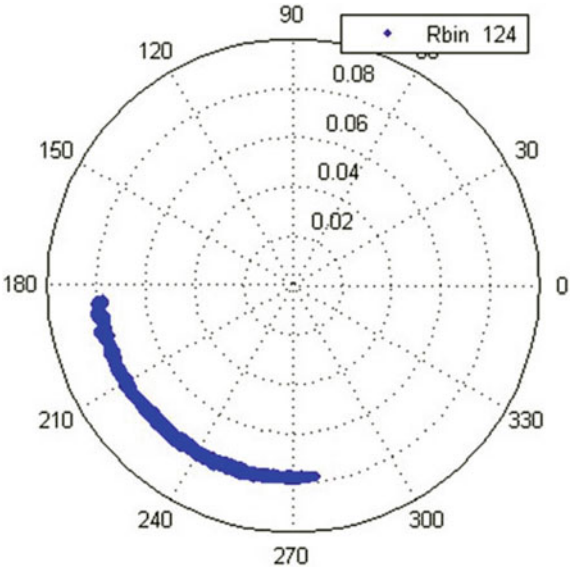

Fig. 13 Phasor plot of HBD Rbin 124

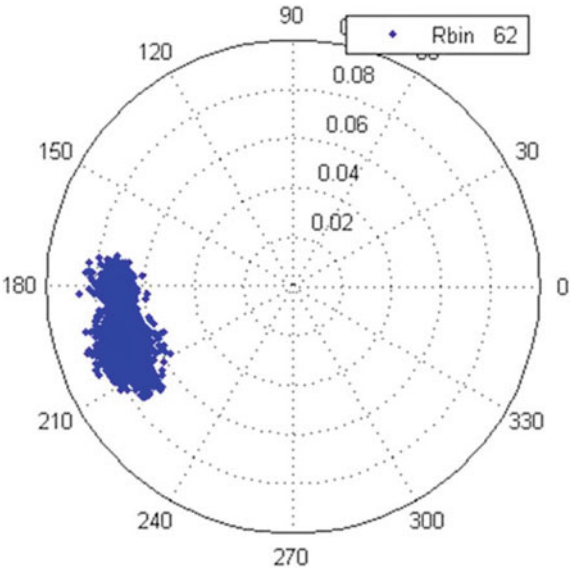

Fig. 14 Phasor plot of RBB Rbin 62

4.5 The Effects of External Factors

Wind Speed and Direction

The use of wind as a source of passive building excitation appeared to be very effective as it was enough in both tests to excite the buildings to a reasonable extent. In both tests, the wind speed was equal to or greater than 35 km/h and acted in the direction parallel to the buildings' weaker axis allowing for maximum potential displacements. This approach whilst effective was time-consuming as the researchers' testing days were dictated by the almost random fluctuations in weather conditions.

This is a disadvantage in using this approach as the researchers were not free to collect data at their own leisure and had to constantly monitor the weather reports for a suitable testing day and time. If this method were to be implemented by a consultant, a generous amount of time would need to be allowed for data to be captured to wait for the ideal wind conditions.

Building Location and Surroundings

The location of the buildings and their surrounding obstructions heavily influenced the ability of the researcher to capture data with the IBIS-FS. The RBB only allowed for testing on side of its face as surrounding buildings were obstructing the view. The side from which the data collection took place was also restricted in that another building's footprint impeded the placement of the IBIS-FS any further than 24 m from the target. For this reason, the HBD was selected as a suitable test subject, and it was in a sparsely populated area of Melbourne allowing for multiple choices of placement of the IBIS-FS. This became very important because the HBD building was more than double the height of the RBB and required the IBIS-FS to be placed further away from the target source. Placing the IBIS-FS, a suitable distance from the target is critical because as the IBIS-FS is tilted further back to observe the building face the number of Rbins within the building's face decreases. For this reason, it was better to place the IBIS-FS an appropriate distance from the building. These issues are more likely to become a problem when collecting data from tall buildings in densely populated areas. The number of obstructions to the line of sight increases, and there is likely to be less space to move the IBIS-FS a suitable distance from the building.

4.6 Data Analysis and Interpretation

Range bin Selection

The Rbins for analysis were selected based on the graph shown in Figs. 7 and 8 for HBD and RBB, respectively, where the Rbins with the higher SNR favoured. The SNR for all the Rbins in both tests was at least above 50, and this corresponds with a high level of accuracy in the measurement of displacements in millimetres as shown

in Fig. 6. Additionally, only Rbins that were higher up the building were selected. The first reason is that higher levels of a building have larger displacements under wind load compared to lower levels, which give more accurate measurements and larger responses in the PSD plots allowing for ease of employing the PP method. Higher Rbins were selected as some trees, street lights and power poles were surrounding the building. These lower Rbins often gave dynamic displacement data of these obstacles rather than the building.

The PSD plots obtained for the HBD via the Excel FFT method and the IBISDV software yielded the exact same results for the value of the experimental first three natural frequencies. The PP method was simple to apply to the HBD PSD plots, as the first three frequency peaks were relatively prominent.

These values compared favourably with the ETABS finite element modelling with errors of 10.4%, 23.3% and 14.1% for the first three modes, respectively. This difference in the frequencies between the theoretical and the experimental is likely due to discrepancies between the decisions made in the finite element modelling and the actual construction of the building on site. Given that the model is not a true representation of the as-built building, it is reasonable to say that the results validate each other to some extent. The values obtained from the EMA could be used to calibrate the finite element model, and the building can be retested in future to observe any changes in the first three frequencies.

The PSD plots of the RBB conversely were not as easily analysed with the PP method. No clear peaks were identified in the Excel FFT spreadsheet, but the PSD plot from the IBISDV software contained a solitary prominent peak. This sole value was used to compare with the empirical Eqs. (1) and (2). Reasonable errors of 11.1% and 25.4% were recorded given the nature of the empirical equations used for comparison.

Overall, the IBISDV software PSD plots were found to be superior to the FFT method in the Excel spreadsheet. The software can produce a peak in the RBB experiment but also displayed the PSD with an overall higher amplitude making it easier to observe any peaks.

Phasor Plots

The polar plots shown in Figs. 13 and 14 give an indication of the signal's phasor over time for the duration of data collection. The HBD phasor tended to have very little deviations in terms of amplitude and a large change in phase angle. The phase angle relates to a proportional change in position of the target Rbin. The RBB phasor plot showed relatively large deviations in the signals' amplitude and smaller changes in phase angle. This correlates with the fact that the RBB is shorter than the HBD, and as such, smaller deflections due to a similar loading pattern are possible. The difference between the variations in amplitude of the signal between the RBB and HBD plots indicates that some façade types could affect the reflection of the microwaves. The RBB had a mostly brick façade with minimal discontinuities up to the height of the building, whereas the HBD had an unfinished glass façade, but had obvious discontinuities in the form of exposed slabs and balconies.

5 Concluding Remarks

The method developed by the researchers required the following key components for obtaining reliable results in using the IBIS-FS for EMA of high-rise irregular buildings:

- The approximate centre of rigidity and theoretical frequencies of the building obtained from a detailed finite element model.
- A floor plan of the building documenting its approximate centre of stiffness.
- Sufficient space at the base of the building to set up the IBIS-FS in a position that allows unobstructed views in line with the building's weaker axis and centre of rigidity.
- A wind speed above 35 km/h acting in the direction of the building's weaker axis.
- A building with sufficient surface discontinuities to allow for reliable data collection.
- Selection of Rbins closer to the top of the building to avoid capturing the dynamic response of objects other than the intended target.

In terms of data analysis, the peak picking method was found to be adequate and easy to apply for the role of determining the natural frequencies.

Recommendation for Further Study
Areas for extension on this research are numerous, and the researchers recommend either a combination or one of the following topics:

- Retrieving data for buildings in densely populated cities using the long-range capabilities of the IBIS-FS.
- Using several Rbins up to the entire length of a building to construct the mode shapes.
- Analysing in depth the effects of different façade materials on the quality of the raw data.
- Utilising alternative methods of modal identification to extract the natural frequencies.

References

1. Pieraccini, M., Fratini, M., Parrini, F., Atzeni, C., Bartoli, G.: Interferometric radar vs. accelerometer for dynamic monitoring of large structures: an experimental comparison. NDT & E Int. 258–264 (2008)
2. Gentile, C., Crosetto, M.: Radar-based operational modal testing of large structures, two case studies in Spain. In: 6th International Operational Modal Analysis Conference. Gijon (2015)
3. Balageas, D.: Introduction to structural health monitoring. In: Balageas, D., Fritzen, C.-P., Güemes, A. (eds.) Structural Health Monitoring. London, UK, ISTE (2006)

4. Stabile, T.A., Perrone, A., Gallipoli, M.R., Giocoli, A., Pignatti, S., Palombo, A., Pascucci, S.: Joint application of non-invasive techniques to characterise the dynamic behaviour of engineering structures. In: Proceedings of 15 WCEE, Lisbon (2012)
5. Doebling, S.W., Farrar, C.R., Prime, M.B.: A summary review of vibration-based damage identification methods. Shock Vib. Dig. **30**(2), 91–105 (1998)
6. Salawu, O.S.: Detection of structural damage through changes in frequency: a review. Eng. Struct. **19**(9), 718–723 (1997)
7. Begg, R.D., Mackenzie, A.C., Dodds, C.J., Loland, O.: Structural integrity monitoring using digital processing of vibration signals. In: Proceedings, 8th Offshore Technology Conference, 3–6 May, Houston, Texas 2 (1994)
8. Poovarodom, N., Charoenpong, K.: Identification of dynamic properties of low-rise RC building by ambient vibration measurements during construction. In: The 14th World Conference on Earthquake Engineering, pp. 1–8. Beijing (2008)
9. Ren, W.-X., Zong, Z.-H.: Output-only modal parameter identification of civil engineering structures. Struct. Eng. Mech. **17**(3–4), 429–444 (2004)
10. Peeters, B., Roeck, G.D.: Reference-based Stochastic subspace identification for output-only modal analysis. Mech. Syst. Signal Process. **13**(6), 855–878 (1999)
11. Yu, E., Skolnik, D., Whang, D.H., Wallace, J.W.: Forced vibration testing of a four-story RC building utilizing the nees@UCLA mobile field laboratory. In: Proceedings of the 8th U.S. National Conference on Earthquake Engineering (2006)
12. Schwarz, B.J., Richardson, M.H.: Experimental Modal Analysis. CSI Reliability Week (1999)
13. Avitabile, P.: Experimental modal analysis: a simple non-mathematical presentation. Sound Vib. **35**(1), 20–31 (2001)
14. Diaferio, M., Foti, D., Giannoccaro, N.I.: Identification of the modal properties of a building of the Greek heritage. Key Eng. Mater. **628**, 150–159 (2015)
15. Simkin, G.B., Beskhyroun, S., Ma, Q.T., Wotherspoon, L.M., Ingham, J.M.: Experimental modal analyses of buildings during the Cook Strait earthquake sequence (2014)
16. Cunha, Á., Caetano, E., Magalhães, F., Moutinho, C.: From input-output to output-only modal identification of civil engineering structures. SAMCO (Structural Assessment, Monitoring and Control) (2006)
17. Bendat, J., Piersol, A.: Engineering Applications of Correlation and Spectral Analysis. Wiley, New York, NY (1993)
18. Hoa, L.T., Tamura, Y., Yoshida, A., Anh, N.D.: Frequency domain versus time domain modal identifications for ambient excited structures. In: International Conference on Engineering Mechanics and Automation (ICEMA), pp. 1–2 (2010)
19. Brincker, R., Ventura, C., Andersen, P.: Damping estimation by frequency domain decomposition. In: 19th International Modal Analysis Conference, vol. 9, pp. 698–703 (2001)
20. Magalhães, F., Caetano, E., Cunha, Á.: Challenges in the application of Stochastic modal identification methods to a cable-stayed bridge. J. Bridge Eng. **12**(6), 746–754 (2007)
21. Andersen, P., Brincker, R., Kirkegaard, P.H.: Theory of covariance equivalent ARMAV models of civil engineering structures. In: Proceedings-SPIE the International Society for Optical Engineering, SPIE International Society for Optical, pp. 518–524 (1996)
22. Bodeux, J.B., Golinval, J.C.: Application of ARMAV models to the identification and damage detection of mechanical and civil engineering structures. Smart Mater. Struct. **10**(3), 479–489 (2001)
23. Chauhan, S.: Subspace algorithms in modal parameter estimation for operational modal analysis, perspectives and practices. In: Proceedings of the IMAC XXXIV a conference and Exposition on Structural Dynamics. Orlando (2016)
24. Taylor, J.D.: Ultra-Wideband Radar Technology. CRC Press (2001)
25. Henderson, F.M., Lewis, A.J.: Manual of remote sensing. In: Principles and Applications of Imaging Radar, 3rd ed. Wiley and Sons (1998)
26. Gentile, C., Bernardini, G.: Radar-based measurement of deflections on bridges and large structures. Eur. J. Environ. Civil Eng. **14**(4), 495–516 (2010)

27. Gentile, C.: Radar-based measurement of deflections on bridges and large structures, advantages, limitations and possible applications. In: IV ECCOMAS Thematic Conference on Smart Structures and Materials, Porto, pp. 1–20 (2009)
28. Ingegneria Dei Sistemi, IBIS Surveyor v.01.00-User Manual. Pisa, Italy (2013)
29. Benedettini, F., Gentile, C.: FE modelling of a cable-stayed bridge based on operational modal analysis. In: Proceedings of the IMAC XXVI, a Conference and Exposition on Structural Dynamics (2008)
30. Pieraccini, M., Fratini, M., Parrini, F., Pinelli, G., Atzeni, C.: Dynamic survey of architectural heritage by high-speed microwave interferometry. IEEE Geosci. Remote Sens. Lett. **2**, 28–30 (2005)
31. Atzeni, C., Bicci, A., Dei, D., Fratini, M., Pieraccini, M.: Remote survey of the leaning tower of Pisa by interferometric sensing. IEEE Geosci. Remote Sens. Lett. **7**(1), 185–189 (2009)
32. Pieraccini, M.: Monitoring of civil infrastructures by interferometric radar: a review. Sci. World J. (2013)
33. Negulescu, C., Luzi, G., Crosetto, M., Raucoules, D., Roullé, A., Monfort, D., Pujades, L., Colas, B., Dewez, T.: Comparison of seismometer and radar measurements for the modal identification of civil engineering structures. Eng. Struct. **51**, 10–22 (2013)
34. Celebi, M., Prescott, W., Stein, R., Hudnut, K., Behr, J., Wilson, S.: GPS monitoring of dynamic behaviour of long-period structures. Earthq. Spectra **15**(1), 55–66 (1999)
35. Park, H.S., Lee, H.M.: A new approach for health monitoring of structures, terrestrial laser scanning. Comput. Aided Civil Infrastruct. Eng. **22**, 19–30 (2007)
36. Knecht, A., Manetti, L.: Using GPS in structural health monitoring. In: SPIES's 8th Annual International Symposium on Smart Structures and Materials. Newport Beach (2001)
37. Willy Weather, Melbourne Wind Forecast. Retrieved 2016, from Willy Weather. http://www.wind.willyweather.com.au/vic/melbourne/melbourne.html (2016)
38. Russo, S.: Using experimental dynamic modal analysis in assessing structural integrity in historic buildings. Open Const. Build. Technol. J. **6**, 357–368 (2014)
39. Moayedi, F., Soleimani-Dashtaki, S., Ventura, E.C.: Determination of modal properties of an irregular 20-story concrete shear wall building. In: Proceedings of the 33rd IMAC, a Conference and Exposition on Structural Dynamics. Orlando (2015)
40. Chun, Y.-S., Yang, J.-S., Chang, K.-K., Lee, L.-H.: Approximate estimations of natural periods for apartment buildings with shear-wall dominant system. In: 12th World Conference on Earthquake Engineering. Auckland (2000)
41. Ellis, B.R.: An assessment of the accuracy of predicting the fundamental natural frequencies of buildings and the implications concerning the dynamic analysis of structures. Proc. Inst. Civ. Eng. **69**, 763–776 (1980)